LIBRARY
Michigan State
University

PLACE IN RETURN BOX to remove this checkout from your record.
TO AVOID FINES return on or before date due.

DATE DUE	DATE DUE	DATE DUE

MSU Is An Affirmative Action/Equal Opportunity Institution
c:\circ\datedue.pm3-p.1

AUTOMATED MEASUREMENT OF 3-D FIBER ORIENTATION DISTRIBUTION IN INJECTION MOLDED COMPOSITES

By

Jeffrey M. Wille

A DISSERTATION

Submitted to
Michigan State University
in partial fulfillment of the requirements
for the degree of

DOCTOR OF PHILOSOPHY

Department of Mechanical Engineering

1993

ABSTRACT

AUTOMATED MEASUREMENT OF 3-D FIBER ORIENTATION DISTRIBUTION IN INJECTION MOLDED COMPOSITES

By

Jeffrey M. Wille

In order to model short fiber composites adequately it is essential to have an accurate measure of the distribution of fiber orientation within the material. Unfortunately, short fiber composites often possess complex three-dimensional distributions which are very difficult to measure. Current surface-analysis based techniques have limited ability to measure orientation components which are perpendicular to the cutting plane, and are incapable of measuring fiber length, which is essential for a correct representation of the fiber orientation distribution. Hence, there is relatively little known about flow-induced fiber orientation and the relationships between fiber orientation and material properties.

A new technique which overcomes these problems is based on optical microscopic sectioning of transparent composites with opaque tracer fibers. With this method a complete 3-D description of the material structure is obtained, from which the fiber orientation distribution is determined by 3-D image analysis. The results from transparent systems can be generalized to more common opaque systems through non-dimensional analysis.

An experimental injection molding apparatus and an imaging system were developed to manufacture and analyze sample materials. Calibration tests demonstrated

the ability of the system to measure the orientations of individual fibers 600 μm in length with an average error of less than 4 degrees in all orientations, and their lengths with an average error of less than 4 percent. The average rate of data acquisition and analysis using a 25 MHz 68030 microprocessor was 11.6 min/mm^3. Experiments with high fiber content (30 wt%) materials with complex fiber orientation distributions demonstrated the suitability of the technique for the analysis of injection molded materials.

The potential of this approach has been demonstrated by investigating the influence of a cylindrical obstacle in the gate of an injection mold on the material properties and flow-induced fiber orientation of rectangular coupons.

The present method is compared quantitatively with published fiber orientation distribution results obtained with a standard surface analysis method and found to be at least as accurate and several times faster when specimen preparation time is considered.

Copyright by

JEFFREY MILTON WILLE

1993

To my wife and parents

for their unconditional love and support.

ACKNOWLEDGMENTS

Many thanks to my advisor, Dr. McGrath, who provided invaluable support and encouragement in the execution of this project, and to my guidance committee for their helpful suggestions and insights. Many thanks also to the German exchange students who contributed their talents in numerous ways. In particular, to Thomas Weber for his assistance in the design and construction of the injector and optimization of the injection process. To Stefan Reimann for his testing and characterization of the injection apparatus and the properties of molded specimens. To Martin Westerbecke for his research of transparent composites, imaging systems, and assistance in the optimization of PMMA/BK-10 processing. To Nils Schöche for his development of the **Fibor** data visualization program and assistance in the production and analysis of sample materials. Also to Bin Lian for his tireless calibration work and contribution to the **Pseudo** calibration program, and to Dan Griffin for his contribution to the writing of the **MCFG** motion control program and the scripting language that allows the automation of complex scanning patterns and image analysis procedures.

I am grateful for the opportunity of working with these outstanding individuals and I am pleased to count them among my friends. I would like to thank the Research Excellence Fund of Michigan for their generous financial support of this project. Most importantly, I would like to thank my wife, Celi, for her assistance and encouragement.

TABLE OF CONTENTS

LIST OF TABLES x

LIST OF FIGURES xi

NOMENCLATURE xiv

DEFINITION OF TERMS xv

1 INTRODUCTION 1

1.1 Objectives 2
1.2 Fiber Reinforced Polymer Materials 3
1.3 Injection Molding of Short Fiber Reinforced Composites 4
1.3.1 Description 4
1.3.2 Characterization of the Mold Filling Process 4
1.3.3 Dimensionless Parameters 6
1.4 Flow-Induced Fiber Orientation 9
1.4.1 Mold-Filling Code 11
1.4.2 Observed Flow-Induced Fiber Orientations 14
1.4.3 Theory of Flow-Induced Fiber Orientations 16
1.5 Fiber Length Degradation 17
1.6 Measurement of Fiber Orientation 18
1.6.1 Importance 19
1.6.2 Imaging Methods 20
1.6.3 Current Methods of 2-D Fiber Orientation Measurement . . . 25
1.6.4 Current Methods of 3-D Fiber Orientation Measurement . . . 28
1.7 Fiber Orientation Prediction 32
1.8 Material Property Prediction 37
1.9 Observed Influence of FOD on Material Properties 41
1.10 Characterization of the Fiber Orientation Distribution 42
1.10.1 Orientation Distribution Function 42

1.10.2 Tensor Representation of the Orientation Distribution 45

2 NEW METHOD OF FIBER ORIENTATION MEASUREMENT 49

2.1 Optical Sectioning 49

2.1.1 Refractive Index Matching 52

2.1.2 Advantages 54

2.1.3 Disadvantages 56

2.2 3-D Image Analysis 56

2.2.1 Preprocessing 57

2.2.2 Image Segmentation 58

2.2.3 Orientation Measurement 64

2.2.4 Length Measurement 66

2.2.5 Additional Measurements 66

3 DEVELOPMENT OF THE APPARATUS 67

3.1 Injection Molding Equipment 67

3.1.1 Overview 67

3.1.2 Fiber Chopper 68

3.1.3 Mold 69

3.1.4 Injector 72

3.1.5 Data Acquisition 76

3.2 Imaging Equipment 76

3.2.1 Overview 76

3.2.2 Microscope 76

3.2.3 Motion Control 77

3.2.4 Stepper Motor Controller 79

3.2.5 Data Acquisition Circuit 79

3.2.6 Video Equipment 79

4 DEVELOPMENT OF THE SOFTWARE 80

4.1 **Chop** 81

4.2 **Acquire** 82

4.3 **MCFG** 85

4.4 **Step** 88

4.5 **Pseudo** 89

4.6 **Thin3D** 90

4.6.1 Uniform Removal of Voxels 92

4.6.2 Prohibiting Shortening of Lines 94
4.6.3 Preserving Connectivity of the Image 95
4.6.4 Implementation Problems With Real Images 102
4.6.5 Program Features 104
4.7 **3D-FODAS** 105
4.7.1 Determination of Fiber Orientation 106
4.7.2 Determination of Fiber Length 106
4.7.3 Presentation of Results 107
4.7.4 Program Features 110
4.8 **DiffFOD** 111
4.9 **Fibor** 113

5 EXPERIMENTAL PROCEDURE **116**
5.1 Testing the Injection Molding Apparatus 116
5.1.1 Calibration 116
5.1.2 Performance Envelope (Characterization) 118
5.1.3 Optimization of Injection Process 118
5.2 Production of Transparent Composite Specimens 119
5.2.1 Combining Matrix and Fiber Materials 119
5.2.2 Refractive Index Matching 119
5.3 Calibration of Software 121
5.3.1 Pseudo Data 124
5.3.2 Single Fiber Tests 124
5.3.3 Orthogonal Specimen 125
5.3.4 Surface Ellipse Measurement 126
5.4 Testing the Repeatability of the Imaging Process 127
5.5 Gate Obstacle Specimens 128
5.5.1 Imaging 131
5.5.2 Mechanical Testing 133
5.6 Cavity Obstacle Specimen 134

6 ANALYSIS **136**
6.1 Image Processing 136
6.2 Image Analysis 137
6.3 Surface Ellipse Analysis 138
6.4 Comparison of FODs 139
6.4.1 Quantitative Analysis (**DiffFOD**) 139

6.4.2 Qualitative Analysis (Fibor) 141
6.5 Analysis of Mechanical Testing Data 141

7 RESULTS AND DISCUSSION 142
7.1 Apparatus 142
7.1.1 Performance 142
7.1.2 Hardware Repeatability (Variability in Processing Conditions) 143
7.1.3 Optimization of the Injection Process 146
7.2 Production of Transparent Composites 147
7.3 Software Calibration Results 149
7.3.1 Pseudo Data 149
7.3.2 Single Fiber Tests 150
7.3.3 Orthogonal Specimen 153
7.3.4 Comparison of Surface Ellipse and Optical Sectioning Methods 159
7.4 Variability in Imaging 162
7.5 Influence of a Gate Obstacle on Fiber Orientation Distribution 167
7.6 Influence of a Gate Obstacle on the Modulus of Elasticity 169
7.7 Comparison of z Component Measurement With Published Results. . 174
7.8 Influence of a Cavity Obstacle 177

8 CONCLUSIONS AND RECOMMENDATIONS 179
8.1 Evaluation of the Injection Apparatus 179
8.2 Evaluation of the Imaging Apparatus 181
8.3 Evaluation of the Software 182
8.4 Influence of Gate Obstacle 185
8.5 Comparison With Literature Data 185
8.6 Evaluation of the Method as a Whole 185
8.7 Recommendations for Future Work 186
8.8 Concluding Remarks 188

APPENDICES 189
A REFRACTIVE INDICES OF THERMOPLASTIC MATERIALS . . 189
B ENGINEERING DRAWINGS 190
B.1 Mold 190
B.2 Injector 195
C INJECTION PROTOCOL 201
D SPECIMEN DATA SHEETS 204

LIST OF REFERENCES **223**

LIST OF TABLES

1.1 Temperature scales for dimensionless parameters. (Davis, 1986) . . . 6
1.2 Four dimensionless parameters for a rectangular cavity. (Richardson, 1988) . . . 8
1.3 Herman's f_p parameter estimated from various FOD measurement techniques. (Wetherhold and Scott, 1990) . . . 27

4.1 Scan sequence for 3-D thinning algorithm. . . . 94
4.2 Adjacency matrix of voxel neighbors. . . . 96
4.3 Icosahedron statistics. . . . 108

5.1 Properties of PMMA. . . . 120
5.2 Properties of BK-10 glass. . . . 120
5.3 Refractive indices of PMMA and BK-10 glass vs wavelength. . . . 122
5.4 Refractive indices of PMMA and BK-10 glass vs temperature. . . . 123
5.5 Transparent specimen naming scheme. . . . 129
5.6 Polished thickness of gate obstacle specimens. . . . 131

7.1 Fiber/Matrix combinations with matched refractive indices. . . . 147
7.2 x-y calibration - PMMA [Fiber 1]. . . . 151
7.3 x-y calibration – PMMA [Fiber 2]. . . . 151
7.4 z calibration – single fiber in epoxy. . . . 152
7.5 x-z calibration with a single fiber in air. . . . 153
7.6 Comparison of FOD tensors from the first set of orthogonal scans. . . 157
7.7 Comparison of FOD tensors from the second set of orthogonal scans. 157
7.8 Differences between combined and individual tensors from first orthogonal scans. . . . 158
7.9 Differences between combined and individual tensors from second orthogonal scans. . . . 158
7.10 Total fiber lengths from orthogonal scans (μm). . . . 159
7.11 Comparison of processing conditions. . . . 174

A.1 Refractive indices of transparent thermoplastics at 23 °C, 589 nm. . . 189

LIST OF FIGURES

1.1 Non-isothermal mold filling model. 5
1.2 Surface ellipse method of orientation measurement. 28
1.3 Eulerian angles. 44

2.1 Example of Hough transform coordinate system. 59
2.2 Illustration of angle segregation algorithm. 61

3.1 Schematic of injection molding apparatus. 68
3.2 Photograph of fiber chopper. 69
3.3 Exploded view of mold assembly. 70
3.4 Photograph of assembled mold. 71
3.5 Exploded view of injector assembly. 74
3.6 Schematic of imaging apparatus. 77
3.7 Photograph of imaging apparatus. 78

4.1 Graphical user interface for **Chop** program. 82
4.2 Graphical user interface for **Acquire** program. 84
4.3 Graphical user interface for Event Timer. 84
4.4 Graphical user interface for **MCFG** program. 87
4.5 Graphical user interface for **Step** program. 89
4.6 Graphical user interface for **Pseudo** program. 90
4.7 Scan directions used in Thin3D. 93
4.8 Application of the adjacency matrix. 97
4.9 Unthinned image. 102
4.10 Thinned image. 103
4.11 Graphical user interface for **Thin3D** program. 105
4.12 Subdivision of the unit icosahedron. 108
4.13 Sample FOD generated by **3D-FODAS**. 109
4.14 Graphical user interface for **3D-FODAS** program. 111
4.15 Ellipsoid angles calculated by **DiffFOD**. 111

4.16 Graphical user interface for **DiffFOD** program. 112
4.17 Sample FOD field produced by **Fibor** 114
4.18 Graphical user interface for **Fibor** program. 115

5.1 Orthogonal calibration specimen location. 126
5.2 Surface image showing fiber ellipses. (100x magnification) 127
5.3 Specimen and gate geometry. 128
5.4 Specimens made without gate obstacle. 130
5.5 Specimens made with gate obstacle. 130
5.6 Scan locations for gate obstacle specimens. 132
5.7 Optical cross section of transparent composite. (100x magnification) . 133
5.8 Centerline scan locations for gate obstacle specimens. 134
5.9 Specimen with cavity obstacle. 135
5.10 Scan locations for specimen with cavity obstacle. 135

6.1 Planar ellipse tensor deviations. 140
6.2 Ellipsoid tensor deviations. 140

7.1 Piston speed data. 143
7.2 Injection temperatures for 18 injections. 144
7.3 Temperature profile. 145
7.4 Fiber length distributions. 146
7.5 Optimization of neat PMMA molding. 147
7.6 Sample composite with poorly distributed fiber material. 148
7.7 Transparency of PMMA w/BK-10 vs PMMA w/E-glass. 149
7.8 Calibration image: uniform fiber orientation distribution. 150
7.9 Orthogonal specimen viewed from the negative z axis. 154
7.10 Orthogonal specimen viewed from the positive x axis. 155
7.11 Orthogonal specimen viewed from the negative y axis. 156
7.12 Optical sectioning versus surface ellipse method: specimen No8. . . . 160
7.13 Optical sectioning versus surface ellipse method: specimen Ob7. . . . 161
7.14 3-D view of a_{11} and a_{33} tensor components from specimen No8. . . . 163
7.15 3-D view of a_{11} and a_{33} tensor components from specimen Ob7. . . . 164
7.16 Repeatability of imaging. 165
7.17 Scan pattern for imaging repeatability experiments. 166
7.18 Tensor components of specimens with and without obstacle, (a), (c), and (e). Significance levels, (b), (d), and (e). 168

7.19 FODs at $x/b = 5.7$ from $z/b = 0.72$ to 0.53 for specimens with 20% glass. 170
7.20 FODs at $x/b = 5.7$ from $z/b = 0.72$ to 0.53 for specimens with 25% glass. 170
7.21 FODs at $x/b = 5.7$ from $z/b = 0.72$ to 0.53 for specimens with 30% glass. 170
7.22 FODs at $x/b = 34$ from $z/b = 0.72$ to 0.53 for specimens with 20% glass. 171
7.23 FODs at $x/b = 34$ from $z/b = 0.72$ to 0.53 for specimens with 25% glass. 171
7.24 FODs at $x/b = 34$ from $z/b = 0.72$ to 0.53 for specimens with 30% glass. 171
7.25 FODs at $x/b = 34$ from $z/b = 0.53$ to 0.34 for specimens with 20% glass. 172
7.26 FODs at $x/b = 34$ from $z/b = 0.53$ to 0.34 for specimens with 25% glass. 172
7.27 FODs at $x/b = 34$ from $z/b = 0.53$ to 0.34 for specimens with 30% glass. 172
7.28 Young's modulus of gate obstacle specimens. 173
7.29 Comparison of specimen No3 at $x/b = 5.7$ with Bay & Tucker results. 175
7.30 Comparison of specimen No3 at $x/b = 34$ with Bay & Tucker results. 176
7.31 Comparison of specimen No1 at $x/b = 7$ with Davis results. 176
7.32 Photograph of FOD field resulting from flow around an obstacle (x-y plane of Obm2). 178
7.33 Projection of measured FOD ellipsoids on x-y plane (Obm2). 178

NOMENCLATURE

a_{ij}	second-order orientation tensor components
a_{ijkl}	fourth-order orientation tensor components
b	half height of mold cavity ($H/2$)
Br	Brinkman number
c_p	specific heat
$\mathbf{p}$	fiber orientation vector
d	fiber diameter
Gz	Graetz number
H	height of mold cavity
I	inertia tensor
k	thermal conductivity
l	fiber length
L	length of mold cavity
n	refractive index
Na	Nahme-Griffith number
Pn	Pearson number
Q	volume flow rate
t_{fill}	time required to fill the mold
U	average flow velocity
W	width of mold cavity
wt%	weight percent
x	flow direction coordinate (zero at gate)
y	transverse (in-plane) coordinate (zero at vertical midplane)
z	optical axis coordinate (zero at horizontal midplane)

Greek

α	thermal diffusivity ($\frac{k}{\rho c_p}$)
η	polymer melt viscosity
χ	volume fraction
θ	Eulerian angle with respect to z axis
ϕ	Eulerian angle in x-y plane with respect to x axis
$\Psi(\theta, \phi)$	orientation distribution function
ρ	density
ζ	temperature exponent of viscosity

Symbols

$\wedge$	logical *and*
$\vee$	logical *or*

Subscripts

f	fiber
m	matrix

DEFINITION OF TERMS

anisotropic Having nonuniform properties with respect to direction.

barrel Part of the injector which heats the material.

cavity Interior of the mold which forms the shape of a part.

cell A portion of a scan that is treated as a unit. An elemental volume within the specimen. Often a scan and a scan cell are one and the same.

data acquisition board An electronic device which allows voltages to be measured by a computer.

fiber The reinforcing component of a composite material.

flash Excess material that invades mold split planes.

FOD Fiber Orientation Distribution: Describes the fiber content of a material as a function of orientation.

frame A single video image.

frame grabbing The capture of video images and conversion to digital format.

gate Part of the mold which controls the flow into the cavity.

injector A device for forcing molten material into a mold.

isotropic Having uniform properties in all directions.

matrix The component of a composite material which surrounds the reinforcing material.

motion controller An electronic device which allows motors to be controlled by a computer.

nozzle Part of the injector which conducts material to the sprue.

piston Part of the injector which forces material out of the barrel and through the nozzle.

pixel The smallest element of a digitized image.

runner A channel which conducts material from the sprue to the mold cavity.

scan A series of 3-D images captured at uniform intervals along the optical axis at a single x-y location, combined as a 3-D image.

servo motor A motor whose speed is proportional to the applied voltage.

SFRT Short fiber reinforced thermoplastic.

sprue The channel which provides entry into mold interior.

stepper motor A motor which can be stepped in discrete increments by energizing its windings in a specified sequence.

vent A channel which allows air to escape from the mold.

voxel A three-dimensional pixel, or volume element.

CHAPTER 1

INTRODUCTION

Since injection molding of fiber reinforced polymers is becoming widespread as a cost-effective method for producing moderate strength parts, there is a growing need for accurate prediction of the material properties of these materials. The properties of composites are strongly dependent on the fiber orientation distribution (FOD), which is typically a complex three-dimensional orientation field which is induced by the flow kinematics during injection. In general, the material properties are a function of the FOD, fiber length distribution, fiber volume fraction, and fiber curvature. Material properties of composites are often highly anisotropic, and vary spatially within the material. Predictions of strength, stiffness, thermal conductivity, shrinkage, and warpage all depend on a knowledge of the FOD. Models have been developed to predict fiber orientation and to predict material properties from the FOD, but there are severe limitations on the current ability to measure fiber orientation, especially in three dimensions. This inability to accurately measure process-induced fiber orientation is a major barrier in short fiber reinforced composites (SFRC) research. The ultimate goal is to learn how to design and control manufacturing processes to produce favorable fiber orientation distributions.

1.1 Objectives

The main objectives of this project were the development of an automated system for measuring 3-D FODs in injection molded thermoplastic composites, and the construction of an apparatus for preparing a variety of sample materials to be analyzed. These goals were achieved through three major thrusts: the development of a laboratory-scale injection molding machine, the development of an imaging system for automated optical sectioning, and the development of 3-D image processing and analysis software.

In pursuing these objectives the following factors were considered to be important: (1) the analysis method should be applicable to materials of industrial importance, (2) the injection molding system should simulate conditions present in industrial injection molding processes as closely as possible, (3) the software should be accurate, robust and convenient to use, and (4) the cost of the system should be low enough to be available to a wide range of users.

The following sections provide background information about the injection molding process in general, and a review of literature regarding injection molding issues. In particular, theoretical and experimental research of fiber orientation measurement techniques and flow induced fiber from the literature are presented, followed by a presentation of the mathematical representation of fiber orientation distributions. The remaining chapters present a new method of fiber orientation measurement that overcomes many of the limitations of the techniques currently used, and the results of its implementation in experimental research of flow induced fiber orientation.

1.2 Fiber Reinforced Polymer Materials

The relatively low strength and low stiffness of most plastics make them less than ideal for many engineering applications. However, when mixed with reinforcing materials to form composites their material properties can be significantly enhanced. Composite materials can be designed to possess desirable properties such as high strength-to-weight ratio, and high strength and stiffness in the direction of applied loading. The reinforcing materials used in composites are usually highly anisotropic resulting in bulk anisotropic behavior. Knowledge of the orientation of the reinforcing material is an essential element in predicting material properties. (Altan, Subbiah, Güçeri, and Pipes, 1989; and Pipes, McCullough, and Taggart, 1982).

The component of a composite which surrounds the reinforcing material is referred to as the matrix. There are two basic types of polymeric (plastic) matrix: thermoplastic and thermosetting. Thermoplastic materials can be remelted after processing, whereas thermosetting cannot.

The reinforcing material may be in the form of fibers, flakes, disks, or spheres; fibers being the most common. Fibers are usually classified as continuous or short. Production of continuous fiber composites generally involves relatively slow and expensive processing such as hand layup, filament winding, or weaving, whereas short fiber composites lend themselves well to rapid and inexpensive molding processes such as injection molding.

Following the selection of materials, the fiber orientation has the strongest influence on most material properties. In a highly aligned material the properties in the direction of alignment may differ by an order of magnitude from the properties transverse to the alignment.

1.3 Injection Molding of Short Fiber Reinforced Composites

Low cost, fast processing, and the ability to form complex shapes has led to injection molding becoming a popular method for producing low cost, moderate strength short fiber composites. Boukhili, Gauvin, and Gosselin (1989) stated that, "The most attractive feature of short fiber reinforced plastics is their adequacy for the injection molding technique, which offers many advantages such as reduced processing time, and heightened economic efficiency."

1.3.1 Description

In a typical injection molding process, pelletized plastic and fiber reinforcement are fed into the barrel of an injection molding machine where heat is applied to melt the material and a feed screw mixes and advances the material toward the nozzle. At the time of injection the screw moves forward and forces the material out through the nozzle and into the sprue of the injection mold. The sprue transports the material to one or more runners which guide the material to the mold cavity or cavities. Once the material has solidified, the mold is opened and the specimen is ejected.

1.3.2 Characterization of the Mold Filling Process

The mold filling process consists of four phases: filling, packing, cooling, and ejection. During the filling phase, material enters the mold and immediately begins cooling due to the lower temperature of the mold walls. Once the mold has been filled, pressure is maintained by the injector while the material solidifies. This reduces the amount of shrinkage by introducing additional material into the mold to fill the volume created by the shrinking. material. The material is allowed to cool inside the mold until it

has reached a temperature where it is dimensionally stable, at which point the mold is opened and the material is ejected from the mold by ejector pins.

The velocity profile in isothermal mold filling is well understood. Polymer melts are usually very viscous, therefore the flow is fully developed almost immediately after entering the mold cavity. However, in practice the mold is usually much colder than the melt and the melt viscosity is very temperature dependent, so heat transfer has a large effect on the flow kinematics. Non-isothermal filling can be divided into three regions: entry, fully-developed, and fountain flow as shown in Figure 1.1. The



Figure 1.1: Non-isothermal mold filling model.

entry region is located at the mold entrance (gate) and is characterized by a developing temperature field. A frozen layer begins to form near the entrance, growing in thickness with distance from the gate and progressively restricting the flow channel. If the mold cavity is long enough, a point is reached where there is a balance between heat lost and viscous dissipation. This fully developed region is characterized by a constant gapwise temperature profile and constant thickness frozen layer. The flow front is characterized by a phenomenon called 'fountain flow' in which the material at the center of the flow spreads out to the mold walls where it freezes (Rose, 1961; and Tadmor, 1974).

Accurate modeling of mold filling can often be achieved with relatively simple constitutive equations. Most injection moldings consist of thin shells, and the viscoelastic and normal stress properties of polymer melts have little effect on cavity filling. Adequate characterization of viscosity is all that is needed for accurate sim-

ulations of mold filling in most injection moldings (Wang et al., 1984). Newtonian fluid constitutive equations have been used with great success.

1.3.3 Dimensionless Parameters

Dimensionless parameters provide a means of quantifying and comparing the filling characteristics of specific mold geometries under different processing conditions. Extensive analysis with scaled governing equations was reported by Pearson and Richardson (1977, 1978, 1979, 1983, 1986a, 1986b, 1986c, 1987). The following is a summary of the dimensionless parameters identified by Pearson and Richardson for use in modeling mold filling. (See Davis (1986) for an overview of the derivation of these parameters.)

The important dimensionless parameters in mold filling are the Graetz number, Nahme number, Brinkman number, and the Pearson number. The mold filling problem involves the four distinct temperature differences or temperature scales listed in Table 1.1, which are directly related to the dimensionless parameters.

Table 1.1: Temperature scales for dimensionless parameters. (Davis, 1986)

Scale	Expression	Description
ΔT_d	$\frac{\eta^* U^2}{k}$	Temp. increase due to viscous dissipation.
ΔT_{cn}	$\frac{\eta^* L U}{\rho b^2 c_p}$	Temp. increase due to axial convection.
ΔT_v	$\frac{1}{\zeta}$	Temp. difference necessary to significantly alter viscosity.
ΔT_Δ	$\lvert T_{in} - T_{wall} \rvert$	Imposed temp. difference between melt and mold wall.

The Graetz number is the ratio of axial convection to transverse conduction, and is defined as

$$\text{Gz} = \text{Graetz number} = \frac{U b^2}{\alpha L} \tag{1.1}$$

where U is the average flow (x) velocity, b is the half height of the channel, α is thermal diffusivity ($k/\rho c_p$), and L is the length of the cavity. The Graetz number can be written alternatively as

$$\mathrm{Gz} = \frac{b^2}{\alpha t_{fill}} \tag{1.2}$$

where t_{fill} is the time required to fill the cavity. A large Graetz number (on the order of 1000) is indicative of a high flow rate condition in which convection heat transfer dominates, and conduction is important only in a thin boundary layer at the wall. The result is a thin frozen layer. Conversely, a small Graetz number (low flow rate) implies that transverse conduction is dominant and the heat-transfer problem is essentially one-dimensional, resulting in a thick frozen layer.

The Nahme-Griffith number is a measure of the amount of temperature rise due to viscous dissipation needed to significantly affect the viscosity and is defined as

$$\mathrm{Na} = \text{Nahme-Griffith number} = \frac{\eta U^2 \zeta}{k} \tag{1.3}$$

where η is the viscosity of the melt, ζ $(= 1/\Delta T_\Delta)$ is the temperature exponent of viscosity, and k is the thermal conductivity.

The Brinkman number is the ratio of the temperature rise due to viscous dissipation and the imposed temperature difference, i.e., it is a measure of the importance of heat generation versus transverse conduction and is defined as

$$\mathrm{Br} = \text{Brinkman number} = \frac{\eta U^2}{k\,|T_{in} - T_{wall}|} \tag{1.4}$$

If Br is large (on the order of 10), viscous dissipation will reduce the thickness of the frozen layer.

The Pearson number is a measure of the effect of the imposed temperature difference on the viscosity.

$$\text{Pn} = \text{Pearson number} = \zeta \, |T_{in} - T_{wall}| \tag{1.5}$$

Injection molding conditions are almost always characterized by a large Pn, which indicates the formation of a frozen layer. The thickness of the frozen layer is roughly $b\text{Gz}^{-1/2}$ (Bay and Tucker, 1992). Note that only three of the four parameters are independent since Pn = Na/Br.

Table 1.2 lists the formulas for the four dimensionless parameters in terms of the volume flow rate for a rectangular cavity geometry.

Table 1.2: Four dimensionless parameters for a rectangular cavity. (Richardson, 1988)

Dimensionless No.	Meaning	Expression
Graetz	$\frac{q_{\text{axial convection}}}{q_{\text{transverse conduction}}}$	$\frac{2H}{WL}\frac{Q}{\alpha}$
Nahme	$\frac{\Delta T_d}{\Delta T_v}$	$\frac{1}{4W^2H^2}\frac{\eta^* \zeta Q^2}{k}$
Brinkman	$\frac{\Delta T_d}{\Delta T_\Delta}$	$\frac{1}{W^2H^2}\frac{\eta^* Q^2}{k\Delta T_\Delta}$
Pearson	$\frac{\Delta T_\Delta}{\Delta T_v}$	$\zeta \Delta T_\Delta$

A Graetz number on the order of one thousand is considered large, while a Brinkman, Nahme, or Pearson number on the order of ten is considered large. Richardson (1989) cataloged six asymptotic solutions based on these dimensionless parameters.

In most injection molded parts the Graetz number is usually quite large, on the order of one to ten thousand. The Brinkman and Nahme numbers are also large, and the size of the Pearson number depends on the material being molded.

Since the dimensionless parameters relate directly to the shape of the velocity profile generated during mold filling, they also relate to the fiber orientation distri-

bution in the finished part. Two parts produced under different conditions, but with similar dimensionless parameters can be expected to produce similar fiber orientation morphologies. Thus these dimensionless parameters should provide a means of quantitatively relating processing conditions to expected fiber orientation results.

One factor in the calculation of the dimensionless parameters that is often unknown is the viscosity, since viscosity is affected by fiber content. However, Bright (1987) found that at shear rates common for injection molding, filled and unfilled melts have very similar viscosities, which implies that the viscosity of fiber/polymer melts can be estimated by the properties of the unfilled polymer. It should be noted, however, that Mutel and Kamal (1991) reported results that conflicted with Bright's findings.

1.4 Flow-Induced Fiber Orientation

It is well-established that fiber orientation is strongly influenced by the injection molding process (Bay and Tucker 1991a, 1992a) and that fiber orientation has a strong influence on the bulk material properties (Pipes et al. 1982). In materials with highly aligned fibers, the mechanical properties in the direction of alignment may be an order of magnitude different from the properties in the transverse direction. Furthermore, the flow patterns in injection molding are, in general, of a complex three-dimensional nature, resulting in complex fiber orientation patterns. And the degree of fiber orientation may vary with minor changes in fabrication conditions (McGee and McCullough, 1984).

The factors which most strongly influence fiber orientation are the mold and gate geometry, melt rheology, flow rate, mold and melt temperature, fiber volume fraction and fiber length. A broad investigation of fiber orientation in injection molding, with

complete characterization of the processing conditions and orientation results has not been reported in the literature. In fact, there are very few experimental results which quantify the processing conditions which produced a given fiber orientation.

General principles of flow-induced fiber orientation that are understood include: Diverging flow tends to orient fibers transverse to the flow direction while converging flow tends to orient fibers parallel to the flow. Shearing flow tends to align fibers in the direction of the shear. Flow rate affects the velocity profile and heat transfer of the melt which in turn affects the flow pattern. The melt and mold temperatures influence the rheology of the flow, as does fiber content and length. Plug flow in the core region may carry the gate-induced fiber orientation relatively undisturbed for long distances.

The following is an overview of the theoretical analysis of flow-induced fiber orientation presented by Doshi, Dealy, and Charrier (1986).

> "A rigorous simulation of the flow of a concentrated suspension of nonspherical particles in a viscoelastic medium such as a polymer melt is not possible at the present time, although several models have been developed by making use of certain simplifying assumptions. For example, Lockett (1980) has presented a qualitative prediction of fiber orientation on the basis of macroscopic flow field considerations. Quantitative treatments, however, are generally based on the equations derived by Jeffery (1922) for describing the motion of an ellipsoid suspended in a Newtonian medium subjected to an arbitrary but homogeneous flow field (a flow field in which the components of the velocity gradient are spatially uniform). Goldsmith and Mason (1967) used these equations to model the motion of a suspended particle in steady simple shear. Predictions have also been made for steady simple uniaxial (Takserman-Krozer and Ziabicki, 1963) and biaxial (Goldsmith and Mason, 1967) extensional flows. The predictions have been found, in general, to be qualitatively in agreement with experimental findings for suspensions (Bell, 1969; Takano, 1974; and Laun, 1984). Goldsmith and Mason (1962) have also demonstrated experimentally the applicability of Jeffery's equations to nonhomogeneous flow fields (e.g., Poiseuille flow) provided that local values of the components of the rate of deformation tensor are used and that particle dimensions are small compared to the channel dimensions.
>
> "Recently, various investigators have used Jeffery's equations for complex flow situations such as injection mold filling, expansion at the en-

> trance to a large cavity, fountain flow phenomena in injection molding, and flow around mold inserts (Givler, Crochet, and Pipes, 1983; Gillespie, Vanderschuren, and Pipes, 1985; and Vincent and Aggasant, 1984) to predict fiber orientation in SFRTP's. These analyses neglect particle-particle and particle-wall interactions and often model the polymetric melt as a Newtonian medium. Efforts have also been made to incorporate particle-particle interactions but these are essentially empirical (Folgar and Tucker, 1984). Attempts to analyze rigorously the motion of suspended particles in a non-Newtonian or viscoelastic medium lead to highly complex mathematical problems that are not suitable for practical applications (Leal, 1975; and Brunn, 1980)."

A comprehensive literature review of suspensions of rodlike particles was compiled by Ganani and Powell (1985). According to their review, Maschmeyer and Hill's 1974 attempt at compiling a master curve of fiber behavior demonstrated the futility of obtaining even a qualitative agreement among data from various laboratories. Ganani and Powell found some general trends and some agreement between reported data, but there is still a lack of sufficient data to make final conclusions.

Ott (1988) also gave a detailed overview of the orientation mechanisms involved in injection molding.

1.4.1 Mold-Filling Code

Early computer simulations of the mold-filling process were reported by several authors. Harry and Parrott (1970) simulated filling of a rectangular plaque. Berger and Gogos (1971) simulated the filling of a center-gated disk, but no comparisons were made with experimental results. Rothe (1972) simulated injection into a long, constant diameter circular tube. His predictions correlated well with experimental observations. Kamal and Kenig (1972) simulated the filling of a center-gated half-disk, but correlation with experimental results was not particularly good. All of these models were based on constitutive equations involving simple power-law shear rates.

Lord and Williams (1975) presented a computer model which computes the temperature, pressure, and velocity fields in a cavity during mold filling using finite differences. The model is structured so that it can be used with complex shapes and commonly used molding compounds with complicated viscosity, shear rate, and temperature relationships, eliminating many of the limitations of earlier models. Predictions from the model were found to be in good agreement with results obtained from exact solutions to special cases and to correctly describe trends observed in experiments.

Hieber and Shen (1980) presented a detailed formulation for simulating the injection-molding filling of thin cavities of arbitrary planar geometry. The modeling is in terms of generalized Hele-Shaw flow for an inelastic, non-Newtonian fluid under non-isothermal conditions. A hybrid numerical scheme is employed in which the planar coordinates are described in terms of finite elements and the gapwise and time derivatives are expressed in terms of finite differences. The simulation was applied to the filling of a two-gated plate mold having an unbalanced runner system. Good agreement was obtained with experimental results in terms of short-shot sequences, weldline formation and pressure traces at prescribed points in the cavity.

Mavridis, Hrymak, and Vlachopoulos (1986) used a general purpose finite element program to give a detailed description of the predicted flow behind an advancing melt front moving at constant speed inside two-dimensional channels and tubes. Their results were in agreement with experimental observations and other approximate analyses.

Eduljee and Gillespie (1990) presented analytical solutions for fiber orientation in dilute solutions (Jeffery's model) for 2-D planar and axisymmetric flow. Viscosity is assumed independent of position along flow direction, but vary through the thickness

of the mold cavity. Fluid mechanics are modeled as a laminate of two fluids where the fluid adjacent to the mold wall exhibits reduced viscosity. Superior correlation with experimental results compared with earlier numerical studies (York, 1982) was observed. This suggests that non-isothermal fluid flow plays an important role in the development of the FOD in molded materials.

Matsuoka, Takabatake, Inoue, and Takahashi (1990) presented a numerical scheme for predicting fiber orientation in 3-D thin-walled molded parts of FRTP. Folgar and Tucker's (1984) model is used to represent the planar orientation behavior of rigid cylindrical objects in concentrated suspensions. The equation is solved about a distribution function of fiber orientation by using a finite difference method with input of velocity data from a mold filling analysis. The mold filling is assumed to be non-isothermal Hele-Shaw flow of a non-Newtonian fluid and analyzed by using a finite element method. Computed orientation parameters were compared with measured thermal expansion coefficients for molded square plates of glass-fiber-reinforced polypropylene. A good correlation was found.

Fiber orientation models have been incorporated into mold-filling simulations to predict fiber orientation in molded parts, such as TGMOLD from the University of Delaware (Friedrichs, Güçeri, Subbiah and Altan, 1991). The governing equations in this model are solved by the finite difference method on an evolving flow domain. The flow formulation is based on the Hele-Shaw and Darcy formulations. Jeffery's (1922) model is employed for short fiber orientation analysis. The numerical results were in good agreement with experimental observations.

PLASTEC[1], C-FLOW[2], and MOLDFLOW[3] are available commercial mold-filling simulation programs. An example of the use of PLASTEC was presented by Reifschneider, Akay, and Ladeinde (1990).

1.4.2 Observed Flow-Induced Fiber Orientations

Several authors have quantified fiber patterns induced by various processing and flow conditions. However, the mold geometries and conditions under which the samples were prepared were rarely similar, making correlations difficult.

Woebcken (1962) conducted experiments with a fan-shaped mold and observed that the fibers oriented transverse to the flow direction below a thin surface layer. Goettler (1972) looked at the influence of gate geometry and found that fibers align in the stretching direction in converging channels. Gandi and Burns (1976) also noted that stretching plays a dominant role. Others have reported the same results with different materials (Bell, 1969; Darlington, 1976; Owen and Whybrew 1976; and Taggart and Pipes, 1979). The common feature observed in these experiments was that converging and shearing flows oriented fibers in the direction of the flow, while diverging flow oriented the fibers transverse to the flow.

Bright, Crowson and Folkes (1978) studied the influence of injection speed on the orientation and found that injection speed had a substantial influence on the FOD. Slow injections produced a thick core region of fibers highly aligned in the flow direction, and a randomly aligned skin layer. Fast injections produced a thinner core with transverse fiber alignment, and a flow-aligned shell. They concluded that a variable speed injection could be used to vary the fiber orientation along the length of a bar.

[1]Technalysis, Indianapolis, Indiana.
[2]Advanced CAE Technology, Inc., Ithaca, New York.
[3]Moldflow, Ltd., Kilsyth, Australia.

Darlington and Bright (1981) researched fiber orientation in rectangular plaques as part of a comprehensive study. They observed practically *no* effect of injection speed or melt temperature. Experiments with short-shots revealed much more complex FOD patterns prior to packing than were observed after packing.

Sanou, Chung, and Cohen (1985) studied the effect of cavity thickness on the FOD of film-gated rectangular plaques. They observed a shell/core structure with parabolic fiber alignment in the core for thicker specimens. A parabolic distribution was always observed near the flow front, while flow-aligned fiber distributions were always observed near the gate. The shell layer was observed to have flow-aligned fibers. Cavity thickness was found to be the dominant factor in influencing the FOD, while flow rate was found to be a secondary factor. Similar results were reported by Favkirov and Fakirova (1985).

An additional skin layer containing a random planar FOD above the shell layer was reported by Kamal, Song, and Singh (1986), Hiersh (1986), Konicek (1987), and Menges and Geisbush (1982).

In 1986, Malzahn and Schultz reported an unusual orientation phenomenon. They observed the development of the fiber orientation in rectangular plaques using a series of controlled short-shots and complete, packed shots. Comparison of the fiber orientation distribution in the short shots and fully-packed shots demonstrated that a transverse fiber orientation throughout the core layer did not occur until after the mold was full. They attributed this phenomenon to stresses developed during the packing stage of the injection molding process. It is difficult to explain, using the prevailing fiber flow theories, how such a dramatic change in fiber orientation could occur during the packing phase.

Mutel and Kamal (1991) investigated the rheological behavior and fiber orientation in slit flow of fiber reinforced thermoplastics using a slit die with an adjustable gap and interchangeable entrance geometries. The effect of entrance geometry and gap width on fiber orientation were observed from digitized photomicrographs of microtomed samples. A skin/core microstructure was observed. Fibers were found to be oriented in the flow direction in the skin region irrespective of the entrance geometry. Various fiber orientation distributions in the core region were realized by using different entrance geometries. They also found that fibers do not have an appreciable effect on viscosity at 5 wt%. But viscosities at 10 and 30 wt% were consistently higher than for unfilled melts. The specific viscosities appeared to be independent of shear rate (0.13 for 10 wt% and 0.30 for 30 wt% fiber filled polypropylene).

Fisa and Rahmani (1991) studied the morphology of weldlines in fiber reinforced polypropylene. Scanning electron micrographs of fractured surfaces revealed that in the core layer where the shear rate is low, the fiber orientation acquired close to the gate was convected for a considerable distance. In flow around an obstacle in the cavity they noted that the junction of the two melt fronts persisted during the entire mold filling stage. The authors stated that, "This observation indicates that the melt in the already formed weldline advances at a substantially lower velocity then the one adjacent to it. As a result this stagnating weldline zone plays a role similar to that of the mold wall, i.e., fibers are deposited onto it by the lateral expansion of the advancing melt front generating the essentially unidirectional structure in the area."

1.4.3 Theory of Flow-Induced Fiber Orientations

Several theories have been proposed to explain the observed flow-induced fiber orientation in injection molded materials. Some are contradictory. The prevailing view-

point is the one presented by Bright et al. (1978) which attributes the main orienting effects to the gapwise velocity profile and the formation of the frozen layer. Transverse alignment induced by expanding flow at the gate is convected down the core region during fast injections. Narrow shear regions near the wall lead to flow-aligned shells. Slow injection produces a more parabolic flow profile, with shear through the thickness inducing flow-direction alignment.

Darlington and Smith (1987) supported the theory that the gapwise velocity profile and freezing at walls are the controlling factors. Fast injections have a blunt flow profile with high shear region at walls while very little shearing occurs in the core region. In slow injections a transverse aligned frozen layer is built by fountain flow.

The random orientation in the skin layer was attributed to fountain flow by Rose (1961), Tadmor (1974). Molecular orientation studies by Mavridis, Hrymak and Vlachopoulos (1988) supported this conclusion.

Although general trends and theories have emerged, precise fiber orientation data and complete documentation of the processing conditions which brought them about are needed to develop accurate models of flow induced fiber orientation.

1.5 Fiber Length Degradation

A complicating factor in modeling injection molding is fiber length degradation or breakage due to high stresses experienced by the fibers during molding, especially in the injection screw (Chin, Liu, and Lee, 1988).

Early work by Schlich et al. (1968) and Filbert (1969) suggested that fiber length is primarily affected by variations in back pressure and gate size. Darlington, Gladwell and Smith (1977) studied the effect of these parameters on the fiber length in edge-gated disks of glass fiber reinforced polypropylene. Fiber data obtained through

contact microradiography demonstrated that a large gate and low back pressure reduced the incidence of fiber breakage, but also lead to "serious fiber agglomeration and increased voiding." Significant degradation was observed only in fibers longer than approximately 1 mm. Back pressure was found to have the greatest influence in fiber length degradation. Despite agglomeration and voiding, the stiffness and strength were improved for the materials with retained fiber length. Fiber orientation showed little variation over the range of molding conditions. Material properties were modeled using Darlington, McGinley, and Smith's (1977) theory, which accounts for fiber length. The predicted and measured stiffness values were in "surprisingly good agreement." In measuring the fiber orientations 2-D projections of the fibers were used to approximate the 3-D FOD. The predicted stiffness values in the core region were found to be significantly higher than the observed results. The error was attributed to inadequate means of measuring the 3-D fiber orientation. The authors stated that, "These high predicted stiffness values are obviously a consequence of neglecting the effect of out of plane fiber alignment which is most significant in the disc core."

Ott (1988) stated that after a typical injection molding of thermoplastic composites, the maximum fiber length is in the region of 0.2 to 0.4 mm. His work demonstrated that fiber damage decreased as molding temperature and gate diameter increased, and increased as back pressure increased.

1.6 Measurement of Fiber Orientation

The following sections deal with the issues of fiber orientation measurement—focusing on how data are gathered and how they are analyzed.

1.6.1 Importance

The following quotations and comments illustrate the importance of fiber orientation measurement, especially in three dimensions, and the lack of available data.

In 1976, Chou and Kelly identified discontinuous fiber composites as "one of the least understood areas of composite material technology."

Chin, Liu and Lee (1988) stated, "Since there are progressive and continuous changes in the fiber orientation throughout molded components, prediction of the mechanical properties of [SFRTs] is possible only if the fiber orientation and its distribution are well-defined."

Altan, Advani, Güçeri and Pipes stated in 1989 that "The characterization of the flow or the fiber orientation in a short fiber suspension is of major concern in current polymer processing research."

Fischer, Schwarz, Mueller, and Fritz (1990) stated, "Due to the high orientation gradients in injection molded parts,—e.g., near the mold wall—a measuring technique with high lateral resolution and three-dimensional orientation representation is required."

And in 1991, O'Connell and Duckett reiterated the importance of fiber orientation measurement and described the current knowledge base, "The properties of [SFRCs] are highly dependent on the microstructure of the sample, since, in a real moulding, a very complex distribution of fibre orientation is often seen. Comparatively little detailed work concerned with fiber orientation, in even the simplest mouldings, has been carried out, however"

The inability to accurately measure fiber orientation distributions has contributed significantly to the lack of available data.

1.6.2 Imaging Methods

In order to determine fiber orientation distributions, data must be gathered about the orientation of individual fibers. This is usually done with an imaging apparatus. There are three general types of imaging methods; shadow imaging, surface imaging, and cross-section imaging. There are abundant examples in the literature of the use of the first two methods in fiber orientation measurement, but an exhaustive search yielded no examples of the third. Each imaging method possesses inherent capabilities and limitations with regard to fiber orientation measurement. For example, shadow methods provide the least information about three-dimensional orientations, while cross-section methods provide the most. Predominantly 2-D fiber orientation distributions such as typically exist in sheet molding compound (SMC) can be adequately imaged with shadow or simple surface image techniques. However, the extraction of 3-D information required for the analysis of injection molded materials demands more complex methods.

Shadow imaging is used to obtain projections of fibers located throughout the thickness of a material. Images obtained by this technique normally do not provide depth information and are, therefore, generally thought of as 2-D techniques. However, under certain circumstances where the fibers have uniform length or a thin cross-section of the material is used, some out-of-plane orientation information can be obtained.

Surface imaging, normally performed on specimens which have been prepared by metallographic polishing techniques, provide information about fibers which intersect the cutting plane. The in-plane component of the fiber orientations can normally be accurately measured from this type of image, and by analyzing the shape of the fiber cross-sections, some information about the out-of-plane component can be obtained.

Cross-section imaging methods are capable of providing images of arbitrary planes inside of a material. These methods have the advantage of being able to provide a complete 3-D description of the morphology of a material by means of a sequence of images through its thickness. However, this type of imaging has not been applied to fiber orientation analysis in the past.

The following sections describe various imaging technologies and their suitability for fiber orientation measurement. A more detailed evaluation of these systems is presented by Westerbecke (1992).

Shadow Imaging Methods

The simplest shadow imaging method is visual inspection by transmitted light. This method is actually a combination of shadow and surface imaging since the human eye can detect surface features as well as patterns in the transmitted light. Darlington, McGinley and Smith (1976) noted that visual inspection is often used as an indication of the FOD, and pointed out the dangers of doing so. They demonstrated that in a specimen with readily observable features (i.e., an apparent dominant FOD direction) stiffness measurements made parallel and perpendicular to the observed texture showed only a 5% anisotropy, with the weak direction lying *parallel* to the texture markings. Physical sectioning showed that the observed texture was due to the presence of voids, not fiber orientation.

X-ray imaging of composites is frequently used to obtain a shadow image of the fibers located throughout the thickness of a specimen. As the x-rays pass through the material they are blocked by fibers at all depths within the material and thereby provide a cumulative image of the material. Due to the high concentration of fibers within composites of engineering importance, a small quantity of tracer fibers, rather

than the entire fiber population, is imaged. Tracers are usually made of metal or high lead content glass. Radiography is one of the most frequently reported methods of fiber imaging in the literature.

There are two general types of x-ray imaging used in fiber orientation measurement, macroradiography and contact microradiography. Macroradiography provides a more global image of the orientation field at the expense of resolution, whereas microradiography provides fine detail of individual fibers in a small region.

Examples of experiments involving microradiography are abundant in the literature: Darlington and McGinley (1975), Bright, Crowson and Folkes (1978), Crawson, Folkes, Chen, Tucker, (1984), Matsuoka, Takabatake, Inoue, and Takahashi (1990).

Darlington and McGinley (1975) presented a detailed description of contact microradiography (CMR) with thin sections. They noted that one advantage of radiography is the fact that surface condition is unimportant. They assessed the suitability of radiography for three-dimensional analysis in the following way,

> "The use of a slice (of known thickness) whose thickness is significantly less than the mean fibre length suggests the possibility of estimating, from the radiograph, the orientation of the fibres to the plane of the slice (in addition to the obvious determination of the orientation in the projected plane). The three-dimensional orientation distribution through the thickness of a moulding could then be assessed from a radiograph of one slice cut perpendicular to the moulded surface. However, unless the fibre distribution is symmetrical about the plane of the slice, the angle of the fibre to the plane of the slice cannot be determined unambiguously from one such radiograph. The use of stereo-CMR (Engstrom, 1956) may overcome this problem."

They found microradiography to be superior to the other commonly available techniques such as metallographic polishing and macroradiography because, it is not restricted to simple mold shapes, translucent or unpigmented materials.

Darlington, McGinley and Smith (1976) used and evaluated several different imaging techniques for qualitative and quantitative assessment of FOD in short glass fiber

reinforced thermoplastics and found contact micro-radiography to be the most versatile.

Fischer et al. (1990) evaluated microradiography as a method for obtaining 3-D information and concluded that it was unsuitable for this purpose as it is a shadow imaging method, and therefore a "clear separation of single fibers and identification of fiber ends is not possible."

Macroradiography can be useful in evaluating the global fiber orientation field, but caution must be exercised when doing so. Darlington, McGinley and Smith (1976) observed that the textures they observed in macroradiographs corresponded to fiber clumps, not individual fibers, which were not representative of the orientation field.

Surface Imaging Methods

Conventional light microscopy is frequently employed to examine the surfaces of specimens which have been cut and polished. Staining or etching may be used to enhance the contrast between fiber and matrix material. Surface imaging using conventional light microscopy is one of the most frequently used imaging methods reported in the literature.

Scanning Electron Microscopy (SEM) involves imaging via a stream of electrons rather than visible light. This method provides greater resolution than that provided by visible light imaging, but it too is a surface method. Under certain circumstances it can provide information about the direction of the out-of-plane fiber orientation component (Konicek, 1987). The imaging field in SEM is usually quite small and therefore has limited usefulness as a tool for determining global variations in the FOD.

Acoustic imaging is a surface method which involves exciting a specimen with high frequency acoustic energy and measuring the reflected waves. Acoustic energy can penetrate opaque materials, but at the high frequencies required to resolve individual fibers ($10\,\mu$m diameter) the penetration depth is negligible. For this reason it is classified as a surface imaging technique. However, acoustic imaging has a unique ability to provide clues about the direction of the out-of-plane component of fiber orientation through the appearance of interference patterns on the surface (Matthaei, 1986).

Cross-section Methods

Cross-section imaging techniques are those which can image discrete planes inside a material. Thus the imaging energy must be capable of penetrating the material being imaged. For optically transparent materials the same types of imaging apparatuses that are used for surface imaging can often be used for optical sectioning. The resolution along the optical axis of optical devices is typically much less than in the transverse direction. The depth of field of the device determines the thickness of the optical slice. The narrower the depth of field, the greater the resolution along the optical axis. The optical axis resolution determines to a great extent the accuracy of out-of-plane orientation measurements. Shadow imaging systems have essentially an infinite depth of field.

Optical light microscopy, then, can be used for cross-sectional imaging. The application of light microscopy for optical sectioning of transparent composites is presented in detail in Chapter 2.

Confocal microscopy is a form of light microscopy which involves the use of a special aperture to exclude out-of-focus information. The aperture blocks light originat-

ing from locations outside of the focal plane, which reduces interference and provides enhanced lateral resolution. Confocal microscopy may also involve a scanning laser and a point detector to increase the imaging resolution. This makes it possible to slice very clean, thin optical sections from thick specimens.

Magnetic Resonance Imaging (MRI) involves placing a specimen inside a strong fluctuating magnetic field and detecting the emissions induced from molecules in the material. This method has the advantage that it can image inside opaque material, but its usefulness is limited by high cost and insufficient resolution to image individual fibers.

1.6.3 Current Methods of 2-D Fiber Orientation Measurement

Methods of fiber orientation measurement can be divided into two categories: those yielding two-dimensional data and those yielding three-dimensional data.

Two-dimensional fiber orientation data is normally obtained from shadow or surface images. Extracting 2-D orientation data generally involves identifying straight lines in the images and measuring their orientation and possibly their length, either by hand or by computer image analysis. The computer method has the advantage of potentially high speed and accuracy since robust algorithms exist for detecting straight lines in two-dimensions. A hybrid, semi-automated method, requires that a person indicate the endpoints of a fiber using a digitizing tablet.

Wetherhold and Scott (1990) made a direct comparison of three fiber orientation measurement techniques: the Fourier transform (optical and numerical), the Hough transform (1962), and semi-manual digitization. They applied the Hough transform to the problem of determining fiber orientation distributions and predicted thermomechanical properties of short fiber composites. The results of the Hough method

were compared with the Fourier transform as a reference standard, and with a manual digitizer pad method. They compared the computational efficiency, and the mean and variance of the estimated FODs. The manual digitization technique involved manual identification of individual fiber endpoints with a digitizing pad.

Optical diffraction methods are based on the principal that the orientation of the far-field (Fraunhofer) diffraction pattern produced by a single fiber is fixed by the orientation of that fiber in the image space, and that diffraction patterns of random ensembles of fibers superpose (McGee and McCullough, 1984). Photographic negatives produced from fiber images, illuminated with coherent light act as diffraction masks with each fiber acting as a diffraction aperture. The Fraunhofer diffraction pattern, or resulting far-field image of this mask, has brightness proportional to the intensity of the aperture's 2-D Fourier transform. The intensity is proportional to the sum of intensities contributed by individual fibers. Using a Fraunhofer diffractometer the intensities can be measured directly, or the Fourier transform can be applied by numerical methods. The intensity distribution in an annular region surrounding the center of the image has a direct correlation with the fiber orientation distribution.

The Hough transform method is based on an algorithm designed to detect straight line segments in binary images. The central idea is to map the image into a suitable parameter space, where line segments in the image are revealed as peaks. The details of the Hough transform method are presented in Chapter 2 and generalized to three-dimensional line detection.

Wetherhold and Scott used simulated images to provide a known fiber orientation distribution which were analyzed with the three methods. The results of their work showed that the direct measurement (digitizer pad) technique was the most robust, but much slower. The numerical Fourier method was found to be computationally

much more demanding than the Hough transform method. The Fourier method also demanded careful selection of the location and thickness of the sampling annulus in the Fourier domain for satisfactory results. The authors concluded that the Hough transform was most efficient, but the FFT method was most accurate. The FFT method was described as "extremely accurate."

Herman's (1976) average orientation parameter, f_p, and its standard deviation were calculated for several calibration images of 180 fibers and the results compared with the true distribution. The results are presented in Table 1.3.

Table 1.3: Herman's f_p parameter estimated from various FOD measurement techniques. (Wetherhold and Scott, 1990)

True f_p value:	*Uniform (0.000)*	*Cos() (0.340)*	*Cos^2() (0.516)*	*Aligned (1.000)*
Digitizer pad				
Average	0.194	0.504	0.665	1.000
Standard Deviation	0.040	0.040	0.027	0.001
Coeff. of variation (%)	45.2	11.5	4.2	0.10
Fourier transform				
Average	0.00	0.336	0.514	0.989
Standard Deviation	0.00	0.000	0.017	0.001
Coeff. of variation (%)	0.00	0.000	3.3	0.10
Hough transform				
Average	0.073	0.318	0.432	0.843
Standard Deviation	0.044	0.035	0.057	0.039
Coeff. of variation (%)	60.8	10.9	13.2	4.6

An in-depth evaluation of the Fourier transform method was presented by McGee and McCullough (1983). They related features of the diffraction pattern to the fiber orientation distribution, and to the shape and aspect ratio of the fibers. They demonstrated that an azimuthal trace of the relative intensity of the diffraction pattern is a direct measure of the fiber orientation distribution. Thus, quantitative measures of the orientation state can be obtained directly from the Fourier intensity profiles,

independent of assumptions concerning the shape of the orientation function. The results of their analyses were in good agreement with known orientation distributions in simulated fiber images. Lovrich and Tucker (1985) developed a digital version of McGee and McCullough's method.

Kaito, Kyotani and Nakayama, (1992) used a Fourier transform technique to analyze the microscopic orientation of liquid crystalline polymer sheets. The method was found to be useful in characterizing the orientation of the fiber morphology.

1.6.4 Current Methods of 3-D Fiber Orientation Measurement

Currently, 3-D data is obtained by analyzing the shape of the elliptical fiber cross sections exposed by physical sectioning. The in-plane orientation angle is determined from the direction of the major axis of the exposed ellipse, while the out-of-plane angle is calculated from the ratio of the major to minor axis as shown in Figure 1.2.

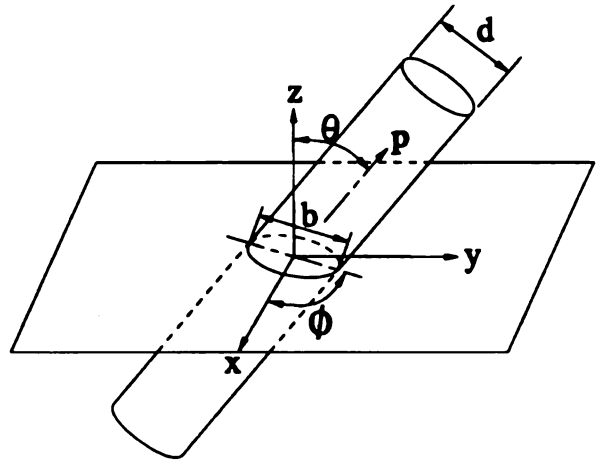


Figure 1.2: Surface ellipse method of orientation measurement.

Darlington and McGinley (1975) commented that, "Examination of individual fibre orientation has been widely performed using microtomed sections or surfaces prepared by metallographic polishing technique. It is, however, a time consuming

and laborious task with the results sometimes disappointing due to lack of contrast between the fibre and matrix."

Darlington, McGinley and Smith (1976) assessed the suitability of the surface ellipse method for 3-D fiber orientation measurement as follows:

> "Some good micrographs by Bowyer and Bader (1972) of polished surfaces of an injection moulded GFPA-66 bar show the difficulty of assessment of orientation intensity by this technique.
>
> "It is possible to determine the orientation of the fibre to the polished surface by measuring the orientation and length of the major and minor axes of the elliptical fibre section. However, these measurements are frequently made difficult and unreliable due to damage to the fibre ends during polishing. An additional problem of lack of contrast between certain matrices and the glass fibres may also occur.
>
> "The fibre damage can easily be seen in scanning electron micrographs of polished surfaces (Darlington and Smith, 1975). The difficulty in defining the extent of the elliptical polished surfaces (in optical micrographs) when the intimate contact between matrix and fibre has been destroyed by the polishing process can also be appreciated from these electron micrographs. In utilizing the ellipticity for the assessment of the three-dimensional orientation of a fibre it should also be noted that an exactly circular cross-section of the glass fibre cannot be assumed (Badami).
>
> "Whether this metallographic polishing technique is used for qualitative or quantitative assessment of fiber orientation distribution, it suffers from the drawback that only fibres intersecting a plane are observed and thus too few fibres may be sampled."

In 1986, Matthaei (1986) proposed the use of acoustic imaging to resolve the direction of the out-of-plane orientation component, noting that at the side of the cut ellipse, where the fiber is diving into the matrix, a banded pattern appears. The distance between the stripes may be used to calculate the angle of inclination of the fiber—although the results of measurement are not always accurate.

The following year, Konicek (1987), suggested a relief etching and scanning electron microscope imaging technique to determine the direction of fiber penetration, and presented a survey of imaging and measurement methods. He noted that a constant fiber diameter cannot be assumed in applying the surface ellipse method. He

found that changing the estimated average diameter from 8 μm to 14 μm changed the estimated value of the transverse orientation component by 50 percent.

In 1988, Fischer and Eyerer demonstrated a computer based measuring strategy to determine fiber orientations from single cross-sections. A means of correcting for the inclination-dependent probability of hitting a fiber was shown as well as a correction for fiber-end (non-elliptical) intersections. The analysis method was based on pattern recognition techniques. The FOD was used to approximate thermal expansion as a function of fiber content and orientation and as a means of verifying their orientation measurements. The correlation was fairly good.

Fischer, Schwarz, Mueller, and Fritz (1990) provided an excellent example of the use of automated analysis of surface images to determine fiber orientation distribution. They emphasized that fiber length and orientation are both important factors in determining material properties and added a level of automation to the image acquisition process by using a computer controlled scanning table. By moving the specimen they were able to increase the magnification and still obtain a global measurement of the FOD field. The field of view was in the range of 0.2 x 0.2 mm to 0.8 x 0.8 mm.

O'Connell and Duckett (1991) described an advanced ellipse measurement technique. Rather than analyze digitized fiber images, O'Connell and Duckett scanned high resolution photographs with an advanced image analyzer designed for analysis of astronomical images. The apparatus provided automated measurement of the location, size and orientation of the major axis, and ellipticity of fiber cross-sections. This approach provided much higher information density and accuracy than could be achieved by more common digitization techniques. A typical negative contained 10,000 fiber images. The negatives were scanned with a spot interval of 0.01 or 0.02 mm, giving an estimated spatial measurement error on the order of 1/10 of a

spot width. This gave a maximum uncertainty in the measurement of the out-of-plane orientation angle, θ of about 9 degrees. If the spatial error were assumed to be on the order of 1 spot width, then the maximum uncertainty would be around 30 degrees. Examination of a typical micrograph shown in the paper reveals a fairly high percentage of touching fibers. The image analyzer treated touching fibers as single fibers, which introduced some bias into the measurements.

Toll and Andersson (1991) presented a complete procedure for the assessment of the 3-D microstructure of discontinuous fiber composites. Image analysis routines were developed which were used to analyze scanned images of metallographically polished surfaces and evaluated spatial orientation distributions and volume fractions of the fibers. The paper dealt with image analysis problems, limitations in the analysis, and the interpretation of the results. Their algorithm had an enhancement over previous computerized image analysis techniques in that it could isolate individual fibers that were in contact with each other. The orientation angles were calculated from the principal moments of inertia of the fiber cross sections. They assumed straight circular cylinders and symmetry of the FOD with respect to the imaging plane. Their evaluation of the accuracy of their technique identified the following sources of error: incomplete polishing, finite image resolution, fiber curvature, and the presence of fiber ends at the cutting plane. The greatest source of error appeared to be the finite imaging resolution. A resolution of one-fifth of a fiber diameter was estimated to produce an uncertainty of up to 35 degrees in the out-of-plane angle for fibers nearly perpendicular to the cutting plane.

A review of the literature shows that 3-D FOD measurement has been performed exclusively with variations of the surface ellipse method. However, the limitations of surface methods include poor resolution of the out-of-plane angle, especially when performed on digitized images; the ambiguity with regard to the direction of the out-

of-plane angle unless special imaging methods are used; non-uniform fiber diameters; the presence of fiber ends at the cutting plane; the difficulty of distinguishing between fiber ends and impurities or voids; and fiber–fiber contact which presents the non-trivial problem of distinguishing individual fibers. A comparison of the theoretical accuracy of the surface ellipse and optical sectioning methods in Chapter 2 shows that the surface methods may have an uncertainty of 30 degrees or more at large out-of-plane angles, compared with the sectioning methods (also presented in Chapter 2) which have a theoretical uncertainty of about 1 degree for fibers with aspect ratios of 10:1 or more, at all orientations.

One of the most serious drawbacks of surface methods, which has not been addressed in the literature, is the inability to measure fiber length. Fibers of different lengths are influenced differently by the flow. Thus any measurement technique that cannot measure both fiber orientation and length cannot yield an accurate description of the orientation distribution, unless there is a monodisperse fiber length distribution.

1.7 Fiber Orientation Prediction

The motion of fibers in a deforming fluid has been a subject of interest for many years. Jeffery (1922) solved the motion of single rigid ellipsoid in a viscous Newtonian fluid, assuming a no-slip condition at the surface. His equation was verified by several researchers for rigid cylindrical fibers with an appropriate equivalent ellipsoidal axis ratio. However, Arp and Mason (1977) showed that fiber-fiber interactions in concentrated solutions alter the orientation behavior of fibers, making quantitative predictions with Jeffery's equation inaccurate for injection molding solutions. Folgar and Tucker (1984) demonstrated that the critical volume fraction at which fiber-fiber interactions begin to be a significant factor is around 0.1 percent.

In 1962, Hand developed a general change equation for the second order tensor which describes the structure of an anisotropic continuum. However, it is difficult to use due to its complexity.

Givler, Crochet and Pipes (1983) developed a numerical scheme for the determination of the fiber orientation state in dilute suspensions. Fiber orientations were calculated from the numerical integration of Jeffery's orientation equation along the streamlines obtained on the basis of the finite element method. Numerical solution of the fiber orientation state were presented for simple shear flow, fountain flow and flow in infinite expansion. The advantage of this method is its capability of predicting fiber orientation in fluids flowing through complex geometries.

Dinh and Armstrong (1984) presented a rheological equation of state for semiconcentrated fiber suspensions derived from Batchelor's (1971) general result for the stress tensor and his cell model approach to obtain an estimate for the drag exerted by neighboring particles on a test particle. The term *semiconcentrated* refers to fiber suspensions in which the average distance between fibers is greater than the fiber diameter, and less than the fiber length. From this equation an explicit constitutive equation and rheological properties model were obtained. Their paper contains a summary of rheological measurements reported by various authors for concentrated fiber suspensions in Newtonian solvents. The model predicts that the viscosity of semiconcentrated fiber suspensions at steady state is identical to that of the Newtonian solvent, which has been observed experimentally in many cases.

Dinh and Armstrong's analysis assumes that the mechanical contact between fibers is rare, so that all interactions between fibers are hydrodynamic. Their analysis focuses on a test fiber, with the surrounding fibers and the fluid matrix replaced by a continuum with equivalent properties. The drag force on the surface of a fiber is

modeled by a line force along the major axis of the particle. With respect to fiber orientation behavior this model is equivalent to Jeffery's model with the aspect ratio equal to infinity. The significant difference between this theory and Jeffery's is that particles no longer rotate in simple shear flow, but approach an equilibrium position oriented in the direction of flow.

Altan, Advani, Güçeri and Pipes (1984) found tensor-based solutions of 2- and 3-D FOD functions in terms of velocity gradients. The governing equation is based on the Dinh-Armstrong (1984) model for semiconcentrated solutions. They found that elongational flow is much more effective at aligning fibers than is shear flow.

Folgar and Tucker (1984) proposed a solution for semiconcentrated solutions by adding a diffusion term to Jeffery's equations. Their model has proven to be a good predictor of FODs and appears frequently in the literature. The solution was derived from a phenomenological standpoint due to the complexity of modeling fiber-fiber interactions in concentrated solutions.

The model assumes: (1) fibers are rigid cylinders, uniform in length and diameter, (2) fibers are sufficiently large that Brownian motion is negligible, (3) the suspension is incompressible, (4) the matrix fluid is sufficiently viscous that particle inertia and particle buoyancy are negligible, (5) the centers of mass of the particles are randomly distributed, and (6) there are no external forces or torques acting on the suspension. The model has two terms: a hydrodynamic term which models the effect of the flow field (Jeffery's equation with infinite aspect ratio), and an interaction (diffusion) term which accounts for collisions. Collisions are assumed to have a randomizing effect on the FOD. A general version of the model for 3-D flow fields also exists (Folgar-Portillo, 1982).

In the Folgar-Tucker model any constant deformation results in steady-state orientation distribution after some time, whereas in Jeffery's model predicts continuous fiber rotation. The Folgar-Tucker model is not reversible whereas Jeffery's is. The irreversible nature is consistent with experimental observations. The model is capable of predicting the orientation distributions resulting from arbitrary deformation fields once the phenomenological interaction coefficient for the suspension has been measured. The biggest defect is that it predicts more rapid alignment in transient states than actually occurs in experiments, although the predictions are still qualitatively correct.

The 2-D Folgar-Tucker model for semiconcentrated suspensions is:

$$\frac{\partial \Psi_\phi}{\partial t} = C_I \dot{\gamma} \frac{\partial^2 \Psi_\phi}{\partial \phi^2} - \frac{\partial}{\partial \phi}[\Psi_\phi(-\sin\phi\cos\phi\frac{\partial v_x}{\partial x} - \sin^2\phi\frac{\partial v_x}{\partial y} + \cos^2\phi\frac{\partial v_y}{\partial x} + \sin\phi\cos\phi\frac{\partial v_y}{\partial y})] \qquad (1.6)$$

where Ψ is the orientation distribution function, C_I is the interaction coefficient, and $\dot{\gamma}$ is the strain rate.

Jackson, Advani, and Tucker (1986) presented a method for predicting the orientation of rigid short fibers in thin compression molded parts. The method extends Folgar and Tucker's model for fiber orientation in a semiconcentrated suspension to the case of spatially non-uniform flows and orientation states. A generalized Hele-Shaw model is used to predict flow and deformation during mold filling. Other assumptions are used that are appropriate for sheet molding compound: fibers that are much longer than the part thickness and a cold material molded in a hot mold. The predictions compared favorably to experiments on sheet molding compound and on a model suspension of nylon monofilaments in silicone oil. At the end of their paper they state,

> "A more fundamental theory of fiber orientation in concentrated suspensions, and a theory for orientation behavior in strongly non-homogeneous flows would be welcome. For the moment, the theory used here seems to be the best available for the compression molding problem...Procedures for more rapid and automatic determination of fiber orientation distributions would greatly ease the experimental burden, and there are promising developments in the offing (Lovrich and Tucker, 1985)."

In 1989, Ferrari and Johnson presented a model which is sufficiently general to include the cases of arbitrary fiber orientation distribution, arbitrary fiber geometry and accounts for fiber-fiber interactions. Unfortunately, the model is very complex and difficult to apply. The authors state that "even for the case of isotropic matrix composites, the computational task is considerable" and recommend using a symbolic manipulator for applying the theory.

Altan, Subbiah, Güçeri, and Pipes (1990) used a numerical method to predict the transient 3-D fiber orientations in very dilute Hele-Shaw flows in irregularly shaped planar cavities. The model is based on the quasi-steady state Hele-Shaw model and Jeffery's equation with infinite aspect ratio from which an equivalent differential representation was obtained. The modified model uses tensor representations of the fiber orientation distribution. Fiber orientation is calculated for a given velocity field, decoupling the flow and fiber orientation fields. The authors stated that, "At the present time, the implementation of an anisotropic flow model on injection molding problems has not been performed and considerable potential difficulties are anticipated in such an attempt."

Shanker, Gillespie, and Güçeri (1990) presented a model for the rheology of fiber suspensions with nonhomogeneous flow fields (i.e., where the velocity gradients vary significantly over the fiber length). The Stokes-Burgers (1938) model is used to approximate the forces and moments on the fiber. The rheological properties are determined using Batchelor's (1971) cell model approach as used by Dinh (1981). Fiber

motions in highly nonhomogeneous flows such as non-isothermal Hele-Shaw flows, commonly observed during injection molding were presented to illustrate the influence of nonhomogeneous flow fields on fiber motions, which are not accounted for in other models.

Reifschneider, Akay, and Ladeinde (1990) presented a method for fiber orientation simulation of thin walled parts of arbitrary three-dimensional shape. Following a filling analysis, transport equations for orientation of short fiber composites were solved using the finite element method. The model is based on Folgar and Tucker's (1984) enhancement of Jeffery's model.

A review of the literature shows that phenomenological models of flow induced fiber orientation exist, and many are capable of predicting fiber orientations which correlate reasonably well with experimental observations. However, no rigorous theory for flow-induced orientation in concentrated suspensions exists at the present time.

1.8 Material Property Prediction

Useful models have been developed to predict effective properties of composites once the fiber orientation state is known.

Halpin and Pagano (1969) proposed a model which approximates the properties of an arbitrary FOD by the combination of many layers of unidirectional fibers. The thickness of each layer is proportional to the amount of fiber in that direction. The behavior of the composite is then modeled with classical laminated plate theory.

The work of Mori and Tanaka (1973) has been the starting point of a series of papers in the literature on composite materials. Basing themselves on Eshelby's (1957) equivalent inclusion idea combined with Mori and Tanaka's concept of 'average stress' in the matrix, these works have dealt with many important micromechanics

problems, such as calculation of effective properties of composites, effects of cracks and void growth in viscous metals.

Semi-empirical approaches have also been employed to derive unidirectional composite stiffness constants. A well known example of this type is the Halpin-Tsai (1976) equation which was derived by simplifying Herman's (1976) solution. Other semi-empirical and numerical approaches can be found in Lees (1968), Conway and Chang (1971) and Chang, Conway, and Weaver (1972). The subject of biased short fiber orientations was also treated by Fukuda and Kawata (1974).

The 'self-consistent' approach of Hill (1965a, 1965b) was followed by Chou, Nomura and Taya (1980) in which the short-fibers are treated as ellipsoidal-shaped inclusions. In this model a single inclusion is assumed to be embedded in a continuous homogeneous medium. Interaction among fibers is taken into account by assuming that the inclusion has the elastic properties of a short fiber while the surrounding material possesses the properties of the composite, from which the unknown elastic property of the composite is solved. Their theory takes into account elastic stiffness of the constituent materials, inclusion aspect ratio, and filler volume fraction. The model differs from the Halpin-Tsai equation at intermediate aspect ratios.

Christensen in 1979 introduced a model for randomly oriented short fiber materials based on the summation of the contributions of orthotropic sub-elements oriented in all directions.

In 1982, Mura presented a comprehensive introduction to effective composite material properties. And in 1987, Benveniste reformulated Mori-Tanaka's theory to calculate effective properties of composites. His solution uses Eshelby's equivalent inclusion idea, and Mori-Tanaka's concept of 'average-stress.'

Takao, Chou, and Taya in 1982 presented a model based on Eshelby's (1957) equivalent inclusion method, and the average induced strain approach of Taya, Mura, and Chou (Taya and Chou, 1981; and Taya and Mura, 1981). Their approach takes into account the interactions among fibers at different orientations. They presented numerical results to demonstrate the effects of fiber elasticity, aspect ratio, volume fraction, and orientation distribution on composite Young's modulus. The results of the analysis were found to lie within predicted bounds.

In 1988, Karger-Kocsis and Friedrich presented a dimensionless reinforcing effectiveness parameter which takes into account the processing-induced fiber layer structure, fiber alignment, fiber volume fraction, fiber aspect ratio, and aspect ratio distribution. Using this parameter they were able to find a semi-empirical linear relationship between fracture toughness of the composite and that of the matrix.

Also in 1988, Sato, Kurauchi, Sato and Kamigaito investigated the influence of fiber diameter on the mechanical properties of short fiber composites using smaller diameter fibers than are conventionally used (7 μm, 4 μm, and 0.5 μm, compared to the usual $\approx$13 μm). Experimental results obtained from specimens with a constant weight fraction of 30% showed that strength and toughness were greatest with 7 μm fibers.

Fan and Hsu (1989) studied the relationship between the stress distribution and fiber orientation in model composites and found their results to be "consistent with most simplistic mechanical models." An analysis using the Eshelby (1957) equivalent inclusion method fit their experimental data exceptionally well.

Ferrari and Johnson (1989) cited numerous papers dedicated to the subject of treating SFR materials as homogeneous "effective" media, including: Hill (1963), Halpin and Pagano (1969), Russell (1973), Laws and McLaughlin (1979), Chou and

Nomura (1980), Taya (1981), Takao et al. (1982), Benveniste (1987), Steif and Hoysan (1987). Also Christensen (1979) and Hashin (1983), which also discuss general homogenization schemes.

Ferrari and Johnson (1989) presented a derivation of the effective elasticities of short-fiber composites with an arbitrarily specified orientation distribution of fibers. The formalism is sufficiently general to include the cases of arbitrary material symmetry of both the fiber and matrix. Fiber-fiber interactions are accounted for by means of a generalized Mori-Tanaka assumption. This solution is expected to model composites for a wide range of concentration levels since it is founded on Mori-Tanaka. However, the model is complex and computationally expensive.

Choy, Leung, and Kowk (1992) found good agreement with laminate theory and experimental results of elastic moduli and thermal conductivity of SFRTs. The difference between predicted and measured values was less than 10 percent. Their thermal diffusivity results showed shell/core structure. Their model took into account properties of constituent materials, fiber volume fraction, aspect ratio, and an orientation factor, λ, where $\lambda = 0$ corresponds to random orientation, and $\lambda = \infty$ corresponds to perfect alignment. The authors stated that, "Despite the importance of [SFRT] materials, there have been few detailed experimental and theoretical studies on the elastic moduli and thermal conductivity, which are properties of great basic interest and technical significance."

A great number of micromechanical models exist for SFRTs, but as Fan and Hsu stated, "...relatively few experimental data are available to be compared with the calculations. Most difficulties arise from the fact that it is nearly impossible to have a real composite system which can be defined and characterized well to be compared

with theoretical calculations." Thus additional data are needed to verify and refine existing models, as well as aid in the development of more rigorous models.

1.9 Observed Influence of FOD on Material Properties

This section presents a description of relationship between fiber orientation distribution and material properties which have been reported in the literature.

Blumentritt, Vu and Cooper (1974) performed a comprehensive evaluation of unidirectional short fiber composites of various matrix and fiber materials and various fiber volume fractions. Strength and modulus were found to increase with fiber volume. Fiber efficiency, which is a measure of how fully the fibers contribute to the material properties, was 0.43 for the elastic modulus, and 0.25 for strength. A fiber efficiency of 1 implies that the material properties can be derived from a simple rule-of-mixtures calculation. A low efficiency value implies very little influence from the fibers on material properties. Low efficiency occurs when the matrix is unable to transfer the load to the fibers effectively. The transverse strength was found to be approximately that of the matrix, whereas the transverse modulus increased with fiber density. No existing model was found to be adequate for predicting the mechanical properties of the experimental composites from the properties of the constituent materials.

Hogg (1986) studied the influence of flow-induced anisotropy on the impact behavior of glass fiber reinforced disks of polypropylene. Weldlines were shown to have a significant influence on the energy absorption capabilities of the test materials at high loading rates.

Karger-Kocsis and Friedrich (1988) studied the relationship between fracture toughness and the microstructure of long and short glass fiber reinforced injection-

molded polyamide composites. They found a semi-empirical relationship between the fracture toughness of the composite and that of the matrix for both long and short fiber composites with the use of a dimensionless reinforcing effectiveness parameter.

Kenig, Trattner, and Anderman (1988) observed a clear correlation between the measured tensile properties and the ratio of skin layer to total thickness of short-fiber liquid crystalline polymer composites.

The influence of weldlines on tensile strength and fatigue resistance was studied by Boukhili, Gauvin, and Gosselin (1989), Vaxman and Narkis (1991), and Fisa and Rahmani (1991). In each case reduction of strength and fatigue resistance were attributed to fiber orientation at the weld line. Analysis of the weld line zone showed fibers oriented almost perfectly in the plane parallel to the weldline.

Fisa and Rahmani found that in the weldline zone every structural feature of the material may be different from the bulk of the material. The presence of weldlines in materials containing 40 wt% fibers reduced the tensile strength by up to 60 percent. They determined that the weldline strength is equal to that of the unreinforced material reduced by the proportion of the area occupied by fibers.

1.10 Characterization of the Fiber Orientation Distribution

The modeling of short fiber reinforced composites requires a rigorous definition of the fiber orientation distribution.

1.10.1 Orientation Distribution Function

The most complete description of the fiber orientation distribution is the fiber orientation distribution function, which gives the amount of fiber material as a function of orientation.

The 2-D orientation distribution function $N(\phi)$ represents the amount of fiber material oriented in direction ϕ. A normalizing condition is applied such that:

$$\int_{-\pi/2}^{\pi/2} N(\phi)d\phi = 1 \tag{1.7}$$

The orientation distribution function provides a full description of the fiber orientation state, but it is not the most convenient representation for modeling purposes. Often, descriptive parameters are derived from the orientation function. For example, the projection of a unit length on the loading direction (i.e., the cosine of the angle) has been used to obtain orientation descriptors for correlating various anisotropic properties (Pipes, McCullough, and Taggart, 1982). Herman's planar orientation parameters f_p and g_p are defined as

$$f_p = 2 < \cos^2\phi > -1, \qquad g = (8 < \cos^4\phi > -3)/5 \tag{1.8}$$

where the quantity inside $< >$ is the weighted average as,

$$< \cos^m\phi > \; = \int_{-\pi/2}^{\pi/2} N(\phi)cos^m(\phi)d\phi. \tag{1.9}$$

A value of $f = 0$ represents a random (planar) orientation, whereas a value of $f = 1$ represents a perfectly aligned state.

The effectiveness of fiber reinforcement is often correlated to such descriptors. Kau (1987) characterized his results by the principal direction and the Hermans' orientation descriptor.

Stein (1961) and Seferis, McCullough, and Samuels (1976) McCullough, Wu, Seferis, Lindenmeyer (1976), White and Spruiell (1981, 1983), McGee and McCullough (1984) presented various descriptors of the orientation field, but these require assumptions about the shape of the FOD. Most require that the FOD be symmetrical.

Chin, Liu, and Lee (1988) used planar Weibull and log-normal statistical distribution functions to characterize the fiber length distribution in SFRTs.

Advani and Tucker (1987) presented a comprehensive and efficient method of describing fiber orientations which has been widely accepted. The following is a summary of their work.

The orientation of a single fiber can be represented in spherical coordinates by the Eulerian angles θ and ϕ or by a unit vector $\mathbf{p}$ oriented along the fiber axis. These measures are related by

$$p_1 = \sin\theta\cos\phi, \quad p_2 = \sin\theta\sin\phi, \quad p_3 = \cos\theta \tag{1.10}$$

where θ and ϕ are the Eulerian angles shown in Figure 1.3.

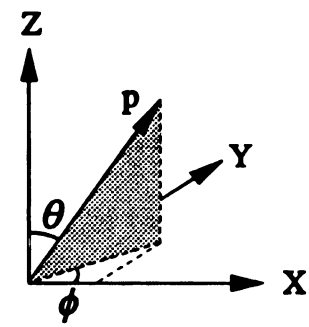


Figure 1.3: Eulerian angles.

The average over all possible directions can be obtained by integrating $\mathbf{p}$ over the unit sphere:

$$\oint d\mathbf{p} = \int_{\phi=0}^{2\pi}\int_{\theta=0}^{\pi} \sin\theta d\theta d\phi \tag{1.11}$$

The most complete description of the orientation distribution is the probability orientation distribution function, $\Psi(\theta,\phi)$ or $\Psi(\mathbf{p})$. Its definition is such that the probability of finding a fiber lying in the angle increment θ to $(\theta + d\theta)$, and ϕ to $(\phi + d\phi)$ is equal to $\Psi(\theta,\phi)\sin\theta\, d\theta\, d\phi$.

Since the ends of a fiber are indistinguishable from each other, Ψ must satisfy the condition:

$$\Psi(\theta,\phi) = \Psi(\pi-\theta,\pi+\phi), \quad \text{or} \quad \Psi(\mathbf{p}) = \Psi(-\mathbf{p}) \tag{1.12}$$

A normalizing condition is also applied to Ψ.

$$\int_{\phi=0}^{2\pi}\int_{\theta=0}^{\pi} \Psi(\theta,\phi)\sin\theta\, d\theta\, d\phi = \oint \Psi(\mathbf{p})d\mathbf{p} = 1 \tag{1.13}$$

1.10.2 Tensor Representation of the Orientation Distribution

The probability orientation distribution function is a complete, unambiguous description of the orientation state, but suffers from the disadvantage of being cumbersome to use.

A more manageable description of the FOD is a tensor based representation. One set of orientation tensors can be defined by forming dyadic products of the vector $\mathbf{p}$ and then integrating the product of these tensors with the distribution function over all possible directions. Because the distribution function is even the odd-order integrals are zero, so only the even-order tensors are of interest. In two-dimensions, the second order tensor components are:

$$a_{ij} = \begin{vmatrix} <\cos^2\phi> & <\sin\phi\cos\phi> \\ <\sin\phi\cos\phi> & <\sin^2\phi> \end{vmatrix} \tag{1.14}$$

where $< >$ denotes an average over a large number of fibers.

Or,

$$a_{ij} = \frac{1}{n}\sum_{k=1}^{n} p_i^k P_j^k. \tag{1.15}$$

To compensate for orientation bias of the fibers in the cutting plane, a weighting function must be added.

$$w(\theta) = \frac{1}{\frac{l}{d}\cos\theta + \sin\theta} \tag{1.16}$$

where l is the fiber length, and d is the diameter. (This correction is necessary only for surface imaging data.) Applying the weighting function the tensor components become

$$a_{ij} = \frac{\sum_{k=1}^{n} p_i^k p_j^k w(\theta^k)}{\sum_{k=1}^{n} w(\theta^k)}. \tag{1.17}$$

In three-dimensions, the second- and fourth-order orientation tensors are:

$$a_{ijkl} = \oint p_i p_j p_k p_l \Psi(\mathbf{p}) d\mathbf{p} \tag{1.18}$$

The second-order orientation tensor a_{ij} has nine components. The symmetry of the tensor $a_{ij} = a_{ji}$ reduces the number of independent components to six, and a normalizing condition of $(a_{11} + a_{22} + a_{33} = 1)$ can be used to reduce the number of independent components to five. Using angle brackets <> to denote the average over all fibers in a region, the tensor components can be written as:

$$a_{11} = < \sin^2\theta \cos^2\phi > \tag{1.19}$$

$$a_{12} = < \sin^2\theta \cos\phi \sin\phi > \tag{1.20}$$

$$a_{13} = < \sin\theta \cos\theta \cos\phi > \tag{1.21}$$

$$a_{22} = < \sin^2\theta \sin^2\phi > \tag{1.22}$$

$$a_{23} = < \sin\theta \cos\theta \sin\phi > \tag{1.23}$$

$$a_{33} = < \cos^2\theta > \tag{1.24}$$

Similarly, the components of the fourth-order orientation tensor can be written as:

$$a_{1111} = < \sin^4\theta \cos^4\phi > \quad (1.25)$$

$$a_{1112} = < \sin^4\theta \cos^3\phi \sin\phi > \quad (1.26)$$

$$a_{1113} = < \sin^3\theta \cos\theta \cos^3\phi > \quad (1.27)$$

$$a_{1122} = < \sin^4\theta \cos^2\phi \sin^2\phi > \quad (1.28)$$

$$a_{1123} = < \sin^3\theta \cos\theta \cos^2\phi \sin\phi > \quad (1.29)$$

$$a_{1133} = < \sin^2\theta \cos^2\theta \cos^2\phi > \quad (1.30)$$

$$a_{1222} = < \sin^4\theta \cos\phi \sin^3\phi > \quad (1.31)$$

$$a_{1223} = < \sin^3\theta \cos\theta \cos\phi \sin^2\phi > \quad (1.32)$$

$$a_{1233} = < \sin^2\theta \cos^2\theta \cos\phi \sin\phi > \quad (1.33)$$

$$a_{1333} = < \sin\theta \cos^3\theta \cos\phi > \quad (1.34)$$

$$a_{2222} = < \sin^4\theta \sin^4\phi > \quad (1.35)$$

$$a_{2223} = < \sin^3\theta \cos\theta \sin^3\phi > \quad (1.36)$$

$$a_{2233} = < \sin^2\theta \cos^2\theta \sin^2\phi > \quad (1.37)$$

$$a_{2333} = < \sin\theta \cos^3\theta \sin\phi > \quad (1.38)$$

$$a_{3333} = < \cos^4\theta > \quad (1.39)$$

In the tensor representation of the orientation distribution, only two independent components are needed to describe planar orientations. Five independent second order components are needed to describe an arbitrary three-dimensional orientation distribution.

The tensor description of the orientation distribution is independent of the reference frame since the rules of tensor transformations can be applied to the orientation tensors. The set of even order tensors completely describe the orientation distribution

function. The fourth-order tensor is sufficient to predict the material properties from FODs exactly (Advani and Tucker, 1987). For most applications the second order tensor is sufficient to describe the orientation distribution, but higher order tensors may be used as needed. The advantage of using the tensor description is that it provides a compact, efficient description of the orientation distribution independent of the coordinate system and requires no assumptions about the shape of the orientation distribution function.

CHAPTER 2

NEW METHOD OF FIBER ORIENTATION MEASUREMENT

The method of fiber orientation measurement presented here is based on a unique imaging technique and custom 3-D image analysis software. The imaging method consists of optically sectioning transparent composites containing opaque tracer fibers using a conventional light microscope. A sequence of images captured at equal intervals is analyzed as a three-dimensional image from which fiber orientation and length are accurately measured. Most material properties models require a measure of the total length of fiber material as a function of direction, which is what the optical sectioning method provides. A limitation of the current implementation (but not of the technique in general) is that it cannot provide a true *fiber length* distribution which could be required by more sophisticated models.

The optical sectioning method overcomes the problem identified by Fan and Hsu (1989) that "it is nearly impossible to have a real composite system which can be defined and characterized well to be compared with theoretical calculations."

2.1 Optical Sectioning

The technique of optical sectioning relies on the narrow depth of field of an optical microscope. Objects or portions of objects that lie within the depth of field are visible,

while those outside are not. The following equation is often used to calculate depth of field for optical microscopy:

$$\delta\,(\mu\text{m}) = n\left[\frac{\lambda}{2\,(\text{N.A.})^2} + \frac{0.34}{\text{V(N.A.)}}\right], \tag{2.1}$$

where n is the refractive index of the media, λ is the wavelength of light, N.A. is the numerical aperture, and V is the total magnification. In the work performed here, $\delta = 5.96\,\mu$m ($n = 1.49$, $\lambda = 0.7\,\mu$m, N.A. = 0.3, and V = 10). This is the approximate range over which objects appear to be in focus to the human eye. For the purposes of optical sectioning, however, the critical factor is whether an object is visible, rather than whether it is in sharp focus. The depth of field in this case is approximately three times as large, or about $17\,\mu$m for the work performed here.

By incrementally moving the imaging plane through the depth of a semi-transparent material it is possible to obtain a complete 3-D representation of its structure. This is the technique that is used here to obtain precise measurement of 3-D fiber orientation and length. In this particular application transparent composite materials composed of transparent plastic material with glass fibers having the same refractive index are analyzed by imaging a small percentage of opaque tracer fibers in the material.

Some limitations are imposed on the technique by the optical physics involved, especially when dealing with real (non-ideal) materials. The limitations of a specific application of the technique depend on the sample material and the characteristics of the imaging device. Possible limitations include: diffraction due to refractive index mismatches and imperfect interfaces between fiber and matrix, obscuring of the optical path by intervening fibers, fuzziness and loss of contrast caused by out-of-focus information, limited resolution along the optical axis, local variations in transmissivity of the material, the presence of impurities, and the finite working distance of the

objective lens. However, these limitations can be minimized by careful preparation of materials and controlled lighting conditions. The obscuring of the optical path places an upper limit on the tracer fiber density. Experience with a light microscope set-up has shown that 0.12 vol% is an approximate upper limit for fibers of 10 μm diameter in a sample 3 mm thick. For tracer fibers 450 μm long this gives approximately 34 fibers/mm^3. As a comparison with surface methods, Davis (1988) reported 60–175 fibers per photograph with 33 wt% glass and a picture width of 0.3 mm. Greater tracer content can be used if the sample thickness is reduced or by using imaging devices which are better at eliminating out-of-plane information. It is difficult to quantify the relationship between tracer density and penetration depth because the relationship is dependent on characteristics of the composite material, the characteristics of the imaging system and the illumination as well as fiber length and diameter. But it appears that doubling the tracer fiber density decreases the penetration depth by more than 50 percent with the system used here. An imaging system with a narrower depth of field and enhanced ability to eliminate out-of-plane information would be better able to image specimens with high tracer fiber densities.

Another phenomenon that is exhibited in optical sectioning is a loss of contrast with increasing penetration depth, even though the image may remain sharp. This is likely due to out-of-plane information arriving at the microscope objective and imperfect transmissivity of the material. An absolute limit is placed on the the penetration depth by the working distance of the objective. Once the objective meets the surface of the material, no further penetration is possible. Objective lens working distances up to 9 mm are common for the relatively small magnifications used here, however, and other factors usually intervene before this limit is reached. One final complication with optical sectioning may occur if the surface of the material is polished and fibers intersect the surface. Because of the difference in wear resistance of the two

materials, the surface may not remain flat during polishing and therefore may cause localized dislocations or distortions of the image.

2.1.1 Refractive Index Matching

Transparent composite materials require a transparent matrix and fiber material which have the same refractive index. If there is a good match between the materials and a good interface between fiber and matrix is achieved, composites can exhibit a high degree of transparency, allowing high fiber content materials to be optically sectioned. The degree to which the indices must be matched depends on the fiber volume fraction, fiber diameter, desired penetration depth, and the characteristics of the imaging system. It is apparent from experimentation, however, that a mismatch of 0.07 yields a material that is practically impenetrable, whereas a mismatch of 0.007 yields a material through which 10 μm fibers can be clearly resolved at a depth of 3 mm.

The refractive index of a material is temperature and wavelength dependent. The change of refractive index with temperature and wavelength is usually different for the constituent materials. Therefore, a perfect match can be achieved only at a specific temperature and wavelength. A simple method to determine where the best match occurs consists of using a photospectrometer to focus a beam of light on one side of the sample while measuring the amount of light transmitted to the other side. As the mismatch of the refractive indices decreases, less light will be scattered as it passes through the material and more light will reach the detector. By applying this procedure for different temperatures over a range of wavelengths the ideal match can be determined.

Dunlop and Howe (1991) reviewed a basic theoretical approach to describing light scattering in (high concentration) filled materials with nearly matching refractive indices (reagent grade PMMA and glass) by the Rayleigh-Gans-Debye Theory (Van de Hulst, 1957; and Kerker, 1969), including modifications necessary to handle high filler concentrations. The result of their analysis is an expression for the optical transmission of a polymer composite as a function of particle size, volume fraction, composite thickness, and refractive index difference between the components. They showed that the model can be used to accurately reproduce the transmission versus temperature curves for polymer/glass mixtures in which the volume fraction exceeds 50%. They stated that glass and plastics have similar dispersion curves. "Excess hazing" (less than perfect transmission due to effects other than refractive index mismatch) is caused by contamination from milling, voiding, internal stresses and inhomogeneities in both the plastic and the glass, which cause light scattering. For dilute systems in which the average distance between particles is at least 3 to 9 times the radius, the intensity, I_z, transmitted without scatter through thickness z is given as:

$$I_z = I_o \exp[-(\frac{3\pi^2\phi z d(\Delta n^2 + \sigma^2)}{\lambda_o^2}(1 - \frac{2}{9}u'^2))] \tag{2.2}$$

In this equation, I_o is the incident intensity, ϕ is the volume fraction of glass, z is the thickness, d is the particle diameter, Δn is the difference in the refractive indices, u' is a dimensionless diffraction parameter, λ_o is the wavelength in a vacuum, and σ is the variance of the refractive index distribution. The variance of the refractive indices results from contaminates and inhomogeneities in the constituent materials. From this equation the relative contributions of the various factors to the degradation of transparency can be determined. The transmission decreases as the volume fraction, thickness, or mismatch in the refractive indices increases. The dependence on particle

size is more complicated because it is coupled to the measuring instrument via the parameter u'. For a high resolution detector, such as the human eye, transmission decreases as particle size decreases as one would expect. However, the opposite result is observed with a typical spectrophotometer.

When the concentration is greater than the dilute suspension criterion spatial correlations between neighboring particles increases. As a result, the effects of interparticle interference no longer average out, and the observed transmission curve becomes broader. Thus the temperature dependence of the haze is decreased by packing, meaning that there is greater transmission over a broader range of temperatures. An interference function, P, can be added to the transmission equation as an additional constant factor in the exponent to account for interparticle separation. Dunlop and Howe found that the function, P, has a constant value of ≈ 0.43 for particle composites with volume fractions around 0.5. This shows that a higher particle density results in a broader temperature range of acceptable transparency.

2.1.2 Advantages

Optical sectioning possesses significant advantages over conventional imaging methods. It allows the length and the orientation of individual fibers to be measured. As was stated earlier, to accurately measure a fiber orientation distribution it is essential to measure fiber length as well as orientation. Optical sectioning allows the out-of-plane component of the fiber orientation to be resolved with much greater accuracy than can be achieved by surface methods and allows fiber orientation information to be obtained as a function of material depth without requiring physical cutting and polishing. The surface ellipse methods are most accurate for orientations nearly parallel to the cutting plane, and are least accurate for orientations perpendicular to the

cutting plane. For fibers that are nearly parallel to the cutting plane a small change in the out-of-plane angle causes a large change in the ellipse aspect ratio, whereas for fibers that are perpendicular to the cutting plane, a small change in the out-of-plane angle has very little effect on the aspect ratio. Optical sectioning typically has greatest out-of-plane angle resolution at large out-of-plane angles.

The pixel quantization of the digitized image determines the resolution of both the ellipse measurements and optical section measurement. The resolution of the out-of-plane angle using the surface ellipse method can be characterized as follows. Let d be the fiber diameter and a be the length of the major axis of the ellipse, both measured in pixels. The out-of-plane angle is simply $\theta = \sin^{-1}(d/a)$. A fiber 5-pixels in diameter oriented perpendicular to the cutting plane would have a measured major axis length of 5 ± 1 pixels. A measured value of 6 pixels gives an apparent angle of 56.4 degrees, an error of 33.6 degrees. To reduce the error to 10 degrees, the magnification would have to be increased by a factor of 13, giving a fiber diameter of 65 voxels. At this magnification an image 640 pixels wide (a typical frame grabber resolution) would span less than 10 fiber diameters. Furthermore, the accuracy of the ellipse axes measurements are limited by complications due to variations in the true fiber diameter, fiber chipping during polishing, the presence of fiber ends at the cutting plane, impurities in the material, indistinct interfaces, and fiber-fiber contact. Thus, even at high magnification it is very unlikely that an error of less than 10 degrees can be achieved in many cases.

In contrast, using only two optical sections separated by one fiber diameter, and assuming an error of 1 pixel in determining the centroids of the fiber cross-sections gives an out-of-plane angle error of 11.3 degrees. If the fiber had an aspect ratio as small as 10:1, and only two optical sections were taken over an interval which included its ends, the error would decrease to 1.1 degrees.

Because cutting and polishing are not required a significant time savings can also be realized by optical sectioning. Cutting and polishing may require several hours to complete, whereas optical sectioning can be started immediately after molding. Experience here has shown that the optical sectioning method is approximately five times faster than cutting and polishing. The method is non-destructive, allowing the same material to be subjected to mechanical or thermal testing for correlating material properties with fiber orientation. And fiber curvature can easily be measured by this method, whereas it cannot be measured at all by surface techniques.

2.1.3 Disadvantages

The range of materials that can be studied by this method is somewhat limited. However, by using special formulations of glass, many types of transparent plastics are candidates for optical sectioning. Another limitation is that the tracer fiber density must be relatively sparse to allow optical access into the sample. This limits the size of the fiber sample population. However, several compatible fiber/matrix combinations have been identified which may be suitable for producing transparent composites (Table 7.1), and non-dimensional analysis methods offer the potential to generalize the results from transparent systems to opaque systems.

2.2 3-D Image Analysis

3-D image analysis is essential to the extraction of fiber orientation data from optical slices. However, computerized image analysis and object recognition is a formidable task even in two dimensions. The image analysis problem in its simplest form is a problem of detecting and measuring lines in three-dimensional space. The problem is complicated by the presence of non-straight fibers, noise, shadows, and other factors.

Ser

Fina

a

clud

24-bit

RGB

pixels

sessing

Inte

Tw

noise e

Nat

Several algorithms were developed with unsatisfactory results before arriving at the final method.

The following sections describe image preparation and 3-D image processing algorithms that were developed and implemented for measuring 3-D FOD's from sequences of optical slices. A description and analysis of the earlier unsuccessful methods is included to illustrate and provide insights into the problem of 3-D line detection.

2.2.1 Preprocessing

Captured images typically consist of 8-bit pixels representing 256 levels of gray, or 24 bit color pixels with 8 bits for each of the primary colors (red, green, and blue; or RGB). Since each image is part of a sequence of images representing a 3-D object, the pixels possess a depth dimension equal to the spacing between images. Pixels possessing a depth dimension are referred to as voxels, or volume elements. The storage requirements and computational load for handling 3-D images can be significantly reduced by converting grayscale or color images to binary images. The simplest method of doing this is a simple thresholding process. Voxels with intensities greater than a given value are assigned a value of 1. Voxels with equal or less intensities are assigned a value of 0. In the case of color images, the pixel intensity is generally calculated by a weighted sum of the RGB components. The NTSC[1] formula for computing intensity is:

$$\text{Intensity} = 0.299 \cdot \text{R} + 0.587 \cdot \text{G} + 0.114 \cdot \text{B} \tag{2.3}$$

Two- or three-dimensional filters may be applied prior to thresholding to reduce noise effects, remove low-frequency variations in intensity due to uneven illumination,

[1] National Television System Committee

enhanc
quality

??

Segm
cific i

to ins
repre
exist
fiber
Thirst

The J
It is s
times
from a
case of

enhance edges, or perform other image enhancement functions as required by the quality of the image.

2.2.2 Image Segmentation

Segmentation, as it is used in image processing, refers to the identification of specific items of interest in an image. In this case the focus is the tracer fibers. If the fibers were isolated from each other it would be a trivial matter to segment the fibers from the matrix simply by identifying contiguous groups of voxels. However, in practice the fibers are often touching, or at least appear to be touching due to insufficient resolution in optical axis direction. In fact, dozens of fibers may be represented in a single contiguous group of voxels. The major challenge in fiber orientation measurement from 3-D images is determining which voxels belong to a given fiber. Several algorithms were developed and tested for this purpose. These include, Thin3D (three-dimensional thinning), 3-D Hough transform, Angle Segregation, and Simulated Annealing. Of these algorithms the 3-D thinning algorithm proved to be superior in terms of speed, robustness and accuracy. However, the Hough transform can be used in conjunction with the 3-D thinning algorithm to overcome some of the problems associated with poor image quality.

3-D Thinning

The 3-D thinning algorithm was developed by the author specifically for this project. It is similar to traditional 2-D thinning or skeletonization algorithms that are sometimes used in optical character recognition. It consists of removing exterior voxels from a cluster in a uniform manner until the centerline of the cluster is reached. In the case of fibers, voxels are removed until only those lying along the medial axis of the

fiber remain. A suitable thinning algorithm must meet the following requirements: It must not disturb the connectivity of the image. That is, it may not cause a contiguous group of voxels to become non-contiguous, and it may not create holes. It must not shorten voxel chains, otherwise all structures would be reduced to single voxels. And it must remove voxels in a uniform manner such that the remaining voxels are at the medial axis of the object. A detailed presentation of the 3-D thinning algorithm is presented in Section 4.6.

Once an image has been thinned it is a simple matter to identify the intersections and endpoints of fibers. Voxels with only one neighbor are endpoints, and voxels with more than two neighbors are intersections. This method was applied with excellent results in terms of speed, accuracy, robustness, and well-defined convergence.

Hough Transform

The Hough transform (Hough, 1962) is a widely-used, patented, 2-D line detection algorithm. It consists of mapping pixel coordinates into a domain in which pixels belonging to single line share the same coordinates. Figure 2.1 is an illustration of such a coordinate system. All of the points lying on a line have the same perpendicular

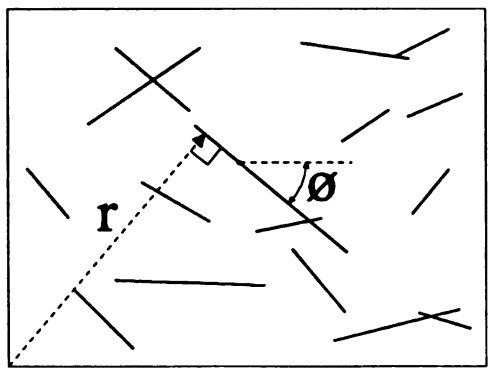


Figure 2.1: Example of Hough transform coordinate system.

distance, r, to the origin for a specific value of θ. This means that each pixel can

contribute evidence of the existence of a line independent of the other pixels belonging to that line. Because of this, the Hough transform can detect discontinuous lines, is robust, and lends itself well to parallel processing. However, the Hough transform has two limitations which keep it from being an acceptable method for the measurement of fiber orientation distributions. First, it cannot accurately determine the lengths of fibers which is essential for an accurate representation of a fiber orientation distribution. Second, curved lines are not detected by the Hough transform which can be a serious limitation with real fiber images in which fibers are not always perfectly straight. Nevertheless, when used in conjunction with the 3-D thinning algorithm, its ability to handle highly discontinuous lines can enhance the accuracy of fiber angle measurements, with a concomitant degradation in the accuracy of fiber length measurement. The Hough transform was adapted to 3-D line detection and included as an option in the 3-D analysis software for use with poor quality images. The details of the 3-D Hough transform are presented in Section 4.7.

Angle Segregation

The Angle Segregation algorithm was developed specifically for this project. The basic premise on which it is based is that voxels belonging to a given line share a similar orientation relative to any reference point on that line. Thus, by selecting a voxel at random and calculating the vectors from that point to each of the voxels that are contiguous with the reference voxel, the most frequently occurring direction or dominant vector can be determined. The voxels are segregated based on how parallel they are to the dominant vector. Determination of the dominant vector is determined by a two step selection process as illustrated in Figure 2.2. The first selection is done by projecting the voxels onto a plane which is divided into sectors whose apexes meet at the projection of the reference voxel. The pair of opposing sectors which contain

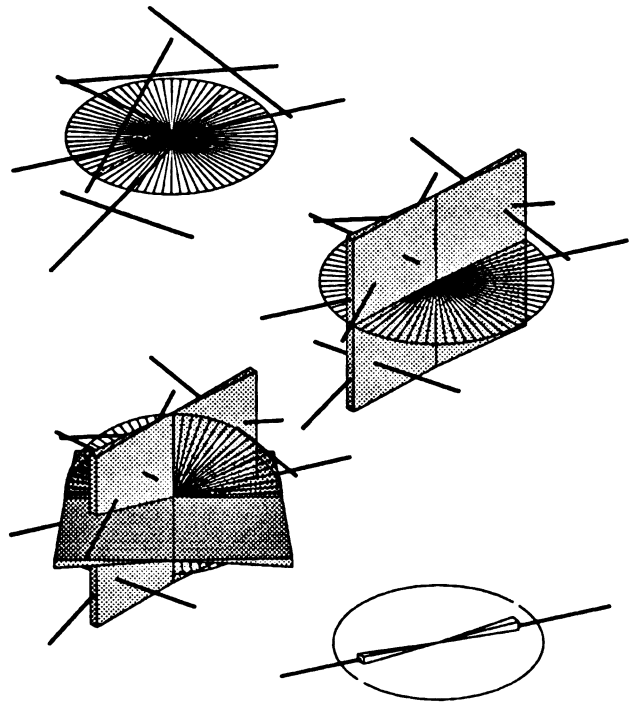


Figure 2.2: Illustration of angle segregation algorithm.

the greatest number of voxels are named the dominant sectors. The voxels whose projections lie outside of these sectors are excluded from the selection process. The second selection is done by projecting the remaining voxels onto a plane orthogonal to the original projection plane. Again the sector pair containing the largest number of voxels is determined and all voxels whose projections lie outside of these dominant sectors are excluded. In the end, only the voxels lying within the intersection of these dominant sectors are selected. A group of voxels that has been segregated by this method consists of voxels within a double-wedge shaped volume with the two apexes located at the initially selected voxel. This group of voxels is further refined by finding the best-fit line through the group and reselecting voxels based on their proximity to the line, which converts the double-cone into a cylinder. A third selection is made by recalculating the best-fit line through the cylindrical group and reselecting the voxels based on a closer proximity to the best-fit line. The voxels included in the final

selection are marked as belonging to one fiber, and a new random voxel is chosen, from which a new angle segregation is made, ignoring the voxels that were already marked. This process continues until a given percentage of the voxels have been marked, at which point the remaining voxels are discarded.

This method proved to be very accurate in determining the orientations of simulated very straight, well-defined lines, but failed with real data. It also exhibited relatively poor efficiency and, in fact, could fail to reach a result. The weaknesses of this algorithm are due to a number of factors. First, the farther a voxel is from the initial voxel, the more likely it is to deviate from the best-fit line and the greater its influence on the orientation of the best-fit line. Therefore, voxels belonging to neighboring fibers can strongly bias the selection process resulting in a poor ability to find a fiber when the fibers are closely grouped. Also, the algorithm has a poor convergence criterion. That is, it is very difficult to know when all of the fiber voxels have been selected and when the remaining voxels are stray voxels caused by noise, or are scattered voxels which belong to fibers but were excluded during the selection process.

Simulated Annealing

Simulated annealing is a well-known algorithm for dealing with otherwise intractable combinatorial optimization problems (Press, 1988). It is often used as a last resort since it is computationally expensive. The solutions generated by simulated annealing are not guaranteed to be optimal, but are usually very nearly optimal.

The simulated annealing algorithm is based on the analogy between the simulation of the annealing of solids and the problem of solving large combinatorial optimization problems (Van Laarhoven, 1987). Solids are annealed by heating them to a high

temperature where all of the molecules are able to randomly arrange themselves. The material is then cooled at a sufficiently slow rate that the molecules are allowed to arrange themselves in a low energy lattice structure. If the cooling occurs too quickly the molecules are frozen in place without having an opportunity to achieve a low-energy state. Perfect organization can be achieved by an infinitely slow cooling. The cooling schedule is the determining factor in the optimality of the result and the time required to arrive at that result. At each temperature in the schedule the material is allowed to reach thermal equilibrium, which is characterized by a probability of being in an energy state, E, given by the Boltzmann distribution:

$$P(E) = \frac{1}{Z(T)} e^{-E/kT} \tag{2.4}$$

where T is the temperature, $Z(T)$ is a normalization factor, k is the Boltzmann constant, E is the total energy of the system, and P is the probability of being in a state with energy E.

To simulate this process, Metropolis et al. (1953) proposed a Monte Carlo method which generates a sequence of states in the following way. Small random perturbations are applied to a randomly chosen particle, which cause a change, ΔE, in the energy of the system. If ΔE is negative, the new state is accepted. If ΔE is positive, then the probability of acceptance of the perturbed state is given by $e^{-\Delta E/kT}$. This general scheme of always taking a downhill step while *sometimes* taking an uphill step, is known as the Metropolis criterion.

There are many similarities between minimizing a cost function and annealing. In optimization, the objective function to be minimized is analogous to the energy, and a control parameter is analogous to kT. The simulated annealing algorithm is a sequence of Metropolis algorithms evaluated at a sequence of decreasing temperatures.

In applying the simulated annealing algorithm to the problem of voxel segregation, the objective function is the total of the sum of squares errors between the voxels in each segregated group of voxels and the best-fit lines through those groups. The perturbations are the assignment of individual voxels to one group or another. If the cooling schedule is slow enough all of the voxels will be assigned to the nearest best-fit line.

The simulated annealing algorithm was applied to the problem of fiber voxel segmentation with limited success. The major drawback, besides lack of speed, is the fact that the simulated annealing algorithm must know beforehand how many fibers are represented in a voxel cluster in order to segregate them. A workaround is to begin by assuming that there is only one fiber and determine the best fit line for all of the voxels in the group. If the fit is unacceptable, then assume there are two fibers, obtain a new solution and again determine the goodness of the fit of the two lines to the two segregated groups of voxels. This process could be repeated, each time incrementing the assumed number of fibers, until a sufficiently good fit were achieved. This, of course, could increase the computation time by more than an order of magnitude which exacerbates an already serious time problem. The advantage of this method over the angle segregation method is that it has well-defined convergence even if it is slow. It was estimated that for a complex image, simulated annealing would require weeks to reach a solution for a single 3-D image using the available computational power.

2.2.3 Orientation Measurement

Once the voxels have been grouped into individual fiber segments it is a straightforward matter to determine the fiber orientation. By treating the voxels as point

masses belonging to a rigid body the inertia tensor about its center of mass can be calculated. The principal moments of inertia can be calculated by solving the Eigenvalue problem. The smallest principal moment of inertia lies in the direction of the fiber axis.

The following is a presentation of the relevant rigid body dynamics concepts summarized from Meirovitch (1970).

The angular momentum of a rigid body about its center of mass is given by:

$$\mathrm{L}_o = \int \mathbf{r} \times (\omega \times \mathbf{r}) dm. \tag{2.5}$$

By employing the following relationship from vector algebra

$$\mathbf{r} \times (\omega \times \mathbf{r}) = \omega(\mathbf{r} \cdot \mathbf{r}) - \mathbf{r}(\omega \cdot \mathbf{r}), \tag{2.6}$$

Equation 2.5 reduces to

$$\mathrm{L}_o = \int [(\omega(\mathbf{r} \cdot \mathbf{r}) - \mathbf{r}(\omega \cdot \mathbf{r})] dm. \tag{2.7}$$

The three components of L are

$$L_x = I_{xx}\omega_x - I_{xy}\omega_y - I_{xz}\omega_z, \tag{2.8}$$

$$L_y = -I_{yx}\omega_x + I_{yy}\omega_y - I_{yz}\omega_z, \tag{2.9}$$

$$L_z = -I_{zx}\omega_x - I_{zy}\omega_y + I_{zz}\omega_z. \tag{2.10}$$

The three quantities

$$I_{xx} = \int (r^2 - x^2) dm, \quad I_{yy} = \int (r^2 - y^2) dm, \quad I_{zz} = \int (r^2 - z^2) dm \tag{2.11}$$

are the moments of inertia and the six quantities

$$I_{xy} = I_{yx} = \int xy\, dm, \quad I_{xz} = I_{zx} = \int xz\, dm, \quad I_{yz} = I_{zy} = \int yz\, dm \tag{2.12}$$

are the products of inertia, where $r^2 = x^2 + y^2 + z^2$. The moments and products of inertia are the components of the second-order inertia tensor. The inertia tensor may be represented as a symmetric matrix called the inertia matrix

$$[I] = \begin{bmatrix} I_{xx} & -I_{xy} & -I_{xz} \\ -I_{yx} & I_{yy} & -I_{yz} \\ -I_{zx} & -I_{zy} & I_{zz} \end{bmatrix}. \tag{2.13}$$

The principal moments of inertia are found by applying the QL algorithm to find the eigenvalues and eigenvectors (Press et al., 1988).

2.2.4 Length Measurement

In addition to the orientation, the fiber length must be known in order to apply appropriate weighting to the fiber orientation distribution. The length of a fiber can be calculated if the voxel density per unit length of the fiber is known. Without thinning it is nearly impossible to determine the voxel density due to the dependence of the apparent z-component of fiber on the intensity of illumination. However, by thinning fibers down to a single voxel thickness, the length can be calculated from its orientation and the number of voxels it contains. The details of the length calculations are presented in Section 4.7.

2.2.5 Additional Measurements

Additional measurements such as location of the midpoint and curvature can be made on a chain of voxels. This information is useful for investigating such things as fiber movement and bending during consolidation.

CHAPTER 3

DEVELOPMENT OF THE APPARATUS

This chapter describes the development of the apparatus used in producing and imaging test specimens for 3-D fiber orientation analysis. It is divided into two main sections; development of the injection molding apparatus and development of the imaging apparatus.

3.1 Injection Molding Equipment

The main objective in developing the injection molding apparatus was to create a flexible system capable of producing high fiber content transparent composite materials under a variety of well defined processing conditions.

3.1.1 Overview

The injection molding apparatus consists of a fiber chopper, modular injection mold, tabletop injection molding unit, and data acquisition equipment. A schematic of the injection apparatus, excluding the fiber chopper, is shown in Figure 3.1

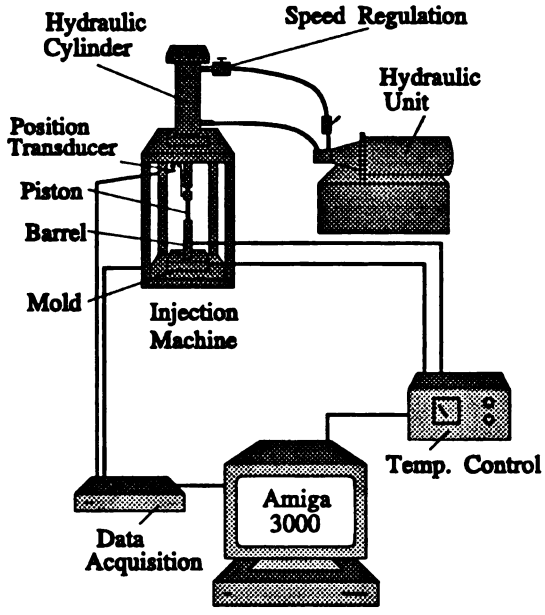


Figure 3.1: Schematic of injection molding apparatus.

3.1.2 Fiber Chopper

The purpose of the fiber chopper is to cut continuous fibers to desired lengths. With this device composite materials can be prepared with fiber lengths typical of those associated with industrial injection molding machines, taking into account breakage in the injection screw.

The fiber chopper is a simple mechanism consisting of a reciprocating blade which slides across a single hole in a die. A pinch-roller driven by a stepper motor advances a tow of fibers through the die by a specified amount during each cycle of the blade. The stepper motor is controlled by a computer which senses the closure of a microswitch activated by the chopper blade. Since the chopper is computer controlled, any desired length that is a multiple of the step size of the motor can be programmed. This allows arbitrary fiber length distributions to be produced.

The fiber chopper mechanism is illustrated in Figure 3.2.

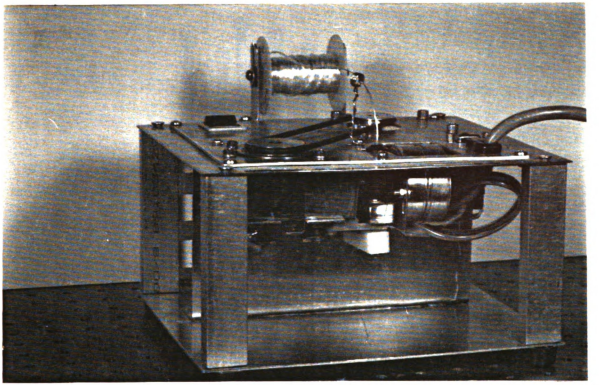


Figure 3.2: Photograph of fiber chopper.

The rate at which fibers can be chopped depends on the cut length and the number of fibers in the tow. During the experimental work for this project the average production rate for BK-10 glass fibers cut at 0.9 mm lengths was about 1 gm/hr.

3.1.3 Mold

The injection mold was designed to be a flexible, low-cost device which could produce a variety of fiber orientation distributions for analysis by the software.

The main considerations in the mold design were:

- easily-varied cavity and gate geometries
- high pressure capability – 2200 bar (32,000 psi)
- temperature measurement and control
- self-heating
- low cost

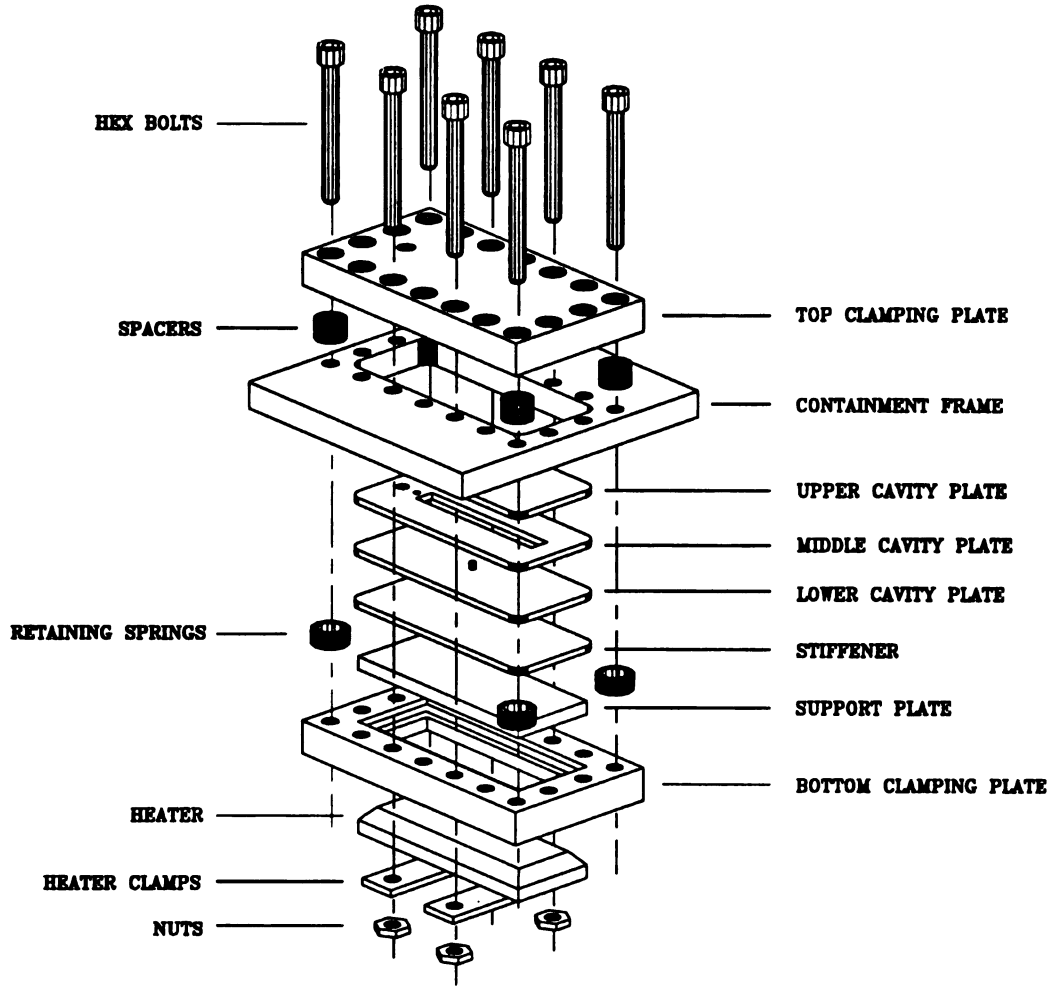


Figure 3.3: Exploded view of mold assembly.

- optical porting

The mold design, shown in schematic form in Figure 3.3 and in a photograph in Figure 3.4, is a sandwich construction consisting of an upper and lower plate which bolt together to compress several inner plates which determine the shape of the gate and cavity. The overall length of the mold is 15.2 cm (6 in). The upper plate houses the thermocouple and injection ports. The lower plate has an open center that can accommodate either a metal supporting plate or a transparent window. The mold can be heated either by foil heaters sandwiched between layers of the mold or by a heater

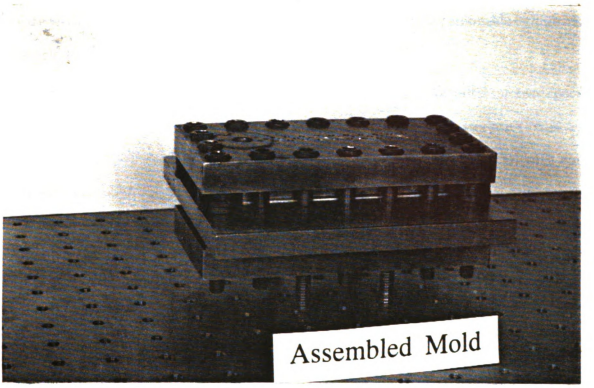


Figure 3.4: Photograph of assembled mold.

located in the cutout of the lower plate. A containment frame plate surrounds the interior layers of the mold to maintain alignment and to prevent lateral displacement of the cavity by the injection pressure.

The outer plates of the mold are made of low carbon steel and serve to provide rigidity and clamping force. The interior plates are made of polished stainless steel and form the cavity and gate. There are typically three interior plates which form the top, sides and bottom of the cavity. The gate may be incorporated in either the top or center plate. This modular construction allows a wide variety of cavity and gate geometries to be studied rapidly and at very low cost. The engineering drawings for the injection mold are located in Appendix B.1.

Among the cavity and gate designs that have been tested in the mold are: dogbone coupons designed for standard tensile test fixtures, a variable sized diverging film gate,

a gate with a removable cylindrical obstacle, and a cavity with a removable cylindrical obstacle to produce weld lines.

The mold has been successfully used to produce a variety of different test specimens with several different materials, including polymethyl methacrylate (PMMA), polypropylene, (PP) and styrene-acrylonitrile copolymer (Lustran® SAN) with and without fiber reinforcement. The mold has also been used under a variety of process conditions ranging from room temperature to 110 °C, and from low pressure up to 2200 bar (32,000 psi).

3.1.4 Injector

The objective in designing the injector was to create as closely as possible the conditions present in an industrial injection molding machine while maintaining very low cost. The reasons for not using a commercial injection machine were the large amount of material that would be wasted and the high cost of conventional injection molds. The BK-10 fibers used in the transparent composite experiments cost approximately $100/lb, and could be chopped at a rate of only 1 gm/hr.

The main considerations in the injector design were:

- high pressure capability – 2200 bar (32,000 psi)
- high temperature capability – 300 °C (572 °F)
- moderate injection rate capability – 15 cm^3/s (0.9 in^3/s)
- ability to process high fiber content materials
- controllable temperature, speed, and pressure
- instrumented temperature, speed, and pressure
- low waste
- removal of entrapped air
- ease of disassembly and cleaning

- low cost

The injector design, shown in Figure 3.5, consists of a hydraulic power unit with a pressure regulator and needle valve, a metal frame which houses a hydraulic cylinder, zone heated injection barrel, piston, heated nozzle and a fixture for holding the mold. The hydraulic cylinder is capable of producing 2200 bar (32,000 psi) inside the barrel of the injector and flow rates of up to 15 cm^3/s (0.9 in^3/s) in the current configuration. The barrel and nozzle temperatures are maintained by thermostatically controlled cylinder heaters. The injector is instrumented for temperature, speed and force measurement.

Much of the design work for the injector was performed by Weber (1992). Further details on the injector design can be found in his paper. Engineering drawings for the injector are located in Appendix B.2.

Testing and Characterization

The mold and injector were tested with various types of plastic and fiber materials, and the processing conditions were optimized for each type of material. In particular, styrene-acrylonitrile (Lustran® SAN), and polymethyl methacrylate (PMMA) were used with carbon and E-glass fibers to produce about 30 specimens. Experiments with neat and fiber filled materials have shown that the apparatus is capable of producing good quality specimens exhibiting good surface finish, transparency, and absence of entrapped air. It has further been demonstrated that the microstructure of molded parts can be altered by changes in processing conditions. For example, the presence of an obstacle in the gate has been shown to have a strong influence on the orientation in the core region.

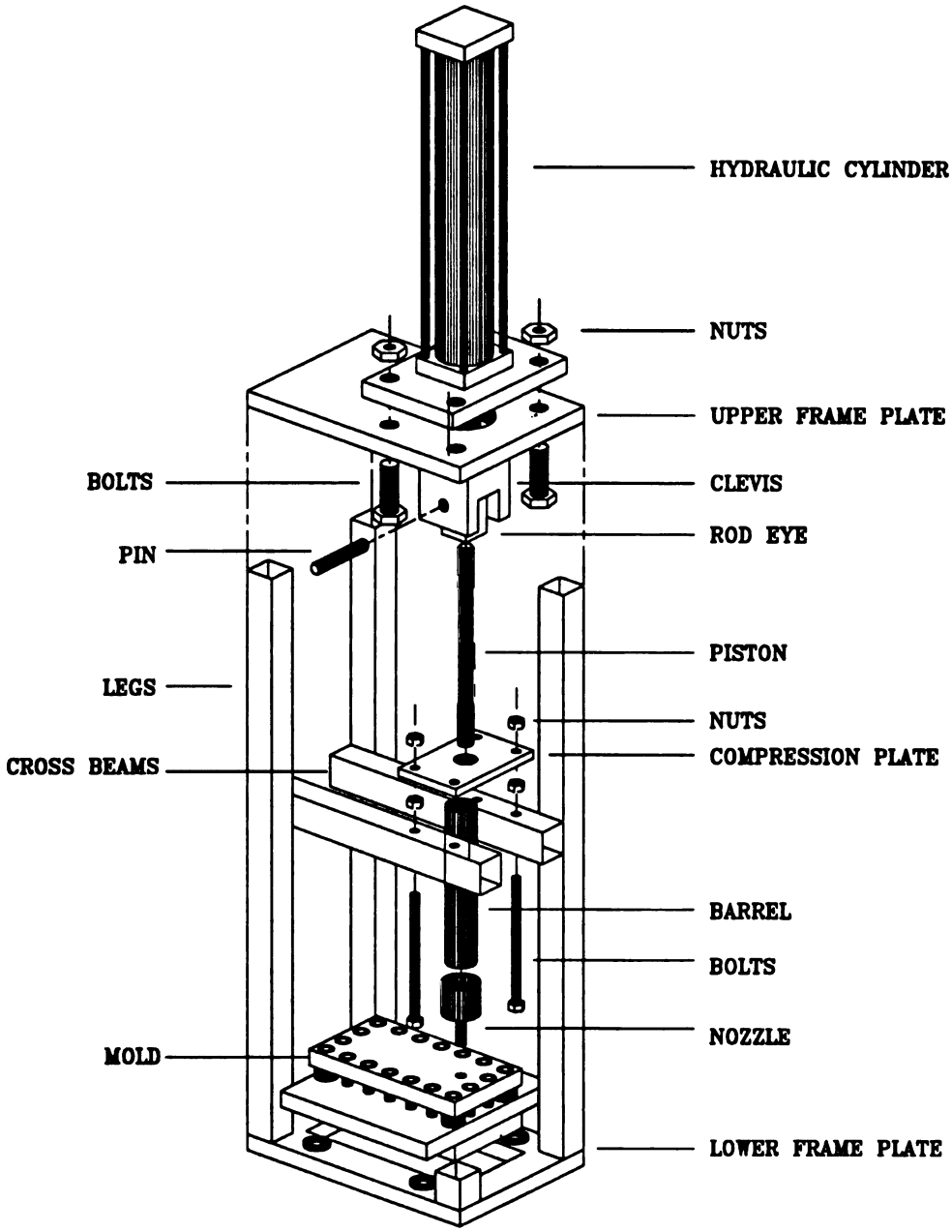


Figure 3.5: Exploded view of injector assembly.

A set of experiments, not presented here, using opaque materials was performed by Reimann (1992) in which he demonstrated that the presence of a cylindrical obstacle in the gate of the injection mold caused an increase in the bending modulus of sample materials made of polypropylene with 30 percent glass fibers.

During the optimization process, the following parameters were varied while observing their influence on the specimen: injection speed, holding pressure, barrel temperature, and mold temperature.

A typical injection process requires approximately 30 minutes per part including equipment setup and sample removal, and proceeds as follows: The mold is cleaned and coated with a silicon-based mold release compound and is assembled. The mold is inserted into the base of the injection frame and the injector is clamped down onto the injection port of the mold. A charge of sample material is introduced into the injection barrel either as powdered plastic mixed with fibers, or as a solid 0.5 in diameter preformed cylinder produced with a standard injection molding machine. Before the the fibers are introduced into the powdered material they are precut to lengths typical of what would be expected to result from breakage in an industrial-type injector. The injector piston is inserted into the barrel and electrical power is supplied to the mold and injector heaters. Once the desired temperatures have been reached the hydraulic power unit is activated and the injection piston forces the plastic/fiber melt into the mold at the rate and pressure determined by the settings of the hydraulic unit. The pressure is held until the material has solidified. The injector and mold are removed, the mold is disassembled, and the sample is removed.

3.1.5 Data Acquisition

The data acquisition equipment for the injection apparatus consists of a Data Translation DT2805 data acquisition board, thermocouples, potentiometer position transducer, and a PCB 208-A03 piezoelectric force transducer. The data acquisition board has eight differential analog input channels, 12-bit resolution, and maximum sampling rate of 2.5 kHz at a gain of 500.

3.2 Imaging Equipment

The objectives in designing the imaging system were to maximize resolution and penetration depth, while minimizing operator intervention.

3.2.1 Overview

The imaging equipment consists of a Nikon Diaphot-TMD inverted microscope, MTI CCD-72 video camera and controller, Galil DMC-400 motion controller board, Oriel motorized micrometer drives, and a Progressive Peripherals 256 frame grabber. A schematic of the imaging apparatus is shown in Figure 3.6

3.2.2 Microscope

The microscope is a Nikon Diaphot-TMD inverted microscope with an Achromat condenser and diffusers. The Achromat condenser provides precise focusing of the light source and helps eliminate out-of-plane information. Diffusers located at the light source and at the entrance to the condenser provide diffuse illumination. The microscope was modified by the attachment of servo motors for remote control of the focus and stage position. A photograph of the microscope is shown in Figure 3.7

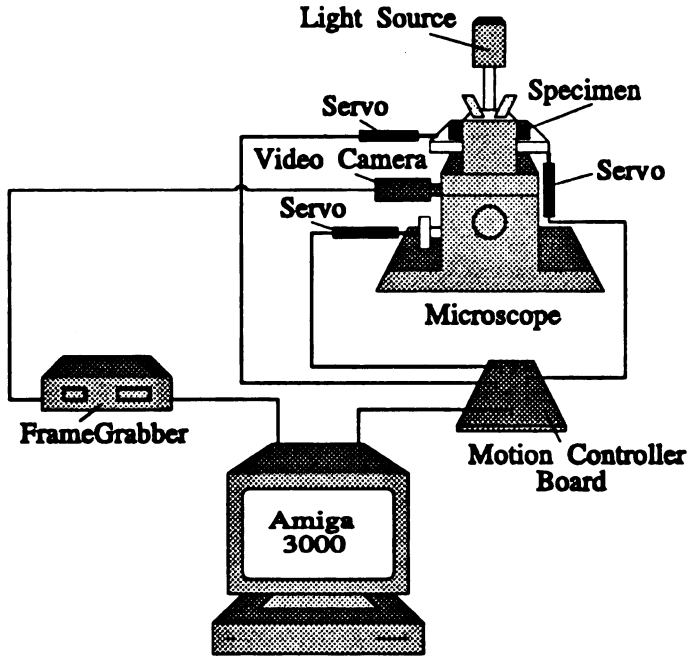


Figure 3.6: Schematic of imaging apparatus.

3.2.3 Motion Control

Two axis control of the microscope was achieved by two Oriel encoder mike drives (servos) driven by a Galil DMC-430-10 PC 3-axis motion controller board. A third axis of motion was added by using a stepper motor driver in conjunction with the digital I/O port of the data acquisition board. Each mike drive consists of a small servo motor with a planetary gear system which drives a 0.48 mm pitch drive screw. The mikes have an angular resolution of 0.019 degree (19,400 quadrature pulses per revolution), a linear resolution of 0.025 μm, a maximum angular speed of 0.67 revolution per second and a maximum linear speed of 322 μm per second. The linear motion of one mike drive is used directly to position the microscope stage in the x direction. Thus the theoretical x axis resolution is 0.025 μm, and the maximum linear speed is 322 μm per second. The elasticity of the motor mounting reduced the accuracy of the stage positioning to approximately 1 μm.

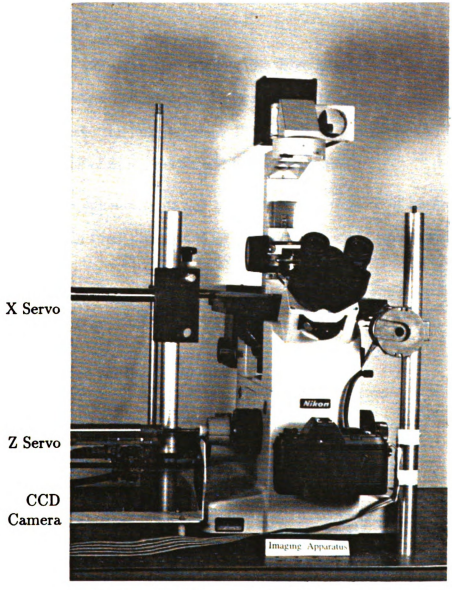


Figure 3.7: Photograph of imaging apparatus.

The stepper motor has an angular resolution of 5.625 degrees (64 steps per revolution), and maximum angular speed of 1.5 revolutions per second. The stepper is used to drive a 0.625 mm pitch drive screw which controls the y position of the stage, giving a linear resolution of 9.8 μm and a maximum linear speed of 625 μm per second in the y direction.

The rotary motion of the second mike drive is used to turn the focus knob of the microscope and thereby control the z axis of the imaging. One revolution of the focus knob moves the imaging plane 100 μm, giving a resolution of 0.005 μm and a maximum speed of 67 μm per second in the z direction.

With these enhancements the microscope was capable of performing arbitrary scan patterns in three-dimensions for extended periods of time without operator intervention.

/note

3.2.4 Stepper Motor Controller

3.2.5 Data Acquisition Circuit

3.2.6 Video Equipment

The microscope images were captured by an MTI CCD-72 video camera and Progressive Peripherals FrameGrabber 256 frame grabber. The CCD camera has an active picture array of 768 by 493 elements. The frame grabber has a resolution of 384 by 480 pixels.

CHAPTER 4

DEVELOPMENT OF THE SOFTWARE

This chapter describes the development of the software used in this project including the details of its implementation and the theory of its operation. All of the software was written by the author, with the exception of the **Fibor** program which was written by Schöche, and parts of **MCFG** and **Pseudo** which were contributed by Griffin and Lian. The software was written in the C programming language and compiled with version 6.2 of the SAS/C[1] compiler for AmigaDOS 2.0[2]. The source code consists of over 25,000 lines (≈450 printed pages) of programming. All of the programs were designed to be robust, accurate, and convenient to use and maintain. They present a consistent graphical user interface (GUI) and provide on-line help in the form of hypertext documents. Hypertext documents are structured, cross-referenced information bases which can be navigated by selecting key words and topics within the text.

A basic understanding of the relevant aspects of the AmigaDOS operating system is important for understanding the operation of the programs. AmigaDOS is a preemptive multitasking operating system with extensive support for interprocess communication. Multitasking means that several programs can be running simultaneously, and preemptive means that a program can take control of the CPU immediately

[1]SAS Institute Inc.
[2]Commodore, Inc.

when it needs to do so. The other programs in the system do not have to explicitly yield control of the CPU. Interprocess communication allows programs to communicate with each other to coordinate events and share information. AmigaDOS has a graphical user interface which supports multiple screens, multiple windows and icons. Icons are pictorial representations of individual programs which are used both to launch the programs and store user default values. The on-screen windows contain graphical elements called *gadgets* which are used to receive and display information. There are several types of gadgets, including text entry, numerical entry, push button, slider, and cycle gadgets. Slider gadgets are used for proportional information. Cycle gadgets have a number of discrete states which are assumed in a specific sequence, advancing each time the gadget is selected, (e.g., high, medium, low).

The programs are presented in the order in which they are used during a typical experiment.

4.1 Chop

The purpose of the **Chop** program is to control the fiber chopper apparatus. It does this by controlling the digital I/O ports of the data acquisition board. Through one port it detects the state of the microswitch that is activated by the motion of the chopper blade. Through a second port it provides signals to the stepper motor controller circuit which energizes the specified windings of the stepper motor. The speed and direction of the motor are determined by the sequence and rate of the signals sent to the stepper motor controller.

On startup the program checks to see if the data acquisition board is already being used so as not to interfere with data acquisition or motion control being performed by other programs. If the board is not in use the program opens a small window

containing a slider and status information. The graphical user interface for **Chop** is shown in Figure 4.1. The user moves the slider to select the desired fiber length.

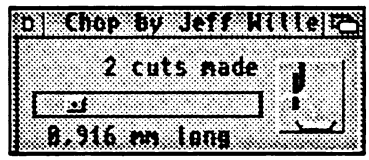


Figure 4.1: Graphical user interface for **Chop** program.

The status information consists of the total number of cuts made and the current length setting. The program continuously monitors the state of the microswitch and advances the fibers by the selected amount each time the microswitch opens or closes. The program reads the default values from its icon and sets the initial values of the corresponding variables. The default values that can be stored include a motor calibration value which specifies the distance the fibers advance for each step of the motor, and the phase of the fiber motion; that is, whether the fibers should be advanced when the microswitch opens or when it closes.

4.2 Acquire

The purpose of this program is to acquire temperature, speed, and force data during the injection molding process. It provides simultaneous real-time graphic and numeric displays of eight channels of information. It has a stopwatch which displays the elapsed time of the experiment, and an event timer which measures the rate at which certain events occur. All data can be logged to a disk file.

External data from thermocouples, position transducers, and force transducers are obtained from a Data Translation DT-2805 data acquisition board. The program sets the gain, sampling rate, and sampling mode of the data acquisition board. It takes control of one of the Amiga 3000's 0.715909 MHz hardware timers to provide

a precision time stamp for each data sample. High speed, precisely-timed data acquisition, independent of system load and independent of the graphical display speed is achieved by spawning a separate task, called the acquisition task, which runs at the highest system priority. The spawned task is responsible for gathering data from the data acquisition board and placing it in a circular buffer. It is solely responsible for all communication with the data acquisition board. A second precision hardware timer is used to provide interrupts for the acquisition task, signalling it to read data from the data acquisition board at the proper intervals. By running at top priority the acquisition task can instantly take control of the CPU whenever it needs to read data. This ensures that no data will be lost even at very high sample rates or high system loads. Since the task which displays the graphic and numeric data runs at lower priority, however, it may receive almost no CPU time at very high acquisition rates. In this case the data will not be displayed in real time. The display task has the capability of logging data to a file, and is also responsible for receiving input from the user. Changes in sampling rate, channel selection, gain, and other changes in the data acquisition board parameters requested by the user are handled by interprocess communication with the acquisition task.

The graphical user interface for **Acquire**, shown in Figure 4.2, consists of a variable-sized window which is mostly occupied by an oscilloscope-like display of the eight channel traces. It also contains a panel displaying the current numeric values of the data. Clicking the mouse button on any of the displayed values toggles that channel on or off. Below the numeric display panel is a group of buttons which allow the user to select the sampling rate, enable data logging, select the filename for logging, pause the display, select the range of channels to be sampled, and enable the event timer. At the top of the window is the stopwatch display which shows elapsed time.

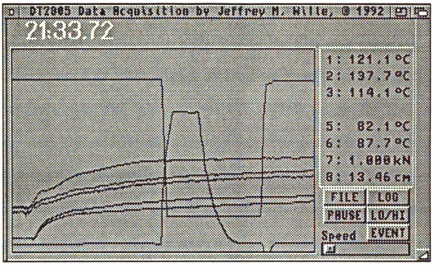


Figure 4.2: Graphical user interface for **Acquire** program.

The event timer is designed to measure the rate of specific events during the injection process. In particular, it measures the amount of time for a given parameter to change from one threshold value to another. For example, it can be programmed to measure the amount of time that it takes for the injection barrel to heat from one temperature to another, or the length of time it takes for the injection piston to move from one position to another. It is primarily used to measure piston speed during injection. The user interface for the event timer is shown in Figure 4.3.

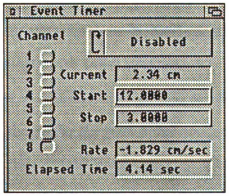


Figure 4.3: Graphical user interface for Event Timer.

Each channel can be easily configured for different types and ranges of data. The modular design of the program allows each channel to have its own calibration curve which can be in the form of an interpolated look-up table or a calibration function. Through the program's icon, the user can set the default values for the range of channels to be acquired, the cold-junction temperature compensation for the thermocouples, the gain of the data acquisition board, the default directory for data storage, the channels which are disabled, the type of data in each channel (temperature, position, or force), the maximum and minimum display values for each data type, the initial event timer parameters (channel number, start threshold, stop threshold, and whether it is initially enabled or disabled), and the initial dimensions of the display window.

4.3 MCFG

MCFG stands for Motion Controller and Frame Grabber. This program controls the focus and stage position of the microscope through the Oriel 3-axis motion controller board, allowing automated scanning in three-dimensions. It also captures images from the microscope's CCD video camera, performs initial image thresholding and other preprocessing, and stores image sequences in the form of animation files. **MCFG** has the ability to communicate with other programs for efficient processing of data. As each sequence of images is stored to disk **MCFG** sends a message which contains the name and location of the file to the next program in the analysis sequence. The recipient can immediately begin work on the image. Since **MCFG** spends most of its time waiting for motors to complete their motion and for images to be transferred from the frame grabber, the analysis programs can take advantage of this available CPU time to process the image, which greatly reduces the time required for analyzing

a data set. **MCFG** can also communicate with a separate stepper motor controller program to provide a fourth axis of motion. This capability was added when a third servo motor was unavailable from the manufacturer and a stepper motor was substituted for the third axis servo. If a suitable replacement servo is found for the third servo axis, the stepper motor may be used to provide additional services such as rotating samples or moving a series of samples onto the stage one at a time to further automate the scanning process.

MCFG works by communicating with a Galil 3-axis motion controller board and a Progressive Peripherals frame grabber. It programs the acceleration, speed, and step size of each axis of the motion controller board and interrogates the board to report current motor positions. It programs the resolution of the frame grabber and tells it when to capture and download images. **MCFG** has a powerful, built-in scripting language for programming complex scan patterns and image processing functions. Nearly all functions of the program can be controlled from within a script.

MCFG can apply various convolutions to an image, but a simple thresholding operation has proven to give acceptable results. A downloaded image consists of individual pixel values ranging from 0–255. The thresholding function is specified as:

$$t(x,y) = \begin{cases} 0, & \text{if pixel } (x,y) \leq 128; \\ 1, & \text{otherwise.} \end{cases} \tag{4.1}$$

The graphical interface for **MCFG**, shown in Figure 4.4, consists of a window containing a series of gadgets through which the user sets the motor step size, speed, acceleration, and calibration factor for each axis. Additional pushbutton gadgets allow the user to step the motors and zero the motor positions, as well as select the video source; grab, process, and save images; select the video output; edit and execute scripts.

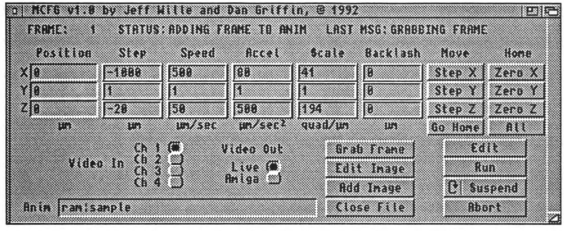


Figure 4.4: Graphical user interface for **MCFG** program.

The current values of motor position, speed, and acceleration are displayed in the gadgets that are used for user input. Thus, many of the gadgets serve a dual purpose of receiving and displaying information. Other gadgets provide output only. These display the current filename, current frame number, and the current status of the program.

MCFG stores image sequences in IFF[3] ANIM[4] Delta 5 format. There are two reasons for this. First, animation format allows the images to be viewed in rapid sequence, up to 60 frames per second, which is useful for human evaluation. Second, animation format provides much needed data compression. The voxel size used in the experiments presented here, which is about as large as practical for resolving 10 μm fibers in a 1 mm^2 2-D image, have dimensions 3.367 x 1.993 x 14.900 μm, or a volume of 100.0 μm^3. A 1 mm^3 scan of sample material contains 10 million voxels and requires 1.19 megabytes of storage if each voxel is stored as a single bit. A cubic centimeter contains 10 billion voxels and requires 1.19 gigabytes of storage. Storing in animation format gives an average 22:1 compression ratio, which reduces storage requirements to about 54 megabytes/cm^3. Animation files can be further compressed

[3]Interchange File Format
[4]IFF format for CEL animations, SPARTA Inc.

by at least another 50 percent by standard archival methods, further reducing storage requirements to about 27 megabytes/cm^3. The high compression ratio in the animation format is achieved in two ways. First, the first frame is compressed by run length compression, which means that series of identical bytes are stored as a single byte and a repeat count. Second, the subsequent images are stored as deltas from the first image. That is, only the portions of the image that change from one frame to the next are stored. The deltas are also compressed by run length compression.

When each file is stored, the voxel dimensions, refractive index of the material, and a title are stored in the file note for use by the analysis program, **3D-FODAS**. (See Section 4.7.)

The program's icon can be used to store the default values for speed, acceleration, step size, etc. for each motor, as well as the framegrabber type, voxel size, refractive index, default storage directory, default filename, and text editor of choice for editing scripts.

4.4 Step

The **Step** program is a stepper motor controller. It can function as a stand-alone program that receives user input directly, or it can be controlled by interprocess communication from another program through its public message port. For example, **MCFG** communicated with this program to the y axis of the microscope stage. All functions of the program are accessible through its communication port so it can act as a server.

Step's user interface, shown in Figure 4.5, contains gadgets for setting the step size, calibration factor, and target position for the motor. Push buttons are used for moving the motor forward and backward, in continuous mode or by discrete steps.



Figure 4.5: Graphical user interface for **Step** program.

The program's icon can be used to set the calibration factor for the motor, default step size, step rate, and default window position.

4.5 Pseudo

This program generates artificial fiber data which is stored in the same animation format as that generated by **MCFG**. This allows the analysis software to be tested independent of the imaging. By creating a known fiber orientation distribution and comparing it with the results of the analysis software, the accuracy of the analysis software can be evaluated.

Through the user interface, or by retrieving a previously created data file the user may set the voxel size, refractive index of the sample, and image dimensions, as well as the number, orientations, lengths and diameter of the fibers in it. The program places the fibers at random locations inside the sample volume. In a complex 3-D fiber distribution it is nearly impossible to manually determine the orientation of all the fibers it contains. By generating known fiber orientation distributions, the problems of imaging and analysis can be uncoupled.

The user interface for this program, shown in Figure 4.6, consists of a scrollable display area in which the fiber orientation, length and count are entered, surrounded by a series of gadgets for entering the image dimensions and voxel size, and the dimensions of the sample volume. There are also gadgets for setting the refractive

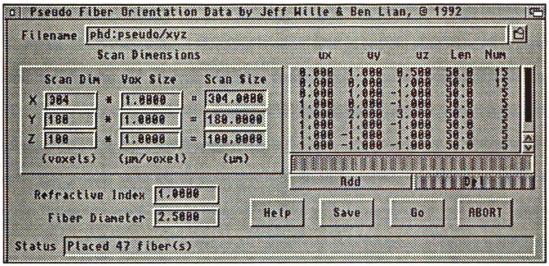


Figure 4.6: Graphical user interface for **Pseudo** program.

index and fiber diameter, and for loading, saving, and editing data. Once the pseudo data have been generated, they can be viewed immediately as an animation, or stored on disk. The program's icon can be used to store the default directory, refractive index, voxel size, image dimensions, and fiber diameter.

4.6 Thin3D

The primary purpose of this program is to aid in determining the locations of fiber ends and intersections, which are used for measuring fiber lengths and orientations. It does this by thinning, or skeletonizing the structures in the image. It also serves to reduce the amount of data in the image while preserving the information necessary for determining fiber length and orientation. Skeletonization refers to reducing a group of pixels or voxels down to a chain of single pixels or voxels. This significantly reduces the computational burden later on. The data for this program is read from a 3-D image (animation) file created by **MCFG** or **Pseudo**. The output of this program is a thinned 3-D image which is stored in animation format.

To explain the utility of 3-D thinning it is helpful to consider the applications of 2-D thinning. Two-dimensional thinning is often used in optical character recognition because it simplifies the analysis of image connectivity. The endpoints of a thinned structure have only one neighboring pixel, whereas pixels at junctions have more than two neighbors. The number of endpoints, junctions, and loops that a character has provides many clues as to which character it is. In this project, 3-D thinning performs a similar function except that instead of dealing with images composed of 2-D pixels it must deal with images composed of 3-D voxels. A 3-D image containing a sufficient number of fibers to provide a statistical measure of the fiber orientation distribution has a high likelihood of fiber-fiber contact, which makes it difficult to determine which voxels belong to a given fiber. Three-dimensional thinning provides a straightforward way of locating fiber endpoints and determining which voxels belong to a given fiber segment.

The 3-D thinning algorithm developed by the author is similar to classical 2-D thinning algorithms. In the 2-D algorithms pixels are usually removed in a uniform manner from the outer edges of a structure, layer by layer, until the midline is reached. Before each pixel is removed tests are made to determine if that pixel is an endpoint, or if its removal will break the continuity of the image. If either test is positive, the pixel is not removed. This, along with the fact that pixels are removed only from the outer edge guarantees that the connectivity of the image is not disturbed by fragmentation or the creation of holes, and that lines are not shortened. Uniformity of pixel removal is often achieved by removing pixels in an ordered sequence (e.g., by first removing pixels from the $+x$ edges, then from $-x$, then $+y$, and finally $-y$). This sequence is repeated until no more pixels can be removed. In determining what effect the removal of a pixel will have on the continuity of the image, only the 8

surrounding pixels locations need be considered since it can only influence the pixels it is touching.

The 3-D algorithm operates in a similar manner, but the scanning must be done from 18 directions rather than just four, and it requires an additional test to ensure the preservation of image connectivity.

The connectivity tests are much more complex for 3-D structures than for 2-D ones since each voxel has 26 neighbors instead of just 8. A great deal of effort was put into optimizing the algorithm due to the large computational burden. A typical 3-D image in this project consists of about 50 two-dimensional images of 320x400 pixels each. Thus during a single pass in which the voxels are examined from all 18 directions 6,400,000 voxels locations must be tested just to determine whether or not they are occupied. Typically 5–6 passes must be made to completely thin an image, and during each pass the voxels must be subjected to complex connectivity tests before they can be removed. Fortunately, in order to determine how the removal of a voxel will affect the connectivity of the image it is only necessary to consider the neighboring 26 voxels. However, those 26 neighbors may exist in 2^{26} = 67,108,864 different combinations. Typical computation times for the algorithm developed here for images of the type described above range from about 3 to 5 minutes on a microcomputer equipped with a 25 MHz, 68030 microprocessor.

4.6.1 Uniform Removal of Voxels

In order to reduce a fiber structure to its midline it is essential to remove the exterior voxels uniformly. **Thin3D** ensures uniform removal of voxels through an appropriate scan direction sequence and by removing a single layer at a time. In order for a voxel to be considered for removal during a given scan, it must lie on the appropriate face

of the structure. In 2-D thinning, scanning is made from four directions: $+x$, $-x$, $+y$, and $-y$. In 3-D thinning, scanning must be made from 18 directions. These can be divided into two groups: the 6 axis directions $\pm x$, $\pm y$, $\pm z$, and the 12 diagonal directions $\pm xy$, $\mp xy$, $\pm yz$, $\mp yz$, $\pm zx$, and $\mp zx$. The 18 directions correspond to the 6 faces and 12 edges of a cube as shown in Figure 4.7.

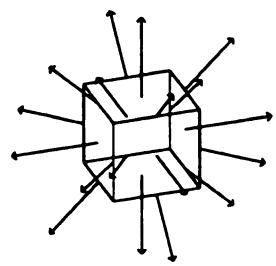


Figure 4.7: Scan directions used in Thin3D.

To keep the thinning from progressing past a single layer on a given scan, two copies of the image are kept in memory. The original is used to locate surface voxels while the copy is used for recording removed voxels. When a scan has been completed, the copy is duplicated and the next scan is executed. If this precaution were not taken, entire structures could be obliterated on a single pass by continuously thinning newly exposed surfaces. This protection, however, does not prevent planar structures that are a single voxel thick from being obliterated by scans perpendicular to the plane. To avoid this problem a structure is required to be at least two voxels thick in the scanning direction.

During scanning of the diagonal directions an undesirable tunneling effect may occur. A voxel located inside the structure may have an edge that is exposed to the surface and thus appear to be a surface voxel. To avoid this tunneling effect, only outside corners are allowed to be removed during diagonal searches. This is implemented by requiring that the two faces of the voxel adjoining the exposed edge be free surfaces.

The requirements for considering a voxel for removal during each scan direction are compiled in Table 4.1. The notation $n_{[i,j,k]}$ represents a location adjacent to a

Table 4.1: Scan sequence for 3-D thinning algorithm.

Dir	Face (vacant)	Back (occup)	Side 1 (vacant)	Side 2 (vacant)
1	n[0, 0, 1]	n[0, 0,-1]	n/a	n/a
2	n[0, 0,-1]	n[0, 0, 1]	n/a	n/a
3	n[0, 1, 0]	n[0,-1, 0]	n/a	n/a
4	n[0,-1, 0]	n[0, 1, 0]	n/a	n/a
5	n[1, 0, 0]	n[-1, 0, 0]	n/a	n/a
6	n[-1, 0, 0]	n[1, 0, 0]	n/a	n/a
7	n[0, 1, 1]	n[0,-1,-1]	n[0, 0, 1]	n[0, 1, 0]
8	n[0,-1,-1]	n[0, 1, 1]	n[0, 0,-1]	n[0,-1, 0]
9	n[0,-1, 1]	n[0, 1,-1]	n[0, 0, 1]	n[0,-1, 0]
10	n[0, 1,-1]	n[0,-1, 1]	n[0, 0,-1]	n[0, 1, 0]
11	n[1, 0, 1]	n[-1, 0,-1]	n[0, 0, 1]	n[1, 0, 0]
12	n[-1, 0,-1]	n[1, 0, 1]	n[0, 0,-1]	n[-1, 0, 0]
13	n[-1, 0, 1]	n[1, 0,-1]	n[0, 0, 1]	n[-1, 0, 0]
14	n[1, 0,-1]	n[-1, 0, 1]	n[0, 0,-1]	n[1, 0, 0]
15	n[1, 1, 0]	n[-1,-1, 0]	n[0, 1, 0]	n[1, 0, 0]
16	n[-1,-1, 0]	n[1, 1, 0]	n[0,-1, 0]	n[-1, 0, 0]
17	n[-1, 1, 0]	n[1,-1, 0]	n[0, 1, 0]	n[-1, 0, 0]
18	n[1,-1, 0]	n[-1, 1, 0]	n[0,-1, 0]	n[1, 0, 0]

reference voxel, where i, j, and k are offsets from the reference voxel position. The entries in the table indicate whether specific neighboring locations must be occupied or vacant in order for a voxel to be considered for removal. For example, during scan number 2, in order for a voxel at location $[i, j, k]$ to be considered for removal, location $[i, j, k + 1]$ must be vacant and location $[i, j, k - 1]$ must be occupied.

4.6.2 Prohibiting Shortening of Lines

Once a voxel has been selected for possible removal, a test is made to determine if it is an endpoint. The test involves a simple count of the occupied neighboring locations.

If there is only one, then it is an endpoint and cannot be removed. If this requirement were not enforced, all lines would be shortened to single voxels.

4.6.3 Preserving Connectivity of the Image

The final sequence of tests are for preserving the connectivity of the image structure. In particular they guarantee that no structures become discontinuous and that no holes are created.

There are at least three possible definitions for continuity of voxels. Two voxels could be considered to be contiguous if: (1) they share a common face; (2) they share a common edge or face; or, (3) they share a common face, edge, or corner. The third definition was used in the algorithm since the fibers are small compared to the voxel size, and fiber voxel structures many times are connected only by edges or corners. The removal of a voxel alters the connectivity of an image if it causes the number of contiguous voxel groups to increase, or if it causes a loop to exist in the final thinned image that would not have existed had the voxel not been removed.

Prohibiting Breaking of Structures

Testing for the fragmentation of a voxel group is done by examining the 26 neighbors of the voxel. With the center voxel in place, all 27 voxels in the 3x3 cube are, by definition, contiguous. If the surrounding 26 voxels are part of one contiguous group, removing the center voxel will not cause a discontinuity. If more than one contiguous group exists in the absence of the center voxel, its removal will cause a discontinuity. Searching the neighbors for a path through all voxels to determine the continuity of the structure could be very costly in terms of computation time, especially using common recursive searching techniques. However, a very efficient method of counting

contiguous voxel groups was developed by the author for this purpose. Each voxel location in the 3x3 cube is assigned a number which corresponds to a single bit of a 32 bit integer. A 32 bit integer constant is created for each voxel location, in which each bit that is set represents a voxel location that is immediately adjacent to it. The adjacency relationships are shown in Table 4.2. This table shows, for example,

Table 4.2: Adjacency matrix of voxel neighbors.

	$n_{[1,0,0]}$	$n_{[1,-1,0]}$	$n_{[0,-1,0]}$	$n_{[-1,-1,0]}$	$n_{[-1,0,0]}$	$n_{[-1,1,0]}$	$n_{[0,1,0]}$	$n_{[1,1,0]}$	$n_{[0,0,1]}$	$n_{[1,0,1]}$	$n_{[1,-1,1]}$	$n_{[0,-1,1]}$	$n_{[-1,-1,1]}$	$n_{[-1,0,1]}$	$n_{[-1,1,1]}$	$n_{[0,1,1]}$	$n_{[1,1,1]}$	$n_{[0,0,-1]}$	$n_{[1,0,-1]}$	$n_{[1,-1,-1]}$	$n_{[0,-1,-1]}$	$n_{[-1,-1,-1]}$	$n_{[-1,0,-1]}$	$n_{[-1,1,-1]}$	$n_{[0,1,-1]}$	$n_{[1,1,-1]}$
$n_{[1,0,0]}$		●	●				●	●	●	●	●	●				●	●	●	●	●	●				●	●
$n_{[1,-1,0]}$	●		●						●	●	●	●						●	●	●	●					
$n_{[0,-1,0]}$	●	●		●	●				●	●	●	●	●	●				●	●	●	●	●	●			
$n_{[-1,-1,0]}$			●		●				●			●	●	●				●			●	●	●			
$n_{[-1,0,0]}$			●	●		●	●		●			●	●	●	●	●		●			●	●	●	●	●	
$n_{[-1,1,0]}$					●		●		●					●	●	●		●					●	●	●	
$n_{[0,1,0]}$	●				●	●		●	●	●				●	●	●	●	●	●				●	●	●	●
$n_{[1,1,0]}$	●						●		●	●						●	●	●	●						●	●
$n_{[0,0,1]}$	●	●	●	●	●	●	●	●		●	●	●	●	●	●	●	●									
$n_{[1,0,1]}$	●	●	●				●	●	●		●	●				●	●									
$n_{[1,-1,1]}$	●	●	●						●	●		●														
$n_{[0,-1,1]}$	●	●	●	●	●				●	●	●		●	●												
$n_{[-1,-1,1]}$			●	●	●				●			●		●												
$n_{[-1,0,1]}$			●	●	●	●	●		●			●	●		●	●										
$n_{[-1,1,1]}$					●	●	●		●					●		●										
$n_{[0,1,1]}$	●				●	●	●	●	●	●				●	●		●									
$n_{[1,1,1]}$	●						●	●	●	●						●										
$n_{[0,0,-1]}$	●	●	●	●	●	●	●	●											●	●	●	●	●	●	●	●
$n_{[1,0,-1]}$	●	●	●				●	●										●		●	●				●	●
$n_{[1,-1,-1]}$	●	●	●															●	●		●					
$n_{[0,-1,-1]}$	●	●	●	●	●													●	●	●		●	●			
$n_{[-1,-1,-1]}$			●	●	●													●			●		●			
$n_{[-1,0,-1]}$			●	●	●	●	●											●			●	●		●	●	
$n_{[-1,1,-1]}$					●	●	●											●					●		●	
$n_{[0,1,-1]}$	●				●	●	●	●										●	●				●	●		●
$n_{[1,1,-1]}$	●						●	●										●	●						●	

that neighbor $n_{[0,-1,1]}$ is adjacent to neighbors $n_{[1,0,0]}$, $n_{[1,-1,0]}$, $n_{[0,-1,0]}$, $n_{[-1,-1,0]}$,

$n_{[-1,\ 0,\ 0]}$, $n_{[\ 0,\ 0,\ 1]}$, $n_{[\ 1,\ 0,\ 1]}$, $n_{[\ 1,-1,\ 1]}$, $n_{[-1,-1,\ 1]}$, and $n_{[-1,\ 0,\ 1]}$. A list of the neighbors of a group of voxels can be obtained by combining the rows corresponding to each voxel. For instance, combining the rows for neighbors $n_{[\ 0,-1,\ 0]}$ and $n_{[\ 0,-1,\ 1]}$ shows that $n_{[\ 1,\ 0,\ 0]}$, $n_{[\ 1,-1,\ 0]}$, $n_{[\ 0,-1,\ 0]}$, $n_{[-1,-1,\ 0]}$, $n_{[-1,\ 0,\ 0]}$, $n_{[\ 0,\ 0,\ 1]}$, $n_{[\ 1,\ 0,\ 1]}$, $n_{[\ 1,-1,\ 1]}$, $n_{[\ 0,-1,\ 1]}$, $n_{[-1,-1,\ 1]}$, $n_{[-1,\ 0,\ 1]}$, $n_{[\ 0,\ 0,-1]}$, $n_{[\ 1,\ 0,-1]}$, $n_{[\ 1,-1,-1]}$, $n_{[\ 0,-1,-1]}$, $n_{[-1,-1,-1]}$, and $n_{[-1,\ 0,-1]}$ are adjacent to this pair. These two examples are illustrated in Figure 4.8.

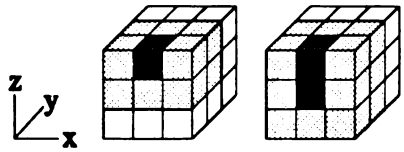


Figure 4.8: Application of the adjacency matrix.

Thus a single 32 bit integer variable can be used to store all the voxel locations that are adjacent to any group of voxels within the cube. By using this technique, a single machine language instruction is required to determine if a given voxel is adjacent to any one of the possible 26 voxels in the cube, and adding all of the adjacent voxel locations of a newly identified voxel requires only a single machine language instruction.

The algorithm is initialized by placing the adjacencies of the first voxel encountered into an integer variable which serves as an accumulator. Each of the remaining voxels is tested to see if it is adjacent to any of the voxels in the accumulator. If it is, the adjacencies of the new voxel are combined with the accumulated adjacencies by a bitwise boolean *or* operation and the process continues until no more voxels can be placed, or there are no more voxels. If all of the voxels can be placed then all of the voxels are contiguous. Otherwise, there are two or more groups.

Prohibiting Creation of Holes

The final tests are those which determine whether a hole will be created. There are two kinds of holes: straight and bent. Detection of straight holes is relatively straightforward. First, the 3x3 cube is tested to see if there exists a straight passage through the center of the cube in the x, y, or z directions. For each passage found, tests are made to see if at least one voxel exists on each of the four sides of the passage. If any side does not have at least one voxel, a straight hole will not be created there. In the other case, a straight hole will *probably* be created. If the voxels surrounding the passage are arranged in a helical configuration, this test will give a false positive result (i.e., it will say that a hole exists when there is none). It would be possible to avoid this false positive by applying additional tests, but at added computational cost. Because a helical configuration is very unlikely in images consisting of straight line elements and given that the voxel may be removed later when surrounding voxels have been removed, and that the existence of an occasional extra voxel has very little effect on the final analysis, it was decided that this test was adequate for detecting straight holes.

The straight hole tests can be described concisely using boolean expressions. In the following expressions the symbol G represents a group of voxel locations and the function $A(G)$ is true if any of the locations in group G is occupied, and false if all are vacant. The expression $n_{[i,j,k]}$ is true if that neighbor location is occupied, and false if vacant. An overbar indicates negation. Thus, $\overline{A}(G)$ is true only if all locations in group G are vacant. The symbol $\vee$ is used to represent logical *or*, and $\wedge$ for logical *and*.

The following neighbor groups are assigned for the straight hole tests. Groups with a single subscript are composed of two voxels locations on opposing faces of the

reference voxel, oriented along the axis named by the subscript. Groups with two subscripts are composed of three voxel locations aligned parallel to the axis named by the first subscript and offset in the direction indicated by the second subscript.

$G_x = n_{[1,0,0]}, n_{[-1,0,0]}$

$G_{x,-y} = n_{[-1,-1,0]}, n_{[0,-1,0]}, n_{[1,-1,0]}$

$G_{x,+y} = n_{[-1,1,0]}, n_{[0,1,0]}, n_{[1,1,0]}$

$G_{x,-z} = n_{[-1,0,-1]}, n_{[0,0,-1]}, n_{[1,0,-1]}$

$G_{x,+z} = n_{[-1,0,1]}, n_{[0,0,1]}, n_{[1,0,1]}$

$G_y = n_{[0,1,0]}, n_{[0,-1,0]}$

$G_{y,-x} = n_{[-1,-1,0]}, n_{[-1,0,0]}, n_{[-1,1,0]}$

$G_{y,+x} = n_{[1,-1,0]}, n_{[1,0,0]}, n_{[1,1,0]}$

$G_{y,-z} = n_{[0,-1,-1]}, n_{[0,0,-1]}, n_{[0,1,-1]}$

$G_{y,+z} = n_{[0,-1,1]}, n_{[0,0,1]}, n_{[0,1,1]}$

$G_z = n_{[0,0,1]}, n_{[0,0,-1]}$

$G_{z,-x} = n_{[-1,0,-1]}, n_{[-1,0,0]}, n_{[-1,0,1]}$

$G_{z,+x} = n_{[1,0,-1]}, n_{[1,0,0]}, n_{[1,0,1]}$

$G_{z,-y} = n_{[\ 0,-1,-1]},\ n_{[\ 0,-1,\ 0]},\ n_{[\ 0,-1,\ 1]}$

$G_{z,+y} = n_{[\ 0,\ 1,-1]},\ n_{[\ 0,\ 1,\ 0]},\ n_{[\ 0,\ 1,\ 1]}$

The following three expressions are the tests for the existence of a straight hole in the x, y, and z directions respectively.

$$H_x = \overline{A}(G_x) \wedge A(G_{x,-y}) \wedge A(G_{x,+y}) \wedge A(G_{x,-z}) \wedge A(G_{x,+z}) \tag{4.2}$$

$$H_y = \overline{A}(G_y) \wedge A(G_{y,-x}) \wedge A(G_{y,+x}) \wedge A(G_{y,-z}) \wedge A(G_{y,+z}) \tag{4.3}$$

$$H_z = \overline{A}(G_z) \wedge A(G_{z,-y}) \wedge A(G_{z,+y}) \wedge A(G_{z,-y}) \wedge A(G_{z,+y}) \tag{4.4}$$

A straight hole or helical structure will be created if

$$H_x \vee H_y \vee H_z \tag{4.5}$$

is true.

Bent holes are defined as those entering one face of the 3x3 cube and exiting another which is not directly opposite the first. There are 12 possible orientations for bent holes. For a bent hole to exist there must be empty voxel locations on any two non-opposing faces of the cube. Additionally, the voxel location between the two empty locations must be filled, and there must be at least one voxel on each side of the hole perpendicular to its plane of symmetry.

The tests for bent holes are:

$$\begin{aligned} H_{-x,-y} &= n_{[-1,\ 0,\ 0]} \wedge n_{[\ 0,-1,\ 0]} \wedge \overline{(n_{[\ 1,\ 0,\ 0]} \vee n_{[\ 0,\ 1,\ 0]})} \wedge n_{[\ 1,\ 1,\ 0]} \wedge \\ &\quad (n_{[\ 0,\ 0,\ 1]} \vee n_{[\ 1,\ 0,\ 1]} \vee n_{[\ 0,\ 1,\ 1]}) \wedge (n_{[\ 0,\ 0,-1]}) \vee n_{[\ 1,\ 0,-1]} \vee n_{[\ 0,\ 1,-1]}) \\ H_{-x,+y} &= n_{[-1,\ 0,\ 0]} \wedge n_{[\ 0,\ 1,\ 0]} \wedge \overline{(n_{[\ 1,\ 0,\ 0]} \vee n_{[\ 0,-1,\ 0]})} \wedge n_{[\ 1,-1,\ 0]} \wedge \end{aligned}$$

$$(n_{[\ 0,\ 0,\ 1]} \vee n_{[\ 1,\ 0,\ 1]} \vee n_{[\ 0,-1,\ 1]}) \wedge (n_{[\ 0,\ 0,-1]}) \vee n_{[\ 1,\ 0,-1]} \vee n_{[\ 0,-1,-1]})$$

$$H_{-z,-x} = n_{[\ 0,\ 0,-1]} \wedge n_{[-1,\ 0,\ 0]} \wedge \overline{(n_{[\ 0,\ 0,\ 1]} \vee n_{[\ 1,\ 0,\ 0]})} \wedge n_{[\ 1,\ 0,\ 1]} \wedge$$

$$(n_{[\ 1,-1,\ 0]} \vee n_{[\ 0,-1,\ 0]} \vee n_{[\ 0,-1,\ 1]}) \wedge (n_{[\ 0,\ 1,\ 0]}) \vee n_{[\ 1,\ 1,\ 0]} \vee n_{[\ 0,\ 1,\ 1]})$$

$$H_{+z,-x} = n_{[\ 0,\ 0,\ 1]} \wedge n_{[-1,\ 0,\ 0]} \wedge \overline{(n_{[\ 0,\ 0,-1]} \vee n_{[\ 1,\ 0,\ 0]})} \wedge n_{[\ 1,\ 0,-1]} \wedge$$

$$(n_{[\ 1,-1,\ 0]} \vee n_{[\ 0,-1,\ 0]} \vee n_{[\ 0,-1,-1]}) \wedge (n_{[\ 0,\ 1,\ 0]}) \vee n_{[\ 1,\ 1,\ 0]} \vee n_{[\ 0,\ 1,-1]})$$

$$H_{+x,-y} = n_{[\ 1,\ 0,\ 0]} \wedge n_{[\ 0,-1,\ 0]} \wedge \overline{(n_{[-1,\ 0,\ 0]} \vee n_{[\ 0,\ 1,\ 0]})} \wedge n_{[-1,\ 1,\ 0]} \wedge$$

$$(n_{[\ 0,\ 0,\ 1]} \vee n_{[-1,\ 0,\ 1]} \vee n_{[\ 0,\ 1,\ 1]}) \wedge (n_{[\ 0,\ 0,-1]}) \vee n_{[-1,\ 0,-1]} \vee n_{[\ 0,\ 1,-1]})$$

$$H_{+x,+y} = n_{[\ 1,\ 0,\ 0]} \wedge n_{[\ 0,\ 1,\ 0]} \wedge \overline{(n_{[\ 0,-1,\ 0]} \vee n_{[-1,\ 0,\ 0]})} \wedge n_{[-1,-1,\ 0]} \wedge$$

$$(n_{[\ 0,\ 0,\ 1]} \vee n_{[\ 0,-1,\ 1]} \vee n_{[-1,\ 0,\ 1]}) \wedge (n_{[\ 0,\ 0,-1]}) \vee n_{[\ 0,-1,-1]} \vee n_{[-1,\ 0,-1]})$$

$$H_{+x,-z} = n_{[\ 1,\ 0,\ 0]} \wedge n_{[\ 0,\ 0,-1]} \wedge \overline{(n_{[\ 0,\ 0,\ 1]} \vee n_{[-1,\ 0,\ 0]})} \wedge n_{[-1,\ 0,\ 1]} \wedge$$

$$(n_{[-1,\ 1,\ 0]} \vee n_{[\ 0,\ 1,\ 0]} \vee n_{[\ 0,\ 1,\ 1]}) \wedge (n_{[\ 0,-1,\ 0]}) \vee n_{[-1,-1,\ 0]} \vee n_{[\ 0,-1,\ 1]})$$

$$H_{+z,+x} = n_{[\ 0,\ 0,\ 1]} \wedge n_{[\ 1,\ 0,\ 0]} \wedge \overline{(n_{[\ 0,\ 0,-1]} \vee n_{[-1,\ 0,\ 0]})} \wedge n_{[-1,\ 0,-1]} \wedge$$

$$(n_{[-1,\ 1,\ 0]} \vee n_{[\ 0,\ 1,\ 0]} \vee n_{[\ 0,\ 1,-1]}) \wedge (n_{[\ 0,-1,\ 0]}) \vee n_{[-1,-1,\ 0]} \vee n_{[\ 0,-1,-1]})$$

$$H_{-y,-z} = n_{[\ 0,-1,\ 0]} \wedge n_{[\ 0,\ 0,-1]} \wedge \overline{(n_{[\ 0,\ 0,\ 1]} \vee n_{[\ 0,\ 1,\ 0]})} \wedge n_{[\ 0,\ 1,\ 1]} \wedge$$

$$(n_{[\ 1,\ 0,\ 0]} \vee n_{[\ 1,\ 1,\ 0]} \vee n_{[\ 1,\ 0,\ 1]}) \wedge (n_{[-1,\ 0,\ 0]}) \vee n_{[-1,\ 1,\ 0]} \vee n_{[-1,\ 0,\ 1]})$$

$$H_{-y,+z} = n_{[\ 0,-1,\ 0]} \wedge n_{[\ 0,\ 0,\ 1]} \wedge \overline{(n_{[\ 0,\ 0,-1]} \vee n_{[\ 0,\ 1,\ 0]})} \wedge n_{[\ 0,\ 1,-1]} \wedge$$

$$(n_{[\ 1,\ 0,\ 0]} \vee n_{[\ 1,\ 1,\ 0]} \vee n_{[\ 1,\ 0,-1]}) \wedge (n_{[-1,\ 0,\ 0]}) \vee n_{[-1,\ 1,\ 0]} \vee n_{[-1,\ 0,-1]})$$

$$H_{+y,-z} = n_{[\ 0,\ 1,\ 0]} \wedge n_{[\ 0,\ 0,-1]} \wedge \overline{(n_{[\ 0,\ 0,\ 1]} \vee n_{[\ 0,-1,\ 0]})} \wedge n_{[\ 0,-1,\ 1]} \wedge$$

$$(n_{[-1,-1,\ 0]} \vee n_{[-1,\ 0,\ 0]} \vee n_{[-1,\ 0,\ 1]}) \wedge (n_{[\ 1,\ 0,\ 0]}) \vee n_{[\ 1,-1,\ 0]} \vee n_{[\ 1,\ 0,\ 1]})$$

$$H_{+y,+z} = n_{[\ 0,\ 1,\ 0]} \wedge n_{[\ 0,\ 0,\ 1]} \wedge \overline{(n_{[\ 0,\ 0,-1]} \vee n_{[\ 0,-1,\ 0]})} \wedge n_{[\ 0,-1,-1]} \wedge$$

$$(n_{[-1,-1,\ 0]} \vee n_{[-1,\ 0,\ 0]} \vee n_{[-1,\ 0,-1]}) \wedge (n_{[\ 1,\ 0,\ 0]}) \vee n_{[\ 1,-1,\ 0]} \vee n_{[\ 1,\ 0,-1]})$$

A bent hole will be created if

$$H_{-x,-y} \vee H_{-x,+y} \vee H_{-z,-x} \vee H_{+z,-x} \vee H_{+x,-y} \vee H_{+x,+y} \vee$$

$$H_{+x,-z} \vee H_{+z,+x} \vee H_{-y,-z} \vee H_{-y,+z} \vee H_{+y,-z} \vee H_{+y,+z} \tag{4.6}$$

is true.

A voxel that passes all of these tests can be removed. Figures 4.9 and 4.10 show a magnified orthogonal view of a sample image before and after thinning.

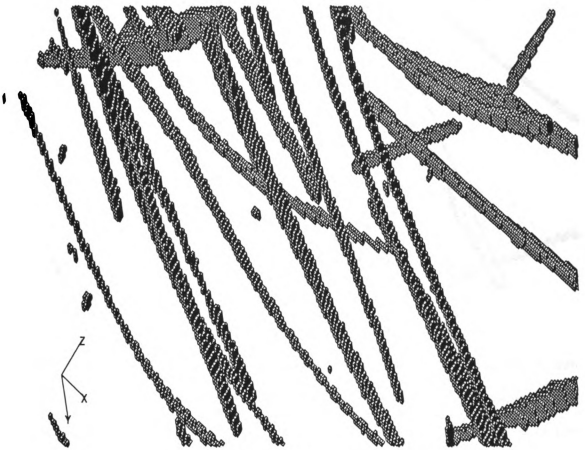


Figure 4.9: Unthinned image.

4.6.4 Implementation Problems With Real Images

Several problems can complicate the thinning process when dealing with non-ideal images. These include the presence of enclosed cavities, the presence of very thick (non fiber-like) structures, and the presence of endpoints that are not fiber ends. Enclosed cavities occur infrequently in clean, sharp images and do not present a

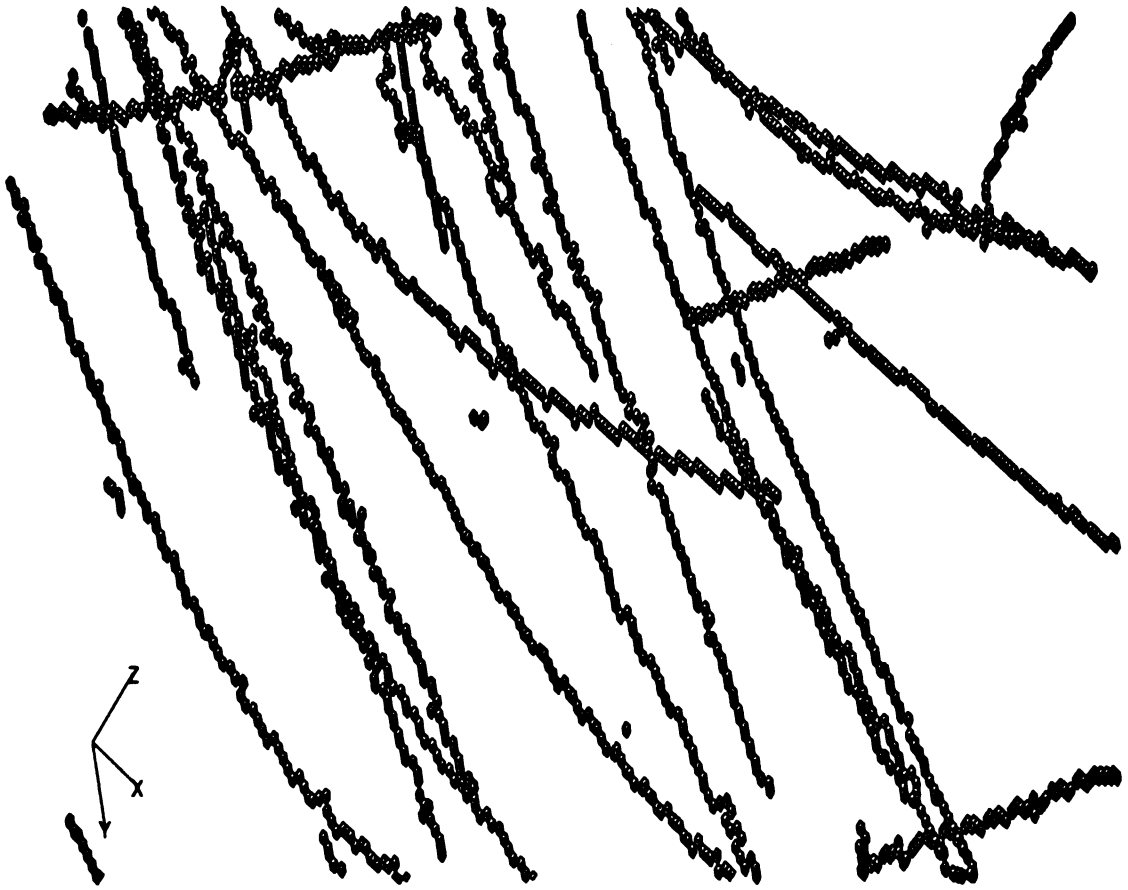


Figure 4.10: Thinned image.

problem in this case. However, if large blobs appear due to dirt, shadows, or non-uniform lighting an enclosed empty voxel location can expand during thinning to form a large, unthinnable bubble since the algorithm does not allow holes to be created in surfaces. This is typically not a problem with thin structures since an enclosed empty voxel would have no room to expand. To deal with the problem of bubble formation a prescan is performed prior to thinning during which cavities are filled. A selected threshold value determines the maximum cavity size that will be filled. The larger this parameter is, the longer the filling process takes. The presence of blobs also greatly increases the total thinning time since they must be eliminated layer by layer. To speed up the thinning of thick structures, after a selected number of passes have been made, the algorithm switches to a faster, non-uniform scanning pattern.

In this mode, all surface voxels that are removable are removed, regardless of their surface orientation. The problem of endpoints that do not represent fiber ends is caused by image noise or fuzziness that can cause bumps to appear on the surface of fibers which cannot be removed due to the non-shortening requirement of the thinning algorithm. As the thinning progresses, these bumps become spurs protruding from the fiber surface. Elimination of these spurs is accomplished by recognizing that the spurs will be, in general, as short as the radius of the fiber. After thinning is completed, a final pass is made in which voxel chains less than a selected threshold length are pruned off. Of course, if thick structures are present in the image, spurs may be created which are significantly longer than the fiber radius. These spurs are difficult to distinguish from true fibers and can be a serious source of error.

4.6.5 Program Features

Thin3D automatically detects whether fiber voxels are represented by 1's or 0's in the 3-D image by comparing the relative amounts of each that are present in the image and assuming that there will always be fewer fiber voxels than matrix voxels.

Thin3D has a batch mode for processing lists of files and it has a public message port through which it can serve as a "daemon," thinning the files whose names it receives through messages from **MCFG** or other programs in the system. A daemon is a process that runs in the background and performs specific services or tasks when it detects that they need to be done. If messages are received faster than they can be processed, **Thin3D** creates a dynamically allocated list of messages and processes them in the order in which they were received.

Thin3D has the ability to display images as a 3-D solid such as those shown in Figures 4.9 and 4.10. Voxels are represented as parallelepipeds having the same

relative dimensions of the voxels, or optionally as cubes. The solid model can be rotated, translated, and magnified by the user and printed to a PostScript printer or to disk file.

The user interface for this program, shown in Figure 4.11, consists of a small window with push buttons for loading, viewing, thinning, saving and printing animations, as well as buttons for processing batches of files, aborting, and requesting help. There are three integer gadgets for setting the cavity fill, fast thinning, and

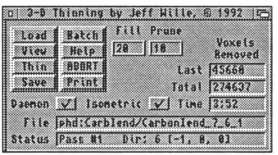


Figure 4.11: Graphical user interface for **Thin3D** program.

pruning thresholds. During thinning, the total number of voxels removed and the number removed during the previous pass are displayed along with the elapsed time. There are two checkmark gadgets for enabling and disabling the "daemon" mode and for controlling the voxel display mode. The program's icon can be used to save the default directory, threshold values, daemon mode, and isometric mode.

4.7 3D-FODAS

This is the main analysis program, which calculates the fiber orientation distribution from a thinned 3-D image. The inputs to the program are a thinned 3-D image, the voxel size and the refractive index of the material. The program allows any subvolume of the image to be selected for analysis, and the signs of the coordinate axes can be reversed to accommodate any imaging convention. **3D-FODAS** has

a powerful, built-in scripting language as well as a convenient batch mode for easy handling of large sets of images and a previewer for viewing animation files before analysis.

4.7.1 Determination of Fiber Orientation

3D-FODAS searches an image until it finds a voxel that is set. Starting at this voxel the program recursively follows all of the voxel chains that are contiguous with that voxel. As it traverses each chain it stores the coordinates of each voxel it finds. Upon reaching another junction or endpoint it takes the list of voxels and treating them as point masses calculates the inertia tensor as presented in Section 2.2.3. The inertia tensor is reduced to tridiagonal form by Householder Reduction. The QL algorithm is then employed to solve the eigenvalue problem and determine the principal moments of inertia (Press et al., 1988). The smallest principal moment of inertia coincides with the axis of the fiber.

4.7.2 Determination of Fiber Length

The length of the fiber is calculated from the number of voxels in the chain, the measured orientation, and the voxel size. The length determination is simplified by the continuity definition used in the thinning process. Under this definition, a voxel is guaranteed to have no more than two neighbors, except at a junction. This means that one component of the fiber length can be obtained simply by multiplying the number of voxels in the chain by the voxel size in the direction of that component. This is true only for the main voxel direction, which is defined as the axis direction which has the greatest voxel density in the direction of the fiber axis. That is, when

traveling in the direction of the fiber, voxel boundaries in the main voxel direction will pass by most frequently. The main voxel direction is defined as:

$$\text{Main voxel direction } (d) = \begin{cases} x & \text{if } p_x/v_x \text{ is largest} \\ y & \text{if } p_y/v_y \text{ is largest} \\ z & \text{if } p_z/v_z \text{ is largest} \end{cases} \tag{4.7}$$

where p_n is the component of the orientation vector in the direction of axis n, and v_n is the voxel size in the direction of axis n.

Once the unit direction vector, and one length component are known, the fiber segment length is simply:

$$L = nv_d/|\mathrm{p}_d| \tag{4.8}$$

where n is the number of voxels in the chain and d is the main voxel direction.

Due to the non-equal voxel dimensions in x, y, and z, the orientation of very short fiber segments can be strongly biased by the largest voxel dimension. To avoid this bias, voxel chains that are shorter than a selected threshold value are discarded.

4.7.3 Presentation of Results

In order to form a spherical histogram of the fiber orientation data, the fibers are binned according to their orientation. Each bin is incremented according to the true length of fiber material found oriented in the bin direction. The bins are defined by dividing the 3-D orientation space according to the faces of a subdivided unit icosahedron. An icosahedron is a polyhedron composed of 20 equilateral triangles. Subdivision of the icosahedron is accomplished by dividing each triangle into four triangles as illustrated in Figure 4.12. The triangle (A,B,C) represents one face of the icosahedron. The points a, b, and c are created by finding the midpoints of line

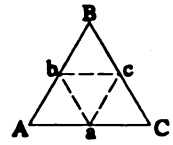


Figure 4.12: Subdivision of the unit icosahedron.

segments AB, BC, and CA and normalizing them to unit length. The number of times the icosahedron is subdivided is referred to as the tessellation order and is selected by the user. The quantization error can be made arbitrarily small by increasing the tessellation order. Order 4 is more than sufficient for most applications. Table 4.3 presents statistics about the subdivided icosahedron. The area values are given as a

Table 4.3: Icosahedron statistics.

Tessellation Order	0	1	2	3	4
Max. Quantization Error	37.83°	20.91°	10.68°	5.38°	2.70°
Number of faces	20	80	320	1280	5120
Number of vertices	12	42	162	642	2562
Area per face	5.00%	1.25%	0.31%	0.08%	0.02%

percentage of the total surface area.

An example of a spherical histogram, or fiber orientation distribution (FOD) plot created with a tessellation order of 2 is shown in Figure 4.13. In this figure, the spherical core (sea level) represents zero fiber material. The elevations of the peaks extending from this level represent the amount of fiber material oriented in the directions of the peaks.

Once the orientation and length of the fiber segment have been determined these data are stored in a Hough transform coordinate system. This has the potential advantage of enhancing the analysis of fragmented images. As discussed previously, the 2-D Hough transform requires two parameters to define a line. The two parameters are divided into intervals defining a 2-D accumulator array in which lines appear as

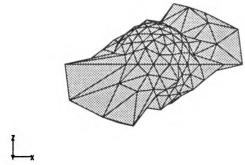


Figure 4.13: Sample FOD generated by **3D-FODAS**.

peaks. In the 3-D case four parameters rather than two are required to define a line, (e.g., two components of a normalized direction vector and two intercept coordinates). One of these four parameters can be eliminated by taking advantage of the discretized nature of the orientation storage space; in this case, the subdivided icosahedron. By numbering each vertex of the icosahedron, all directions can be represented by a single number. Thus a three-dimensional line can be fully specified by an orientation index number and two intercept coordinates. To minimize errors due to the quantization of orientations, the intercept coordinates are chosen to be those of the coordinate plane that is most perpendicular to the fiber. For example, if the fiber were parallel to the z-axis, its x, y intercept coordinates would be used in the transformation. The 3-D Hough transform can be represented as $H(i, j, k)$ where i is the index of the icosahedron vertex, and j, k is the intercept of the plane most perpendicular to direction i. Thus by detecting maxima in the i, j, k space, the location of fiber segments can be obtained, even if the fiber voxels are discontinuous.

Once all of the fiber structures in the image have been traversed, the orientation data consists of a collection of orientation vectors corresponding to the vertices of the subdivided icosahedron whose lengths are proportional to the amount of fiber material found in each orientation. This is the fiber orientation distribution. It is displayed by

3D-FODAS as a spherical plot which can be rotated in three-dimensions. Clicking the mouse on a vertex displays the length and orientation of that vertex. The plot can be sent directly to a PostScript printer for a high quality hard copy or to a plot file. Several different types of data files can be saved to disk including a fiber orientation distribution file listing all orientations and the corresponding amount of fiber material, and the accumulators of the Hough transform. The data is also reduced to tensor form for direct application in tensor based models. A display of the fiber segment length distribution is also available. It should be noted that a fiber which is intersected by several other fibers appears to **3D-FODAS** as a series of fiber segments whose lengths add up to the total fiber length. Thus the weighting of the fiber orientation distribution is correct, but the fiber length distribution is not—it gives only the fiber segment length distribution. The length data is provided only as an indication of the amount of fiber crossings and discontinuities in the image. Of course, the length distribution data will be correct if there are no fiber intersections or discontinuities in the image.

4.7.4 Program Features

The user interface for **3D-FODAS**, shown in Figure 4.14, consists of a window containing gadgets for selecting the file(s) to be analyzed, reversing axes, displaying and setting the dimensions of the scan volume, the refractive index, the threshold for discarding short voxel chains, the tessellation order, the Hough transform parameters, and for previewing animations, analyzing images, batch processing, script processing, aborting, and obtaining help. The status line displays the current status of the program at all times. The program's icon can be used to set the default directory, and the default values for the parameters listed above.

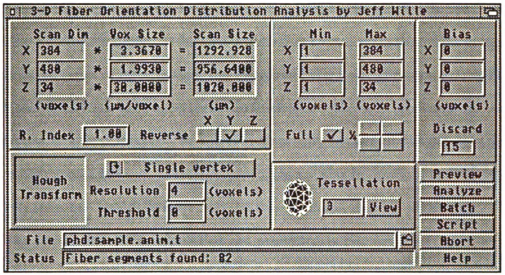


Figure 4.14: Graphical user interface for **3D-FODAS** program.

4.8 DiffFOD

The purpose of this program is to combine and compare fiber orientation distributions. In particular it displays the orientation and lengths of the principal axes of the fiber orientation tensor. The orientation information is displayed in a readily interpreted form: the rotation angle, ϕ, of the major axis in the x-y plane, the elevation angle, θ', of the major axis from the x-y plane, and the rotation angle, β, of the intermediate axis about the major axis as illustrated in Figure 4.15.

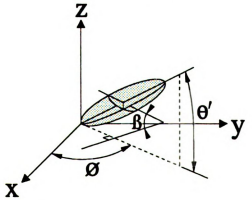


Figure 4.15: Ellipsoid angles calculated by **DiffFOD**.

Any FOD can be compared with a reference distribution, in which case the display will show the differences between the two orientation tensor statistics. The program can display three types of information, the reference FOD data, the comparison FOD data, and the difference between them. In each case, the average value for each column of data is also displayed. In the difference display, an additional column is displayed which gives the tensor deviation, which is a scalar measure of the difference between two tensors. The difference may be due to shape and/or orientation. The details of the tensor deviation calculation are presented in Section 6.4.1.

A powerful feature of **DiffFOD** is its ability to combine several FODs together. This is useful for combining results from a series of similar specimens, or from a neighborhood of a single specimen to provide a greater number of tracer fibers in the sample population.

The user interface for this program, shown in Figure 4.16, consists of a scrollable main display area where the FOD names and data are displayed. There are gadgets

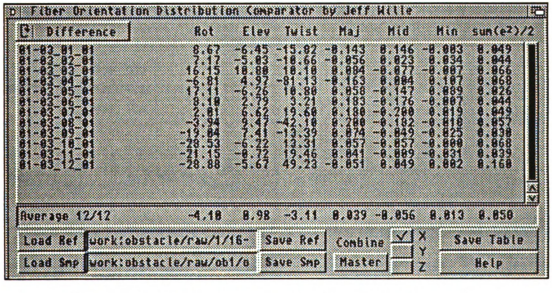


Figure 4.16: Graphical user interface for **DiffFOD** program.

for loading and saving reference and sample FODs, and for saving the comparison

and raw data. A cycle gadget cycles the display between reference, sample, and difference displays. Three gadgets labeled X, Y, and Z allow the user to select which axes will be combined. A final gadget, labeled "Master" creates a master FOD field by combining the FODs from two or more similar specimens cell by cell to create a representative specimen FOD. The program's icon can be used to set the default directory, combination flags, and display mode.

4.9 Fibor

The purpose of this program is to provide a graphic representation of the fiber orientation distribution field of a specimen. This allows the human observer to visualize global trends in the fiber orientation. The orientation field can be viewed from any of the three coordinate planes and at any layer within the specimen. **Fibor** reads the FOD files created by **3D-FODAS** and calculates the projection of the orientation tensor ellipsoid by solving the eigenvalue problem for the appropriate four-component 2-D tensor taken from the nine-component 3-D FOD tensor.

$$a_{ij} = \begin{vmatrix} a_{11} & a_{12} & a_{13} \\ a_{21} & a_{22} & a_{23} \\ a_{31} & a_{32} & a_{33} \end{vmatrix}$$

$$a_{xy} = \begin{pmatrix} a_{11} & a_{12} \\ a_{21} & a_{22} \end{pmatrix}, \quad a_{yz} = \begin{pmatrix} a_{22} & a_{23} \\ a_{32} & a_{33} \end{pmatrix}, \quad a_{xz} = \begin{pmatrix} a_{11} & a_{13} \\ a_{31} & a_{33} \end{pmatrix}.$$

The projected ellipses have major and minor axes whose lengths and orientations are the eigenvalues and eigenvectors of the four-component tensor. The eigenvalues are:

$$\lambda_e = \frac{a_{ii} + a_{jj}}{2} \pm \sqrt{\frac{(a_{ii} + a_{jj})^2}{4} - a_{ii}a_{jj} + a_{ij}^2}. \tag{4.9}$$

In this equation and the one below repeated indexes do not imply summation. The eigenvectors are:

$$\mathbf{v}_e = \begin{pmatrix} -a_{ij} \\ a_{ii} - \lambda_e \end{pmatrix} \tag{4.10}$$

Fibor loads the selected FOD files and calculates the projection of the FOD tensor ellipsoids on the selected plane. The user can magnify and scroll the display using the cursor keys to allow close inspection of selected regions, or reduce the display size for an overall view of the fiber orientation distribution field. An example of a FOD field produced by **Fibor** is shown in Figure 4.17.

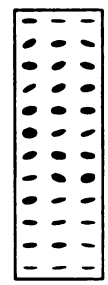


Figure 4.17: Sample FOD field produced by **Fibor**

The user interface for **Fibor**, shown in Figure 4.18, consists of a window with gadgets for selecting a group of FOD files and the projection plane. Output can be directed to the screen, printer, or a disk file, and there is an on-line help facility. The program's icon can be used to set the default directory, voxel dimension, and index of refraction. Further details and documentation for this program are presented by Schöche (1992).

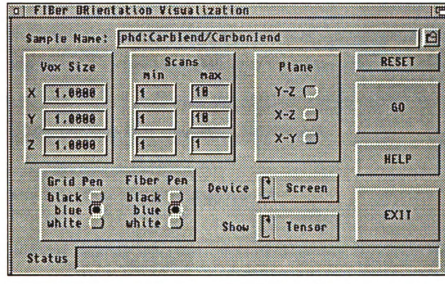


Figure 4.18: Graphical user interface for **Fibor** program.

CHAPTER 5

EXPERIMENTAL PROCEDURE

The experimental work included: testing the apparatus, development of the procedure to prepare transparent materials, calibration and testing of the software, testing the imaging apparatus, manual surface measurement of fiber orientation for comparison with the sectioning method, and molding of test specimens under varying conditions for comparison of the resulting fiber orientation distributions.

5.1 Testing the Injection Molding Apparatus

Testing of the injection molding apparatus consisted of gaining experience with the equipment, calibration, measurement of its capabilities, and optimizing the processing parameters for various materials.

5.1.1 Calibration

The thermocouples and data acquisition equipment were calibrated with a Hewlett-Packard 2804 A Quartz Thermometer and a hand-held Omega 450 ATT thermocouple thermometer. The quartz thermometer and the thermocouples attached to the data acquisition board were bound together and allowed to come to room temperature. The cold junction temperature compensation parameter in the data acquisition soft-

ware was adjusted until the thermocouple readings were within 0.5 °C of the quartz thermometer. The bound thermocouples and thermometer were immersed in a water bath and their reading were compared at 0 and 100 °C. The thermocouple values differed from that of the thermometer by less than 1 °C. One of the thermocouples from the data acquisition board and the thermocouple from the hand-held unit were coated with heat conductive silicon paste and inserted into adjacent thermocouple wells in the wall of the injection barrel. The barrel was heated to 240 °C at which temperature the difference between the readings was found to be less than 2 °C, which was considered to be sufficient accuracy for the experimental procedures.

The position transducer was calibrated by attaching a linear scale along side the injection piston and adjusting the slope and offset parameters of the linear calibration function in the data acquisition software to achieve less than 1 mm error, measured at 25.4 mm intervals, over the 15 cm length of the piston's travel. This gives a maximum error of 0.7 percent for a 15 cm measurement.

The injection pressure was adjusted by a pressure regulator on the hydraulic power unit. The pressure gage on the hydraulic unit was used as the indicator of the cylinder pressure without calibration.

The injection speed was calibrated with the event timer in conjunction with the position transducer. The timer was set to measure the time required for the piston to move from 12 cm above the zero position to 3 cm above the zero position. The needle valve controlling the flow rate to the hydraulic cylinder was adjusted until the desired piston speed was achieved. Repeated tests with the speed set at 8.3 cm/s showed variations of no greater than 0.2 cm/s, or 2.4 percent.

To characterize the relationship between the temperature profile of the material inside the injection barrel with the externally measured wall temperature a series of

thermocouples were placed along the axis of the barrel at 0.0, 0.5, 1.0, and 1.5 inches from the nozzle. The 85 watt mold heater was turned on for 5 minutes at which time the nozzle (100 watt), lower barrel (50 watt), and upper barrel (155 watt) heaters were also turned on, which represents a typical heating cycle. The target mold temperature of 110 °C and barrel/nozzle temperature of 200 °C were reached after 11.5 minutes total heating time. The target temperatures were held for another 5 minutes. The four internal material temperatures, nozzle temperature, and two barrel temperatures were recorded during the entire procedure.

5.1.2 Performance Envelope (Characterization)

The capabilities of the injection apparatus were investigated by running a series of injections under a variety of conditions. The maximum injection rates were measured under low load conditions, whereas the maximum injection pressures were measured under high load conditions.

5.1.3 Optimization of Injection Process

To demonstrate the capability of the injection apparatus for dealing with a variety of materials, including high-fiber content materials, and to gain experience with the machine, a series of specimens were produced with styrene–acrylonitrile copolymer (Lustran® San), polymethyl-methacrylate (PMMA) and polypropylene with and without fiber reinforcement.

A series of specimens were produced with each type of material, during which the processing conditions such as barrel temperature, mold temperature, injection rate and injection pressure were varied. The resulting specimens were inspected, and the operating conditions were adjusted until high quality specimens could be produced.

Quality was judged in terms of complete mold filling, lack of shrinkage, absence of voids and bubbles, and smooth finish.

5.2 Production of Transparent Composite Specimens

The preparation of transparent composite specimens was a major task in the experimental procedure. The challenges included finding materials with matched refractive indices, cutting the fibers to the desired length, mixing fiber and matrix material uniformly, and molding the specimens with good interfaces between fiber and matrix and few voids.

5.2.1 Combining Matrix and Fiber Materials

The fibers were prepared by cutting with the fiber chopper apparatus. The feed mechanism was programmed to advance the fibers 0.916 mm between each cut. Both glass (13 μm diameter) and carbon (10 μm diameter) fibers were chopped to the same length. The critical fiber length for 13 μm diameter fibers is 195 μm (Kelly and Tyson, 1965). The critical length is the length at which the fiber begins to behave as a continuous fiber with regard to load bearing capability. In order to achieve a uniform distribution of fibers, the powdered matrix material and fibers were mixed in a beaker with a high speed whip.

5.2.2 Refractive Index Matching

The task of finding compatible materials for producing transparent materials was undertaken in two parts: literature research and experimentation. Through the literature search several thermoplastics were identified which have refractive indices very near those of commonly available glass fibers (see Table 7.1). Much of the literature

search was conducted by Westerbecke (1992). A detailed discussion of refractive index matching, imaging issues, and alternative imaging technologies, are presented in his paper.

The materials that were selected for the experimental work were polymethylmethacrylate (PMMA) and BK-10 glass fibers. Tables 5.1 and 5.2 list the properties of PMMA and BK-10 respectively.

Table 5.1: Properties of PMMA.

Transparency	τ	92%
Refractive index	n_D	1.491
Index temperature coefficient	dn/dt	-12.5×10^{-5}/°C
Melting temperature	T_m	85–100 °C
Glass transition temperature	T_g	100 °C
Processing temperature range	T_l	163–260 °C
Molding pressure range	p	345–1379 bar
Young's modulus	E	2240–3250 N/mm^2
Density	ρ	1.17–1.20 g/cm^3
Thermal conductivity	k	0.167–0.251 J/m·s·°K
Thermal diffusivity	α	8.9×10^{-4} cm^2/s
Heat capacity	c	1.46×10^{-3} J/kg·°K
Linear thermal expansion	α_{th}	$50–90 \times 10^{-6}$ cm/cm°C
Volumetric thermal expansion	B	$1.50–2.70 \times 10^4$ m^3/m^3·°K

Source: *Modern Plastics Encyclopedia*, McGraw-Hill, New York, 1976.

Table 5.2: Properties of BK-10 glass.

Transparency at 500 nm	τ_{500}	99.9%
Refractive index	n_D	1.49776
Index temperature coefficient	dn/dt	3.4×10^{-6}/° C
Glass transition temperature	T_m	532 °C (990 °F)
Young's modulus	E	72,000 N/mm^2
Density	ρ	2.39 g/cm^3
Linear thermal expansion	α_{th}	5.8×10^{-8} cm/cm°C

Source: Schott Glass Technologies

A photospectrometer was used to determine the wavelength and temperature which gave the best refractive index match. A 3.2 mm thick specimen of PMMA with 30 wt% (17 vol%) glass fiber content was placed between the light source and detector of the photospectrometer. The light transmission of the material was measured over all wavelengths of the visible spectrum and over a temperature range of −20 °C to 100 °C.

It was determined that the best match occurred near 10 °C and 400 nm. Examination of the specimen using the microscope and CCD video camera at 10 °C versus room temperature showed no significant difference in image quality, nor did the introduction of a low-pass optical filter cause any significant change. Therefore, it was concluded that the refractive indices at room temperature were as closely matched as necessary for the spectral sensitivity of the CCD camera and no special filters or temperature control were required. Table 5.3 shows a comparison of the refractive indices of PMMA and BK-10 as functions of wavelength. Table 5.4 shows the refractive indices of PMMA and BK-10 as functions of temperature.

5.3 Calibration of Software

The calibration of the software was done in several parts. The first part involved generating pseudo data consisting of 3-D images generated by the **Pseudo** program. This allowed measured FODs to be compared with known distributions. In this way the analysis software evaluation was uncoupled from the imaging process. The second part of the calibration involved imaging individual fibers of known orientation and length and comparing the measured results with the known values. A special calibration specimen with a 1.5 mm square cross section was produced which allowed the same volume to be imaged from four different directions. Finally, specimens Ob7

Table 5.3: Refractive indices of PMMA and BK-10 glass vs wavelength.

	PMMA[†]	BK-10[‡]
λ (nm)	n	n
1060.0		1.48827
1014.0	1.483	1.48887
851.1		1.49127
706.5		1.49419
656.3	1.488	1.49552
643.8	1.489	1.49589
632.8		1.49624
589.3		1.49776
587.6	1.491	1.49782
546.1		1.49960
486.1	1.496	1.50296
480.0		1.50337
435.8	1.503	1.50690
404.7	1.507	1.51014
365.0		1.51562

[†]The Handbook of Plastic Optics, U.S. Precision Lens Inc.

[‡]Schott Glass Technologies

Table 5.4: Refractive indices of PMMA and BK-10 glass vs temperature.

($\lambda = 588\,\text{nm}$)	PMMA[†]	BK-10[‡]
Temperature (°C)	n	n
23	1.4920	1.4913
25	1.4910	1.4910
30	1.4893	1.4904
35	1.4890	1.4898
40	1.4890	1.4891
45	1.4880	1.4885
50	1.4875	1.4879
55	1.4873	1.4873
60	1.4862	1.4866
65	1.4858	1.4860
70	1.4851	1.4854
75	1.4848	1.4848
80	1.4838	1.4841
85	1.4830	1.4835
90	1.4810	1.4829

[†]Source: Westerbecke (1992)

[‡]Schott Glass Technologies

and No8 (defined in Section 5.5) were physically cut at various depths and analyzed by both the optical sectioning and surface ellipse methods to allow a quantitative comparison of the two methods to be made.

5.3.1 Pseudo Data

The Pseudo program was used to generate several 3-D test images which consisted of straight fibers 600 μm long and 10 μm in diameter which were oriented in the directions of the vertices of a twice subdivided icosahedron. The pseudo fibers were placed in random locations inside the sample volume. The voxel size was set to be 3.367 x 1.993 x 14.9 μm to reflect the attributes of the imaging system. The images contained fiber images of a known orientation distribution which could be directly compared with the results of the image analysis to quantify the accuracy of the analysis software.

5.3.2 Single Fiber Tests

The first step in evaluating the capabilities of the system with real fiber data was to acquire 3-D images of individual fibers of known orientations and evaluate the measured data produced by the analysis software.

To evaluate the accuracy of the measurement of the in-plane component of the fiber orientation a sparse population of short tracer fibers was molded into a PMMA sample and placed on a rotary indexing table mounted on the microscope stage. Two neighboring fibers were selected and positioned at the center of the field of view. The fibers were scanned in their original position, the table was indexed by 10 degrees in the horizontal plane, and the scanning was repeated. This was done for a total of 90 degrees of rotation. The term *scan* refers to a sequence of images taken at

progressive depths along the optical axis (z) at one horizontal (x-y) location. A scan *cell* refers to a portion of a scan that is treated as a unit during analysis. (Often the entire scan is treated as a cell. However, the software has the capability of dividing a scan into as many cells as desired.)

To evaluate the accuracy of out-of-plane measurements a thin epoxy specimen with a long straight carbon fiber embedded in it was mounted on an rotary indexer oriented perpendicular to the optical axis. The indexer was adjusted so that the fiber was initially in the horizontal plane oriented in the direction of the x axis. The fiber was scanned in its original position and in 10 degree increments to ± 40 degrees in the x-z plane. Further rotation was impossible due to contact with the objective lens of the microscope. This same procedure was repeated for the y-z plane.

To investigate steeper inclination angles including the direction of the optical axis, a y-shaped fiber holder was constructed of very fine copper wire. A single fiber was stretched between the arms of the holder and positioned in front of the objective. This fixture allowed the fiber to be rotated in all directions without any interference from the objective lens itself. Experiments similar to the ones described above were performed with this single fiber in air.

5.3.3 Orthogonal Specimen

All of the experiments described up to this point involved individual fibers with little or no interference from neighboring fibers. In order to evaluate the ability of the method to deal with higher fiber concentrations, an 82.5 x 10.3 x 3.2 mm (3.25 x 0.406 x 0.125 in) specimen was produced with 30 wt% BK-10 glass fibers and 0.1 wt% carbon tracer fibers. A slender piece with a 1.5 mm square cross section was cut out of the middle of the specimen as shown in Figure 5.1. This specimen had a small enough

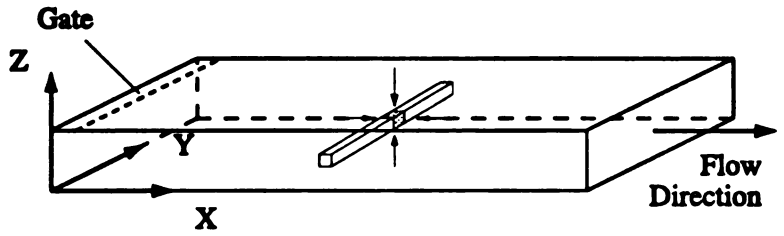


Figure 5.1: Orthogonal calibration specimen location.

cross section that the same volume could be imaged from four orthogonal directions. Since there is a significant difference in the resolving power of the microscope in the image plane versus the optical axis an axis-dependent systematic error in the analysis could be revealed by comparing the results of these four scans.

Each side of the specimen was scanned beginning 350 μm from the surface at 14.9 μm intervals for 53 steps. The imaging area of the video camera was 797 x 1077 μm. Thus the scanned volume was 797 x 797 x 1077 μm. This process was repeated at two locations 1 mm apart. Lian prepared and scanned this specimen.

5.3.4 Surface Ellipse Measurement

In order to allow a direct comparison between the optical sectioning method and the surface ellipse method two PMMA specimens (Ob7 and No8) containing 20 wt% 13 μm diameter BK-10 glass fibers and 0.1 wt% carbon fibers were physically sectioned at non-dimensional depths of z/b = 0.94, 0.75, 0.56, and 0.10, where b is half the thickness of the sample and z is the distance from the midplane along the optical axis. At each surface the exposed fiber ellipses were measured and the specimens were optically sectioned at 14.9 μm intervals for 20 steps. The scans were done in three adjacent rows of 12 cells, spanning the width of the specimen with the edge of the first scan located 20 mm from the gate. The material preparation, imaging, and data analysis were performed by Lian.



Figure 5.2: Surface image showing fiber ellipses. (100x magnification)

The surface images were captured with the frame grabber and the major and minor axes of the fiber ellipses were identified manually. A data file containing the coordinates of ellipse features was generated by positioning the mouse pointer at the appropriate locations. Figure 5.2 is a photograph of a polished surface of a specimen containing 30 wt% glass, 0.1 wt% tracer fibers which was used in the surface ellipse analysis.

5.4 Testing the Repeatability of the Imaging Process

To evaluate the repeatability of the imaging system, specimen No5 was repeatedly scanned at the same location, but with independent operators setting up the lighting conditions and camera settings. Two different scan patterns were used. In one pattern the specimen was scanned 10 times at a single x-y location from the surface to a depth

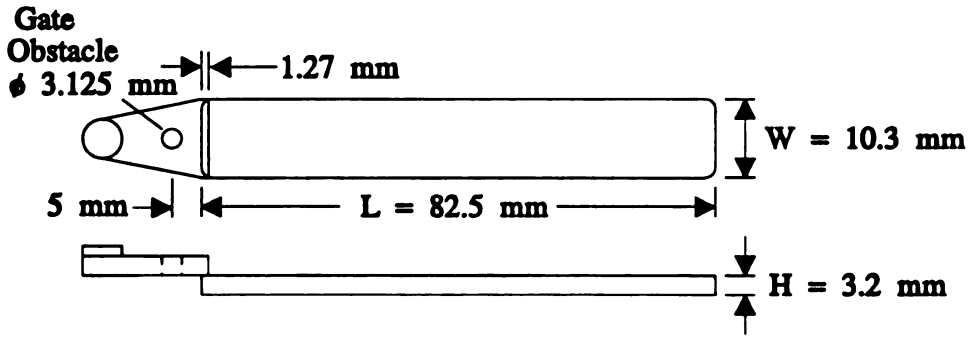


Figure 5.3: Specimen and gate geometry.

of 700 μm at 14.9 μm intervals. In the second scan pattern, four adjacent x-y locations, sharing a common corner centered at the original scan location, were scanned three times each over the same z range. The results from each type of scan pattern were combined and the components of the resulting fiber orientation ellipsoid were plotted as functions of penetration depth. The repeatability experiments and analysis were performed by Schöche.

5.5 Gate Obstacle Specimens

A series of rectangular transparent specimens were molded with and without a cylindrical obstacle in the gate to determine the influence of the obstacle on the fiber orientation. A total of 18 specimens were prepared with PMMA, 13 μm diameter BK-10 glass fibers, and 10 μm diameter carbon tracer fibers. Both types of fibers were 0.916 mm long. The mold cavity was 82.5 x 10.3 x 3.2 mm with a diverging film gate. The specimen and gate geometry are shown in Figure 5.3. (See also the mold drawings in Appendix B.1.)

Of the 18 samples, nine were molded with a 3.125 mm (0.125 inch) diameter cylindrical obstacle in the gate, and nine without. Within each of these two batches 3

specimens were molded with 20% glass, 3 with 25% glass, and 3 with 30% glass as shown in Table 5.5.

Table 5.5: Transparent specimen naming scheme.

Glass Content	Without Obstacle	With Obstacle
30%	No1–3	Ob1–3
25%	No4–6	Ob4–6
20%	No7–9	Ob7–9

The decision to place a cylindrical object in the gate to produce a unique fiber orientation was made based on observations in the literature that the core orientation induced at the gate was often carried down the full length of the molding. It was expected that the obstacle would increase the shear forces in the flow and induce a greater degree of alignment without requiring modification of the cavity geometry. Variations of the injection temperature or pressure could have been used to alter the fiber orientation, but temperature and pressure changes can also alter the properties of the matrix through thermal degradation or altering the density.

The photographs in Figures 5.4 and 5.5 show the specimens that were produced. The specimens are designated from left to right: No1–No9 for the no-obstacle specimens, and Ob1–Ob9 for the obstacle specimens. The injection protocol is given in Appendix C and the data sheets containing detailed information about the processing conditions for each specimen are found in Appendix D.

Because a textured surface finish was normally present on the molded specimens it was necessary to polishing them to obtain a sufficiently smooth surface for imaging. Table 5.6 shows the final thickness of each specimen after polishing. All of the specimens were 3.2 mm thick before polishing.

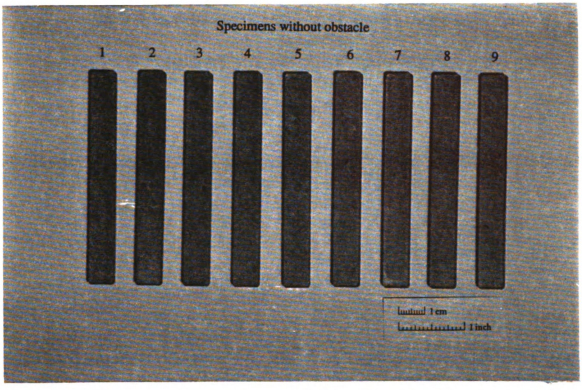


Figure 5.4: Specimens made without gate obstacle.

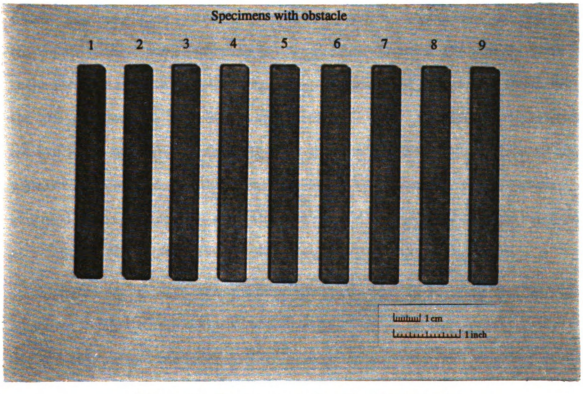


Figure 5.5: Specimens made with gate obstacle.

Table 5.6: Polished thickness of gate obstacle specimens.

Specimen	Thickness (μm)		Specimen	Thickness (μm)
No1	2.80		Ob1	3.10
No2	2.75		Ob2	3.10
No3	2.80		Ob3	3.10
No4	2.75		Ob4	3.10
No5	2.70		Ob5	3.10
No6	2.90		Ob6	3.10
No7	2.95		Ob7	3.10
No8	3.05		Ob8	3.10
No9	2.95		Ob9	3.20

5.5.1 Imaging

In order to measure the influence of the gate obstacle the specimens were each imaged in a series of scans across their width. The size of the CCD camera's field of view for a 10x objective lens was 1.077 x 0.797 mm, requiring 12 scans to cover the entire sample width. The coordinate system used with the specimens was defined as: the x or 1 coordinate is the distance from the gate in the flow direction, the y or 2 coordinate is the distance from the vertical longitudinal midplane, and the z or 3 coordinate is the distance from the horizontal midplane (optical axis). A series of three adjacent rows of scans were made, beginning at a distance of 5 mm from the gate to allow a statistical comparison of the orientation tensor components. Twenty images were captured at 14.9 μm intervals along the optical axis (z) at each x-y location, beginning at a depth of 447 μm from the unpolished surface as shown in Figure 5.6.

A similar set of scans were made at the midsection (in the gage length) of the specimen to allow correlation with tensile testing results. The scans were made at 37, 41, and 45 mm from the gate. At each position 40 images in two groups of 20 were captured along the optical axis beginning at the polished surface.

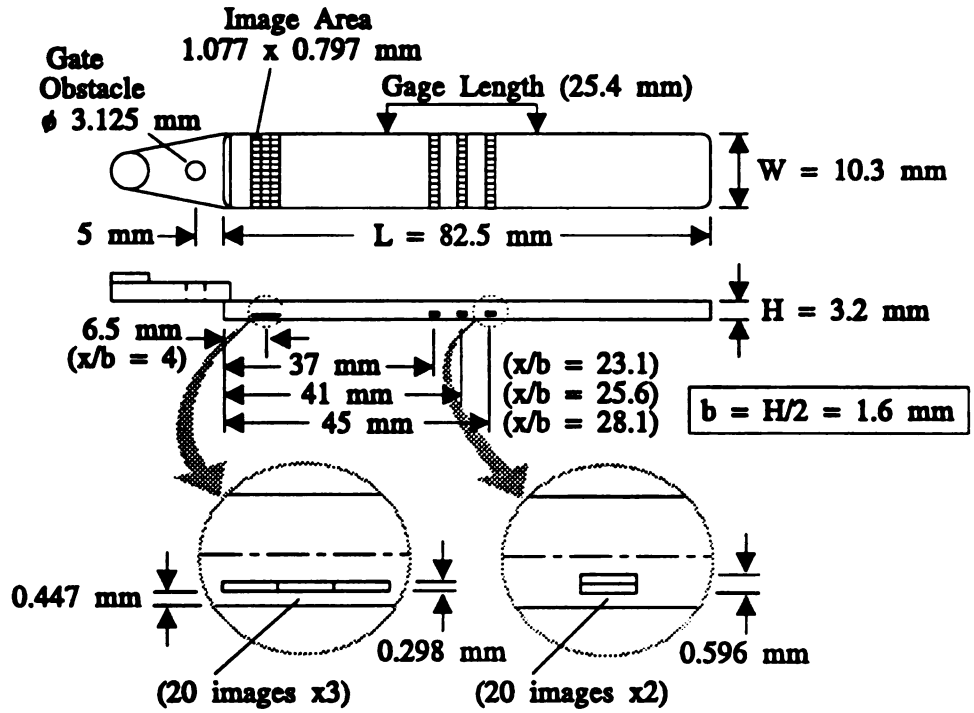


Figure 5.6: Scan locations for gate obstacle specimens.

Figure 5.7 is a photomicrograph of a typical optical cross section of a specimen containing 30 wt% glass, 0.1 wt% tracer fibers used in the optical sectioning analysis. Most of the fibers in this image are oriented parallel to the imaging plane, although some fibers can be observed to extend out of the focal plane. Note that some of the fibers are curved and that many fibers appear to intersect each other. Thresholding the image effectively reduces the depth of field, resulting in fewer apparent intersections.

The imaging described up to this point was restricted to a fairly small penetration depth to minimize the scan time and volume of data generated. To illustrate the ability of the method to measure the z-component of the fiber orientation and probe deep into the material a series of scans were made along the vertical midplane of the specimen over a range of $z/b = 0.72$ to 0.1 and from $z/b = -0.72$ to -0.1.



Figure 5.7: Optical cross section of transparent composite. (100x magnification)

The longitudinal positions of the scans were chosen to match data reported in the literature. The scan locations are illustrated in Figure 5.8.

Schōche contributed significantly to the preparation and analysis of these materials.

5.5.2 Mechanical Testing

The 18 gate obstacle specimens were tested in an Instron tensile tester. Reflective tape was attached to mark the limits of the 19 mm (0.75 in) gage length. The specimens were gripped with cleated grips without end tabs. An ASTM-D-3039 laser extensometer was used to monitor the strain, and a 1000 lb load cell was used to monitor the load. The crosshead rate was 0.2 in/min. The specimens were tested in

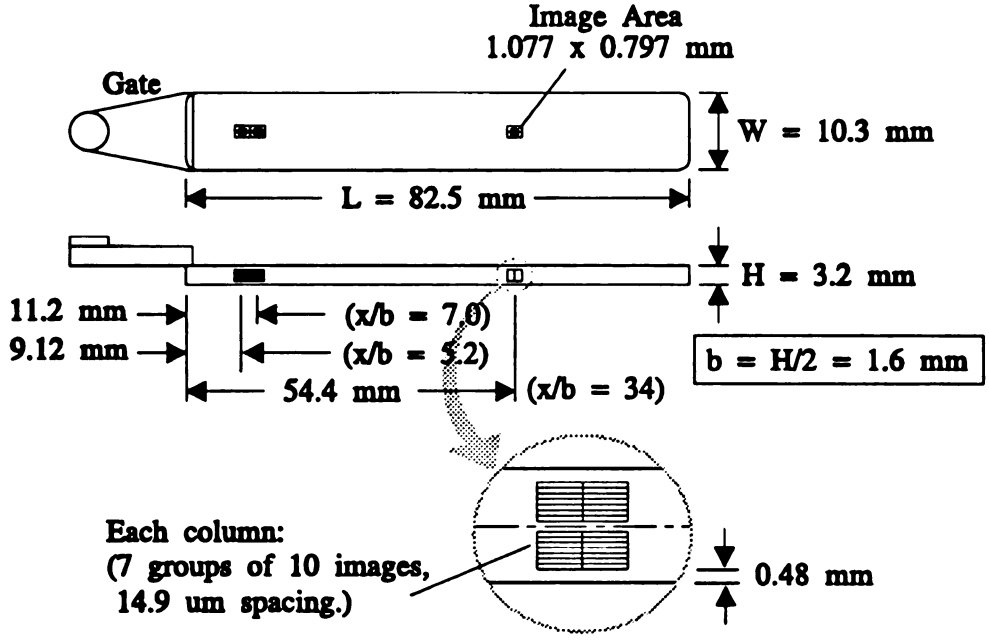


Figure 5.8: Centerline scan locations for gate obstacle specimens.

the elastic range to a maximum strain of about 0.5 percent, which resulted in the fracture of one of the specimens. The mechanical testing was performed by Lian.

5.6 Cavity Obstacle Specimen

To visualize the fiber orientation field resulting from flow around an obstacle an additional specimen, designated Obm2, was made with an obstacle in the middle of the cavity using the same injection protocol as that used for the gate obstacle specimens. The obstacle was a 3.125 mm (0.125 inch) diameter cylinder located on the midline of the specimen at a distance of 30 mm (2.17 inch) from the gate end ($x/b = 17.2$, $y/b = 0.0$). A diagram of Obm2 is shown in Figure 5.9.

The specimen was imaged on a 12 x 30 grid of 1.077 x 0.797 mm rectangular areas surrounding the obstacle. At each location, 50 images were captured along the optical axis beginning at the polished surface at 14.9 μm intervals. The scan locations are illustrated in Figure 5.10.

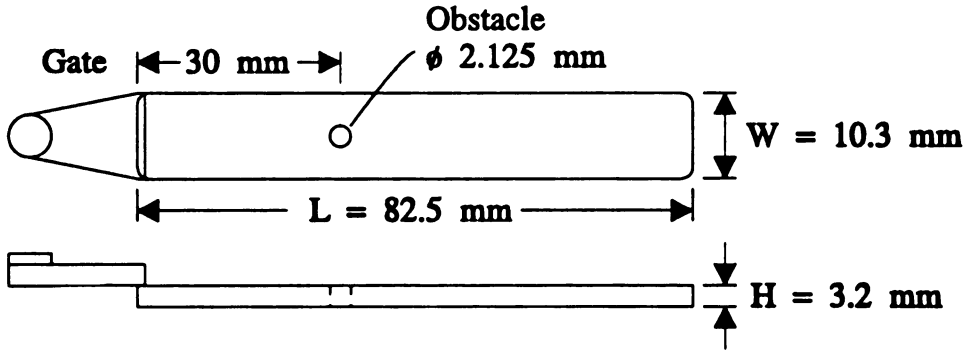


Figure 5.9: Specimen with cavity obstacle.

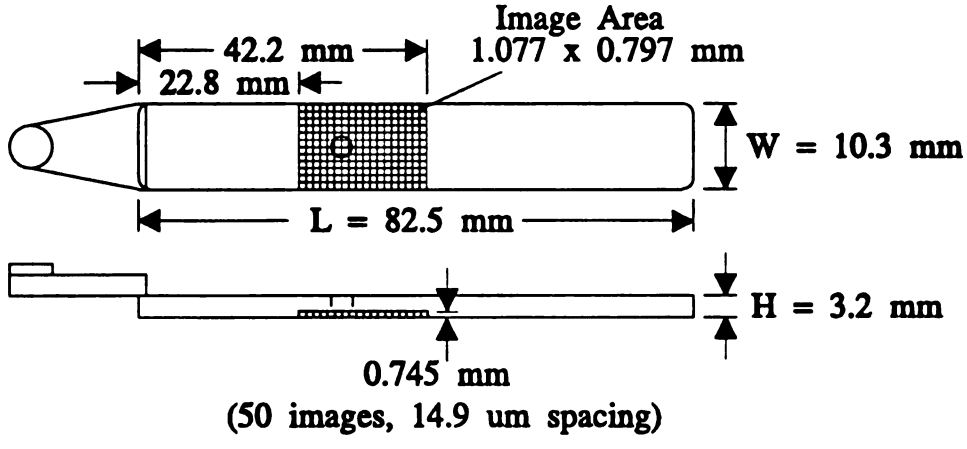


Figure 5.10: Scan locations for specimen with cavity obstacle.

CHAPTER 6

ANALYSIS

This chapter outlines the procedure used to analyze the 3-D image data and tensile testing data. In particular, the parameters used in the analysis software are given as well as the calculations used to determine the Young's Modulus of the tensile specimens. The details of the image analysis method were presented in detail in Chapter 4 and are not repeated here.

6.1 Image Processing

The acquired images were converted to binary format by thresholding the pixels at a value of 128. Due to anomalous behavior of the frame grabber the leftmost two columns of pixels contained erroneous data and were discarded. The resulting binary images were thinned with the **Thin3D** algorithm using the following parameters: *fill* = 20 (cavities with volumes less than or equal to 20 voxels were filled), *crush* = 7 (the fast thinning mode was begun on pass number 7), and *prune* = 5 (voxel chains having one free end and consisting of 5 voxels or less were pruned from the final images).

6.2 Image Analysis

The images were analyzed by **3D-FODAS** with the following settings: *tessellation* = 3 (the unit icosahedron was subdivided 3 times for a maximum quantization error of 5.38°), *discard* = 15 (chains less than 15 voxels long were discarded), *neighbors* = 0, and *threshold* = 0 (no Hough transform manipulation of the data was performed). Note that 15 voxels is 50.5 μm in the x direction, 29.9 μm in the y direction, and 223.5 μm in the z direction. Less than 5% of the tracer fibers were less than 223.5 micron long. And of these 5%, very few would likely be oriented in the z direction.

The statistical significance (p value) of the differences between tensor components obtained from specimens with and without gate obstacles were calculated from the mean and standard deviations of the measurements. The t statistic of the difference between the means was calculated using

$$t(\overline{x}_2 - \overline{x}_1) = \frac{\overline{x}_2 - \overline{x}_1}{\sqrt{S_p^2(\frac{1}{n_1} + \frac{1}{n_2})}} \tag{6.1}$$

$$S_p^2 = \frac{(n_1 - 1)S_1^2 + (n_2 - 1)S_2^2}{(n_1 - 1) + (n_2 - 1)}. \tag{6.2}$$

The t-distribution is:

$$F(t) = \int_{-\infty}^{t} \frac{\Gamma(\frac{n+1}{2})}{\sqrt{n\pi}\Gamma(\frac{n}{2})}(1 + \frac{x^2}{2})^{-\frac{n+1}{2}} dx \tag{6.3}$$

where n is the number of degrees of freedom, and Γ is the gamma function.

$$\text{d.f.} = n_1 + n_2 - 2 \tag{6.4}$$

Since there were three samples in each group, d.f. = 4.

$$\Gamma(n) = \int_0^{\infty} e^{-x} x^{n-1} dx. \tag{6.5}$$

The combined area in the tails of the t-distribution below $-t$ and above $+t$ is the p statistic. This statistic represents the probability of observing a difference in means equal to or greater than the observed difference if the experiment were performed many times, under the assumption that the means of the two sample populations are equal. A p value less than 0.10 represents a statistically significant difference at an α level of 0.10.

6.3 Surface Ellipse Analysis

The 3-D orientation of glass fibers were calculated from measurements of the ellipses they formed at the cutting plane. This is a deviation from the optical sectioning experiments in which the carbon fibers were analyzed. During the data acquisition process the ends of the major and minor axes were identified manually. The ends of major axes were labeled p_1 and p_2, and the ends of the minor axis were labeled, p_3 and p_4. The in-plane orientation angle, ϕ, for each fiber was calculated from the coordinates of the major axis endpoints.

$$\phi = \tan^{-1}\left(\frac{y_2 - y_1}{x_2 - x_1}\right), \qquad -\frac{\pi}{2} < \phi < \frac{\pi}{2}. \tag{6.6}$$

The out-of-plane angle, θ, for each fiber was calculated from the aspect ratio of the ellipse.

$$\theta = \cos^{-1}(b/a) = \cos^{-1}\left(\pm\sqrt{\frac{(x_4 - x_3)^2 + (y_4 - y_3)^2}{(x_2 - x_1)^2 + (y_2 - y_1)^2}}\right), \qquad 0 < \theta < \pi. \tag{6.7}$$

The terms were added when x_1 was less than x_2 and subtracted when x_1 was greater than x_2.

To compensate for the non-uniform probability of fibers with different values of θ crossing the cutting plane, a weighting function $W(\theta)$ was applied to each fiber,

$$W(\theta_n) = \frac{1}{\frac{l}{d}\cos\theta_n + \sin\theta_n} \tag{6.8}$$

where l is the fiber length, d is the fiber diameter. This function is inversely proportional to the z extent of the fiber volume.

This weighting factor was applied to the calculation of the tensor components as shown in the following equation.

$$< a_{ij} > = \frac{\sum_n W(\theta_n) a_{ij}^{(n)}}{\sum_n W(\theta_n)} \tag{6.9}$$

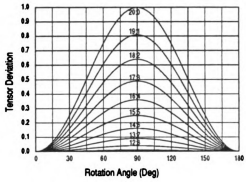
6.4 Comparison of FODs

6.4.1 Quantitative Analysis (DiffFOD)

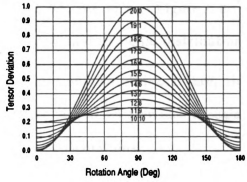
A measure of the similarity between two tensors can be made by taking the square root of the sum of squares of the differences between corresponding elements of the tensor array. This comparison is convenient because it takes into account differences due to both shape and orientation. The difference, or deviation, between FOD tensors a_{ij} and b_{ij} is calculated as follows:

$$\text{Dev} = 1/2 \sum_{i=1}^{3} \sum_{j=1}^{3} (a_{ij} - b_{ij})^2 \tag{6.10}$$

The factor of 1/2 normalizes the difference so that it ranges from 0 to 1. In Figure 1(a) the magnitude of the tensor difference is plotted as a function of the angle of rotation between two coplanar ellipses of various aspect ratios, representing planar fiber orientations of various degrees of alignment. Figure 1(b) is a similar plot, except that it compares the difference between an ellipse with an infinite aspect ratio (unidirectional alignment) and an ellipse of various aspect ratios. As the aspect ratios tend



(a) Two ellipses

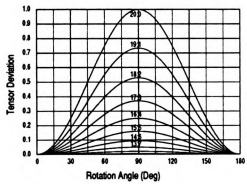


(b) Line w/ ellipse

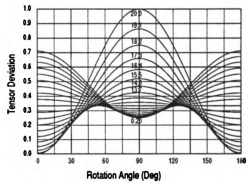
Figure 6.1: Planar ellipse tensor deviations.

toward unity the ellipses become circles (perfectly random planar fiber orientation) and the difference between the tensors becomes constant for all rotation angles.

Figures 6.2(a) and 6.2(b) are the three-dimensional equivalents of Figures 6.1(a) and 6.1(b). That is, Figure 6.2(a) represents the difference between two ellipsoids of



(a) Two ellipsoids



(b) Line w/ ellipsoid

Figure 6.2: Ellipsoid tensor deviations.

revolution of various aspect ratios rotated relative to each other. As the aspect ratios tend toward unity, the ellipsoids become spheres (perfectly random 3-D orientation),

and the difference between tensors becomes a constant for all rotation angles. As they continue toward zero aspect ratio, the ellipsoids become disks. Figure 6.2(b) represents a 3-D ellipsoidal distribution compared with a unidirectional distribution.

In all cases, the more similar in shape and orientation two ellipsoids are, the smaller is the tensor deviation value. Thus the tensor deviation provides a scalar measure of the difference between two fiber orientation distributions.

6.4.2 Qualitative Analysis (Fibor)

A qualitative representation of the data was obtained by viewing the fiber orientation distribution fields with **Fibor**.

6.5 Analysis of Mechanical Testing Data

Linear regression of the load-strain curves for the samples was used to determine Young's modulus. The regression was performed on the linear portion of the curve following any initial noise.

CHAPTER 7

RESULTS AND DISCUSSION

This chapter contains the results of the hardware tests, imaging tests, software calibration, fiber orientation analysis experiments, and a comparison with published results.

7.1 Apparatus

The results of experiments designed to test the capabilities of the hardware and optimization the injection process are presented in this section.

7.1.1 Performance

The injection mold was shown to be capable of withstanding injection pressures in excess of 2200 bar (32,000 psi), and wall temperatures in excess of 120 °C (248 °F). The maximum wall temperature was limited by the breakdown temperature of the heaters. The maximum internal cavity volume is approximately 9 x 3 x 1 cm (3.5 x 1.2 x 0.4 in).

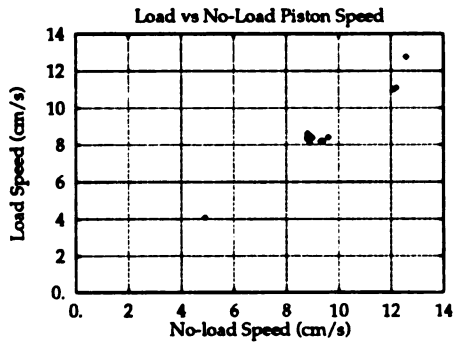
The injector with a 3.81 cm (1.5 in) diameter, 15.2 cm (6 in) stroke hydraulic cylinder was shown to be capable of injecting 1.7 in^3 of material at injection pressures of up to 2200 bar (32,000 psi), and flow rates up to 15 cm^3/s (0.9 in^3/s). An alternate

hydraulic cylinder with a 5.1 cm (2 in) bore raised the maximum injection pressure to 3900 bar (56,900 psi) and decreased the maximum flow rate to 8 cm^3/s (0.51 in^3/s). Similarly, a smaller diameter bore would increase the maximum injection rate while lowering the maximum injection pressure. The maximum barrel and nozzle temperatures were shown to be approximately 300 °C (572 °F).

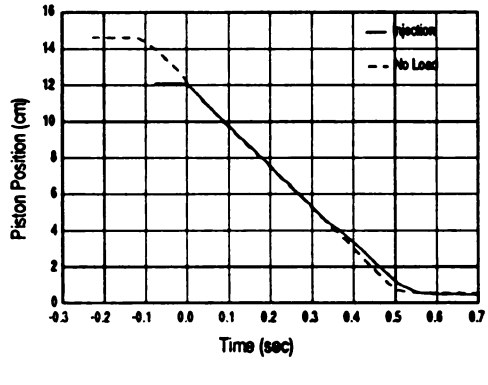
7.1.2 Hardware Repeatability (Variability in Processing Conditions)

This section demonstrates the degree of reproducibility and uniformity of the measured processing conditions, including piston speed, barrel temperatures, mold temperatures, and fiber lengths.

Figure 7.1(a) shows the difference between the actual piston speed during injection and no-load piston speed with an injection pressure of 1320 bar (19,200 psi). A speed reduction of about 10–20 percent is observed during injection due to the viscosity of the melt. A comparison of the piston position during no-load injection and an actual injection is shown in Figure 7.1(b). Time zero in this figure corresponds to the time



(a) Piston speed (load vs no load)



(b) Piston position profile

Figure 7.1: Piston speed data.

when the valve on the hydraulic cylinder power unit was actuated to direct the flow

of hydraulic fluid to the injection cylinder. During the initial 0.35 seconds, the loosely packed material is compacted. At this point the melt begins to be forced through the sprue and a brief decrease in the piston speed is observed. During the remainder of the mold-filling process the piston speed is slightly lower ($\approx$ 10% less) than the no-load speed.

The temperatures at various locations of the injection apparatus during the injections of the gate obstacle samples (Ob1–Ob9 and No1–No9) are shown in Figure 7.2. The first 9 injections were made with the gate obstacle in place, the second 9 injections

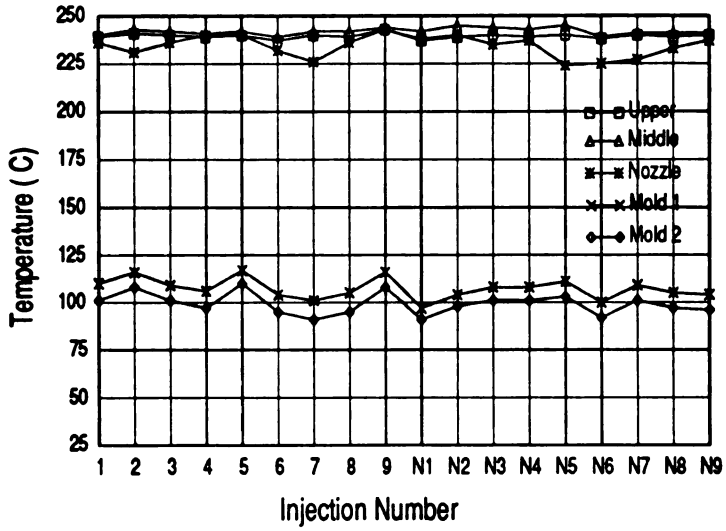


Figure 7.2: Injection temperatures for 18 injections.

were made without. The upper two curves, labeled 'Upper' and 'Middle', represent the barrel temperatures at 2.54 cm inch and 6.35 cm from the nozzle respectively. The third curve in the cluster, labeled 'Nozzle', represents the nozzle temperature. The lower 2 curves, labeled 'Mold 1' and 'Mold 2', represent the mold temperatures at 4.45 and 8.25 cm from the injection port. To a first approximation the barrel and nozzle are "isothermal" at about 230–240 °C, whereas the mold is isothermal at 100–120 °C. The reproducibility is of order $\pm$ 5–10 °C.

Figure 7.3 shows the temperature distribution inside the barrel for a typical injection compared with the externally measured barrel, nozzle, and mold temperatures.

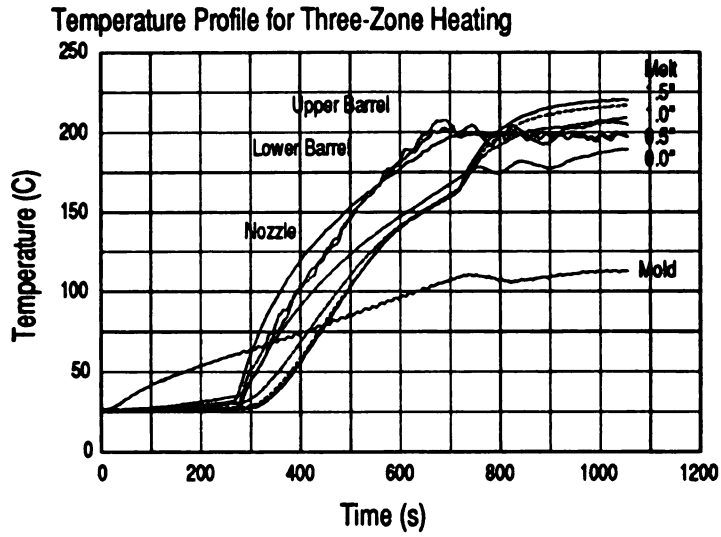
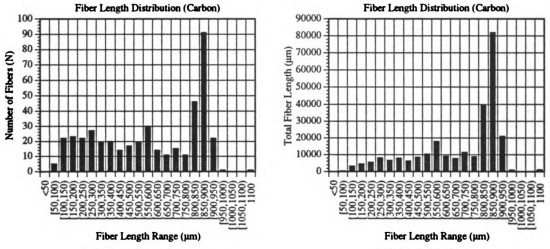


Figure 7.3: Temperature profile.

The injector and mold external temperatures are reached in approximately 12 minutes (700 seconds). At this point a distinct change in the slope of the melt temperatures are observed due to the melting of the plastic material. As the external temperatures are held for another 7 minutes, the melt temperatures begin to approach steady state. The thermocouple located in the nozzle was placed at the surface of the plastic, not embedded inside it as the others were. This accounts for the much lower temperature observed at this location. There is a temperature spread of about 20 °C between the other four locations, increasing with distance from the nozzle. It is also important to note that the average internal temperature is approximately 20 °C greater than the measured wall temperature. This must be taken into account when setting the thermostat settings and interpreting results.

The length distribution of carbon fibers before processing is shown in Figure 7.4. In subfigure (a) the vertical axis represents the number of fibers in each length range,



(a) Unweighted (b) Weighted

Figure 7.4: Fiber length distributions.

whereas in subfigure (b) the vertical axis represents the amount of fiber material in each range. The latter is more relevant to the presentation of the fiber orientation distribution since it is the amount of material, not the number of fibers, that is used to weight the fiber orientation distribution.

7.1.3 Optimization of the Injection Process

This section shows an example of the optimization of the injection process. Figure 7.5 shows a series of PMMA samples produced in the experimental apparatus. This type of optimization is required for each new material. The first three specimens did not completely fill the mold due to low injection temperature. The fourth specimen contains entrapped air, which was attributed to insufficient venting. The final specimen demonstrates the optimized results with good surface finish, absence of entrapped air, good transparency, and low shrinkage.

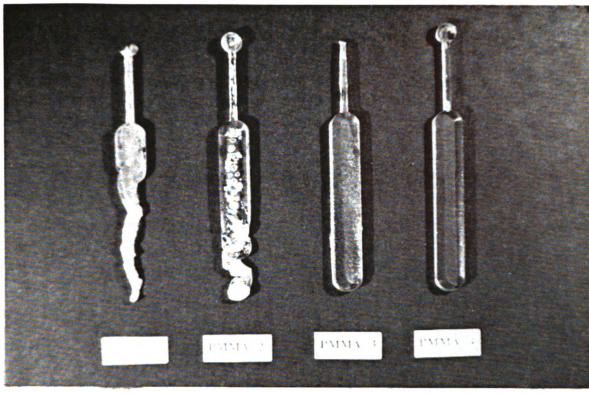


Figure 7.5: Optimization of neat PMMA molding.

7.2 Production of Transparent Composites

Table 7.1 lists some fiber/matrix combinations that were identified as having similar refractive indices and are, therefore, candidates for producing transparent composite

Table 7.1: Fiber/Matrix combinations with matched refractive indices.

Matrix	Fiber	Index (n)
Polymethyl-methacrylate	BK-10 Glass	1.49 ± 0.01
High-density Polyethylene	Quartz	1.55 ± 0.01
Acrylic styrene (NAS)	E-Glass	1.56 ± 0.01
Styrene acrylonitrile (SAN)	C-Glass	1.57 ± 0.01
Polystyrene	D-Glass	1.59 ± 0.01
Polysulfone	D-Glass	1.63 ± 0.01

materials. Appendix A contains a list of refractive index data of various thermoplastic materials.

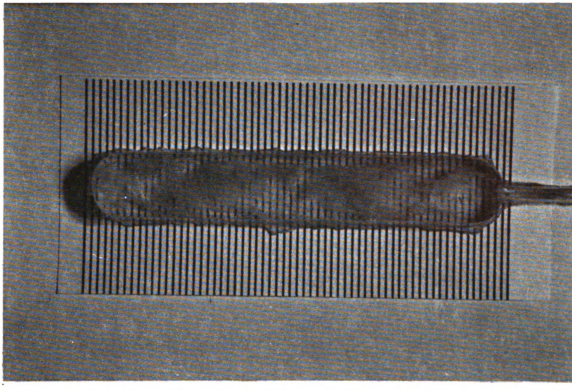


Figure 7.6: Sample composite with poorly distributed fiber material.

Figure 7.6 illustrates early attempts at mixing fiber and plastic materials. The clumping of fiber material was caused by excessive fiber length, which allowed the fibers to become entangled. By cutting the fibers shorter and blending them with powdered plastic, a uniform mixture was achieved.

The result of refractive index matching is illustrated in Figure 7.7. In this photograph the upper specimen is made of PMMA (n = 1.491) and 30 wt% BK-10 glass fibers (n = 1.498). Note that the transparency is quite good. The lower specimen was made with PMMA and 30 wt% E-Glass fibers (n = 1.56), a commonly used reinforcing fiber. Note that this combination produced an opaque sample. The refractive index matching tests with PMMA and BK-10 indicate that a mismatch of about 0.007 between the refractive indices of the constituent materials resulted in transparency adequate for optical sectioning in a 3 mm thick sample of PMMA with 30 wt% BK-10 glass fibers.

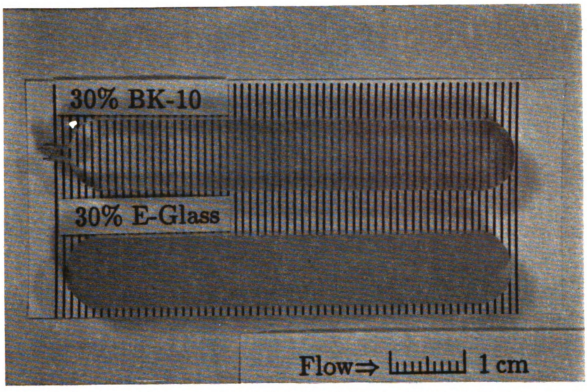


Figure 7.7: Transparency of PMMA w/BK-10 vs PMMA w/E-glass.

7.3 Software Calibration Results

This section presents the results of the software calibrations. These include results from simulated images as well as images of fibers with known orientations.

7.3.1 Pseudo Data

The following spherical plot is the result of the analysis of a pseudo data calibration image consisting of 81 fibers 10 μm in diameter and 600 μm in length oriented in the directions of the vertices of a twice-subdivided icosahedron. The voxel dimensions in the image were 3.3670 x 1.9930 x 10.0000 μm. A perfect analysis would have yielded a perfect sphere, with the accuracy limited by the voxel resolution. Figure 7.3.1 shows the actual FOD obtained from the analysis.

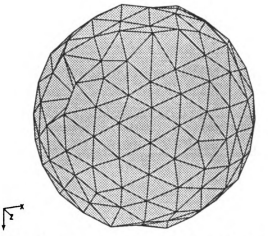


Figure 7.8: Calibration image: uniform fiber orientation distribution.

The tensor form of the measured FOD is:

$$Tensor = \begin{vmatrix} 0.3373 & -0.0014 & -0.0005 \\ & 0.3365 & -0.0012 \\ sym & & 0.3263 \end{vmatrix}$$

A perfectly uniform distribution is represented by a diagonal matrix with 0.3333 on the diagonals. The deviation (Equation 6.10 between the ideal and actual tensors is 0.0038 compared with a maximum possible deviation of 1, which is an excellent result.

The average measured fiber length was 576 μm, which is a 4% error. The thinning algorithm employed in the image analysis tends to shorten fibers by approximately one fiber diameter. Correcting for this bias gives an average measured fiber length of 586 μm, which is a 2.3% error with a standard deviation of 52.37 μm.

7.3.2 Single Fiber Tests

Tables 7.2 and 7.3 list the results obtained from optically sectioning two short horizontally-oriented carbon fibers in a sample of PMMA. The samples were rotated in the horizontal plane at 10 degree increments. The largest error in the orientation angle measurements for the two fibers is less than three degrees. The magnitude of

Table 7.2: x-y calibration - PMMA [Fiber 1].

True Angle (°)	Measured Angle (°)	Error Angle (°)	Measured Length† (μm)	Error (%)
0°	0.0	0.0	299.7	-1.3
10°	9.0	-1.0	296.6	-2.3
20°	18.0	-2.0	297.4	-2.1
30°	31.5	1.5	301.3	-0.8
40°	40.5	0.5	294.6	-3.0
50°	49.5	-0.5	301.4	-0.8
60°	58.5	-1.5	303.9	0.1
70°	72.0	2.0	295.5	-2.7
80°	81.0	1.0	298.6	-1.7
90°	90.0	0.0	295.0	-2.9

†True length = 303.7 μm

Table 7.3: x-y calibration – PMMA [Fiber 2].

True Angle (°)	Measured Angle (°)	Error Angle (°)	Measured Length† (μm)	Error (%)
25.2	27.0	1.8	374.1	1.7
35.2	36.0	0.8	366.2	-0.5
45.2	45.0	-0.2	366.4	-0.4
55.2	54.0	-1.2	379.4	3.1
65.2	67.5	2.3	364.6	-0.9
75.2	76.5	1.3	368.9	0.2
85.2	85.5	0.3	373.8	1.6
95.2	94.5	-0.7	373.8	1.6
105.2	103.5	-1.7	368.9	0.2
115.2	117.0	1.8	371.3	-0.9

†True length = 368.0 μm

these errors are in the range of the quantization error for the binning. The calculated angles prior to binning are expected to be more accurate than these results demonstrate, which means that the angle error would be reduced by binning on an icosahedron which has been further subdivided. The maximum error in the length measurement was approximately 3 percent. Note that the images for these calibrations were obtained under ideal circumstances. No overlapping of fibers was present and the images were very clean.

Table 7.4 presents the results obtained from optically sectioning a single carbon fiber in Norland Optical Adhesive 61.[1] The fiber was first oriented parallel to the

Table 7.4: z calibration – single fiber in epoxy.

	x-z Plane		y-z Plane	
True Angle (°)	Measured Angle (°)	Error Angle (°)	Measured Angle (°)	Error Angle (°)
-40°	-38.5	1.5	-38.4	1.6
-30°	-30.5	-0.5	-30.4	-0.4
-20°	-20.1	-0.1	-19.1	0.9
-10°	-10.2	-0.2	-10.8	-0.8
0°	0.0	0.0	0.0	0.0
10°	8.1	-1.9	10.8	0.8
20°	20.1	0.1	19.1	0.9
30°	31.7	1.7	31.0	1.0
40°	39.4	-0.6	38.4	1.6

imaging plane, and then rotated out of the imaging plane in 10 degree increments. The left half of the table shows rotations in the x-z plane, the right half shows rotations in the y-z plane. The specimen from which these images were obtained contained several additional fibers, some of which overlapped the fiber under investigation. Note that the error in the measurement of these out-of-plane angles was less than 2 degrees. The measured length of the fiber is not presented because the fiber was longer than the

[1]Norland Products, Inc., New Brunswick, N.J.

field of view and thus appeared to become longer with increasing angles of rotation. The range of rotation angles was limited to plus or minus 40 degrees due to physical interference between the specimen and the microscope objective.

Table 7.5 shows the results obtained from optically sectioning a single carbon fiber in air. In this case rotations were made in the x-z plane in 10 degree increments for

Table 7.5: x-z calibration with a single fiber in air.

True Angle (°)	Measured Angle (°)	Error Angle (°)
0	0.0	0.0
10	10.2	0.2
20	20.1	0.1
30	26.6	-3.4
40	38.5	-1.5
50	50.4	0.4
60	58.3	-1.7
70	70.2	0.2
80	78.1	-1.9
90	90.0	0.0

a total rotation of 90 degrees. The maximum error in the measured angles was 3.4 degrees. Similar results were found for the y-z plane.

7.3.3 Orthogonal Specimen

Figures 7.9 through 7.11 demonstrate the results obtained from scanning the same sample volume of a calibration specimen of PMMA with 30% BK-10 fibers and 0.1% carbon fibers from four orthogonal directions. Refer to Figure 5.1 for the location and geometry of the specimen.

Each set of four figures shows the same FOD viewed from the same reference direction. Each figure within a set was obtained from a different scan direction and

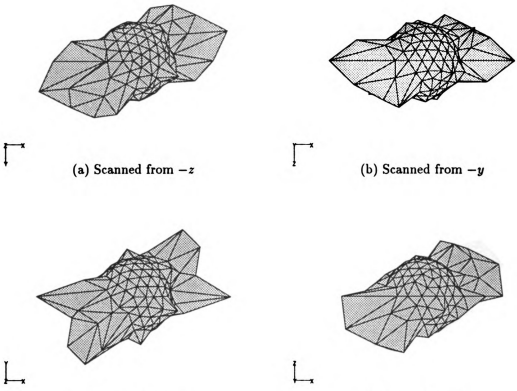
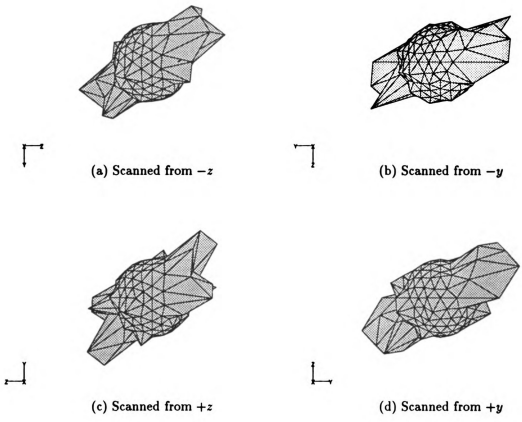


Figure 7.9: Orthogonal specimen viewed from the negative z axis.

then the results were transformed mathematically to a common reference orientation. Note that while the details of the FOD are not identical in each view, the basic shapes and orientations are similar. This result is significant because it was obtained from a sample with a high tracer fiber content and a complex fiber orientation distribution. Two sets of scans were performed at two different locations. The results presented here are from the worst case.

The following tensors are the ellipsoidal representations of the FODs measured from the first set of orthogonal scans presented in the preceding figures.



(a) Scanned from $-z$

(b) Scanned from $-y$

(c) Scanned from $+z$

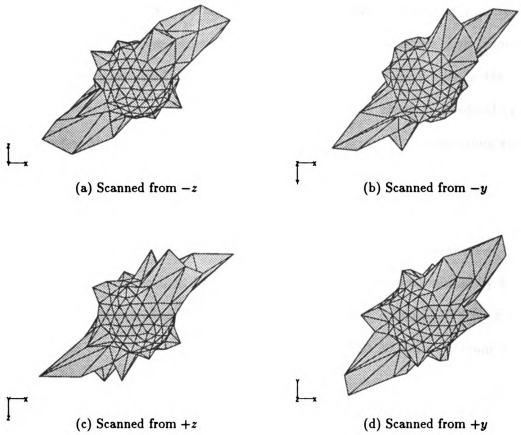
(d) Scanned from $+y$

Figure 7.10: Orthogonal specimen viewed from the positive x axis.

Tensors from first set of orthogonal scans:

$$-Z = \begin{vmatrix} 0.4730 & -0.1402 & 0.2800 \\ & 0.1985 & -0.1662 \\ sym & & 0.3284 \end{vmatrix}, \quad -Y = \begin{vmatrix} 0.4370 & -0.3062 & -0.0787 \\ & 0.4116 & 0.1321 \\ sym & & 0.1514 \end{vmatrix}$$

$$+Z = \begin{vmatrix} 0.4243 & 0.1423 & -0.2697 \\ & 0.2210 & -0.1705 \\ sym & & 0.3547 \end{vmatrix}, \quad +Y = \begin{vmatrix} 0.4096 & 0.2536 & 0.1222 \\ & 0.4137 & 0.1794 \\ sym & & 0.1767 \end{vmatrix}$$



(a) Scanned from $-z$ (b) Scanned from $-y$

(c) Scanned from $+z$ (d) Scanned from $+y$

Figure 7.11: Orthogonal specimen viewed from the negative y axis.

Tensors from second set of orthogonal scans:

$$-Z = \begin{vmatrix} 0.4467 & 0.1369 & -0.2546 \\ & 0.2425 & -0.1932 \\ sym & & 0.3107 \end{vmatrix}, \quad -Y = \begin{vmatrix} .3996 & 0.1419 & -0.2370 \\ & 0.2382 & -0.1872 \\ sym & & 0.3622 \end{vmatrix}$$

$$+Z = \begin{vmatrix} 0.4530 & 0.1275 & -0.2761 \\ & 0.2063 & -0.1846 \\ sym & & 0.3407 \end{vmatrix}, \quad +Y = \begin{vmatrix} 0.3854 & 0.1095 & -0.2708 \\ & 0.1953 & -0.1714 \\ sym & & 0.4193 \end{vmatrix}$$

Because the specimen was rotated about its x axis, the x components of the orientation tensors are expected to be similar, a result that is confirmed by a comparison of the upper-left elements of the tensors. If the imaging were free of any bias the

remaining tensor elements would also be very similar. However, examination of the remaining elements, especially the diagonal ones, shows a greater similarity between the tensors obtained from scans on opposite sides of the specimen than from scans on adjacent sides. This result suggests that there is some inherent bias in the imaging. Such a result is not surprising given that the resolution along the optical (z) axis is 7.5 times less than that in the y direction, and rotation of the specimen essentially reversed the y and z axes.

To evaluate the magnitude of the bias it is useful to examine a more easily interpreted description of the orientation tensor, such as the the orientation of the major axis of the tensor ellipsoid and the lengths of the major axes calculated by **DiffFOD**. The descriptive tensor characteristics are given in Tables 7.6 and 7.7. (See Figure 4.15 for the angle definitions.) The first column gives the in-plane rotation angle ϕ of

Table 7.6: Comparison of FOD tensors from the first set of orthogonal scans.

Scan Dir	Rot (ϕ)	Elev (θ')	Twist (β)	Maj	Int	Min
$-Z$	-25.79	30.02	-11.44	0.769	0.158	0.072
$-Y$	-18.79	34.97	-7.60	0.767	0.156	0.077
$+Z$	-29.35	33.03	-6.57	0.752	0.156	0.092
$+Y$	-28.78	36.87	-9.97	0.746	0.175	0.079
Combined	-25.70	33.64	-9.71	0.755	0.160	0.085

Table 7.7: Comparison of FOD tensors from the second set of orthogonal scans.

Scan Dir	Rot (ϕ)	Elev (θ')	Twist (β)	Maj	Int	Min
$-Z$	30.93	31.06	-20.75	0.746	0.192	0.062
$-Y$	33.70	34.94	-28.02	0.728	0.174	0.098
$+Z$	27.54	31.95	-25.78	0.763	0.177	0.060
$+Y$	28.59	38.21	-27.68	0.747	0.162	0.091
Combined	30.19	34.04	-25.56	0.746	0.176	0.078

the major axis with respect to the x axis. The second column gives the out-of-plane elevation angle $\theta' = \frac{\pi}{2} - \theta$ of the major axis with respect to the x-y plane. The third column gives the rotation, or twist, of the intermediate axis about the major axis. The remaining three columns give the lengths of the major, intermediate and minor axes respectively.

A further comparison of the tensors was made by combining the FODs from the four scan directions to obtain a composite result which was compared with the individual tensors. The results are shown in Tables 7.8 and 7.9. The columns in this

Table 7.8: Differences between combined and individual tensors from first orthogonal scans.

Scan Dir	Rot (ϕ)	Elev (θ')	Twist (β)	Maj	Int	Min	Diff
$-Z$	-0.09	-3.62	-1.73	0.015	-0.002	-0.012	0.002
$-Y$	6.91	1.33	2.10	0.012	-0.004	-0.008	0.005
$+Z$	-3.65	-0.61	3.13	-0.002	-0.004	0.007	0.001
$+Y$	-3.08	3.23	-0.27	-0.009	0.015	-0.006	0.002
Average	3.43	2.20	1.81	0.010	0.006	-0.008	0.003

Table 7.9: Differences between combined and individual tensors from second orthogonal scans.

Scan Dir	Rot (ϕ)	Elev (θ')	Twist (β)	Maj	Int	Min	Diff
$-Z$	0.67	-2.87	4.17	0.002	0.016	-0.018	0.002
$-Y$	3.43	1.01	-3.10	-0.015	-0.003	0.018	0.001
$+Z$	-2.73	-1.98	-0.86	0.020	0.000	-0.020	0.001
$+Y$	-1.68	4.28	-2.77	0.003	-0.014	0.011	0.004
Average	2.13	2.54	2.73	0.010	0.008	0.017	0.002

table are similar to those of the preceding tables except that the angles and lengths are the differences between the composite and individual tensors, rather than absolute measurements. Also, there is an additional column containing the tensor deviation,

which is the square root of the sum of the squares of the differences between the individual tensor components, divided by two. The maximum possible deviation between two tensors is 1. The maximum difference in the angle measurements is less than 7 degrees (average 3.43 degrees), and the maximum major axis length difference is 0.020, which is 2 percent of the worst possible case. This indicates that observed bias does not have a strong influence on the orientation measurements, at least for the range of fiber orientations present in the calibration specimen. An error of less than 7 degrees in the fiber orientation distribution is probably adequate for most applications.

As a final test between the orthogonal specimens, the total measured fiber length from each scan was summed in Figure 7.10. The maximum length difference for

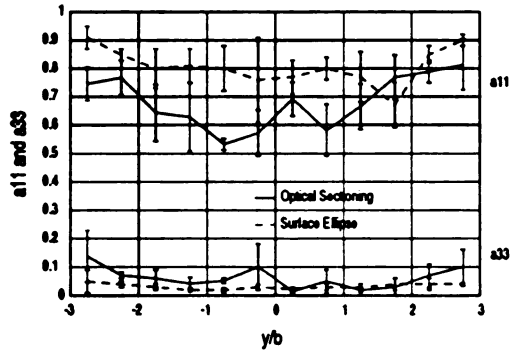
Table 7.10: Total fiber lengths from orthogonal scans (μm).

Dir	Ortho1	Ortho2
$-Z$	18,463	19,444
$-Y$	18,950	19,919
$+Z$	19,483	18,611
$+Y$	18,224	18,485

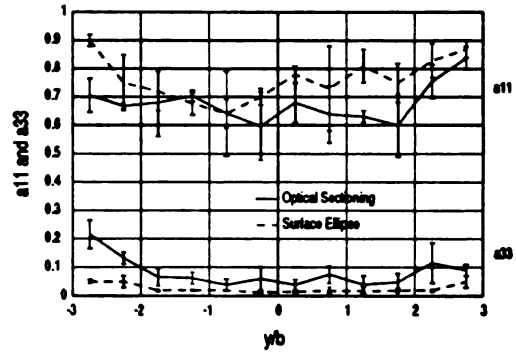
Ortho1 is 6.5%, and for Ortho2, 7.2%. This suggests that the fibers had approximately equal visibility from all directions.

7.3.4 Comparison of Surface Ellipse and Optical Sectioning Methods

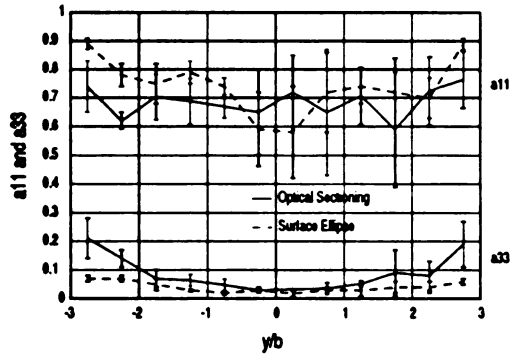
Figures 7.12 and 7.13 show comparisons of tensor components a_{11} and a_{33} acquired by the optical sectioning and the surface ellipse methods from specimens No8 and Ob7 as functions of depth (z component). Both specimens contained 20 wt% BK-10 glass fibers and 0.1 wt% carbon fibers. The tensor component a_{11} is a measure of the degree



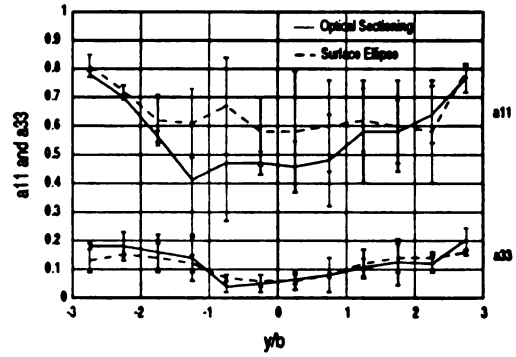
(a) Surface at $z/b = 0.94$



(b) Surface at $z/b = 0.75$

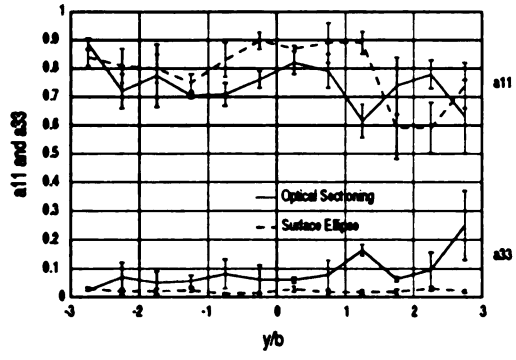


(c) Surface at $z/b = 0.56$

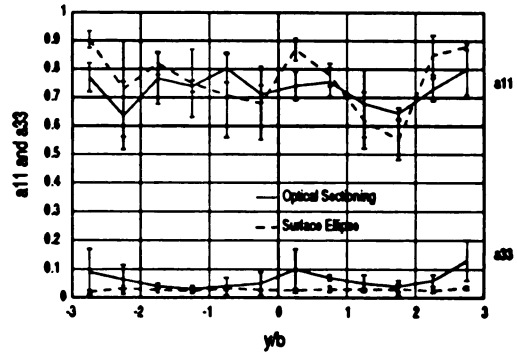


(d) Surface at $z/b = 0.12$

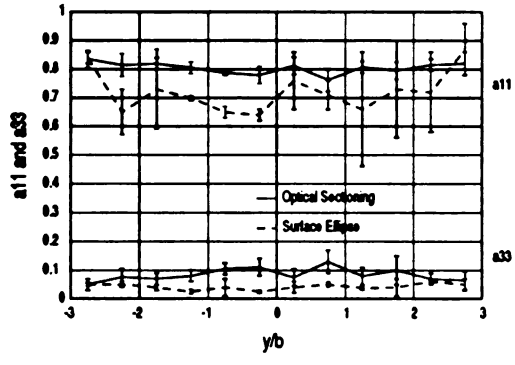
Figure 7.12: Optical sectioning versus surface ellipse method: specimen No8.



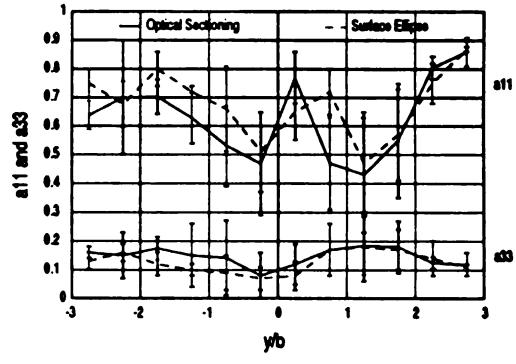
(a) Surface at $z/b = 0.94$



(b) Surface at $z/b = 0.75$



(c) Surface at $z/b = 0.56$



(d) Surface at $z/b = 0.12$

Figure 7.13: Optical sectioning versus surface ellipse method: specimen Ob7.

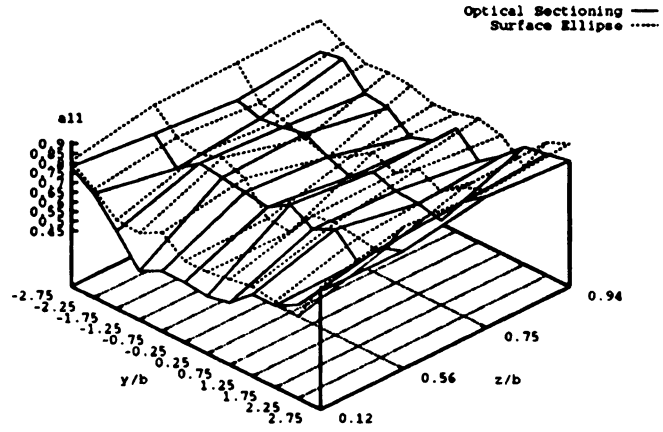
of orientation in the flow direction, and a_{22} is a measure of the degree of orientation in the transverse (width) direction. A value of 1 represents perfect alignment in the specified direction, while a value of 0 represents no alignment in that direction.

The horizontal axis represents the lateral y/b scan location. The vertical axis represents the magnitude of the tensor components. Each set of four plots is presented in order of increasing depth into the sample. The original (unpolished) surface of the sample corresponds to $z/b = 1$, and the midplane of the sample corresponds to $z/b = 0$. Portions of the curves show statistically significant differences in the measurements, but there do not appear to be any strong trends in the differences between the measurements. The optical sectioning method gave somewhat lower values for a_{11} and higher values for a_{33}, but the opposite case is observed in some of the curves. The optical sectioning method also tended to predict higher a_{33} values near the edges of the sample. These results suggest that the measurements made by optical sectioning are consistent with the results obtained from surface measurements. This is the expected result given that the fiber orientation distributions did not contain strong z components, which is the best condition for accurate measurements by surface analysis.

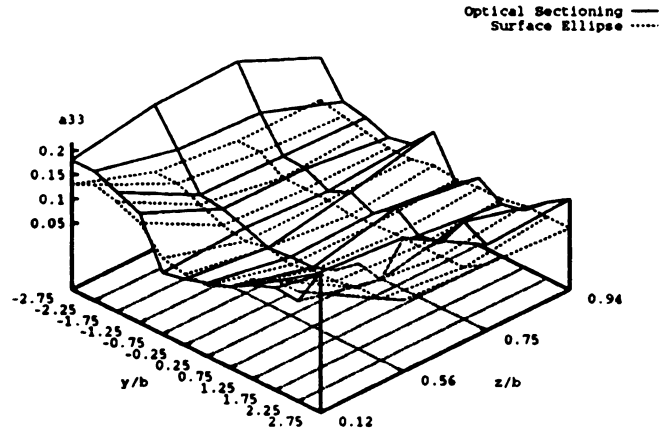
Figures 7.14 and 7.15 present results of the previous plots combined into surface contours for a global comparison of variations of the tensor components with respect to depth. The solid and dotted grids represent data obtained by the optical sectioning and and surface ellipse methods respectively.

7.4 Variability in Imaging

The graphs in Figure 7.16 are the results of the imaging repeatability experiments. The six orientation tensor components are given as functions of dimensionless pen-

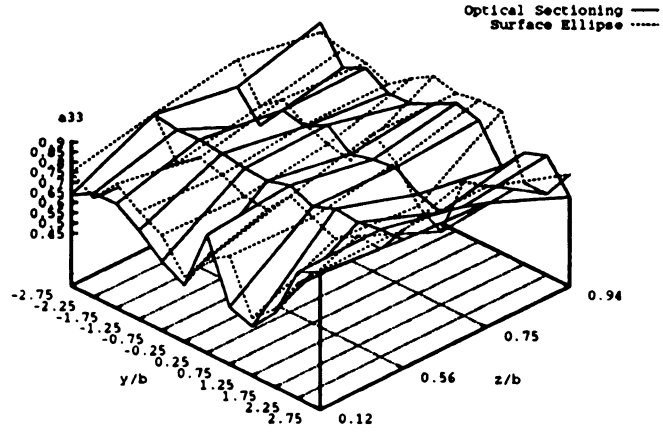


(a) a_{11} measurements.

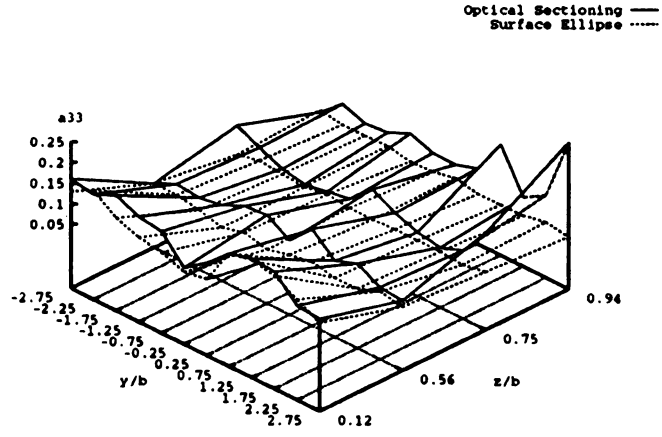


(b) a_{33} measurements.

Figure 7.14: 3-D view of a_{11} and a_{33} tensor components from specimen No8.

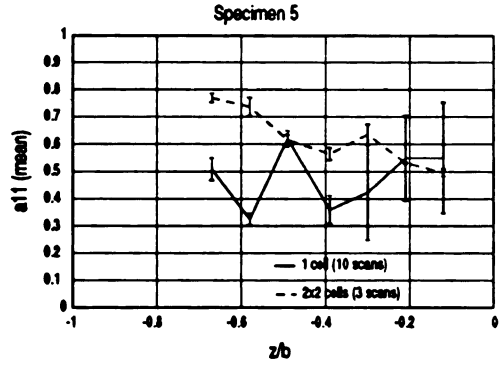


(a) a_{11} measurements.

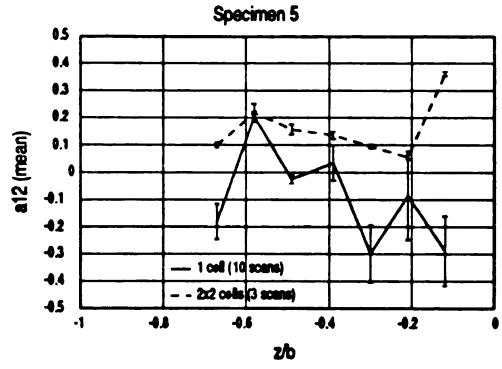


(b) a_{33} measurements.

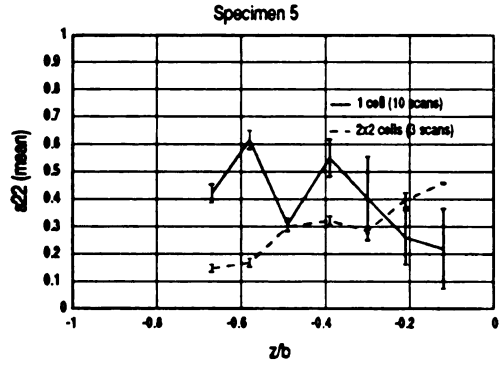
Figure 7.15: 3-D view of a_{11} and a_{33} tensor components from specimen Ob7.



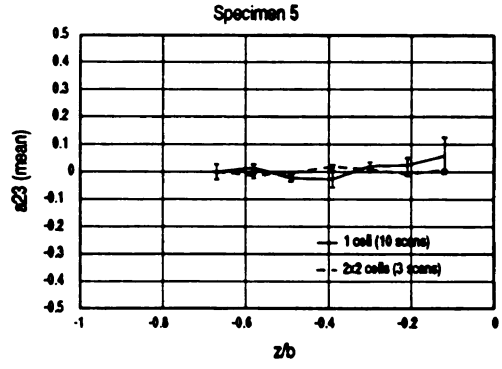
(a) a_{11}



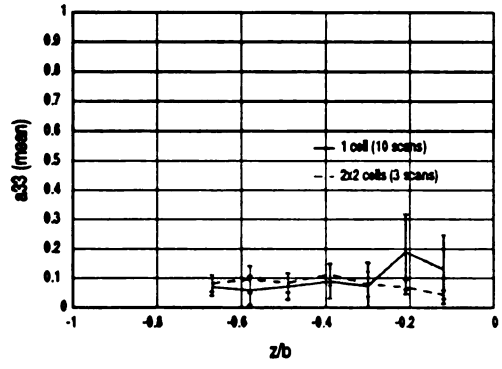
(b) a_{12}



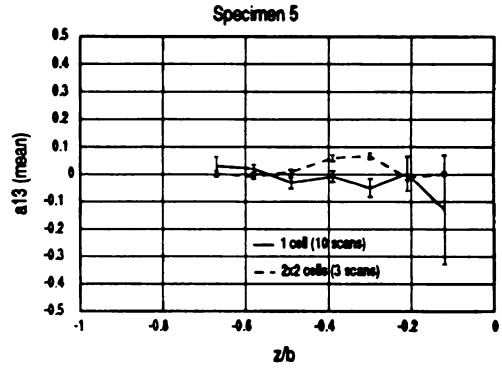
(c) a_{22}



(d) a_{23}



(e) a_{33}



(f) a_{13}

Figure 7.16: Repeatability of imaging.

etration depth. The solid lines represent data obtained from a single x-y location scanned 10 times and combined into an average result. The dashed lines represent data obtained from four adjacent scan locations sharing a common corner at the center of the single scan location, each scanned 3 times and combined. The scan pattern is illustrated in Figure 7.17.

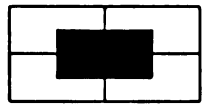


Figure 7.17: Scan pattern for imaging repeatability experiments.

Direct comparisons between the single cell results and the 2x2 cell results have limited validity since the 2x2 cells cover an area four times as large as the single cell scans. However, since the scans were made in the same vicinity, the results are expected to be similar under the assumption of continuously varying orientation fields. The quantity of greatest interest is the standard deviation of the various measurements which result from variations in lighting conditions. These variations are quantified by the error bars. It is apparent from the data that averaging the results of four adjacent scans reduces the variability considerably. The erratic behavior of the mean values of the single cell scans is probably an indication of insufficient tracer fiber density which can be overcome by averaging adjacent scans. There were an estimated 35 fibers per cubic micron in the sample images as opposed to Davis' (1988) results, for example, in which 60–175 fibers per surface image were reported. The cost of averaging is the reduced spatial resolution of the fiber orientation distribution field. However, the benefits of averaging can be realized without a loss of spatial resolution if the orientation field can be assumed to be locally invariant with respect to one axis. In that case a series of adjacent scans could be made in the direction of invariance and combined to give an average result. This type of averaging was used with the

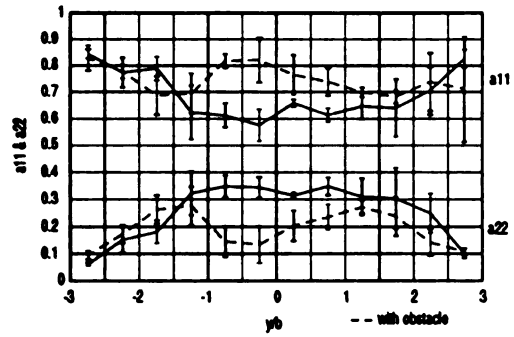
gate obstacle specimen analysis to provide a larger sample population of tracer fibers and thereby reduce the variability of the data.

7.5 Influence of a Gate Obstacle on Fiber Orientation Distribution

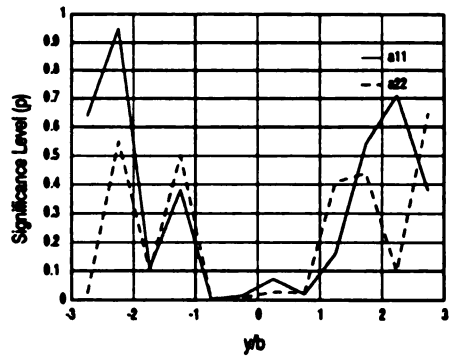
This section presents the results of the 18 specimens designed to illustrate the influence of an obstacle located within the gate of the mold. The plots in the left column of Figure 7.18 show the x and y related orientation tensor components (a_{11} and a_{22}) across the width of the specimens near the gate end ($x/b = 5.7$). The right column shows the level of significance (p value) of the difference between the obstacle and no obstacle results. Portions of the curve which are less than 0.10 indicate a statistically significant difference at an α level of 0.10. The solid curves were generated from specimens made without the gate obstacle, the dashed curves were generated from specimens made with the gate obstacle. Each curve was constructed from the combined data from 3 specimens. Each specimen was scanned across its width in three adjacent rows and the data were combined into one representative row. Thus each curve contains data from 9 sets of scans. See Figure 5.6 for a complete description of the scan locations.

Each plot shows that the fibers tend toward a unidirectional orientation in the flow direction near the edges of the samples. Perfect alignment in the flow direction corresponds to $a_{11} = 1$. Toward the middle of the samples ($y/b = 0$) the orientation becomes less aligned in the flow direction and tends toward a random orientation. The presence of the gate obstacle increased the alignment of the fibers near the middle of the sample presumably by increasing the shear forces in the gate.

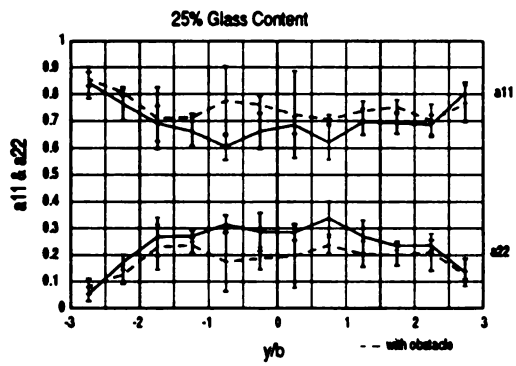
Figures 7.19–7.24 are a graphical representation of the fiber orientation tensors from which the plots in Figure 7.18 were derived. The flow direction is from left to



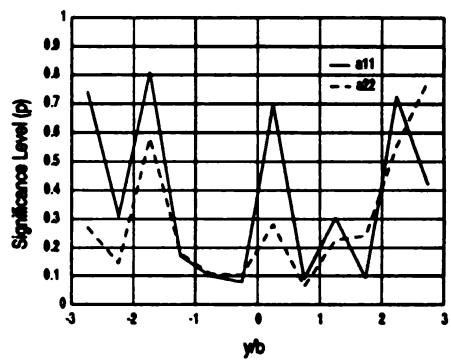
(a) 20% glass content



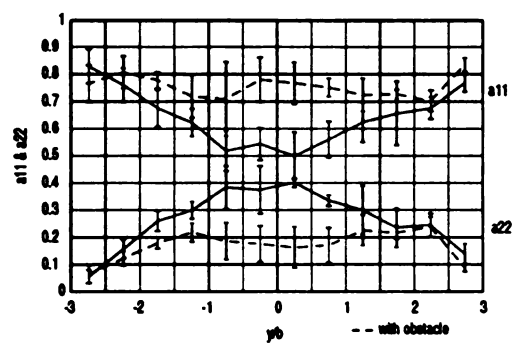
(b) 20% glass content



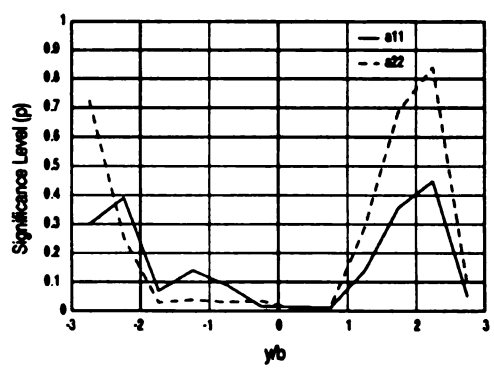
(c) 25% glass content



(d) 25% glass content



(e) 30% glass content



(f) 30% glass content

Figure 7.18: Tensor components of specimens with and without obstacle, (a), (c), and (e). Significance levels, (b), (d), and (e).

right. The high degree of alignment near the sides of the specimen as well as the increasing randomness of the fiber orientations toward the midline of the specimen are clearly visible.

Figures 7.19–7.21 are the results obtained from $z/b = 0.72$ to 0.53 at a distance of $x/b = 5.7$ from the gate. Note that the ellipses located near the centerline have a larger aspect ratio in the specimens made with the gate obstacle, indicating a higher degree of alignment.

Figures 7.22–7.24 show similar results obtained at half the length of the specimen from the gate ($x/b = 57$) and near the surface ($z/b = 0.72$ to 0.53).

Figures 7.25–7.27 are results from the same longitudinal position as Figures 7.22–7.24, but starting at a depth of 600 μm into the sample ($x/b = 57$, $z/b = 0.53$ to 0.34).

These results show that the presence of an obstacle in the gate induces a greater degree of alignment in the flow direction in the core region and that this alignment persists far downstream of the gate. If the flow were fully developed, there would be no difference between the specimens with and without the obstacle. It appears that the orientation that is induced at the gate is convected downstream with little modification, which is consistent with a plug flow condition.

7.6 Influence of a Gate Obstacle on the Modulus of Elasticity

The results of the tensile tests are given in Figure 7.28. The results show that the modulus increased with increasing fiber content and that specimens produced with the gate obstacle were generally stiffer than those without. The differences between the modulus values for the specimens with 25 and 30 wt% fibers were statistically significant at an α level of 0.05. These results are consistent with the observed

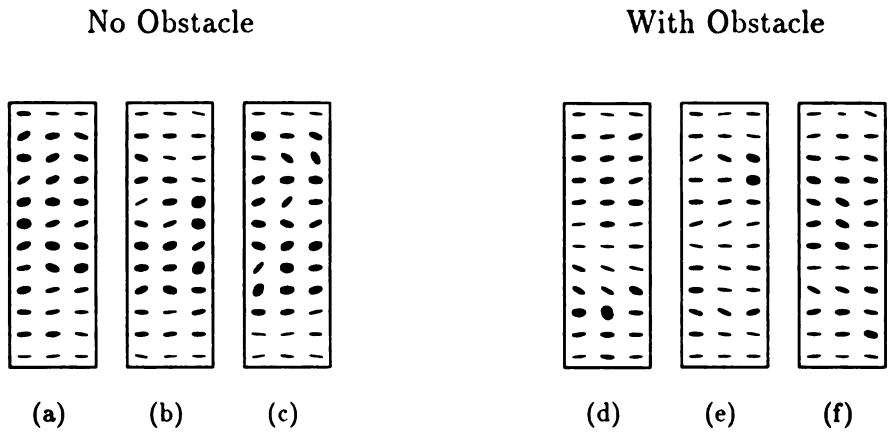


Figure 7.19: FODs at $x/b = 5.7$ from $z/b = 0.72$ to 0.53 for specimens with 20% glass.

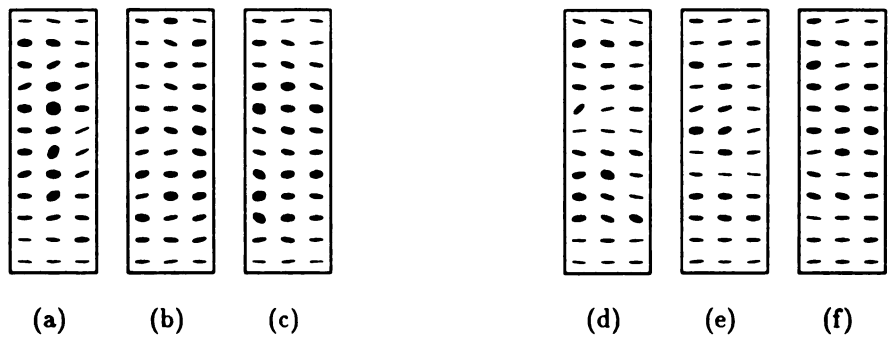


Figure 7.20: FODs at $x/b = 5.7$ from $z/b = 0.72$ to 0.53 for specimens with 25% glass.

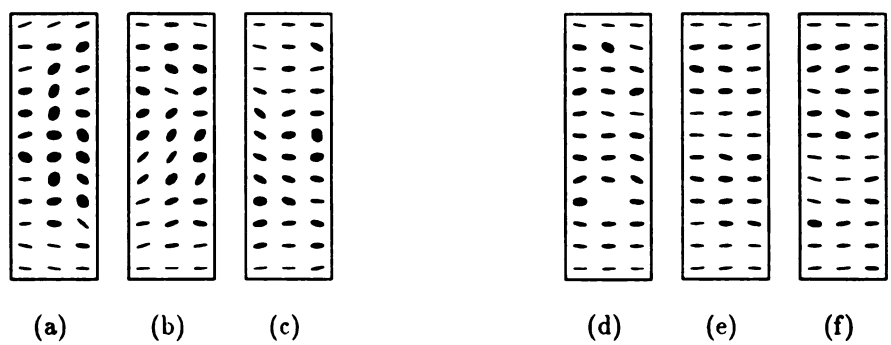


Figure 7.21: FODs at $x/b = 5.7$ from $z/b = 0.72$ to 0.53 for specimens with 30% glass.

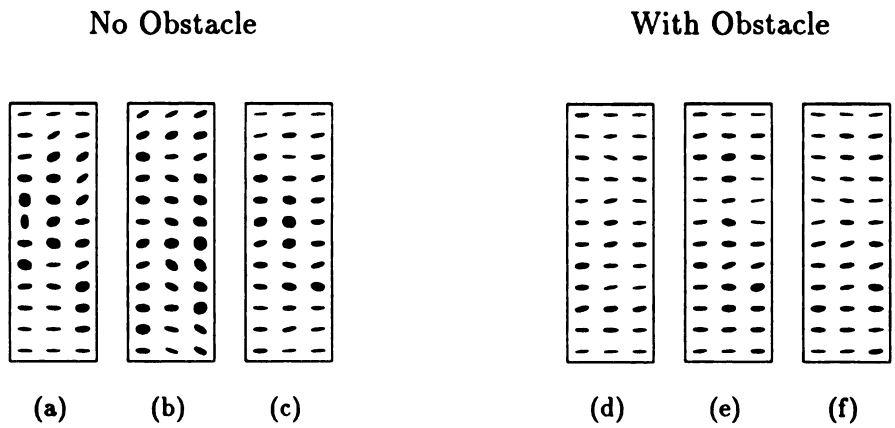


Figure 7.22: FODs at $x/b = 34$ from $z/b = 0.72$ to 0.53 for specimens with 20% glass.

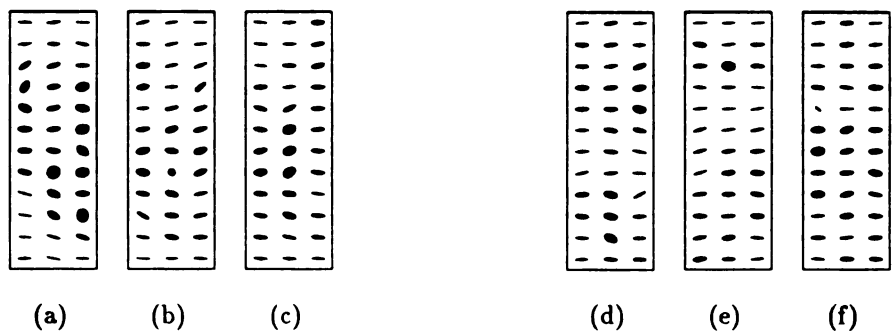


Figure 7.23: FODs at $x/b = 34$ from $z/b = 0.72$ to 0.53 for specimens with 25% glass.

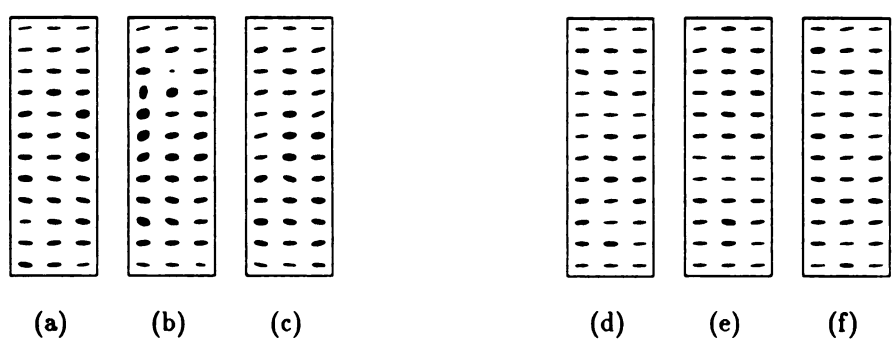


Figure 7.24: FODs at $x/b = 34$ from $z/b = 0.72$ to 0.53 for specimens with 30% glass.

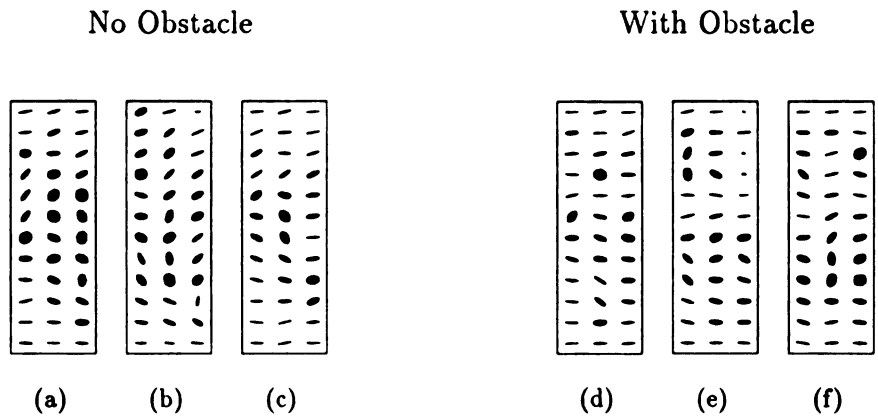


Figure 7.25: FODs at $x/b = 34$ from $z/b = 0.53$ to 0.34 for specimens with 20% glass.

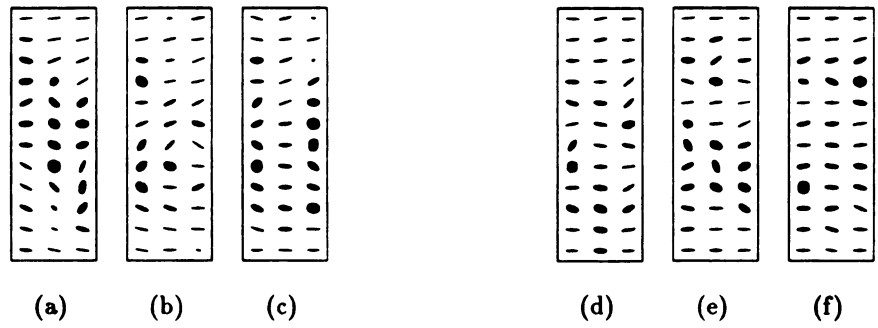


Figure 7.26: FODs at $x/b = 34$ from $z/b = 0.53$ to 0.34 for specimens with 25% glass.

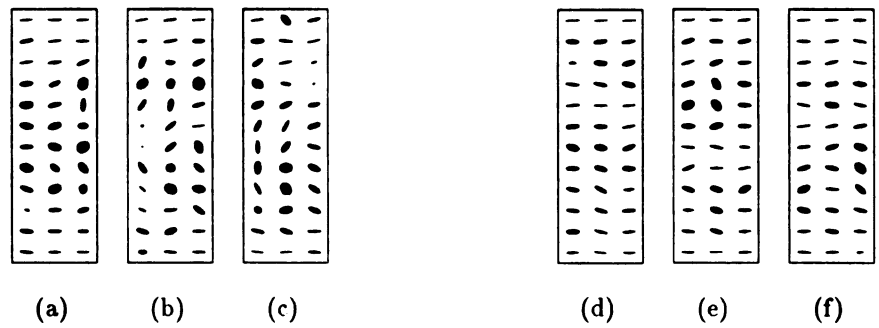


Figure 7.27: FODs at $x/b = 34$ from $z/b = 0.53$ to 0.34 for specimens with 30% glass.

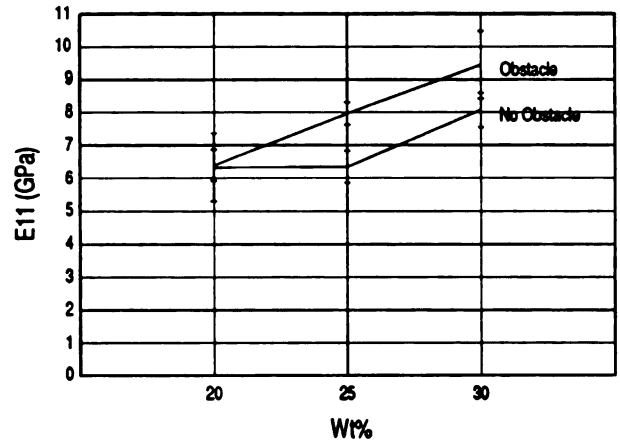


Figure 7.28: Young's modulus of gate obstacle specimens.

difference in fiber orientation. Specimens with greater alignment in the longitudinal direction were stiffer in uniaxial tension than those with less alignment.

Blumentritt, Vu, and Cooper's 1974 results for unidirectional short fiber composites provide a useful comparison of fiber efficiency. The results reported by Blumentritt et al. are for PMMA composites with 10 μm diameter, 6.35 mm long glass fibers. Note that these fibers are approximately 7 times longer than the fibers used here. The Young's modulus for 20 wt% fibers was reported to be 10.5 GPa, compared with 6.3 GPa observed here for specimens with and without the gate obstacle. The Young's modulus for 30 wt% fibers was reported to be 15.0 GPa, compared with 8.07 GPa for specimens without the obstacle, and 9.45 GPa for specimens with the obstacle. The lower modulii reported here are due to non-unidirectional fiber orientation and shorter fiber lengths.

7.7 Comparison of z Component Measurement With Published Results.

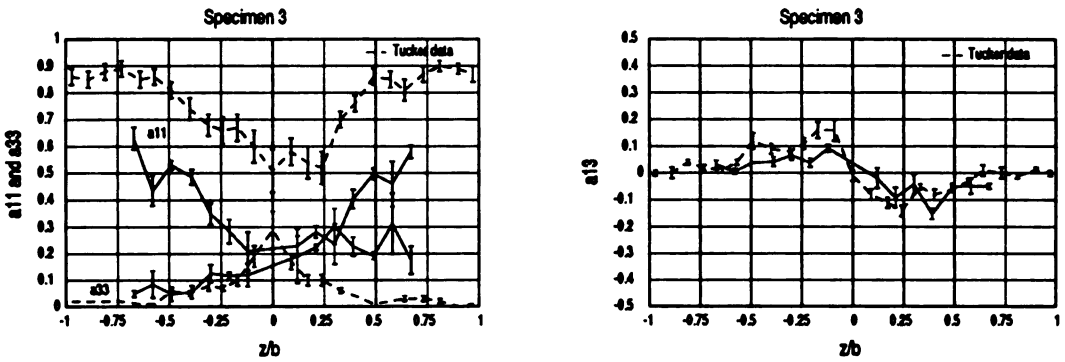
This section presents a comparison of x and z component measurements with results found in the literature. Comparisons were made with results obtained by Bay and Tucker (1991), and Davis (1988). It should be noted that the experimental conditions were not identical and so the results are not expected to be identical, but are expected to show similar trends and patterns. A comparison of the processing conditions under which the specimens were produced are listed in Table 7.11.

Table 7.11: Comparison of processing conditions.

	Wille	Bay & Tucker	Davis
Matrix material	PMMA	Nylon 6/6	Nylon 6/6
Fiber content (wt%)	30	43	33
Fiber length (μm)	900	210	230
Fiber diameter (μm)	13	11	11
Cavity length (mm)	82.5	203	203
Cavity width (mm)	10.3	25.4	25.4
Cavity depth (mm)	3.18	3.18	3.18
Barrel temp. (°C)	240	276	282
Mold temp. (°C)	100	24	24
Flow rate (cm^3/s)	19	49	6
Gz	207	114	272
Br	3.8	0.02	4.2
Pn	5.7	6.0	9.9

It should be noted that the literature results were obtained by cutting the samples in the x-z plane, whereas the results obtained here were from a series of x-y optical sections, perpendicular to the plane of interest. Nevertheless, similar fiber orientation patterns were measured.

Figure 7.29 is a comparison of specimen No3 with Bay and Tucker's results. These plots give the a_{11}, a_{33}, and a_{13} components of the orientation tensor as functions of depth. These data were obtained near the gate end of the specimen. The data for



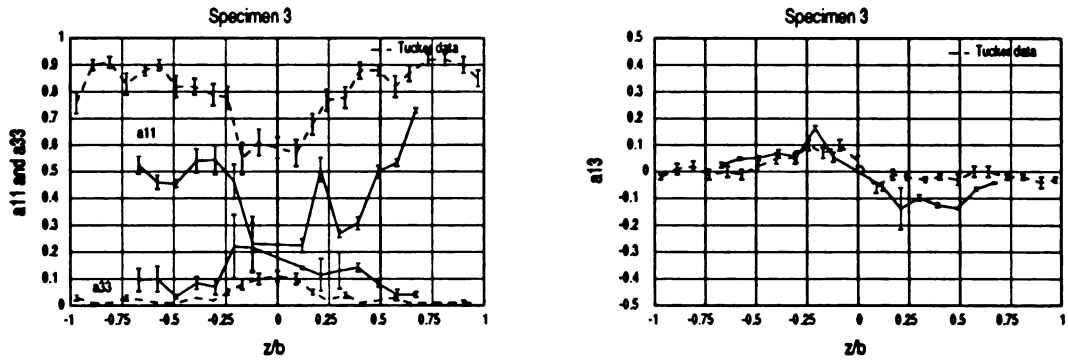
(a) a_{11} and a_{33}.

(b) a_{13}

Figure 7.29: Comparison of specimen No3 at $x/b = 5.7$ with Bay & Tucker results.

Specimen 3 do not extend to the surfaces because the surface material was removed by polishing. Note that while the magnitude of a_{11} is different for the two experiments they both tend toward unity at the surfaces and reach a minimum near the midplane. The lower value of a_{11} measured here may be due to the much longer fibers and narrower cavity width used here which would tend to restrict the rotation of the fibers, preventing them from becoming as flow-aligned as their counterparts in the literature. The a_{33} results are similar on one half of the specimen, but differ dramatically on the other half. This is an unexpected result with no immediate explanation. The a_{13} results are very similar and possess a shape indicative of a parabolic orientation profile.

Figure 7.30 contains plots similar to those in Figure 7.29. The difference is that these data were collected farther from the gate. The shapes of the curves are nearly identical to the previous set, with the exception that the a_{33} curve does not exhibit the unexpected result seen in the previous plot. The striking similarity between the curves obtained at different distances from the gates indicates that either the flow is fully developed shortly after exiting the gate or there is a plug flow condition.



(a) a_{11} and a_{33}.

(b) a_{13}

Figure 7.30: Comparison of specimen No3 at $x/b = 34$ with Bay & Tucker results.

A comparison of the a_{11} and a_{33} orientation tensor components for Specimen 1 and Davis' results is shown in Figure 7.31.

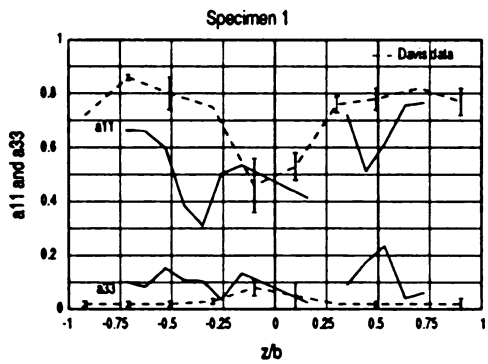


Figure 7.31: Comparison of specimen No1 at $x/b = 7$ with Davis results.

A data point at $z/b = 0.27$ was removed due to the presence of a large fiber clump which produced a large bias in the measurement.

As in the previous plots, the shapes of the curves are somewhat similar, and the a_{11} components measured here are lower than the published results. This is consistent with the reason suggested earlier for the difference in results since Bay and Tucker, and Davis used the same fiber length and cavity width.

7.8 Influence of a Cavity Obstacle

Figure 7.32 is a photograph of the specimen with an obstacle in the cavity. Note the fiber pattern around the hole and the knit line downstream of it. Figure 7.33 is a projection of the measured orientation ellipsoids onto the x-y plane obtained from specimen Obm2 (30 wt% glass, 0.1 wt% carbon) generated by **Fibor**.

The knit line is visible as a line of very thin ellipses oriented along the centerline indicating a highly aligned fiber orientation. Notice also the high degree of fiber alignment present between the obstacle and the walls of the specimen.

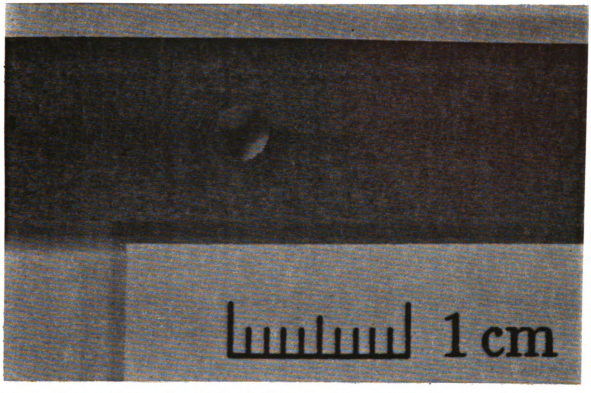


Figure 7.32: Photograph of FOD field resulting from flow around an obstacle (x-y plane of Obm2).

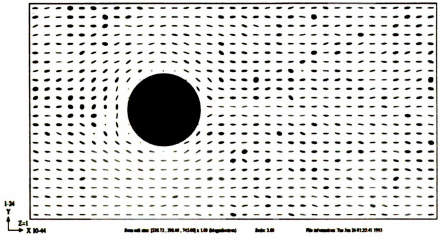


Figure 7.33: Projection of measured FOD ellipsoids on x-y plane (Obm2).

CHAPTER 8

CONCLUSIONS AND RECOMMENDATIONS

8.1 Evaluation of the Injection Apparatus

The fiber chopper was found to be useful in the preparation of the fiber materials, although it was slower than would be desired. It performed very well with little operator intervention for unbroken fiber tows. However, the BK-10 fibers were supplied in short lengths of badly frayed tows which required frequent operator assistance. The fiber length analysis showed that it produced fibers of the desired length with a relatively small length distribution. For future work, longer, smoother fiber tows and a faster fiber chopper would be desirable for more rapid production of specimens.

The injection mold proved to be reliable and versatile. Several different mold cavities were used with very little effort and cost. The acquired temperature data exhibited some variability due to electrical noise from the hydraulic power unit and non-ideal thermal contact of the thermocouples with the barrel and mold walls. Recommendations include using higher wattage heaters to reduce heat-up time, a solid lower clamping plate for greater stiffness, a hydraulic clamping device to close the mold for faster setup and takedown time, and surface mounted pressure transducers inside the mold.

The injector also proved to be reliable and well-suited for the application. The maximum speed, temperature and pressure were more than adequate for the experimental work. Repeatability of speed, pressure and temperature were good. Recommendations include using a speed transducer rather than a position transducer, and a better method for attaching thermocouples for more precise temperature control. More sophisticated controls on the hydraulic unit would allow variable pressure and speed during injection.

The cost of the final construction of the injection apparatus was well under $4,000, including the hydraulic unit, hydraulic cylinder, barrel, nozzle, piston, heaters, frame and transducers. The amount of waste material generated during a typical injection was about 4.0 gm, or 54% for a 3.7 gm specimen.

Polypropylene samples were very easy to mold and gave good results with little effort. PMMA was more difficult, but with carefully controlled temperature and injection speed, good samples with very few voids were produced. Some difficulty was encountered with achieving good surface finish with PMMA, but polishing the samples was a satisfactory solution.

The apparatus was shown to be very versatile for studying injections of a variety of materials under a variety of conditions.

The strengths of the apparatus include the ability to handle high fiber content materials, flexibility, low waste production, low cost, optical accessibility, and low fiber breakage. The weaknesses of the apparatus include the absence of a mixing screw, its discontinuous mode of operation, and the limitation of its cavity shape to planar geometries.

8.2 Evaluation of the Imaging Apparatus

The imaging apparatus proved to be adequate for the task, but higher resolution in the optical axis direction and greater ability to exclude out-of-focus information would be very desirable to allow increased tracer fiber density. Confocal microscopy should be considered as an alternative imaging method. Nevertheless, the resolution and discrimination of the microscope in the optical axis direction were sufficient to obtain accurate out-of-plane orientation data. The servos and motion control system were invaluable in performing countless hours of scanning.

The main difficulties encountered in the imaging process were the presence of fiber clumps, shadows, and uneven illumination due to the variable transmissivity of the sample materials. The problem of fiber clumps has since been resolved by blending the tracer fibers with distilled water and powdered plastic and then drying it prior to introducing it into the barrel. The shadow problem could likely be reduced by more diffuse lighting conditions. More uniform optical properties of the sample materials could likely be achieved by better mixing of the melt, perhaps in a screw-type injection molding machine. If sufficient uniformity is unachievable, localized histogram equalization of the digitized images could be used to compensate.

The accuracy of the imaging data was observed to decrease with increasing penetration depth. This problem could be alleviated somewhat by using confocal microscopy which reduces out-of-plane information and may provide a narrower depth of field.

The repeatability studies showed that operator judgment can have some influence on the measured fiber orientation distribution. For this reason it is important to find a reliable method of providing uniform, consistent illumination. Adaptive lighting

could be achieved with the computer controlling the intensity of the illumination based on analysis of the acquired images.

The frame grabber was the limiting factor in the speed of image acquisition. The main reason for this was that it was an external device which transferred the data to the computer via the parallel port. An internal frame grabber attached directly to the computer's data bus could decrease the imaging time by an order of magnitude.

The strength of optical sectioning is that it can provide a complete, unambiguous representation of the 3-D structure of a material. This means that the fiber orientation distribution can be evaluated as a function of position inside the material, and fiber length and curvature can be measured. The 3-dimensionality of the fiber orientation in injection molded composites requires a method capable of measuring 3-D orientation, which makes optical sectioning an ideal choice for data gathering.

The limitations of optical sectioning include a limited choice of sample materials and limited tracer fiber density. However, non-dimensional analysis offers the potential to transfer the results obtained from transparent systems to more common systems. Also, glass manufacturers can produce custom formulations which greatly increases the number of potential combinations. Higher tracer fiber densities can likely be used with enhanced imaging methods, and averaging of multiple scans can be used to increase the size of the sample population.

8.3 Evaluation of the Software

The calibration experiments demonstrated the ability of the software to accurately determine fiber orientation distributions from 3-D images. The software is robust, meaning that it performs well under a wide range of conditions, traps errors effectively, and is not prone to crashing. When errors are detected a description of the problem

is given to the user to help eliminate the source of the error. The graphical user interfaces reduce user error by providing a convenient means of setting default values and providing direct visual access to the program's features and status. All of the programs use dynamic memory allocation so that there is no set limit on the size or complexity of images and data sets that can be analyzed. The use of interprocess communication allows the programs to work together efficiently. On-screen graphic display of results provides immediate feedback to the user for rapid evaluation of the data.

The results of the pseudo data analysis demonstrated the high accuracy of the analysis technique in measuring fiber orientation and fiber length in complex images. The accuracy of angle measurements was shown to be better than 3 degrees, and the average corrected fiber length measurement was less than 9 percent for fiber lengths of 600 μm.

The calibration tests with individual fibers at known orientations demonstrated the ability of the imaging system and analysis software to achieve results similar to those obtained from the pseudo data images.

Analysis of the orthogonal sample with high tracer fiber content gave evidence of the ability of both the imaging system and software to extract accurate 3-D fiber orientation distributions from complex, high fiber density images. Since only two calibrations were done with a complex orientation distribution and the true orientation distribution was not known, it is not possible to make a conclusive statement regarding the accuracy of the result. However, the good agreement between the fiber orientation distributions obtained from orthogonal scans provides strong evidence that the method performs well with high fiber concentrations.

The good correlation observed between the surface ellipse and optical sectioning methods at small out-of-plane orientation angles is evidence not only that the optical sectioning method gives reasonable results, but that the tracer fiber orientation distribution is similar to that of the bulk fiber orientation distribution. The tracer fibers were analyzed in the optical sectioning experiments while in the surface ellipse method the glass fibers were analyzed.

The time required for image thinning by **Thin3D** depended on the information density of the images. On average the time was about 6 seconds per frame, or 5 minutes per 50-frame scan. The analysis time of **3D-FODAS** was about 15 seconds per scan. The computation time required by **Thin3D** could likely be reduced by factor of 5 by further optimization and by using a faster microprocessor.

Errors may originate from two possible sources: imaging and thinning. The apparent lengths of fibers, especially ones with large z orientation components, vary with the intensity of the illumination. Dirt, shadows and similar contamination of the images can also contribute to erroneous data. During thinning, some shortening of fibers is inevitable, and since voxels have non-equal dimensions in x, y, and z, the removal of a voxel has non-equal influence in different directions. This effect may have contributed to the small bias observed in the orthogonal specimen results. The fibers in the orthogonal specimen were shorter than those in the calibration experiments and so the thinning process would tend to shorten the fibers by a larger percentage of the total length, which would be more pronounced in the z direction. An accurate characterization of this bias could be used to minimize this effect and increase the accuracy of the technique.

The software system developed here has been shown to be capable of accurate fiber orientation and length measurements from 3-D images which are not readily measurable by other means.

Recommendations for further development of the software include smarter thresholding and preprocessing to compensate for variability in illumination.

8.4 Influence of Gate Obstacle

It was shown that the conditions present at the gate of the mold can have a far-reaching influence on the fiber orientation of a part. The obstacle induced a greater degree of alignment in the flow direction, which was observed to persist at least to the middle of the specimen.

8.5 Comparison With Literature Data

The comparisons made with published orientation results were not entirely conclusive, but similar trends in the fiber orientation distributions were observed. The differences between the observed fiber orientations were attributed to differences in fiber length and cavity width.

8.6 Evaluation of the Method as a Whole

The combination of experimental apparatus and software have proven to be a useful, accurate, and inexpensive means of short fiber orientation research of injection molded parts. With this technique it is possible to obtain information that is not available by other means. Based on the experience of this project, when material preparation time is taken into account the optical sectioning method was about five times faster

than the manual surface ellipse method. If the surface image analysis were automated the speed advantage would be reduced to about four times.

The usefulness and suitability of this technique and its associated apparatus and software are evident in the recent interest expressed by various companies and organizations.

A representative of Structural Dynamics Research Corporation, after seeing the capabilities of the system, stated that the experimental setup and data were exactly what was needed by them and others to develop, refine, and verify the fiber orientation calculations of simulation programs. NIST (National Institute of Standards and Technology) has expressed interest in obtaining a copy of the analysis software for use in their analysis of short fiber composites. And two plastics manufacturing companies, Monsanto and Himont, have also shown interest in the analysis method.

Experimental results provide evidence that orientation of the measured fiber orientation distribution is accurate to within 7 degrees or less. As a point of reference, a change of 7 degrees in the orientation angle of a unidirectional continuous fiber composite causes a reduction in the predicted Young's modulus of about 8% based on Cook's (1968) model, and about 3% for Voigt's (1910) model. This can be used as an upper limit, as the influence would be less for short fibers and non-unidirectional orientations.

8.7 Recommendations for Future Work

With regard to imaging technique, additional work should be done to investigate the extent of the loss of accuracy due to the degradation of image quality with penetration depth.

A specimen with a well-defined, complex fiber orientation would be extremely valuable for calibrating the system.

The use of opaque BK-10 fibers would eliminate the possibility that the tracer fibers behave differently than the bulk fibers.

The optical port could be used to photograph flow-front propagation during injection and help determine the development of the fiber orientation distribution and aid in the study of fiber-fiber interactions. Several authors observed significant changes in the FOD during the packing phase which are not explained by currently held mold-filling theories. The possibility of significant orientation effects due to void formation and reduction, or "foam filling" should be investigated.

The software could be enhanced by adding the ability to measure fiber curvature, bunching, whole fiber length and void formation. The merits of the Hough transform need to be evaluated to extend the maximum penetration depth.

The transparency of the specimens could allow birefringence analysis of stresses and/or molecular orientation (Wu and White, 1991; and Folkes and Russell, 1980).

Research needs to be conducted to determine the relative importance of the out-of-plane orientation component on the material properties. Some researchers have suggested that 3-D orientation is important even in sheet-molding compound where fibers orientations are normally assumed to be planar.

Additional work needs to be done in the area of non-dimensional analysis so that results from transparent systems can be applied to commonly used opaque systems.

8.8 Concluding Remarks

With the rapid growth of injection molded short fiber composites there is an urgent need for a better understanding of the behavior of these materials and how their properties are influenced by processing conditions. An accurate description of the fiber orientation distribution is essential to this understanding and requires accurate measurement of both fiber lengths and orientations. The technique presented here can provide greater accuracy of orientation measurement than traditional means and can quantify fiber length as well as orientation. Because physical cutting is not required, optical sectioning can be considerably faster than surface based techniques. The flexibility and low cost of the system make well suited for a wide range of applications including the study of melt rheology, fountain flow, weldline formation, void formation, flow around obstacles, and the influences of processing conditions on the fiber orientation.

Further work needs to be done to identify additional materials which are suitable for this type of analysis and to extend non-dimensional analysis techniques to apply the results to opaque materials.

Additional work is needed to demonstrate the full potential of this approach. Optical sectioning can be an excellent source of much needed information for understanding the behavior of short fiber composites.

APPENDICES

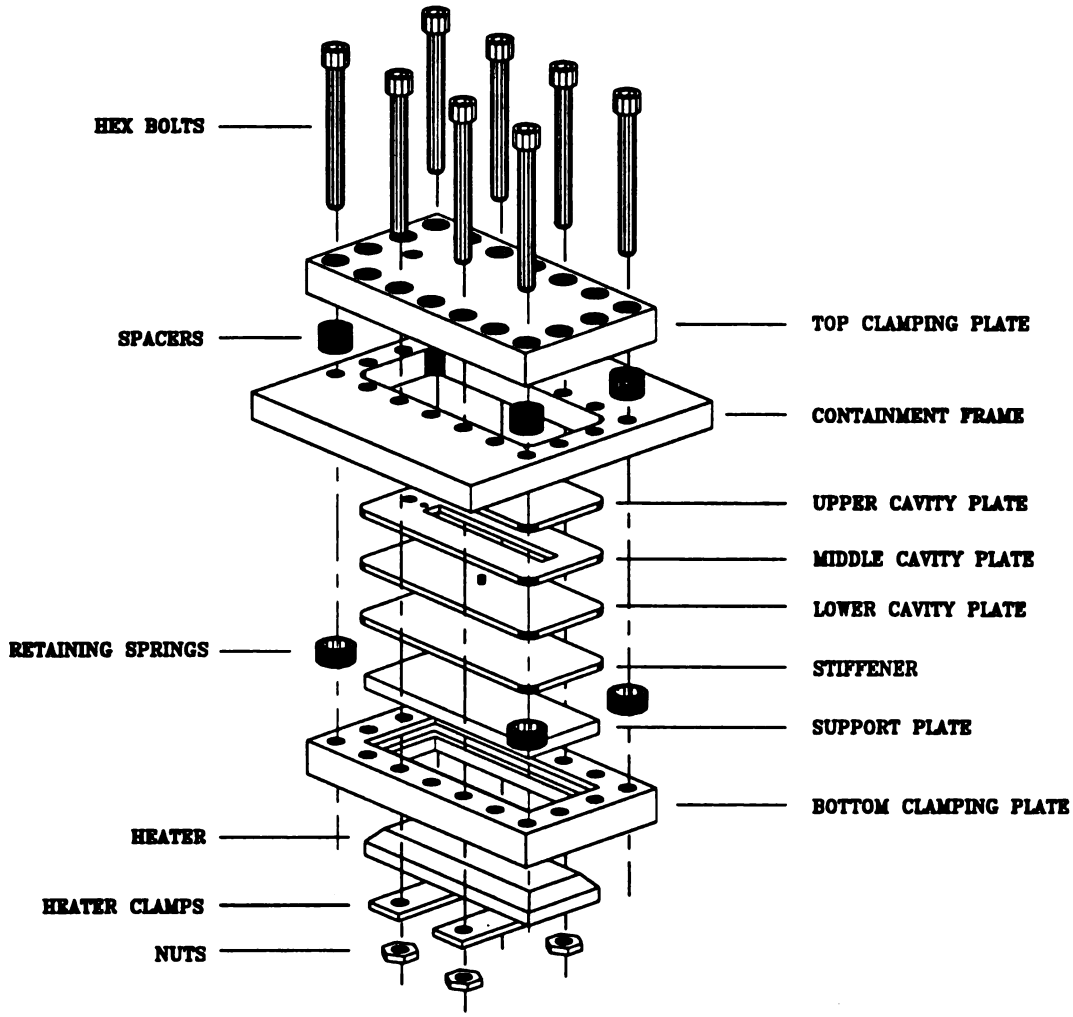
A REFRACTIVE INDICES OF THERMOPLASTIC MATERIALS

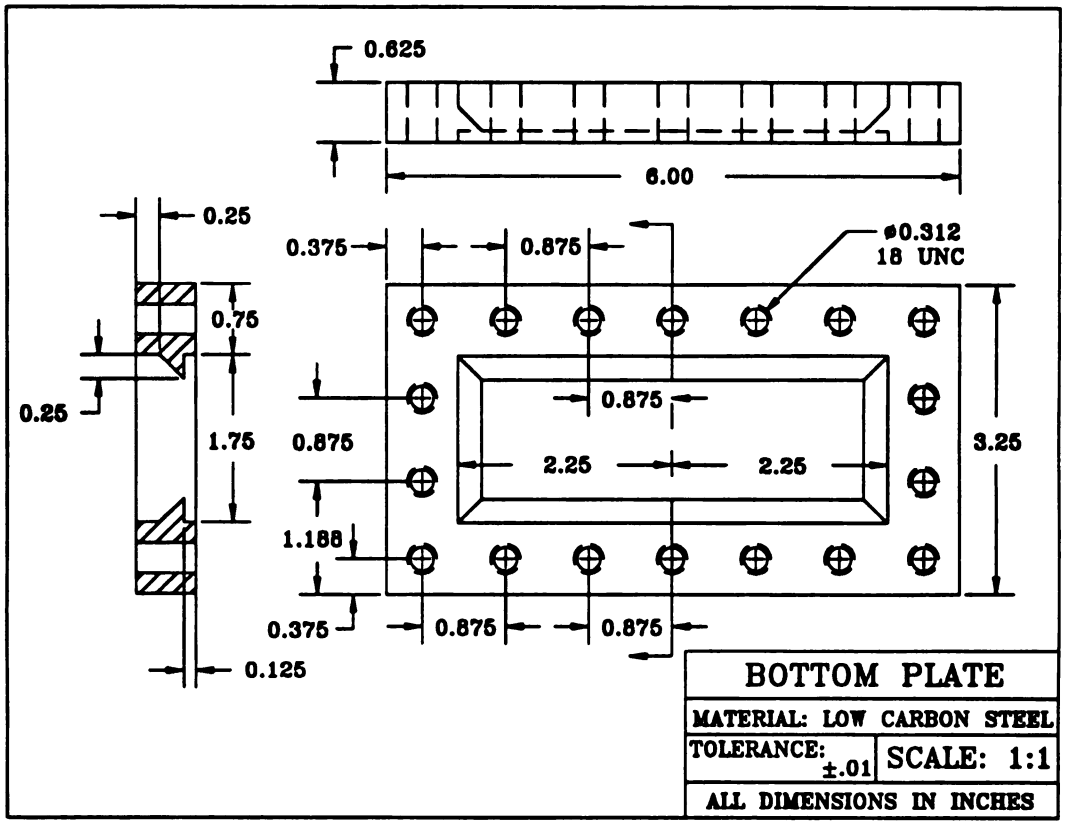
Table A.1: Refractive indices of transparent thermoplastics at 23 °C, 589 nm.

Polymer	Index (n_D)
Polychlorine tetra-fluorine ethylene	1.430
Polyethyl acrylate	1.469
Polymethyl methacrylate (PMMA)	1.491
Polypropylene	1.503
Allyl diglycol carbonate (ADC)	1.504
Polyisobutene	1.508
Polyvinylalcohol	1.510
Polyacrylonitrile	1.519
Polyethylene	1.520
Nylon (optical)	1.535
Acrylonitrile-butadiene-styrene	1.538
Polyvinyl chloride	1.545
Polystyrene acrylonitrile	1.567
Polyphenyl methacrylate	1.571
Polycarbonate	1.586
Polystyrene	1.590
Polysulfone	1.633

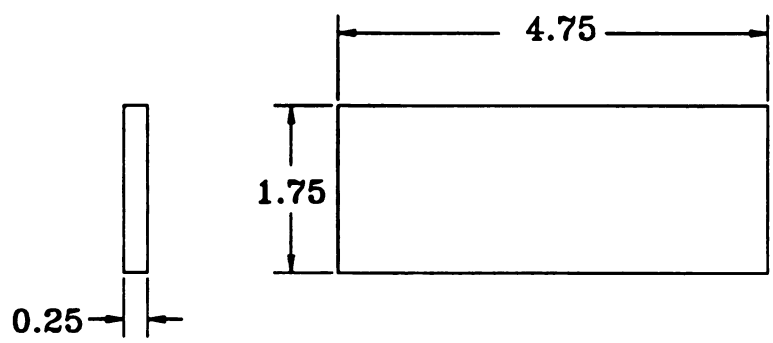
B ENGINEERING DRAWINGS

B.1 Mold

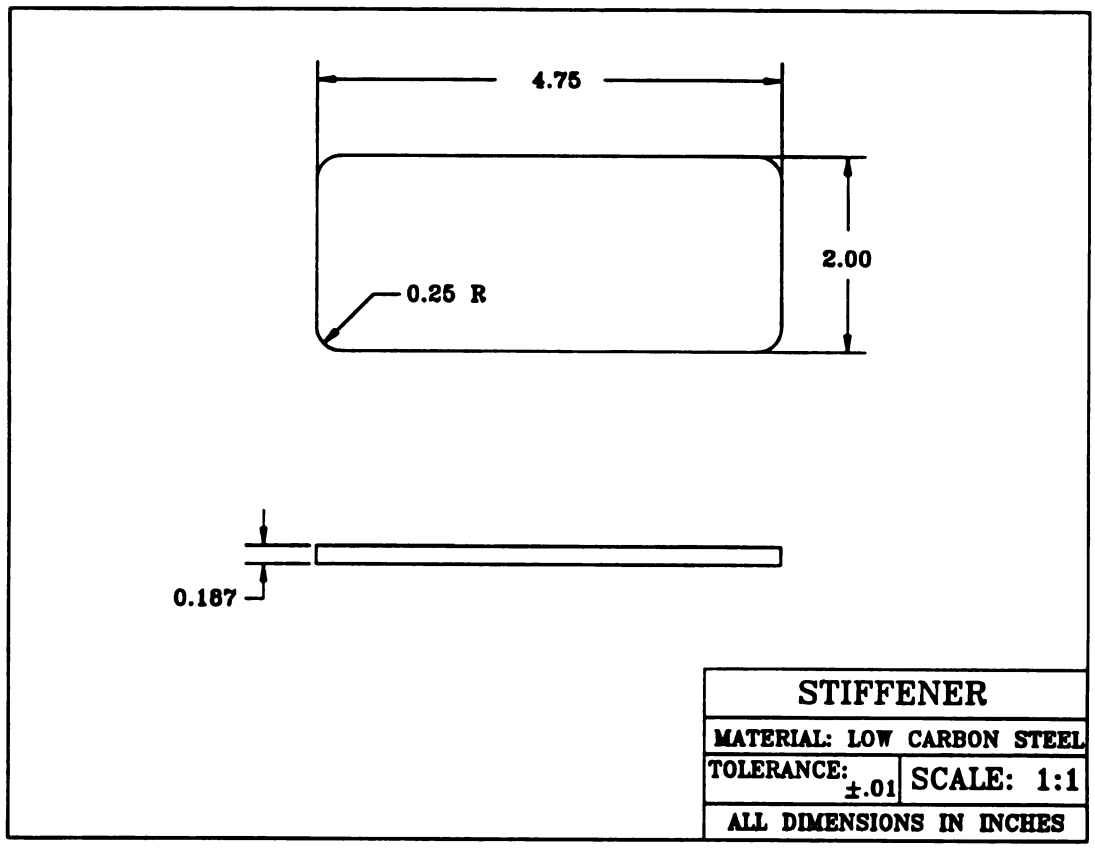




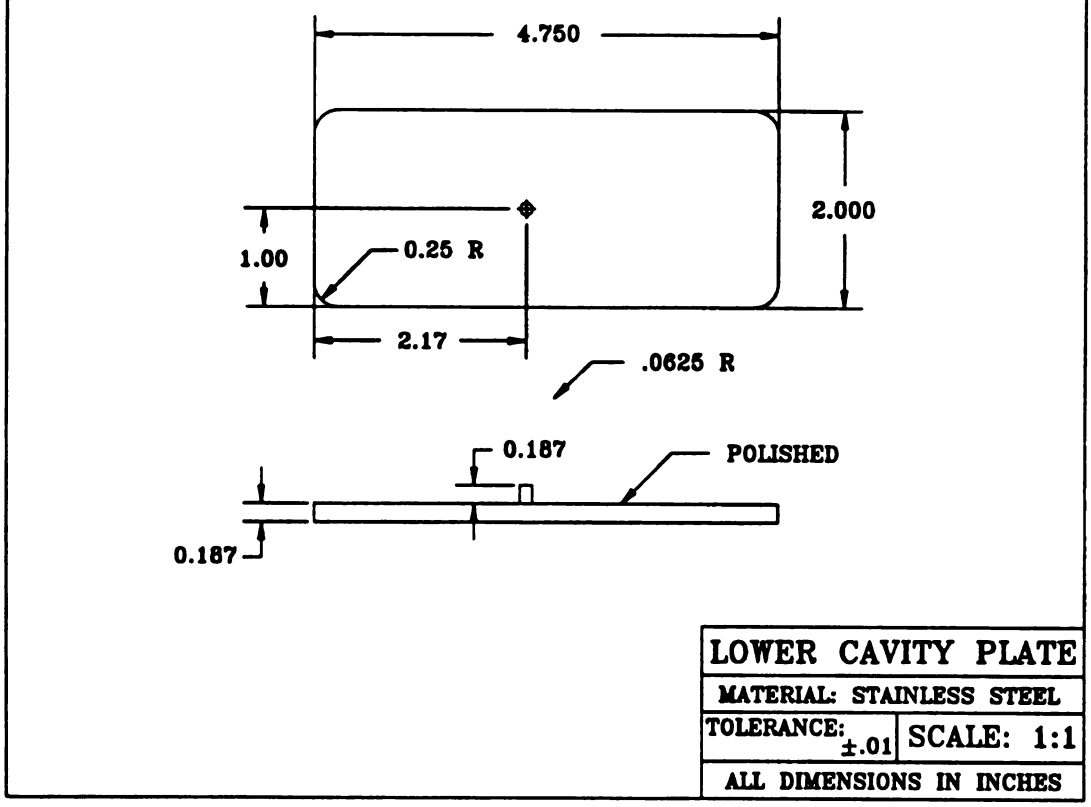
BOTTOM PLATE	
MATERIAL: LOW CARBON STEEL	
TOLERANCE: ±.01	SCALE: 1:1
ALL DIMENSIONS IN INCHES	



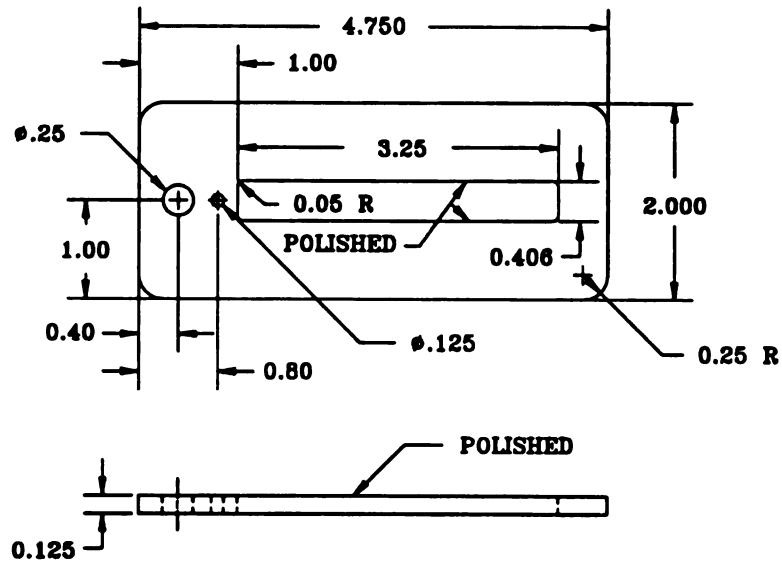
SUPPORT PLATE	
MATERIAL: LOW CARBON STEEL	
TOLERANCE: ±.01	SCALE: 1:1
ALL DIMENSIONS IN INCHES	



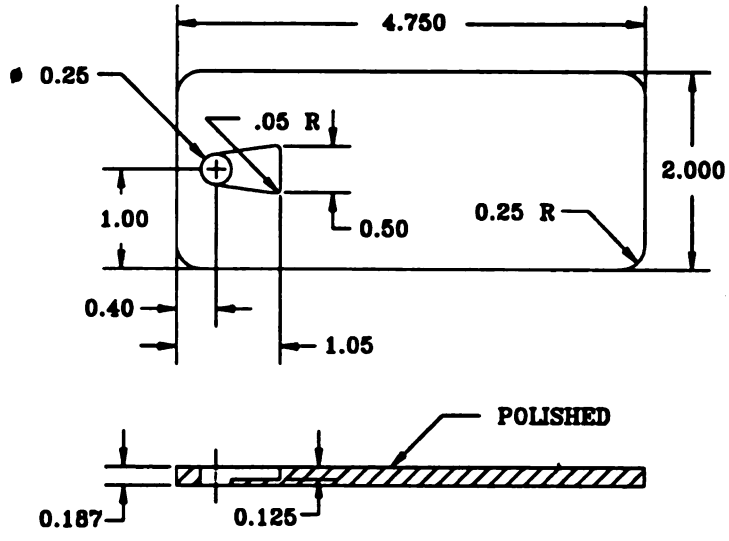
STIFFENER	
MATERIAL: LOW CARBON STEEL	
TOLERANCE: ±.01	SCALE: 1:1
ALL DIMENSIONS IN INCHES	



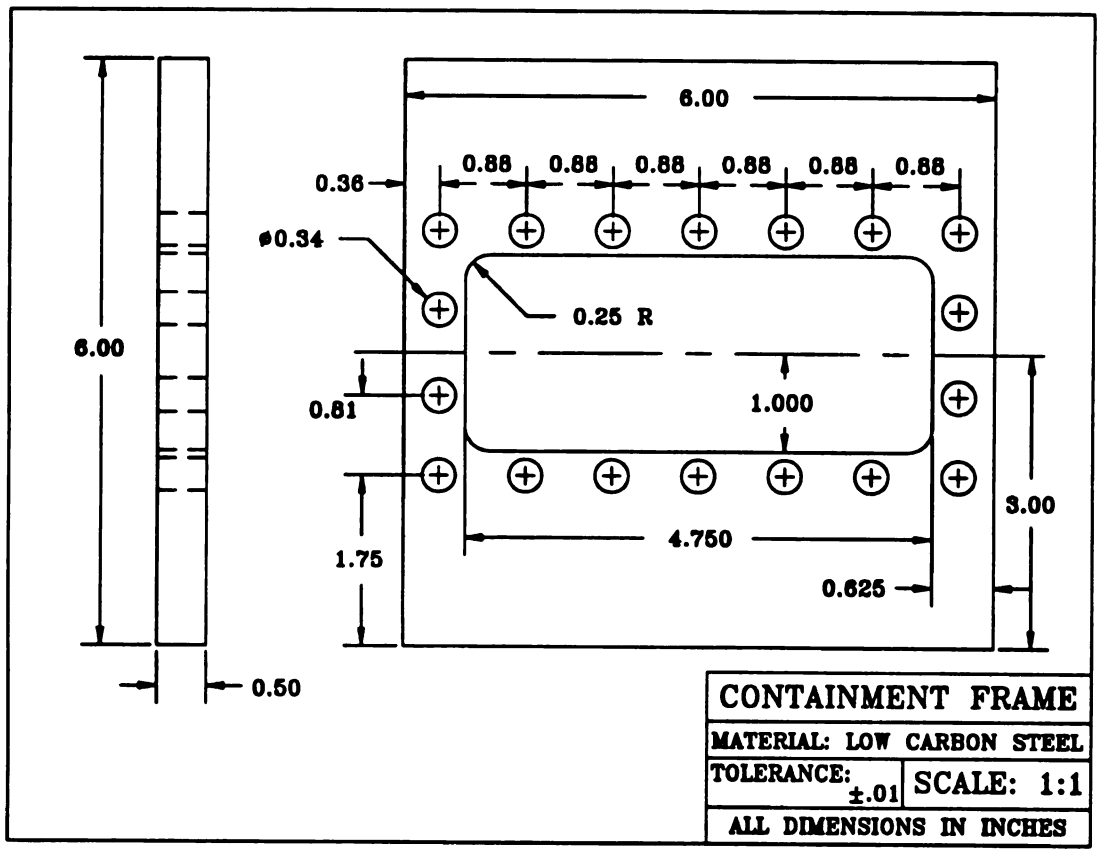
LOWER CAVITY PLATE	
MATERIAL: STAINLESS STEEL	
TOLERANCE: ±.01	SCALE: 1:1
ALL DIMENSIONS IN INCHES	

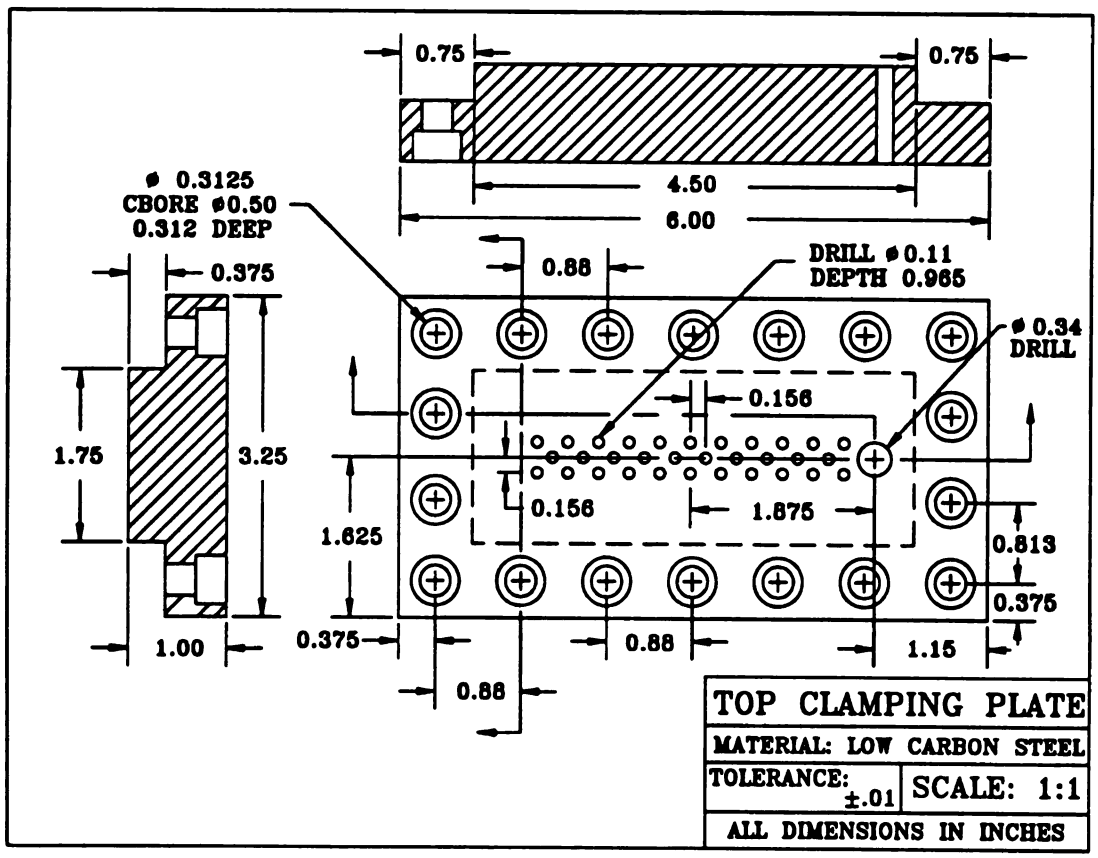


MIDDLE CAVITY PLATE	
MATERIAL: STAINLESS STEEL	
TOLERANCE: ±.01	SCALE: 1:1
ALL DIMENSIONS IN INCHES	

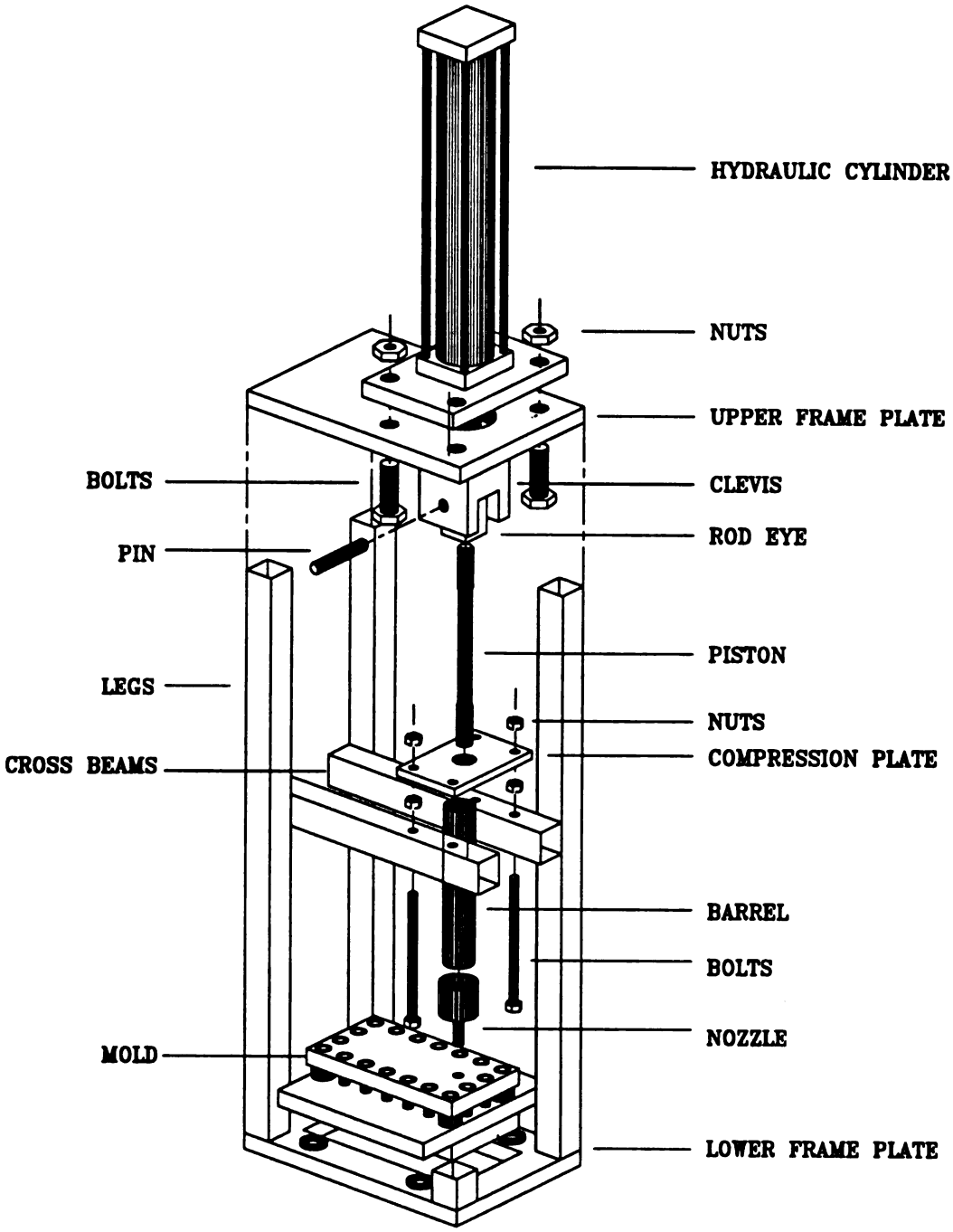


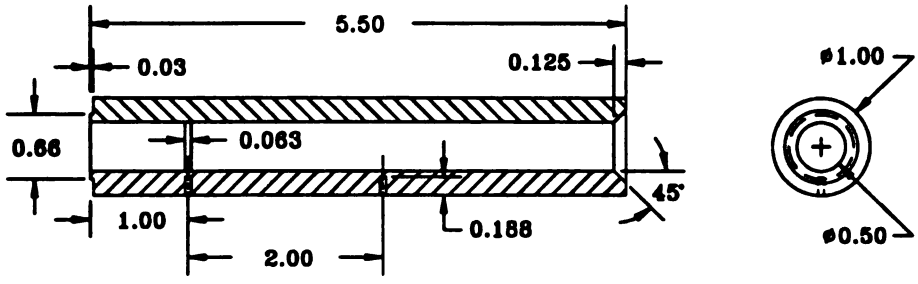
UPPER CAVITY PLATE	
MATERIAL: STAINLESS STEEL	
TOLERANCE: ±.01	SCALE: 1:1
ALL DIMENSIONS IN INCHES	


6.00
0.36
0.88
0.88
0.88
0.88
0.88
0.88
ø0.34
0.25 R
6.00
0.81
1.000
3.00
1.75
4.750
0.625
0.50
CONTAINMENT FRAME
MATERIAL: LOW CARBON STEEL
TOLERANCE: ±.01
SCALE: 1:1
ALL DIMENSIONS IN INCHES

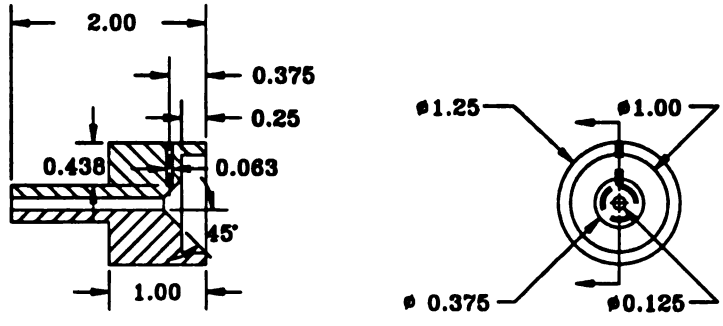

0.75
0.75
4.50
6.00
ø 0.3125
CBORE ø0.50
0.312 DEEP
0.88
DRILL ø0.11
DEPTH 0.965
ø 0.34
DRILL
0.375
0.156
1.75
3.25
0.156
1.875
1.625
0.813
0.375
1.00
0.375
0.88
1.15
0.88
TOP CLAMPING PLATE
MATERIAL: LOW CARBON STEEL
TOLERANCE: ±.01
SCALE: 1:1
ALL DIMENSIONS IN INCHES

B.2 Injector

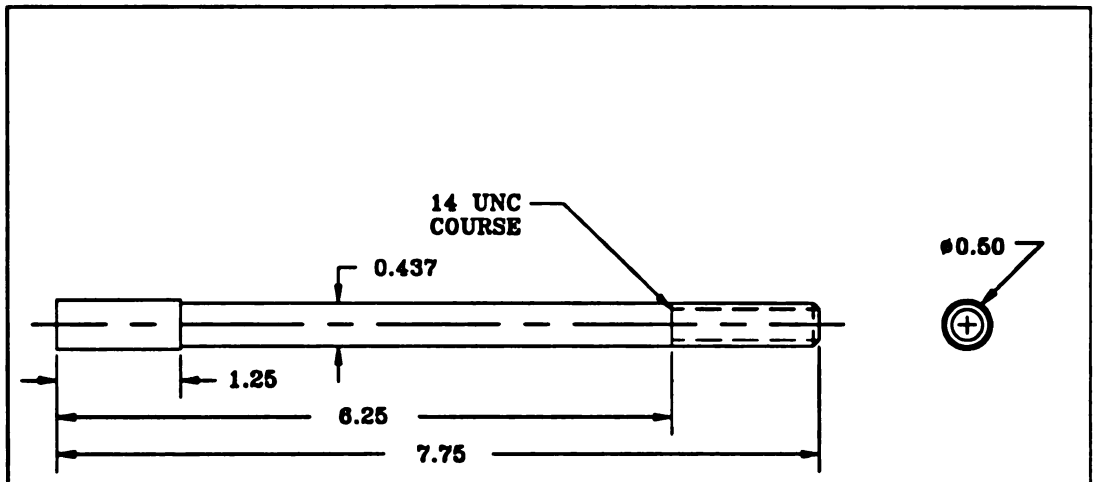

HYDRAULIC CYLINDER
NUTS
UPPER FRAME PLATE
BOLTS
CLEVIS
PIN
ROD EYE
PISTON
LEGS
NUTS
CROSS BEAMS
COMPRESSION PLATE
BARREL
BOLTS
NOZZLE
MOLD
LOWER FRAME PLATE



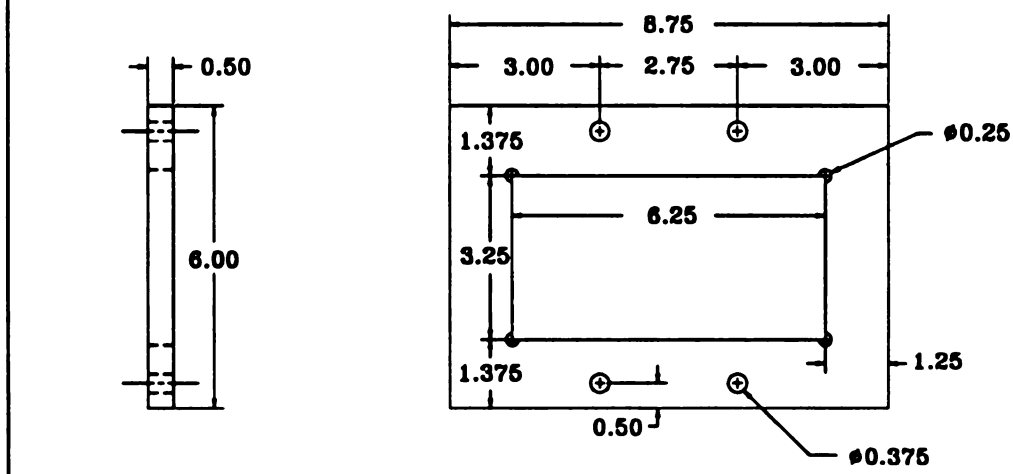
BARREL	
MATERIAL: STAINLESS STEEL	
TOLERANCE: ±.01	SCALE: 1:1
ALL DIMENSIONS IN INCHES	



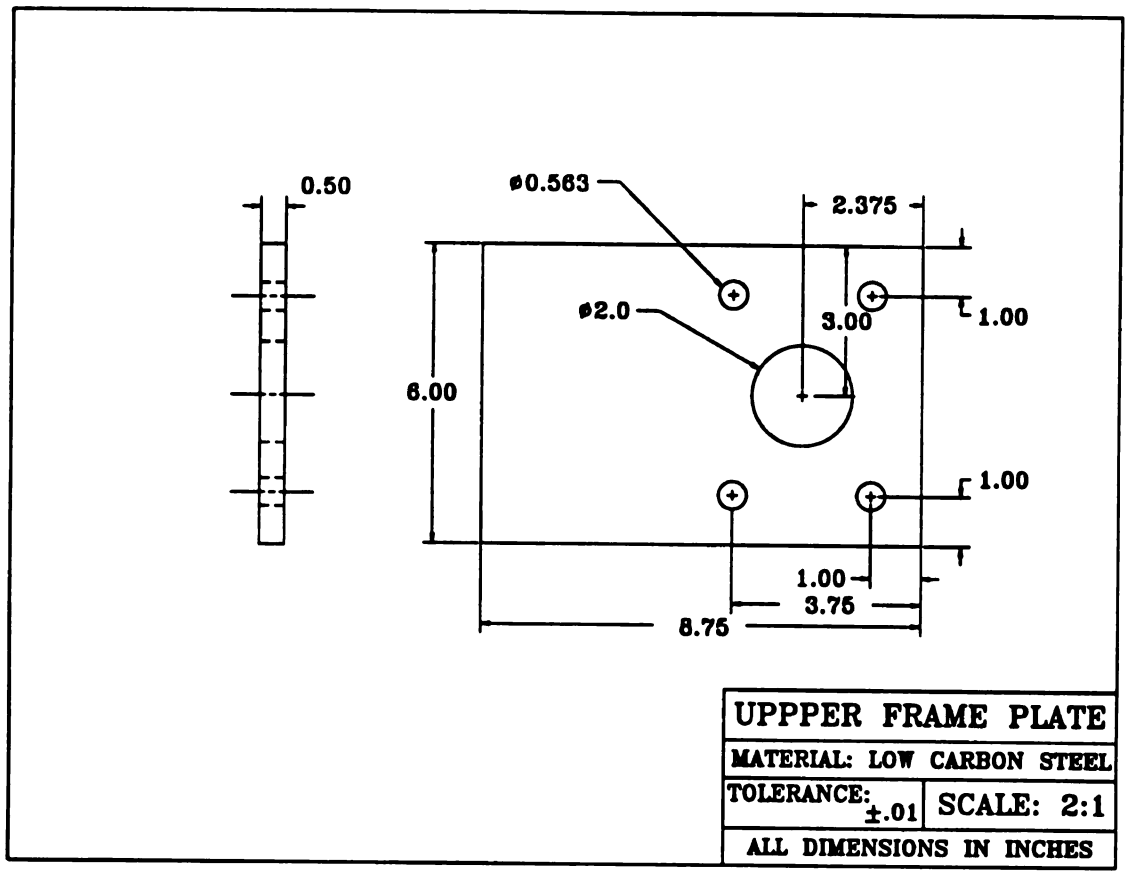
NOZZLE	
MATERIAL: STAINLESS STEEL	
TOLERANCE: ±.01	SCALE: 1:1
ALL DIMENSIONS IN INCHES	



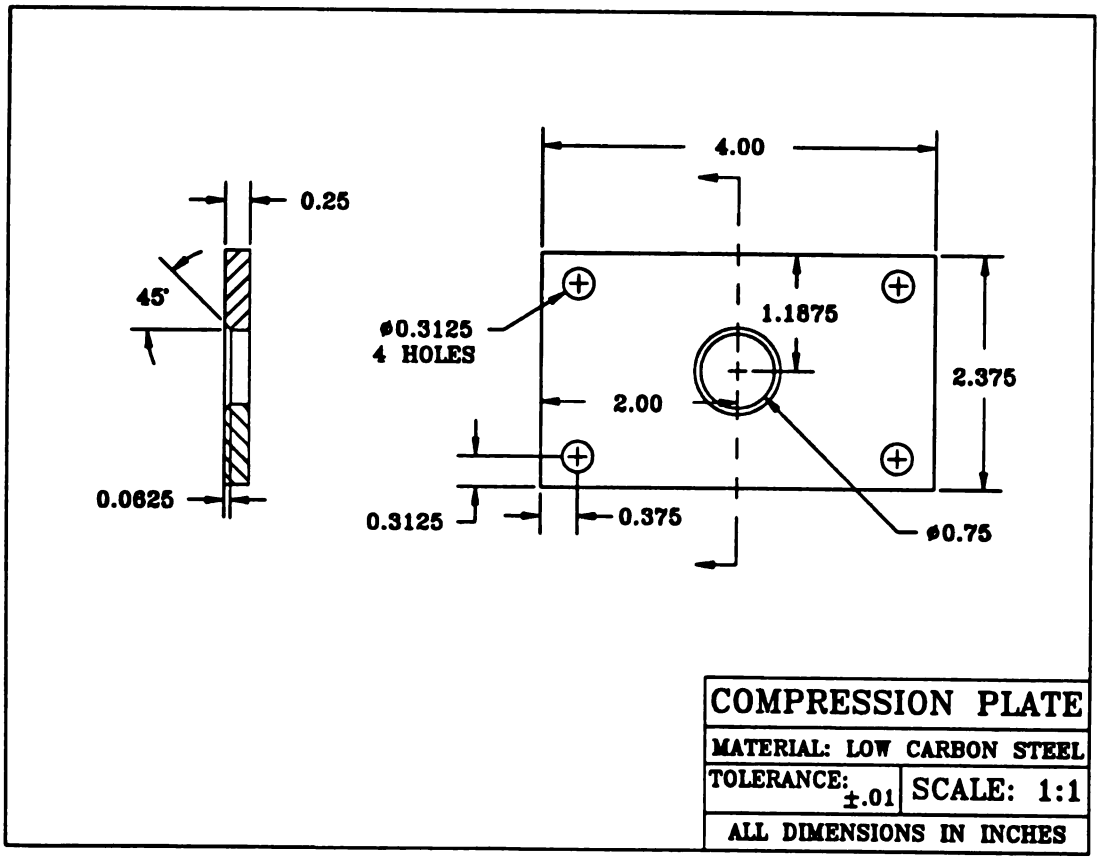
PISTON	
MATERIAL: STAINLESS STEEL	
TOLERANCE: ±.01	SCALE: 1:1
ALL DIMENSIONS IN INCHES	



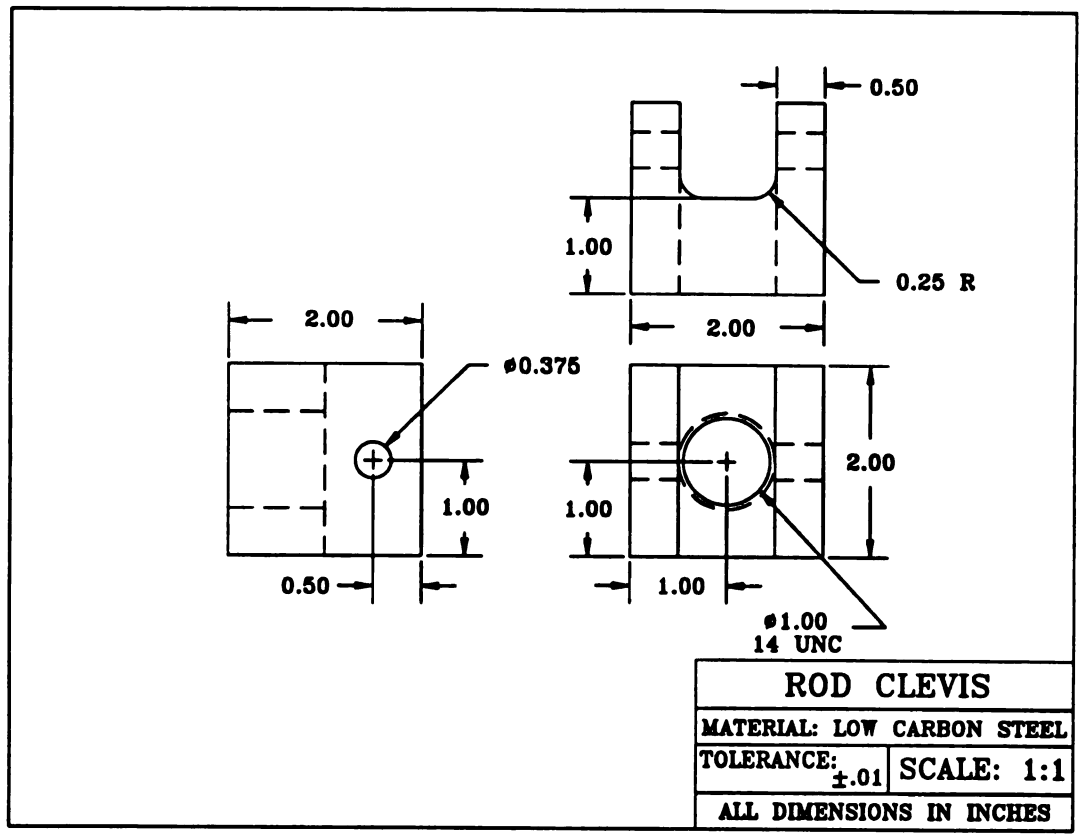
LOWER FRAME PLATE	
MATERIAL: LOW CARBON STEEL	
TOLERANCE: ±.01	SCALE: 2:1
ALL DIMENSIONS IN INCHES	



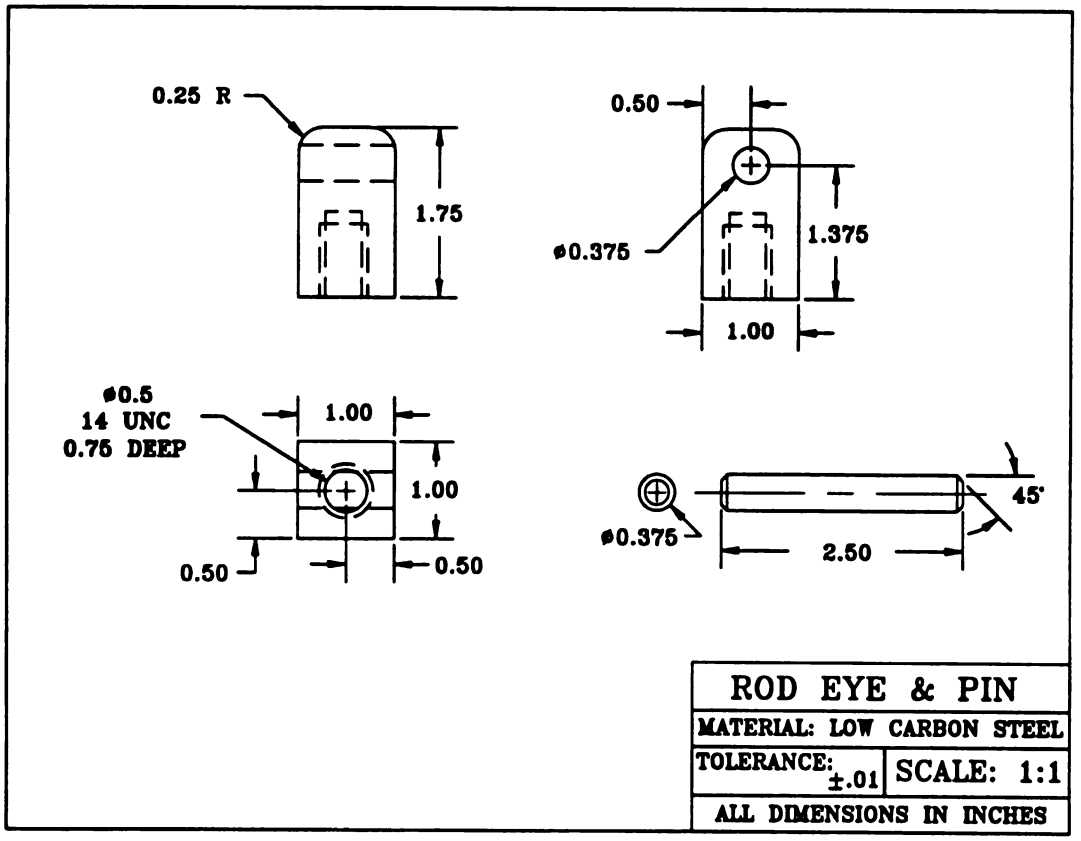
UPPPER FRAME PLATE	
MATERIAL: LOW CARBON STEEL	
TOLERANCE: ±.01	SCALE: 2:1
ALL DIMENSIONS IN INCHES	



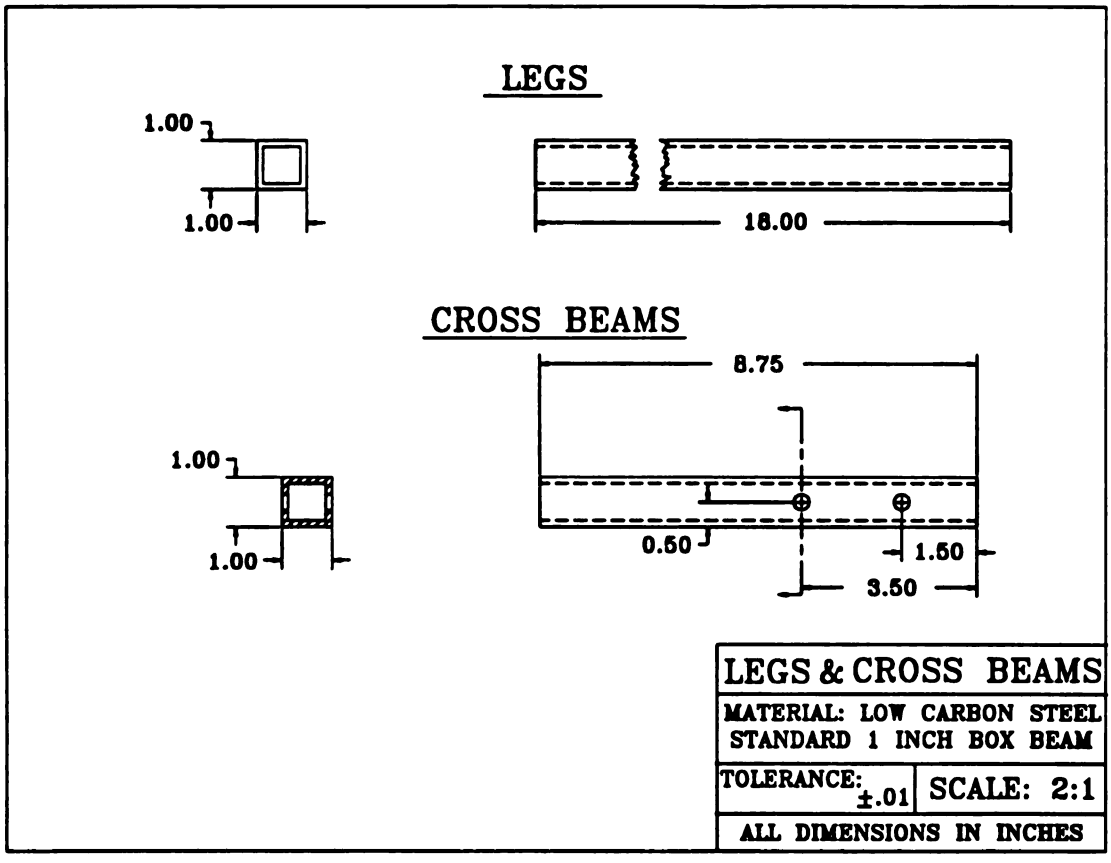
COMPRESSION PLATE	
MATERIAL: LOW CARBON STEEL	
TOLERANCE: ±.01	SCALE: 1:1
ALL DIMENSIONS IN INCHES	



ROD CLEVIS	
MATERIAL: LOW CARBON STEEL	
TOLERANCE: ±.01	SCALE: 1:1
ALL DIMENSIONS IN INCHES	



ROD EYE & PIN	
MATERIAL: LOW CARBON STEEL	
TOLERANCE: ±.01	SCALE: 1:1
ALL DIMENSIONS IN INCHES	


LEGS
1.00
1.00
18.00
CROSS BEAMS
8.75
1.00
1.00
0.50
1.50
3.50
LEGS & CROSS BEAMS
MATERIAL: LOW CARBON STEEL
STANDARD 1 INCH BOX BEAM
TOLERANCE: ±.01
SCALE: 2:1
ALL DIMENSIONS IN INCHES

C INJECTION PROTOCOL

- Calibration
  1. Calibrate thermocouples with HP 2804-A quartz thermometer.
  2. Calibrate position transducer with precision rule.
  3. Determine piston threshold positions for piston speed measurement.
  4. Check position transducer for adequate travel.
  5. Set injection pressure by adjusting the pressure regulator on the hydraulic power unit.
  6. Set injection speed by adjusting the needle valve at the hydraulic cylinder. Measure speed with event timer.
- Cleaning and Coating
  1. Clean injector barrel, piston and nozzle with wire brush and clean cloth.
  2. Coat injector and mold parts with mold-release compound.
  3. Wipe dry.
- Mold Assembly (See Figure 3.3)
  1. Place Bottom Clamping Plate on table.
  2. Place Support Plate on Bottom Clamping Plate.
  3. Place Lower Cavity Plate on Support Plate, polished side up.
  4. Place Middle Cavity Plate on Lower Cavity Plate.
  5. Place Upper Cavity Plate on Middle Cavity Plate, polished side down with injection holes aligned.
  6. Place retaining springs on the four corner bolt holes of the Bottom Clamping Plate.
  7. Place Containment Frame over Cavity Plates so that it rests on the four retaining springs.
  8. Place spacers on the four corner bolt holes of the Containment Frame.
  9. Place Top Clamping Plate on the assembly with the injection holes aligned.
  10. Insert 18 clamping bolts and tighten to 15 N·m (125 in·lbf).
  11. Clamp heater on the bottom of the assembly with two heater clamps.
  12. Check that the heater wires are properly insulated.
- Injector Assembly (See Figure 3.5)
  1. Put assembled mold in the injection machine frame.
  2. Plug nozzle with the same type of material as is being injected.
  3. Insert nozzle into mold.
  4. Put nozzle heater around the nozzle

5. Insert thermocouple into thermocouple hole
6. Insert barrel on the nozzle.
7. Put clamping plate on barrel and finger tighten bolts.
8. Insert piston and lock it with clevis pin.
9. Slowly drive piston down half way into the barrel.
10. Tighten clamping plate bolts 3/4 turn after finger tightening.

- Connections

1. Insert connectors for the two barrel thermostats and data acquisition thermocouples.
2. Inject heat sink compound into thermocouple wells.
3. Insert thermocouples into the mold thermocouple wells.
4. Start data acquisition program and observe thermocouple readings.
5. Make sure all power supplies are off and wires are disconnected.
6. Check power supply voltage setting.
7. Connect all heater wires to their corresponding power supplies.

- Material Preparation

1. Determine total material weight required for the injection.
2. Determine desired weight percentage of materials.
3. Weigh out the materials with precision balance.
4. Mix the materials well so that the fibers are uniformly distributed and not clumped.

- Loading

1. Withdraw and remove piston.
2. Pour material into barrel.
3. Reinsert piston.
4. Drive it down a few millimeters into barrel.

- Heating

1. Zero data acquisition timer.
2. Turn on mold heater and adjust voltage.
3. Wait for mold to heat up to target temperature.
4. Set thermostats for desired barrel temperature.
5. Turn on barrel heaters and check voltages.
6. Turn on nozzle heater and check voltage.
7. Observe thermocouple readings.
8. Holding time begins when the barrel reaches the target temperature.

- Injection
  1. Wait for prescribed holding time.
  2. Enable the event timer for injection speed measurement.
  3. Turn on hydraulic power unit.
  4. Turn off mold and barrel heaters (leave nozzle heater on).
  5. Drive piston down and hold pressure for prescribed time.
  6. Turn off hydraulic unit.
- Disconnect
  1. Withdraw and remove piston.
  2. Remove clamp plate using insulated gloves (very hot).
  3. Turn off nozzle heater
  4. Disconnect all heater leads and connectors.
  5. Remove all thermocouples.
  6. Remove barrel using insulated gloves (very hot).
  7. Remove nozzle using insulated gloves (very hot).
  8. If material remains in the nozzle, heat and clean immediately.
  9. Extract any remaining plastic from the barrel.
  10. Clean residual material from piston with wire brush.
  11. Remove mold using insulated gloves and allow to cool.
- Mold Disassembly
  1. Remove heater clamps.
  2. Remove all bolts.
  3. Disassemble mold.
  4. Remove specimen.

D SPECIMEN DATA SHEETS

Obstacle1	Molded Weight: 3.800 g	
Material	**Content [wt%]**	**Weight [g]**
Matrix: PMMA	*70*	*5.6*
Fibers: BK-10	*30*	*2.4*
Tracers: Carbon	*0.1*	*0.008*
Total:	*100*	*8.008*

Power Supply	**Voltage [V]**	**Current [A]**	**Power [W]**	**Thermst [°C]**
Mold	*13*	*6.5*	*85*	—
Upper Barrel	*18*	*8.6*	*155*	*250*
Lower Barrel	*8*	*6.2*	*50*	*250*
Nozzle	*10*	*11*	*110*	—

Elapsed Time [min]	T_{upper} [°C] **I**	T_{lower} [°C] **II**	T_{nozzle} [°C] **III**	T_{mold1} [°C] **IV**	T_{mold2} [°C] **V**
$t_{mold} = 0$	*24*	*24*	*24*	*25*	*25*
$t_{barrel} = 60$	*37*	*37*	*37*	*70*	*70*
$t_{nozzle} = 60$	*37*	*37*	*37*	*70*	*70*
$t_{target} = 84$	*234*	*238*	*221*	*100*	*93*
$t_{inject} = 93$	*239*	*240*	*236*	*110*	*101*

Timer Start Threshold [cm]: *12*	Timer Stop Threshold [cm]: *3*
Injection Speed (Piston) [cm/s]: *8.2*	No Load Piston Speed [cm/s]: *9.3*
Hydraulic Pressure [psi]: *1,200*	Injection Pressure [psi]: *19,200*
Holding Time [s]: *10*	Cooling Time [min]: *15*

Remarks:

- *Textured surface, transparent*
- *Each side polished: 4 min 1000, 2 min 2400, 2 min 4000 (300 rpm)*
- *Final thickness: 3.10 mm*

Obstacle2	Molded Weight: 3.840 g	
Material	**Content [wt%]**	**Weight [g]**
Matrix: PMMA	*70*	*5.6*
Fibers: BK-10	*30*	*2.4*
Tracers: Carbon	*0.1*	*0.008*
Total:	*100*	*8.008*

Power Supply	**Voltage [V]**	**Current [A]**	**Power [W]**	**Thermst [°C]**
Mold	*13*	*6.5*	*85*	—
Upper Barrel	*18*	*8.6*	*155*	*250*
Lower Barrel	*8*	*6.2*	*50*	*250*
Nozzle	*10*	*11*	*110*	—

Elapsed Time [min]	T_{upper} [°C] **I**	T_{lower} [°C] **II**	T_{nozzle} [°C] **III**	T_{mold1} [°C] **IV**	T_{mold2} [°C] **V**
t_{mold} = *0*	*23*	*23*	*23*	*23*	*23*
t_{barrel} = *86*	*41*	*41*	*66*	*81*	*81*
t_{nozzle} = *86*	*41*	*41*	*66*	*81*	*81*
t_{target} = *95*	*237*	*240*	*204*	*92*	*87*
t_{inject} = *118*	*241*	*243*	*231*	*116*	*108*

Timer Start Threshold [cm]: *12*	Timer Stop Threshold [cm]: *3*
Injection Speed (Piston) [cm/s]: *8.1*	No Load Piston Speed [cm/s]: *8.9*
Hydraulic Pressure [psi]: *1,200*	Injection Pressure [psi]: *19,200*
Holding Time [s]: *10*	Cooling Time [min]: *15*

Remarks:

- *Textured surface, transparent*
- *Each side polished: 4 min 1000, 2 min 2400, 2 min 4000 (300 rpm)*
- *Final thickness: 3.10 mm*

Obstacle3	Molded Weight: 3.860 g	
Material	**Content [wt%]**	**Weight [g]**
Matrix: PMMA	*70*	*5.6*
Fibers: BK-10	*30*	*2.4*
Tracers: Carbon	*0.1*	*0.008*
Total:	*100*	*8.008*

Power Supply	**Voltage [V]**	**Current [A]**	**Power [W]**	**Thermst [°C]**
Mold	*13*	*6.5*	*85*	—
Upper Barrel	*18*	*8.6*	*155*	*250*
Lower Barrel	*8*	*6.2*	*50*	*250*
Nozzle	*10*	*11*	*110*	—

Elapsed Time [min]	T_{upper} [°C] **I**	T_{lower} [°C] **II**	T_{nozzle} [°C] **III**	T_{mold1} [°C] **IV**	T_{mold2} [°C] **V**
$t_{mold} = 0$	*25*	*25*	*25*	*27*	*27*
$t_{barrel} = 51$	*37*	*38*	*48*	*72*	*71*
$t_{nozzle} = 51$	*37*	*38*	*48*	*72*	*71*
$t_{target} = 65$	*239*	*240*	*231*	*94*	*86*
$t_{inject} = 75$	*240*	*242*	*236*	*109*	*101*

Timer Start Threshold [cm]: *12*	Timer Stop Threshold [cm]: *3*
Injection Speed (Piston) [cm/s]: *8.5*	No Load Piston Speed [cm/s]: *8.9*
Hydraulic Pressure [psi]: *1,200*	Injection Pressure [psi]: *19,200*
Holding Time [s]: *10*	Cooling Time [min]: *15*

Remarks:

- *Textured surface, transparent*
- *Each side polished: 4 min 1000, 2 min 2400, 2 min 4000 (300 rpm)*
- *Final thickness: 3.10 mm*

Obstacle4	Molded Weight: 3.710 g	
Material	**Content [wt%]**	**Weight [g]**
Matrix: PMMA	*75*	*6.0*
Fibers: BK-10	*25*	*2.0*
Tracers: Carbon	*0.1*	*0.008*
Total:	*100*	*8.008*

Power Supply	**Voltage [V]**	**Current [A]**	**Power [W]**	**Thermst [°C]**
Mold	*13*	*6.5*	*85*	—
Upper Barrel	*18*	*8.6*	*155*	*250*
Lower Barrel	*8*	*6.2*	*50*	*250*
Nozzle	*10*	*11*	*110*	—

Elapsed Time [min]	T_{upper} [°C] **I**	T_{lower} [°C] **II**	T_{nozzle} [°C] **III**	T_{mold1} [°C] **IV**	T_{mold2} [°C] **V**
$t_{mold} = 0$	*23*	*23*	*23*	*24*	*24*
$t_{barrel} = 60$	*42*	*42*	*52*	*76*	*76*
$t_{nozzle} = 60$	*42*	*42*	*52*	*76*	*76*
$t_{target} = 68$	*227*	*230*	*210*	*87*	*82*
$t_{inject} = 82$	*239*	*241*	*240*	*106*	*97*

Timer Start Threshold [cm]: *12*	Timer Stop Threshold [cm]: *3*
Injection Speed (Piston) [cm/s]: *8.4*	No Load Piston Speed [cm/s]: *8.9*
Hydraulic Pressure [psi]: *1,200*	Injection Pressure [psi]: *19,200*
Holding Time [s]: *10*	Cooling Time [min]: *10*

Remarks:

- *Textured surface, transparent*
- *Each side polished: 4 min 1000, 2 min 2400, 2 min 4000 (300 rpm)*
- *Final thickness: 3.10 mm*

Obstacle5	Molded Weight: 4.660 g (with runner)	
Material	**Content [wt%]**	**Weight [g]**
Matrix: PMMA	*75*	*6.0*
Fibers: BK-10	*25*	*2.0*
Tracers: Carbon	*0.1*	*0.008*
Total:	*100*	*8.008*

Power Supply	**Voltage [V]**	**Current [A]**	**Power [W]**	**Thermst [°C]**
Mold	*13*	*6.5*	*85*	—
Upper Barrel	*18*	*8.6*	*155*	*250*
Lower Barrel	*8*	*6.2*	*50*	*250*
Nozzle	*10*	*11*	*110*	—

Elapsed Time [min]	T_{upper} [°C] **I**	T_{lower} [°C] **II**	T_{nozzle} [°C] **III**	T_{mold1} [°C] **IV**	T_{mold2} [°C] **V**
$t_{mold} = 0$	*25*	*25*	*29*	*32*	*32*
$t_{barrel} = 60$	*40*	*42*	*62*	*78*	*78*
$t_{nozzle} = 60$	*40*	*42*	*62*	*78*	*78*
$t_{target} = 69$	*241*	*242*	*213*	*95*	*88*
$t_{inject} = 85$	*240*	*242*	*240*	*117*	*110*

Timer Start Threshold [cm]: *12*	Timer Stop Threshold [cm]: *3*
Injection Speed (Piston) [cm/s]: *8.4*	No Load Piston Speed [cm/s]: *9.0*
Hydraulic Pressure [psi]: *1,200*	Injection Pressure [psi]: *19,200*
Holding Time [s]: *10*	Cooling Time [min]: *10*

Remarks:

- *Textured surface, transparent*
- *Each side polished: 4 min 1000, 2 min 2400, 2 min 4000 (300 rpm)*
- *Final thickness: 3.10 mm*

Obstacle6	Molded Weight: 3.700 g	
Material	**Content [wt%]**	**Weight [g]**
Matrix: PMMA	*75*	*6.0*
Fibers: BK-10	*25*	*2.0*
Tracers: Carbon	*0.1*	*0.008*
Total:	*100*	*8.008*

Power Supply	**Voltage [V]**	**Current [A]**	**Power [W]**	**Thermst [°C]**
Mold	*13*	*6.5*	*85*	—
Upper Barrel	*18*	*8.6*	*155*	*250*
Lower Barrel	*8*	*6.2*	*50*	*250*
Nozzle	*10*	*11*	*110*	—

Elapsed Time [min]	T_{upper} [°C] **I**	T_{lower} [°C] **II**	T_{nozzle} [°C] **III**	T_{mold1} [°C] **IV**	T_{mold2} [°C] **V**
$t_{mold} = 0$	*23*	*23*	*23*	*23*	*23*
$t_{barrel} = 57$	*37*	*37*	*41*	*70*	*70*
$t_{nozzle} = 57$	*37*	*37*	*41*	*70*	*70*
$t_{target} = 67$	*232*	*235*	*215*	*83*	*77*
$t_{inject} = 86$	*237*	*239*	*232*	*104*	*95*

Timer Start Threshold [cm]: *12*	Timer Stop Threshold [cm]: *3*
Injection Speed (Piston) [cm/s]: *8.4*	No Load Piston Speed [cm/s]: *8.9*
Hydraulic Pressure [psi]: *1,200*	Injection Pressure [psi]: *19,200*
Holding Time [s]: *10*	Cooling Time [min]: *10*

Remarks:

- *Textured surface, transparent*
- *Each side polished: 4 min 1000, 2 min 2400, 2 min 4000 (300 rpm)*
- *Final thickness: 3.10 mm*

Obstacle7	Molded Weight: 4.460 g (with runner)	
Material	**Content [wt%]**	**Weight [g]**
Matrix: PMMA	*80*	*6.4*
Fibers: BK-10	*20*	*1.6*
Tracers: Carbon	*0.1*	*0.008*
Total:	*100*	*8.008*

Power Supply	**Voltage [V]**	**Current [A]**	**Power [W]**	**Thermst [°C]**
Mold	*13*	*6.5*	*85*	—
Upper Barrel	*18*	*8.6*	*155*	*250*
Lower Barrel	*8*	*6.2*	*50*	*250*
Nozzle	*10*	*11*	*110*	—

Elapsed Time [min]	T_{upper} [°C] **I**	T_{lower} [°C] **II**	T_{nozzle} [°C] **III**	T_{mold1} [°C] **IV**	T_{mold2} [°C] **V**
$t_{mold} = 0$	*22*	*23*	*25*	*24*	*22*
$t_{barrel} = 60$	*36*	*41*	*59*	*75*	*75*
$t_{nozzle} = 60$	*36*	*41*	*59*	*75*	*75*
$t_{target} = 68$	*228*	*224*	*199*	*87*	*82*
$t_{inject} = 78$	*240*	*242*	*226*	*101*	*91*

Timer Start Threshold [cm]: *12*	Timer Stop Threshold [cm]: *3*
Injection Speed (Piston) [cm/s]: *8.4*	No Load Piston Speed [cm/s]: *8.8*
Hydraulic Pressure [psi]: *1,200*	Injection Pressure [psi]: *19,200*
Holding Time [s]: *10*	Cooling Time [min]: *10*

Remarks:

- *Textured surface, transparent*
- *Each side polished: 4 min 1000, 2 min 2400, 2 min 4000 (300 rpm)*
- *Final thickness: 3.10 mm*

Obstacle8	Molded Weight: 4.460 g	
Material	**Content [wt%]**	**Weight [g]**
Matrix: PMMA	*80*	*6.4*
Fibers: BK-10	*20*	*1.6*
Tracers: Carbon	*0.1*	*0.008*
Total:	*100*	*8.008*

Power Supply	**Voltage [V]**	**Current [A]**	**Power [W]**	**Thermst [°C]**
Mold	*13*	*6.5*	*85*	—
Upper Barrel	*18*	*8.6*	*155*	*250*
Lower Barrel	*8*	*6.2*	*50*	*250*
Nozzle	*10*	*11*	*110*	—

Elapsed Time [min]	T_{upper} [°C] **I**	T_{lower} [°C] **II**	T_{nozzle} [°C] **III**	T_{mold1} [°C] **IV**	T_{mold2} [°C] **V**
t_{mold} = *0*	*32*	*32*	*30*	*36*	*34*
t_{barrel} = *64*	*36*	*42*	*55*	*77*	*76*
t_{nozzle} = *64*	*36*	*42*	*55*	*77*	*76*
t_{target} = *73*	*237*	*240*	*213*	*93*	*86*
t_{inject} = *82*	*239*	*242*	*236*	*105*	*95*

Timer Start Threshold [cm]: *12*	Timer Stop Threshold [cm]: *3*
Injection Speed (Piston) [cm/s]: *8.3*	No Load Piston Speed [cm/s]: *8.8*
Hydraulic Pressure [psi]: *1,200*	Injection Pressure [psi]: *19,200*
Holding Time [s]: *10*	Cooling Time [min]: *14*

Remarks:

- *Textured surface finish, transparent*
- *Each side polished: 4 min 1000, 2 min 2400, 2 min 4000 (300 rpm)*
- *Final thickness: 3.10 mm*

Obstacle9	Molded Weight: 3.760 g	
Material	**Content [wt%]**	**Weight [g]**
Matrix: PMMA	*80*	*6.4*
Fibers: BK-10	*20*	*1.6*
Tracers: Carbon	*0.1*	*0.008*
Total:	*100*	*8.008*

Power Supply	**Voltage [V]**	**Current [A]**	**Power [W]**	**Thermst [°C]**
Mold	*13*	*6.5*	*85*	—
Upper Barrel	*18*	*8.6*	*155*	*250*
Lower Barrel	*8*	*6.2*	*50*	*250*
Nozzle	*10*	*11*	*110*	—

Elapsed Time [min]	T_{upper} [°C] **I**	T_{lower} [°C] **II**	T_{nozzle} [°C] **III**	T_{mold1} [°C] **IV**	T_{mold2} [°C] **V**
$t_{mold} = 0$	*24*	*24*	*24*	*24*	*24*
$t_{barrel} = 75$	*40*	*50*	*55*	*77*	*82*
$t_{nozzle} = 75$	*40*	*50*	*55*	*77*	*82*
$t_{target} = 83$	*238*	*233*	*230*	*84*	*94*
$t_{inject} = 100$	*243*	*244*	*243*	*116*	*108*

Timer Start Threshold [cm]: *12*	Timer Stop Threshold [cm]: *3*
Injection Speed (Piston) [cm/s]: *8.4*	No Load Piston Speed [cm/s]: *8.9*
Hydraulic Pressure [psi]: *1,200*	Injection Pressure [psi]: *19,200*
Holding Time [s]: *10*	Cooling Time [min]: *18*

Remarks:

- *Very good surface finish, transparent*
- *Little flash (clamping bolts not tightened)*
- *Final thickness: 3.20 mm*

NoObstacle1	Molded Weight: 3.743 g	
Material	**Content [wt%]**	**Weight [g]**
Matrix: PMMA	*70*	*5.6*
Fibers: BK-10	*30*	*2.4*
Tracers: Carbon	*0.1*	*0.008*
Total:	*100*	*8.008*

Power Supply	**Voltage [V]**	**Current [A]**	**Power [W]**	**Thermst [°C]**
Mold	*12*	*6.0*	*72*	—
Upper Barrel	*18*	*8.6*	*155*	*250*
Lower Barrel	*8*	*6.2*	*50*	*250*
Nozzle	*10*	*11*	*110*	—

Elapsed Time [min]	**T_{upper} [°C] I**	**T_{lower} [°C] II**	**T_{nozzle} [°C] III**	**T_{mold1} [°C] IV**	**T_{mold2} [°C] V**
$t_{mold} = 0$	*22*	*24*	*22*	*24*	*24*
$t_{barrel} = 54$	*34*	*37*	*33*	*66*	*66*
$t_{nozzle} = 54$	*34*	*37*	*33*	*66*	*66*
$t_{target} = 62$	*228*	*227*	*233*	*79*	*73*
$t_{inject} = 79$	*237*	*242*	*238*	*97*	*91*

Timer Start Threshold [cm]: *12*	Timer Stop Threshold [cm]: *3*
Injection Speed (Piston) [cm/s]: *16.0*	No Load Piston Speed [cm/s]: *17.5*
Hydraulic Pressure [psi]: *1,200*	Injection Pressure [psi]: *19,200*
Holding Time [s]: *10*	Cooling Time [min]: *10*

Remarks:

- *Good, but some textured surface, transparent*
- *Each side polished:*
  9 min 320, 8 min 1000, 2 min 2400, 11 min 4000 (300 rpm)
- *Final thickness: 2.8 mm*

NoObstacle2	Molded Weight: 3.830 g	
Material	**Content [wt%]**	**Weight [g]**
Matrix: PMMA	*70*	*5.6*
Fibers: BK-10	*30*	*2.4*
Tracers: Carbon	*0.1*	*0.008*
Total:	*100*	*8.008*

Power Supply	**Voltage [V]**	**Current [A]**	**Power [W]**	**Thermst [°C]**
Mold	*13*	*6.5*	*85*	—
Upper Barrel	*18*	*8.6*	*155*	*250*
Lower Barrel	*8*	*6.2*	*50*	*250*
Nozzle	*10*	*11*	*110*	—

Elapsed Time [min]	T_{upper} [°C] **I**	T_{lower} [°C] **II**	T_{nozzle} [°C] **III**	T_{mold1} [°C] **IV**	T_{mold2} [°C] **V**
$t_{mold} = 0$	*23*	*24*	*23*	*24*	*23*
$t_{barrel} = 50$	*32*	*38*	*50*	*67*	*68*
$t_{nozzle} = 50$	*32*	*38*	*50*	*67*	*68*
$t_{target} = 60$	*239*	*243*	*203*	*82*	*76*
$t_{inject} = 78$	*239*	*245*	*240*	*104*	*98*

Timer Start Threshold [cm]: *12*	Timer Stop Threshold [cm]: *3*
Injection Speed (Piston) [cm/s]: *16.5*	No Load Piston Speed [cm/s]: *17.5*
Hydraulic Pressure [psi]: *1,200*	Injection Pressure [psi]: *19,200*
Holding Time [s]: *10*	Cooling Time [min]: *10*

Remarks:

- *Rough textured surface, transparent*
- *Each side polished:*
  9 min 320, 8 min 1000, 2 min 2400, 11 min 4000 (300 rpm)
- *Final thickness: 2.75 mm*

NoObstacle3	Molded Weight: 3.730 g	
Material	**Content [wt%]**	**Weight [g]**
Matrix: PMMA	*70*	*5.6*
Fibers: BK-10	*30*	*2.4*
Tracers: Carbon	*0.1*	*0.008*
Total:	*100*	*8.008*

Power Supply	**Voltage [V]**	**Current [A]**	**Power [W]**	**Thermst [°C]**
Mold	*13*	*6.5*	*85*	—
Upper Barrel	*18*	*8.6*	*155*	*250*
Lower Barrel	*8*	*6.2*	*50*	*250*
Nozzle	*10*	*11*	*110*	—

Elapsed Time [min]	T_{upper} [°C] **I**	T_{lower} [°C] **II**	T_{nozzle} [°C] **III**	T_{mold1} [°C] **IV**	T_{mold2} [°C] **V**
$t_{mold} = 0$	*23*	*23*	*23*	*23*	*23*
$t_{barrel} = 66$	*39*	*43*	*51*	*75*	*76*
$t_{nozzle} = 66$	*39*	*43*	*51*	*75*	*76*
$t_{target} = 76$	*236*	*241*	*226*	*91*	*86*
$t_{inject} = 90$	*240*	*244*	*235*	*108*	*101*

Timer Start Threshold [cm]: *12*	Timer Stop Threshold [cm]: *3*
Injection Speed (Piston) [cm/s]: *16.2*	No Load Piston Speed [cm/s]: *17.9*
Hydraulic Pressure [psi]: *1,200*	Injection Pressure [psi]: *19,200*
Holding Time [s]: *10*	Cooling Time [min]: *10*

Remarks:

- *Good surface, but some textured areas, transparent*
- *Each side polished:*
  9 min 320, 8 min 1000, 2 min 2400, 11 min 4000 (300 rpm)
- *Final thickness: 2.8 mm*

NoObstacle4	Molded Weight: 3.660 g	
Material	**Content [wt%]**	**Weight [g]**
Matrix: PMMA	*75*	*6.0*
Fibers: BK-10	*25*	*2.0*
Tracers: Carbon	*0.1*	*0.008*
Total:	*100*	*8.008*

Power Supply	**Voltage [V]**	**Current [A]**	**Power [W]**	**Thermst [°C]**
Mold	*13*	*6.5*	*85*	—
Upper Barrel	*18*	*8.6*	*155*	*250*
Lower Barrel	*8*	*6.2*	*50*	*250*
Nozzle	*10*	*11*	*110*	—

Elapsed Time [min]	T_{upper} [°C] **I**	T_{lower} [°C] **II**	T_{nozzle} [°C] **III**	T_{mold1} [°C] **IV**	T_{mold2} [°C] **V**
$t_{mold} = 0$	*22*	*22*	*22*	*23*	*22*
$t_{barrel} = 103$	*44*	*48*	*41*	*82*	*83*
$t_{nozzle} = 103$	*44*	*48*	*41*	*82*	*83*
$t_{target} = 111$	*239*	*239*	*227*	*94*	*89*
$t_{inject} = 125$	*239*	*243*	*237*	*108*	*101*

Timer Start Threshold [cm]: *12*	Timer Stop Threshold [cm]: *3*
Injection Speed (Piston) [cm/s]: *16.1*	No Load Piston Speed [cm/s]: *17.5*
Hydraulic Pressure [psi]: *1,200*	Injection Pressure [psi]: *19,200*
Holding Time [s]: *10*	Cooling Time [min]: *10*

Remarks:

- *Textured surface, transparent*
- *Each side polished:*
  9 min 320, 8 min 1000, 2 min 2400, 11 min 4000 (300 rpm)
- *Final thickness: 2.75 mm*

NoObstacle5	Molded Weight: 3.690 g	
Material	**Content [wt%]**	**Weight [g]**
Matrix: PMMA	*75*	*6.0*
Fibers: BK-10	*25*	*2.0*
Tracers: Carbon	*0.1*	*0.008*
Total:	*100*	*8.008*

Power Supply	**Voltage [V]**	**Current [A]**	**Power [W]**	**Thermst [°C]**
Mold	*13*	*6.5*	*85*	—
Upper Barrel	*18*	*8.6*	*155*	*250*
Lower Barrel	*8*	*6.2*	*50*	*250*
Nozzle	*10*	*11*	*110*	—

Elapsed Time [min]	T_{upper} [°C] **I**	T_{lower} [°C] **II**	T_{nozzle} [°C] **III**	T_{mold1} [°C] **IV**	T_{mold2} [°C] **V**
$t_{mold} = 0$	*24*	*24*	*24*	*30*	*24*
$t_{barrel} = 72$	*42*	*44*	*39*	*83*	*83*
$t_{nozzle} = 72$	*42*	*44*	*39*	*83*	*83*
$t_{target} = 80$	*238*	*240*	*211*	*96*	*90*
$t_{inject} = 92$	*240*	*245*	*224*	*111*	*103*

Timer Start Threshold [cm]: *12*	Timer Stop Threshold [cm]: *3*
Injection Speed (Piston) [cm/s]: *11.0*	No Load Piston Speed [cm/s]: *12.1*
Hydraulic Pressure [psi]: *1,200*	Injection Pressure [psi]: *19,200*
Holding Time [s]: *10*	Cooling Time [min]: *10*

Remarks:

- *Textured areas, transparent*
- *Each side polished:*
  9 min 320, 8 min 1000, 2 min 2400, 11 min 4000 (300 rpm)
- *Final thickness: 2.7 mm*

NoObstacle6	Molded Weight: 3.680 g	
Material	**Content [wt%]**	**Weight [g]**
Matrix: PMMA	*75*	*6.0*
Fibers: BK-10	*25*	*2.0*
Tracers: Carbon	*0.1*	*0.008*
Total:	*100*	*8.008*

Power Supply	**Voltage [V]**	**Current [A]**	**Power [W]**	**Thermst [°C]**
Mold	*13*	*6.5*	*85*	—
Upper Barrel	*18*	*8.6*	*155*	*250*
Lower Barrel	*8*	*6.2*	*50*	*250*
Nozzle	*10*	*11*	*110*	—

Elapsed Time [min]	T_{upper} [°C] **I**	T_{lower} [°C] **II**	T_{nozzle} [°C] **III**	T_{mold1} [°C] **IV**	T_{mold2} [°C] **V**
$t_{mold} = 0$	*36*	*36*	*38*	*44*	*44*
$t_{barrel} = 45$	*38*	*42*	*61*	*77*	*77*
$t_{nozzle} = 45$	*38*	*42*	*61*	*77*	*77*
$t_{target} = 53$	*234*	*235*	*208*	*90*	*84*
$t_{inject} = 60$	*238*	*239*	*225*	*100*	*92*

Timer Start Threshold [cm]: *12*	Timer Stop Threshold [cm]: *3*
Injection Speed (Piston) [cm/s]: *8.4*	No Load Piston Speed [cm/s]: —
Hydraulic Pressure [psi]: *1,200*	Injection Pressure [psi]: *19,200*
Holding Time [s]: *10*	Cooling Time [min]: *10*

Remarks:

- *Textured surface, transparent*
- *Each side polished:*
  9 min 320, 8 min 1000, 2 min 2400, 11 min 4000 (300 rpm)
- *Final thickness: 2.90 mm*

NoObstacle7	Molded Weight: 3.580 g	
Material	**Content [wt%]**	**Weight [g]**
Matrix: PMMA	*80*	*6.4*
Fibers: BK-10	*20*	*1.6*
Tracers: Carbon	*0.1*	*0.008*
Total:	*100*	*8.008*

Power Supply	**Voltage [V]**	**Current [A]**	**Power [W]**	**Thermst [°C]**
Mold	*13*	*6.5*	*85*	—
Upper Barrel	*18*	*8.6*	*155*	*250*
Lower Barrel	*8*	*6.2*	*50*	*250*
Nozzle	*10*	*11*	*110*	—

Elapsed Time [min]	T_{upper} [°C] **I**	T_{lower} [°C] **II**	T_{nozzle} [°C] **III**	T_{mold1} [°C] **IV**	T_{mold2} [°C] **V**
t_{mold} = *0*	*23*	*23*	*23*	*23*	*23*
t_{barrel} = *107*	*44*	*44*	*41*	*79*	*78*
t_{nozzle} = *107*	*44*	*44*	*41*	*79*	*78*
t_{target} = *114*	*232*	*234*	*206*	*91*	*85*
t_{inject} = *127*	*240*	*241*	*227*	*109*	*101*

Timer Start Threshold [cm]: *12*	Timer Stop Threshold [cm]: *3*
Injection Speed (Piston) [cm/s]: *11.1*	No Load Piston Speed [cm/s]: *12.2*
Hydraulic Pressure [psi]: *1,200*	Injection Pressure [psi]: *19,200*
Holding Time [s]: *10*	Cooling Time [min]: *18*

Remarks:

- *Textured surface, transparent*
- *Each side polished:*
  9 min 320, 8 min 1000, 2 min 2400, 11 min 4000 (300 rpm)
- *Final thickness: 2.95 mm*

NoObstacle8	Molded Weight: 3.970 g	
Material	**Content [wt%]**	**Weight [g]**
Matrix: PMMA	*80*	*6.4*
Fibers: BK-10	*20*	*1.6*
Tracers: Carbon	*0.1*	*0.008*
Total:	*100*	*8.008*

Power Supply	**Voltage [V]**	**Current [A]**	**Power [W]**	**Thermst [°C]**
Mold	*13*	*6.5*	*85*	—
Upper Barrel	*18*	*8.6*	*155*	*250*
Lower Barrel	*8*	*6.2*	*50*	*250*
Nozzle	*10*	*11*	*110*	—

Elapsed Time [min]	T_{upper} [°C] **I**	T_{lower} [°C] **II**	T_{nozzle} [°C] **III**	T_{mold1} [°C] **IV**	T_{mold2} [°C] **V**
$t_{mold} = 0$	*24*	*24*	*25*	*25*	*26*
$t_{barrel} = 70$	*42*	*43*	*57*	*72*	*78*
$t_{nozzle} = 70$	*42*	*43*	*57*	*72*	*78*
$t_{target} = 80$	*229*	*232*	*210*	*90*	*86*
$t_{inject} = 89$	*239*	*241*	*233*	*105*	*97*

Timer Start Threshold [cm]: *12*	Timer Stop Threshold [cm]: *3*
Injection Speed (Piston) [cm/s]: *8.2*	No Load Piston Speed [cm/s]: *9.4*
Hydraulic Pressure [psi]: *1,200*	Injection Pressure [psi]: *19,200*
Holding Time [s]: *10*	Cooling Time [min]: *9*

Remarks:

- *Textured surface finish, transparent, some flash*
- *Each side polished:*
  9 min 320, 8 min 1000, 2 min 2400, 11 min 4000 (300 rpm)
- *Final thickness: 3.05 mm*

NoObstacle9	Molded Weight: 3.580 g	
Material	**Content [wt%]**	**Weight [g]**
Matrix: PMMA	*80*	*6.4*
Fibers: BK-10	*20*	*1.6*
Tracers: Carbon	*0.1*	*0.008*
Total:	*100*	*8.008*

Power Supply	**Voltage [V]**	**Current [A]**	**Power [W]**	**Thermst [°C]**
Mold	*13*	*6.5*	*85*	—
Upper Barrel	*18*	*8.6*	*155*	*250*
Lower Barrel	*8*	*6.2*	*50*	*250*
Nozzle	*10*	*11*	*110*	—

Elapsed Time [min]	T_{upper} [°C] **I**	T_{lower} [°C] **II**	T_{nozzle} [°C] **III**	T_{mold1} [°C] **IV**	T_{mold2} [°C] **V**
$t_{mold} = 0$	*21*	*21*	*22*	*23*	*23*
$t_{barrel} = 65$	*42*	*44*	*54*	*79*	*79*
$t_{nozzle} = 65$	*42*	*44*	*54*	*79*	*79*
$t_{target} = 75$	*238*	*240*	*233*	*98*	*91*
$t_{inject} = 81$	*240*	*241*	*237*	*104*	*96*

Timer Start Threshold [cm]: *12*	Timer Stop Threshold [cm]: *3*
Injection Speed (Piston) [cm/s]: *8.4*	No Load Piston Speed [cm/s]: *9.6*
Hydraulic Pressure [psi]: *1,200*	Injection Pressure [psi]: *19,200*
Holding Time [s]: *10*	Cooling Time [min]: *15*

Remarks:

- *Textured surface, transparent*
- *Each side polished:*
  9 min 320, 8 min 1000, 2 min 2400, 11 min 4000 (300 rpm)
- *Final thickness: 2.95 mm*

Obm2		
Material	**Content [wt%]**	**Weight [g]**
Matrix: PMMA	*70*	*5.6*
Fibers: BK-10	*30*	*2.4*
Tracers: Carbon	*0.1*	*0.008*
Total:	*100*	*8.008*

Power Supply	**Voltage [V]**	**Current [A]**	**Power [W]**	**Thermst [°C]**
Mold	*13*	*6.5*	*85*	—
Upper Barrel	*18*	*8.6*	*155*	*250*
Lower Barrel	*8*	*6.2*	*50*	*250*
Nozzle	*10*	*11*	*110*	—

Elapsed Time [min]	T_{upper} [°C] **I**	T_{lower} [°C] **II**	T_{nozzle} [°C] **III**	T_{mold1} [°C] **IV**	T_{mold2} [°C] **V**
$t_{mold} = 0$	*24*	*24*	*24*	*24*	*24*
$t_{barrel} = 20$	*41*	*46*	*49*	*48*	*48*
$t_{nozzle} = 20$	*41*	*46*	*49*	*48*	*48*
$t_{target} = 50$	*260*	*263*	*258*	*107*	*98*
$t_{inject} = 55$	*262*	*266*	*261*	*109*	*100*

Timer Start Threshold [cm]: *12*	Timer Stop Threshold [cm]: *3*
Injection Speed (Piston) [cm/s]: *4.1*	No Load Piston Speed [cm/s]: *4.9*
Hydraulic Pressure [psi]: *1,200*	Injection Pressure [psi]: *19,200*
Holding Time [s]: *10*	Cooling Time [min]: *10*

Remarks:

- *Good surface, transparent*
- *Polished*
- *Final thickness: 3.0 mm*

LIST OF REFERENCES

Advani, S.G, and Tucker, C.L. (1985). A Tensor Description of Fiber Orientation in Short Fiber Composites. *SPE Technical Paper, 31*, pp. 1113–1118.

Advani, S.G., and Tucker, C.L. (1987). The Use of Tensors to Describe and Predict Fiber Orientation in Short Fiber Composites. *Journal of Rheology, 31*, pp. 751–784.

Advani, S.G. (1987). *Prediction of Fiber Orientation During Processing of Short Fiber Composites.* Unpublished doctoral dissertation, University of Illinois at Urbana-Champaign.

Altan, M.C., (1989). Rheology of Fiber Suspensions and Orientation Analysis in Flow Processes. Center for Composite Materials Report CCM-89-24, University of Delaware, Newark, Delaware 19716, USA.

Altan, M.C., Advani, S.G., Güçeri, S.I., and Pipes, R.B. (1989). On the Description of the Orientation State for Fiber Suspensions in Homogeneous Flows. *Journal of Rheology, 33*(7), pp. 1129–1155.

Altan, M.C., Subbiah, S., Güçeri, S. I., and Pipes, R. B. (1990). Numerical Prediction of Three-Dimensional Fiber Orientation in Hele-Shaw Flows. *Polymer Engineering and Science, 30*(14), pp. 848–859.

Arp, P.A. and Mason, S.G. (1977). Interactions Between Two Rods in Shear Flow. *J. Coll. Interf. Sci., 59*, p. 378.

Badami, D.V. private communication with Darlington, McGinley, and Smith (1976).

Bader, M.G. and Chou, T.W. (1979). On the Strength of Discontinuous-Fiber Composites with Polymeric Matrices. *New Developments and Applications in Composites*, ed. D. Wilsdorf, TMS-AIME.

Batchelor, G.K. (1971). *Journal of Fluid Mechanics, 46*, p. 813.

Bay, R.S., and Tucker, C.L. (1991a). Fiber Orientation in Simple Injection Moldings. Part I: Theory and Numerical Methods. *Plastics and Plastic Composites: Material Properties, Part Performance, and Process Simulation, MD-29, ASME*, pp. 445–471.

Bay, R.S., and Tucker, C.L. (1991b). Fiber Orientation in Simple Injection Moldings. Part II: Experimental Results. *Plastics and Plastic Composites: Material Properties, Part Performance, and Process Simulation, MD-29, ASME*, pp. 473–492.

Bay, R.S., and Tucker, C.L. (1992a). Fiber Orientation in Simple Injection Moldings. Part I: Theory and Numerical Methods. *Polymer Composites, 13*(4), pp. 317–331.

Bay, R.S., and Tucker, C.L. (1992b). Fiber Orientation in Simple Injection Moldings. Part II: Experimental Results. *Polymer Composites, 13*(4), pp. 332–341.

Bay, R.S., and Tucker, C.L. (1992c). *Polymer Engineering and Science, 32*, p. 240.

Bell, J.P. (1969). Flow Orientation of Short Fiber Composites. *Journal of Composite Materials, 3*, p. 244.

Benveniste, Y. (1987). A New Approach to the Application of Mori-Tanaka's Theory in Composite Materials. *Mechanics of Materials, 6*, pp. 147–157.

Berger, J.L. and Gogos, C.G. (1971). *Technical Papers*, 29th Annual Technical Conference, Society of Plastics Engineers, *8*, New York.

Berger, J.L. and Gogos, C.G. (1973). *Polymer Engineering Science*, *13*, p. 102.

Bird, B.R., Armstrong, R.C., and Hassager, O. (1987). *Dynamics of Polymeric Liquids: Volume 1, Fluid Mechanics*, Wiley, New York.

Blanc, S., Philipon, S., Vincent, M., Aggasant, J.F., Alglave, H., Muller, R., and Froelich, D. (1987). Important Flow Parameters in Determining Fiber Orientation. *Int. Plym. Proc.*, *2*, p. 21.

Blumentritt, B.F., Vu, B.T., and Cooper, S.L. (1974). The Mechanical Properties of Oriented Discontinuous Fiber-Reinforced Thermoplastics I. Unidirectional Fiber Orientation. *Polymer Engineering Science*, *14*(9), pp. 633–640.

Boukhili, R., Gauvin, R., and Gosselin, M. (1989). The Effect of Weld-Lines on the Fatigue Resistance of Short Glass Fiber Reinforced Polycarbonate. *Journal of Thermoplastic Composite Materials*, *2*, pp. 78–90.

Bowyer, W.H. and Bader, M.G. (1972) *J. Mater. Sci.*, *7*, p. 1315.

Bright, P.F., Crowson, R.J., and Folkes, M.J. (1978). A Study of the Effect of Injection Speed of Fiber Orientation in Simple Mouldings of Short Glass Fibre-Filled Polypropylene. *Journal of Materials Science*, *13*, pp. 2497–2506.

Bright, P.F. and Darlington, M.W. (1981). Factors Influencing Fiber Orientation and Mechanical Properties of Fibre-Reinforced Thermoplastics Injection Moldings, *Plastics and Rubber Processing Applications*, *1*(2), pp. 139–142.

Brunn, P. (1980). *Journal of Non-Newtonian Fluid Mechanics*, *7*, p. 271.

Bur, A.J., and Gallant, F.M. (1991). Fluorescence Monitoring of Twin Screw Extrusion. *Polymer Engineering and Science*, *31*(19), pp. 1365–1371.

Burgers, J. (1938). *Second Report on Viscosity and Plasticity*, North Holland Publ., Amsterdam.

Camacho, C.W. and Tucker, C.L., Yalvac, S., and McGee, R.L. (1990). *Polym. Compos.*, *11*, p. 229.

Castro, J. and Macosko, C. (1987). Studies of Mold Filling and Curing in the Reaction-Injection Molding Process. *A.I.Ch.E. Journal*, *28*, pp. 250-260.

Chamis, C.C and Sendeckyj, G.P. (1968). Critique on Theories Predicting Thermoelastic Properties of Fibrous Composites, *Journal of Composite Materials*, *2*, p. 232.

Chang, C.I., Conway, H.D., and Weaver, T.C. (1972). The Elastic Constants and Bond Stresses for Three-Dimensional Composite Reinforced by Discontinuous Fibers. *Fiber Science and Technology*, *5*, pp. 143–162.

Chen, C.Y., and Tucker, C.L. (1984). Mechanical Property Predictions for Short Fiber/Brittle Matrix Composites. *Journal of Reinforced Plastic Composites*, *3*, pp. 120–129.

Chin, W.K., Liu H.T., and Lee, Y.D. (1988). Effects of Fiber Length and Orientation Distribution on the Elastic Modulus of Short Fiber Reinforced Thermoplastics. *Polymer Composites*, *9*(1), pp. 27–35.

Chou, T.W. and Kelly, A. (1976). "Fiber Composites" in *Challenges and Opportunities in Materials Science and Engineering, Mat. Sci. Eng., 25*, p. 35.

Chou, T.W. and Nomura, S. (1980). Fiber Orientation Effects on the Thermoelastic Properties of Short-Fiber Composites. *Fiber Science and Technology, 14*, pp. 279–291.

Chou, T.W., Nomura, S., and Taya, M. (1980). A Self-Consistent Approach to the Elastic Stiffness of Short-Fiber Composites. *Journal of Composite Materials, 14*, pp. 178–188.

Choy, C.L., Leung, W.P., and Kowk, K.W. (1992). Elastic Moduli and Thermal Conductivity of Injection-Molded Short-Fiber-Reinforced Thermoplastics. *Polymer Composites, 13*(2), pp. 69–80.

Conway, H.D., and Chang, C.I. (1971). The Effective Elastic Constants and Bond Stresses for a Fiber Reinforced Elastic Sheet. *Fiber Science and Technology, 5*, pp. 249–260.

Christensen, R.M. (1979). *Mechanics of Composite Materials*, Wiley-Interscience, New York.

Chu, J.N., Wu, G.M. and Schultz, J.M. (1988). Effects of Microstructrure on Failure in Peek and its Short-Fiber Composites. *Composite Mechanics*, pp 93–102.

Cook, J. (1968). The Elastic Constants of an Isotropic Matrix Reinforced with Imperfectly Oriented Fibres. *British Journal of Applied Physics (J. Phys. D.) Sec. 2, 1*, pp. 799–812.

Curtiss, A.C., Hope, P.S., and Ward, I.M. (1982). Modulus Development in Oriented Short-Glass-Fiber Reinforced Polymer Composites. *Polymer Composites, 3*, p. 138.

Darlington, M.W., Gladwell, B.K., and Smith, G.R. (1977). Structure and Mechanical Properties in Injection Molded Discs of Glass Reinforced Polypropylene. *Polymer, 18*, pp. 1269–1274.

Darlington, M.W., and McGinley, P.L. (1975). Fiber Orientation Distribution in Short Fibre Reinforced Plastics. *Journal of Materials Science–Letters, 10*, pp. 906–910.

Darlington, M.W., McGinley, P.L., and Smith, G.R. (1976). Structure and Anisotropy of Stiffness in Glass Fibre-Reinforced Thermoplastics. *Journal of Materials Science, 11*, pp. 877–886.

Darlington, M.W., McGinley, P.L., and Smith, G.R. (1977). *Plast. Rubber Mater. Appl., 2*, p. 51.

Darlington, M.W. and Smith, G.R. (1975). *Polymer, 16*, p. 459.

Darlington, M.W. and Smith, G.R. (1977). *Proc. Inst. Civ. Eng. Conf. 'Fibre Reinforced Materials: Design and Engineering Applications' London*, p. 57.

Darlington, M.W., and Smith, G.R. (1987). Some Features of the Injection Molding of Short Fiber Reinforced Thermoplastics in Center Sprue-Gated Cavities. *Polymer Composites, 8*, p. 16.

Davis, R.B. (1988). *Experimentation on Fiber Orientation in Injection Molded Short-Fiber Reinforced Composites.* Unpublished master's thesis, University of Illinois at Urbana-Champaign.

Delpy, U., and Fischer, G. (1985). Effect of Mold-Filling Conditions on Fiber Distribution in Injection-Molded Disks and on the Mechanical Properties of Such Disks. *Advances in Polymer Technology, 5*, p. 19.

Denton, D.L., and Munson-McGee, S.H. (1985). Use of X-Radiographic Tracers to Measure Fiber Orientation in Short Fiber Composites, Special Technical Publication 873, ASTM, Philadelphia.

Dinh, S.M., and Armstrong, R.C. (1984). A Rheological Equation of State for Semiconcentrated Fiber Suspensions. *Journal of Rheology, 28*(3), pp. 207–227.

Doshi, S.R., Dealy, J.M., and Charrier, J.M. (1986). Flow Induced Fiber Orientation in an Expanding Tubing Die. *Polymer Engineering and Science, 26*(7), pp. 468–478.

Dunlap, P.N. and Howe S.E. (1991). Design of Particulate Composites for Optical Applications. *Polymer Composites, 12*(1), pp. 39–47.

Eduljee, R.F., and Gillespie, J.W. Jr. (1990). Analytical Solutions for Fiber Orientation in 2-D Flows of Dilute Suspensions. *Polymer Composites, 11*(1), pp. 56–64.

Eduljee, R.F., Gillespie, J.W. Jr., and McCullough, R.L. (1991). On the Application of Micromechanics to the Prediction of Macroscopic Thermal Residual Stresses in Short-Fiber Reinforced Polyetheretherketone. *Polymer Engineering and Science, 31*(17), pp. 1257–1263.

Engstrom, A. (1956). in "Physical Techniques in Biological Research," *3*, edited by G. Oster and A.W. Pollister (Academic Press, New York), p. 495.

Eshelby, J.D. (1957). The Determination of the Elastic Field of an Ellipsoidal Inclusion and Related Problems. *Proceedings of the Royal Society (London), A241*, p. 376.

Fakirov, S., and Fakirova, C. (1985). Direct Determination of the Orientation of Short Glass Fibers in an Injection-Molded (Polyethylen Terephthalate) System. *Polymer Composites, 6*(1), pp. 41–46.

Fan, C.F., and Hsu, S.L. (1989). Effects of Fiber Orientation on the Stress Distribution in Model Composites. *Journal of Polymer Science: Part B: Polymer Physics, 27*, pp. 2605–2619.

Ferrari, M., and Johnson, G.C. (1989). Effective Elasticities of Short-Fiber Composites With Arbitrary Orientation Distribution. *Mechanics of Materials, 8*, pp. 67–73.

Filbert, W.C. (1969). *Soc. Plast. Eng. J., 25*, p. 65.

Fisa, B., and Rahmani, M. (1991). Weldline Strength in Injection Molded Glass Fiber–Reinforced Polypropylene. *Polymer Engineering and Science, 31*(18), pp. 1330–1336.

Fischer, G. and Eyerer, P. (1985). Fiber Orientation and Thermal Expansion of Short Fiber Reinforced Thermoplasics. *SPE Technical Paper, 31*, p. 532.

Fischer, G. and Eyerer, P. (1988). Measuring Spatial Orientation of Short Fiber Reinforced Thermoplastics by Image Analysis. *Polymer Composites*, *9*(4), pp. 297–304.

Fischer, G., Schwarz, P., Mueller, U., and Fritz, U. (1990). Measuring Spatial Fiber Orientation—A Method for Quality Control of Fiber Reinforced Plastics. *Advances in Polymer Technology*, *10*(2), pp. 135–141.

Folgar, F. (1983). *Fibre Orientation Distribution in Concentrated Suspensions: A Predictive Model.* Unpublished doctoral dissertation, University of Illinois, Urbana-Champaign.

Folgar, F. and Tucker, C. (1984). Orientation Behavior of Fibers in Concentrated Suspensions. *Journal of Reinforced Plastic Composites*, *3*, pp. 98–119.

Folkes, M.J, and Russell, D.A.M. (1980). Orientation Effects During the Flow of Short Fiber Reinforced Thermoplastics. *Polymer*, *21*, pp. 1252–1258.

Friedrichs, B., Güçeri, S.I., Subbiah, S., and Altan, M.C. (1991). Simulation and Analysis of Mold Filling Processes with Polymer-Fiber Composites: TGMOLD. *Processing of Polymers and Polymeric Composites*, *MD-19*, pp. 73–90.

Friedrichs, B., Walter, R. (1987). Fracture Toughness of Short Fiber/Thermoplastic matrix Composites, Compared on the Basis of Different Test Methods. *Polymer and Composites Group*, Technical University Hamburg-Harburg, West Germany.

Fukuda, H. and Kawata, K. (1974). On Young's Modulus of Short Fiber Composites. *Fibre Science and Technology*, *7*, pp. 207–222.

Fuller, G. G., and Ylitalo, C.M. (1990). Optical Rheology of Polymeric Liquids. *Polymer Rheology and Processing.*

Ganani, E. and Powell, R.L. (1985). Suspensions of Rodlike Particles: Literature Review and Data Correlations. *Journal of Composite Materials*, *19*, pp. 194–215.

Gillespie, J.H., Vanderschuren, J.A., and Pipes, R.B. (1983). *SPE ANTEC Tech. Papers*, *32*, p. 684.

Givler, R.C. (1983a) in *Transport Phenomenon in Material Processing*, M.M. Chen, J. Mazumder, C.L. Tucker eds. ASME, New York.

Givler, R.C. (1983b). *Numerical Techniques for the Prediction of Flow Induced Fiber Orientation.* Unpublished Doctoral Dissertation, Center for Composite Materials, University of Delaware.

Givler, R.C, Crochet, M.J., and Pipes, R.B. (1983). Numerical Prediction of Fiber Orientation in Dilute Suspensions. *Journal of Composite Materials*, *17*, pp. 330–343.

Givler, R.C. (1986). Quantitative Description of In Situ Fiber Orientation State with Image Processing Techniques, Sandia Report, SAND86-0075, Sandia National Laboratory, October 1986. [TJ 267.S29 1986]

Goettler, L.A. (1970a). Flow Orientation of Short Fibers in Transfer Molding. *Proceedings of the 25th Annual Conference, SPI RP/C Div., Sect. 14-A.*

Goettler, L.A. (1970b). Controlling Flow Orientation in Molding of Short-Fiber Compounds. *Modern Plastics*, *47*, p. 140.

Goettler, L.A. (1984). Mechanical Property Enhancement in Short Fiber Composites Through the Control of Fiber Orientation During Fabrication. *Polymer Composites, 1*, p. 60.

Goldsmith, H.L. and Mason, S.G. (1962). *J. Colloid Sci., 17*, p. 448.

Goldsmith, H.L. and Mason, S.G. (1967). *Rheology, 4*, E.R. Eirich, Ed., Academic Press, New York.

Gutowski, T.G., Cai, Z., Bauer, S., and Boucher, D. (1987). Consolidation Experiments for Laminate Composites. *Journal of Composite Materials, 21*, pp. 650–669.

Halpin, J.C. and Tsai, S.W. (1967). Environmental Factors in Composite Materials Design. *AFML TR, 67*, p. 423.

Halpin, J.C., and Pagano, N.J. (1969). The Laminate Approximation for Randomly Oriented Fibrous Composites. *Journal of Composite Materials, 3*, p. 720.

Halpin, J.C., Jerine, K, and Whitney, J.M. (1971). *Journal of Composite Materials, 5*, p. 36.

Halpin, J.C. and Kardos, J.L. (1978). *Polymer Engineering Science, 18*, p. 496.

Hand, G.L. (1962) *Journal of Fluid Mechanics, 13*, p. 33.

Harris, J.B, and Pittman, J.F.T. (1975). Equivalent Ellipsoidal Aspect Ratios of Slender Rod-Like Particles. *J. of Coll. Interf. Sci. 50*, p. 280.

Harry, D.H. and Parrott, R.G. (1970). *Polymer Engineering Science, 10*, p. 209.

Hashin, Z. and Shtrikman, S. (1962a). *J. Mech. Phys. Solids, 10*, p. 335.

Hashin, Z. and Shtrikman, S. (1962b). *J. Mech. Phys. Solids, 10*, p. 343.

Hashin, Z. and Shtrikman, S. (1963). *J. Mech. Phys. Solids, 127*, p. 335.

Hashin, Z. and Rosen, B.W. (1964). The Elastic Modulii of Fiber-Reinforced Materials. *Journal of Applied Mechanics, 31*, pp. 223–232.

Hashin, Z. (1983). Analysis of Composite Materials—A Survey. *Journal of Applied Mechanics, 50*, p.481.

Hegler, R. (1984). Fiber Orientation in the Processing of Short-Fiber Reinforced Thermoplastics. *Kunststoffe German Plastics, 74*, pp. 12–17.

Heiber, N. (1987). Melt-Viscosity Characterization and its Application to Injection Molding. *Injection and Compression Molding Fundamentals*, A.I. Isayev, ed., Marcel Dekker, New York.

Hermans, J.J. (1967). The Elastic Properties of Fibre Reinforced Materials When the Fibers are not Aligned. *Proc. Konigl. Nederl*, Akad. van Weteschappen Amsterdam, Series B, *70*, pp. 1–9.

Hieber, C.A., and Shen, S.F. (1980). A Finite- Element/Finite Difference Simulation of the Injection- Molding Filling Process. *Journal of Non-Newtonian Fluid Mechanics, 7*, pp. 1–32.

Hill, R. (1963). Elastic Properties of Reinforced Solids: Some Theoretical Principles. *J. Mech. Phys. Solids, 11*, p. 357.

Hill, R. (1965a). Theory of Mechanical Properties of Fiber-Strengthened Materials–III. Self-Consistent Model, *J. of Mech. Phys. Solids, 13*, pp. 189–198.

Hill, R. (1965b). A Self-Consistent Mechanics of Composite Materials. *J. of Mech. Phys. Solids, 13*, pp. 213–225.

Hisch, A.E. (1987). Applied Fiber Orientation Prediction in Injection Molding, Proceedings of the 45th Annual Technical Conference of the SPE, Los Angeles.

Hogg, P.J. (1986). The Influence of Flow-induced Anisotropy on the Impact Behavior of Injection-moulded Short-fibre Composites. *Composites Science and Technology, 29*, pp. 89–102.

Hough, R.V. (1962). Method and Means for Recognizing Complex Patterns. US Patent 306954.

Jackson, W.C., Advani, S.G., and Tucker C.L. (1986). Predicting the Orientation of Short Fibers in Thin Compression Moldings. *Journal of Composite Materials, 20*, pp. 539–557.

Jackson, W.C. (1983). Unpublished master's thesis. University of Illinois, Urbana.

Jackson, W.C., Folgar, F. and Tucker, C.L. (1984). Prediction and Control of Fiber Orientation in Molded Parts. *Polymer Blends and Composites in Multiphase Systems*, C.D. Han, ed., *Adv. Chem. Ser. 206*, p. 279, ACS, Washington. [Chem: QD 1.A355 No. 206]

Jeffery, G.B. (1922). The Motion of Ellipsoidal Particles Immersed in a Viscous Fluid. *Proceedings Royal Society (London), 102a*, pp. 161–179.

Kaito, A., Kyotani, M. and Nakayama, K. (1992). Application of Fourier Transform infrared microspectroscopy to the analysis of microscopic Orientation in liquid crystalline polymer sheets. *Polymer, 33(13)*, pp. 2672–2678.

Kamal, M.R. and Kenig, S. (1972). *Technical Papers*, 30th Annual Technical Conference, Society of Plastics Engineers, p. 679, Chicago.

Karnis, A. and Mason, S.G. (1966). Particle Motions in Sheared Suspensions XIX. Viscoelastic Media. *Trans. Soc. Rheol., 10*(2), p. 571.

Katti, S.S., and Schultz, J.M. (1982). Injection Molding: Microstructure and Properties–a review. *Polymer Engineering Science, 22*, pp. 1001-1018.

Kau, H.T. (1987). Determination of the Orientation of Short Glass Fibers in Sheet Molding Compound (SMC). *Polymer Composites, 8*(2), pp. 82–83.

Kelly, A., and Tyson, W.R. (1965). Tensile Properties of Fiber Reinforced Metals; Copper/Tungsten and Copper/Molybdenum. *J. Mech. Phys. Solids, 13*, pp. 178–188.

Kenig, S., B. Trattner, and H. Anderman. (1988). Orientation Development in Molding of Short-Fiber Liquid Crystalline Polymer Composites. *Polymer Composites, 9*(1), pp. 20–25.

Kerker, M. (1969). *The Scattering of Light*, Academic Press, New York.

Knibbs, R.H., and Morris, J.B. (1974). The Effects of Fibre Orientation on the Physical Properties of Composites. *Composites*, pp. 209–218.

Knutsson, B.A., White, J.L., and Abbas, K.B. (1981). Rheological and Extrusion Characteristics of Glass Fiber-Reinforced Polycarbonate. *Journal of Applied Polymer Science, 26*, pp. 2347–2362.

Kocsis, J.K., and Friedrich K. (1988). Fracture Behavior of Injection- Molded Short and Long Glass Fiber-Polyamide 6.6 Composites. *Composites Science and Technology, 32*, pp. 293–325.

Konicek, T.S. (1987). A Method to Determine Three-Dimensional Fiber Orientation in Fiber Reinforced Polymers. Unpublished master's thesis, University of Illinois as Urbana-Champaign.

Laun, H.M. (1984). *Colloid. Polym. Sci., 262*, p. 257.

Laws, N. and McLaughlin, R. (1979). The Effect of Fibre Length on the Overall Moduli of Composite Materials. *Journal of Mech. Phys. Solids, 27*, pp. 1–13.

Leal, L.G. (1975). *Journal of Fluid Mechanics, 69*, p. 305.

Lee, W.I. (1987). A Model of the Manufacturing Process of Thermoplastic Matrix Composites. *Journal of Composite Materials, 21*, pp. 1017–1055.

Lees, J.K. (1968). A Study of the Tensile Modulus of Short Fiber Reinforced Plastics. *Polymer Engineering Science, 8*, pp. 186–194.

Lockett, F.J. (1980). *Plast. Rubber. Process., 6*, p. 85.

Lord, H. and Williams, G. (1975). Mold-Filling Studies for the Injection Molding of Thermoplastic Materials. Part II: The Transient Flow of Plastic Materials in the Cavities of Injection Molding Dies. *Polymer Engineering and Science, 15*(8), pp. 569–582.

Lovrich, M.L., and Tucker, C.L. (1985). Automated Measurement of Fiber Orientation in Short Fiber Composites. *SPE Technical Paper, 31*, pp. 1119–1122.

Malzahn, J.C., and Schultz, J.M. (1986). Transverse Core Fiber Alignment in Short-Fiber Injection-Molding. *Composites Science and Technology, 25*, pp. 187–192.

Maschmeyer, R.O., and Hill, C.T. (1974). *Advances in Chemistry, 134*, p. 95.

Matthaei, E. (1986). Bremen.

Matsuoka, T., Takabatake, J., Inoue, Y., and Takahashi, H. (1990). Prediction of Fiber Orientation in Injection Molded Parts of Short-Fiber-Reinforced Thermoplastics. *Polymer Engineering and Science, 30*(16), pp. 957–966.

Mavridis, H., Hrymak, A.N., and Vlachpoulos, J. (1986). Finite Element Simulation of Fountain Flow in Injection Molding. *Polymer Engineering and Science, 26*(7), pp. 449–454.

Mavridis, H., Hrymak, A.N., and Vlachpoulos, J. (1988). The Effect of Fountain Flow on Molecular Orientation in Injection Molding. *Journal of Rheology, 32*, p. 639.

McGee, S.H. (1982) The Influence of Microstructure on the Elastic Properties of Composite Materials. Unpublished doctoral dissertation, Department of Chemical Engineering, University of Delaware, Newark, Delaware.

McCullough, R.L., Wu, C.T., Seferis, J.C., and Lindenmeyer, P.H. (1976). *Polymer Engineering Science, 16*, p. 371.

McGee, S.H. and McCullough, R.L. (1984). Characterization of Fiber Orientation in Short-fiber Composites. *Journal of Applied Physics, 55*(5), pp. 1394–1403.

Menges, G., and Geisbusch, P. (1982). The Glass Fiber Orientation and its Influence on Mechanical Properties of Thermoplastics Injection Moldings –An Appraisal Method. *Colloid & Polymer Science, 260*, p. 73.

Metropolis, N., Rosenbluth, A., Rosenbluth, M., Teller, A., and Teller, E. (1953). Equation of State Calculations by Fast Computing Machines. *Journal of Chem. Physics, 21*, p. 1087.

Meirovitch, L. (1970). Methods of Analytical Dynamics. McGraw-Hill Book Company.

Michaeli, W., and Menges, G. (1989). Prediction of Product Properties in Extrusion and Injection Molding. *Advances in Polymer Technology, 9*(1), pp. 69–85.

Mori, T., and Tanaka, K. (1973). Average Stress in Matrix and Average Elastic Energy of Materials With Misfitting Inclusions. *Acta Metal., 21*, p. 571.

Mukhopadhyay, A.K. (1981). Unpublished doctoral dissertation, University of Delaware.

Mura, T. (1982). *Micromechanics of Defects in Solids*, Martinus Nijhoff, The Hague.

Mutel, A.T., and Kamal, M.R. (1991). Rheological Behavior and Fiber Orientation in Slit Flow of Fiber Reinforced Thermoplastics. *Polymer Composites, 12*(3), pp. 137–145.

O'Connell, P.A., and R.A. Duckett. (1991). Measurements of Fibre Orientation in Short-Fibre-Reinforced Thermoplastics. *Composite Science and Technology, 42*, pp. 329–347.

Ott, S. (1988). Calculation of the Properties and Orientation in Injection Moulded Parts. *Engineering Plastics, ed. K.M. Watkinson.??*, pp. 437–466.

Owen, M.J., Thomas, D.H., and Found M.S. (1978). Flow Patterns and Fiber Orientation in Molding Polyester BMC. *Modern Plastics*, pp. 61–65.

Owen, M.J., and Whybrew, K. (1976). Fibre Orientation and Mechanical Properties in Polyester Dough Moulding Compounds (DMC). *Plastic and Rubber, 1*(6), pp. 231–237.

Pearson, J.R.A. (1977). Variable-Viscosity Flows in Channels with High Heat Generation, *Journal of Fluid Mechanics, 83*, p. 119.

Pearson, J.R.A. (1985). *Mechanics of Polymer Processing*, Elsevier Applied Science, London.

Pearson, J.R.A. (1987). Polymer Flows Dominated by High Heat Generation and Low Heat Transfer, *Polymer Engineering & Science, 18*, p. 5.

Pipes, R.B., McCullough, R.L., and Taggart, D.G. (1982). Behavior of Discontinuous Fiber Composites: Fiber Orientation. *Polymer Composites, 3*, p. 120.

Press, W.H., Flannery, B.P., Teukolsky, S.A., and Vetterling, W.T. (1988). *Numerical Recipes in C: The Art of Scientific Computing*, Cambrigde University Press, Cambridge.

Reifschneider, L.G., Akay, H.U., and Ladeinde, F. (1990). Fiber Orientation Prediction for Three-Dimensional Injection and Compression Molded Parts. *Computer Modeling and Simulation of Manufacturing Processes, MD-20, PED-48, ASME*, pp. 129–137.

Reimann, S. (1992). Investigations on an Experimental Injection Unit. Unpublished Studienarbeit Thesis, Michigan State University, East Lansing.

Richardson, S.M. (1979). Extended Leveque Solutions for Flows of Power-law Fluids in Pipes and Channels. *Journal of Heat and Mass Transfer*, *22*, p. 1417.

Richardson, S.M. (1983). Injection Moulding of Thermoplastics: Freezing During Mould Filling. *Rheo. Acta*, *22*, p. 223.

Richardson, S.M. (1983). Molding. *Computational Analysis of Polymer Processing*, Pearson, J.R.A, and Richardson, S.M. ed., Applied Sci. Pub., London.

Richardson, S.M. (1986). Injection Moulding of Thermoplastics: Freezing of Variable-Viscosity Fluids. Part I: Developing Flows with Very High Heat Generation. *Rheo. Acta*, *25*, p. 180.

Richardson, S.M. (1986). Injection Moulding of Thermoplastics: Freezing of Variable-Viscosity Fluids. Part II: Developing Flows with Very Low Heat Generation. *Rheo. Acta*, *25*, p. 308.

Richardson, S.M. (1986). Injection Moulding of Thermoplastics: Freezing of Variable-Viscosity Fluids. Part III: Fully-developed Flows. *Rheo. Acta*, *25*, p. 372.

Richardson, S.M. (1987). Flows of Variable-Viscosity Fluids in Ducts With Heated Walls. *Journal of Non-Newtonian Fluid Mechanics*, *25*, p. 137.

Richardson, S.M. (1989). Simplified Geometry Models. *Fundamentals of Computer Modeling for Polymer Processing*, Tucker, C.L. ed., Hanser, Munich.

Rose, W. (1961). Fluid-Fluid Interfaces in Steady Motion. *Nature*, *191*, p. 242.

Rothe, J. (1972). *Kunstoffe*, *62*, p. 142.

Russell, W. (1973). On the Effective Moduli of Composite Materials: Effect of Fiber Length and Geometry at Dilute Concentration. *J. Appl. Math. Phys. (ZAMP)*, *24*, p. 591.

Sanou, M., Chung, B., and Cohen, C. (1985). Glass Fiber-Filled Thermoplastics. II. Cavity Filling and Fiber Orientation in Injection Molding. *Polymer Engineering and Science*, *25*, pp. 1008-1016.

Sato, N., Kurauchi, T., Sato S., Kamigaito, O. (1988). Reinforcing Mechanism by Small Diameter Fiber in Short Fiber Composite. *Journal of Composite Materials*, *22*, pp. 850–873.

Schlich, W.R., Hagan, R.S., Thomas, J.R., Thomas, D.P., and Musselman, K.A. (1968). *Soc. Plast. Eng. J.*, *24*, p. 43.

Schöche, N. (1993). Fiber Orientation in Transparent Short Fiber-Reinforced Thermoplastics. Unpublished Diplomarbeit Thesis, Michigan State University, East Lansing.

Schwarz, P., Fischer, G., and Mueller, U. (1988). IBAS Meeting, Boppard.

Seferis, J.C., McCullough, R.L., and Samuels, R.J. (1976). *Polymer Engineering Science*, *16*, p. 334.

Seferis, J.C. (1986). *Polymer Composites*, *7*(3), p. 158.

Shanker, R., Gillespie, J.W. Jr., and Güçeri, S.I. (1990). Rheology of Fiber Suspensions in Nonhomogeneous Flow Fields: Translation Induced Stresses. *Computer*

Modeling and Simulation of Manufacturing Processes, MD- 20, PED-48, pp. 265–272.

Solc, J., Nichols, K., and Schiller, L. (1992). Relationship between Filler Geometry and Anisotropy in Injection Molded Engineering Thermoplastic Composites. *ANTEC*, pp. 2628–2630.

Soto, C.A. (1991). Homogenization and Optimal Bounds in Linear Elasticity, MMM-990, Michigan State University.

Steif, P.S. and Hoysan, S.F. (1987). An Energy Method for Calculating the Stiffness of Aligned Short-Fiber Composites. *Mechanics of Material, 6*, p. 197.

Stein, R.S. (1961). *Journal of Polymer Science, 50*, p. 339.

Stephenson, R.C, Turner, S., and Whale, M. (1979). The Mean Stiffness of Thermoplastic Composites. *Composites, 10*, pp. 153–160.

Suchsland, O. and McMillin, C. W, (1983). On the Measurement of Fiber Orientation in Fiberboard. *Forest Products Journal, 33*(10), pp. 39–42.

Tadmor, Z. (1974). Molecular Orientation in Injection Molding. *Journal of Applied Polymer Science, 18*, p. 1753.

Tadmor, Z., and Gogos, C.G. (1979). *Principles of Polymer Processing*, Wiley, New York.

Taggart, D.G., and Pipes, R.B. (1979). Processing Induced Fiber Orientations in Transfer and Injection Molding, Report No. 12, Center for Composite Materials, University of Delaware, Newark, Delaware.

Takano, M. (1974). Monsanto/Washington Univ. Assoc., HPC Program Report 70-116.

Takao, Y., Chou, T.W., and Taya, M. (1982). Effective Longitudinal Young's Modulus of Misoriented Short Fiber Composites. *Journal of Applied Mechanics, 49*, pp. 536–540.

Takserman-Krozer, R. and Ziabicki, A. (1963). *Journal of Polymer Science, 1*, p. 491.

Taya, M. (1981). On the Stiffness and Strength of an Aligned Short-Fiber Reinforced Composite Containing Penny-Shaped Cracks in the Matrix. *Journal of Composite Materials, 15*, p. 198.

Taya, M., and Chou, T.W. (1981). On Two Kinds of Ellipsoidal Inhomogeneities in an Infinite Elastic Body: An Application to a Hybrid Composite. *International Journal of Solids and Structures, 17*, pp. 553–563.

Taya, M., and Mura, T. (1981). On Stiffness and Strength of an Aligned Short-Fiber Reinforced Composite Containing Fiber-End Cracks Under Uniaxial Applied Stress. *ASME Journal of Applied Mechanics, 48*, pp. 361–367.

Toll, S., and Andersson, P.-O. (1991). Microstructural Characterization of Injection Moulded Composites Using Image Analysis. *Composites, 22*(4), pp. 298–306.

Tucker, C.L. (1987). Compression Molding of Polymers, Injection and Compression Molding Fundamentals, ed. Avraam I. Isayev.

Van de Hulst, H.C. (1957). *Light Scattering By Small Particles*, John Wiley & Sons, New York.

Van Laarhoven, P.J.M. and Aarts. E.H.L. (1987). Simulated Annealing: Theory and Applications, D. Riedel Publishing Co.

Vaxman, A, Narkis, M., Siegmann, A., and Kenig, S. (1991). Weld-Line Characteristics in Short Fiber Reinforced Thermoplastics. *Polymer Composites*, *12*(3), pp. 161–168.

Vincent, M., and Aggasant, J.F. (1984). *Proc. IX Intl. Cong. on Rheo.*, *3*, p. 757, Mexico.

Vincent, M., and Aggasant, J.F. (1985). Important Flow Parameters in Determining Fiber Orientation. *Rheol. Acta*, *24*, p. 603.

Vincent, M., and Aggasant, J.F. (1986). Experimental Study and Calculations of Short Glass Fiber Orientation in a Center Gated Molded Disc. *Polymer Composites*, *7*, p. 76.

Voigt, W. (1910). *Lehrb d Kristallphysik*, (Teubner).

Walpole, L.J. (1966a). *J. Mech. Phys. Solids*, *14*, p. 151.

Walpole, L.J. (1966b). *J. Mech. Phys. Solids*, *14*, p. 289.

Wang, V., Hieber, C., and Wang, K. (1986). Dynamic Simulation and Graphics for the Injection Molding of Three-Dimensional Thin Parts. *Journal of Polymer Engineering* *7*, pp. 21–45.

Weber, T. (1992). Design and Construction of an Experimental Plastic Extruder. Unpublished Studienarbeit Thesis, Michigan State University, East Lansing.

Weber, M. E., and Kamal, M.R. (1992). Mechanical and Microscopic Investigation of Whisker-Reinforced Silicone Rubber. *Polymer Composites*, *13*(2), pp. 133–145.

Westerbecke, M. (1992). Measurement of the 3-dimensional Fiber Orientation in Injection Molded Parts. Unpublished Diplomarbeit Thesis, Michigan State University, East Lansing.

Wetherhold, R.C., Dick, W.A., and Pipes, R.B. (1980). Thickness Effects on Material Properties in a Glass/Thermoplastic PET Injection Molding Compound, SAE Technical Paper, 800812.

Wetherhold, R.C., and Scott, P.D. (1990). Prediction of Thermoelastic Properties in Short-Fiber Composites Using Image Analysis Techniques. *Composites Science and Technology*, *37*, pp. 393–410.

White, J.L., and Spruiell, J.E. (1981). *Polymer Engineering Science*, *21*, p. 859.

White, J.L., and Spruiell, J.E. (1983). *Polymer Engineering Science*, *23*, p. 247.

Woebcken, W. (1962). Effects of Processing Techniques on Structure of Molded Parts. *Modern Plastics*, *40*, p. 146.

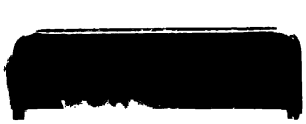
Wu, C.D. and McCullough, R.L. (1977), in *Developments in Composite Materials*, G.S. Holisten, ed., Applied Science Publishers, London.

Wu, J.P., and White, J.L. (1991). Study of Birefringence Character of Injection- and Compression-Molded Polycarbonate and its Interpretation. *Polymer Engineering and Science*, *31*(9), pp. 652–660.

Xavier, S.F., Tyagi, D., and Misra, A. (1982). Influence of Injection-Molding Parameters on the Morphology and Mechanical Properties of Glass Fiber-Reinforced Polypropylene Composites. *Polymer Composites*, *3*, p. 88.

York, J.L. (1982). Fiber Orientation in Curvilinear Flow. Unpublished master's thesis, University of Delaware.






MICHIGAN STATE UNIV. LIBRARIES
31293015553096